UNIVERSIDAD COMPLUTENSE DE MADRID

FACULTAD DE CIENCIAS FÍSICAS

THE ROLE OF INTERFACES IN HETEROSTRUCTURES: STRAINED MANGANITES AND SILICON FOR QUANTUM COMPUTING

EL PAPEL DE LAS INTERCARAS EN HETEROESTRUCTURAS: EL EFECTO DEL ESTRÉS EN MANGANITAS Y EL SILICIO PARA COMPUTACIÓN CUÁNTICA

TESIS DOCTORAL DE:

ALEJANDRA JULIETTE BAENA VASQUEZ

DIRIGIDA POR:

MARÍA JOSÉ CALDERÓN PRIETO

Madrid, 2014

©Alejandra Juliette Baena Vasquez, 2013

The role of interfaces in heterostructures: Strained manganites and Silicon for quantum computing

Alejandra J. Baena

Instituto de Ciencias de Materiales de Madrid (CSIC)

A thesis submitted for the degree of

Doctor of Physics

Director: *Dra. María José Calderón Prieto*

Tutor: Dra. Arantzazu Mascaraque Susunaga

2013 May

Contents

List of Figures v

List of Tables xi

General Introduction 1

Part I: Strained Manganites 5

1 Introduction 7

1.1 Transition Metal Oxides: Strongly Correlated Electron Systems 7

1.2 Effects of Complex Oxide Interfaces 13

1.3 Manganites 15

1.3.1 The first experimental works 16

1.3.2 The first theoretical approaches 18

1.3.3 Colossal magnetoresistance (CMR) 21

1.4 Manganite Thin Films and Heterostructures 21

1.5 Strain Effect in Manganites 26

2 Model 33

2.1 Relevant Interactions in Manganites 33

2.1.1 Double exchange (DE) interaction 33

2.1.2 Jahn Teller Effect 36

2.1.3 Antiferromagnetic AF superexchange interaction 38

2.1.4 Relevant Parameters 39

2.2 Strain effects in Manganites 40

2.3 Interface Effects in Manganites 42

3 Results **45**

3.1 Half-doped bulk manganites 45

3.1.1 Without Strain 45

3.1.2 With Strain 47

3.2 Metallic manganite/insulator interface 50

3.2.1 Without Strain 50

3.2.2 With Strain 54

4 Discussion and Conclusions **63**

Part II: Silicon for Quantum Computing **69**

5 Introduction **73**

5.1 Quantum Computing 73

5.2 Quantum bits 74

5.3 Quantum Operations 77

5.4 Advantages of building a Quantum Computer 79

5.5 Experimental Requirements for a Quantum Computer 80

5.5.1 Conditions for a quantum computation 82

5.6 Quantum Computer Proposals 83

5.7 Silicon for Quantum Computation 85

5.7.1 Features of the Silicon-Based Computer with Dopants: Kane Proposal 87

5.7.1.1 Single Qubit Operation: Nuclear qubit 90

5.7.1.2 Two-Qubit Operations: Spin Qubit 92

5.8 Quantum Confinement in Si Nanostructures: Dopants 97

5.8.1 Spin Relaxation and Decoherence 98

5.8.1.1 Spin Decoherence 99

5.8.1.2 Observed Coherence T_2 in Si 100

5.8.2 Orbital and valley relaxation 101

5.9 Silicon Based Quantum Computer Fabrication 103

5.9.1 Single dopants in MOS-based architectures: Top-down approach 103

5.9.2 Single dopants in crystalline silicon: Bottom-up approach 110

6 Relevant Silicon Features For Quantum Computing **113**
6.1 Bulk silicon: valley degeneracy 113
6.2 Valley Effects At The Donor 115
6.3 Valley Effects on the Interface V_{VO}^{I} 118
6.3.1 Valley Orbit Coupling at Interface V_{VO}^{I} 120
6.4 Valley Qubits Proposal 124

7 Model **125**
7.1 Donor States 126
7.2 Interface States 128
7.3 Full-Multivalley Hamiltonian 130

8 Results **137**
8.1 Full Spectrum of Eigenvalues of the 6-Valley Model 137
8.2 Evolution of Valley Composition of the Three Lowest States 138
8.2.1 Real V_{VO}^{I} 138
8.2.2 Area around F_{ch} 141
8.2.3 Complex V_{VO}^{I} 143

9 Discussion and Conclusions **151**

References **177**

List of Figures

1.1 Undistorted perovskite unit cell structure 10

1.2 d orbitals in the cubic crystal field 10

1.3 Sketch of the competition between the Hund's coupling J_H and the crystal field splitting (CFS) 11

1.4 Prototypical cases: The orbital spin pattern in $LaVO_3$ and $LaMnO_3$ . . 12

1.5 Prototypes of correlated electron systems: Phase diagram of a family of layered Ruthenates and phase diagram of Cuprates 13

1.6 Annular dark field (ADF) image of $LaTiO_3/SrTiO_3$ 15

1.7 Schematic phase diagram of $R_{1-x}A_xMnO3$ 17

1.8 PCMO with ($x = 0.3$) thin film based for ReRAM device 23

1.9 Schematic diagrams of and the tunnel magnetoresistance for four $La_{0.7}Ca_{0.3}MnO_3$ /$NdGaO_3$ /$La_{0.7}Ca_{0.3}MnO_3$ junctions 25

1.10 ρ-T and Magnetization versus Temperature curves for the PSMO with ($x = 0.5$) films on (001)-oriented LSAT, LAO and STO 28

1.11 Sketch of uniform tensile strain in manganites 29

1.12 Curie temperature T_C and saturation magnetization M_S of (001) and (110) LCMO films 30

2.1 Semi-classical model for double exchange interaction 34

2.2 Jahn-Teller modes of distortion: Q_1, Q_2 and Q_3 37

2.3 Sketch of the strain effect in a cubic lattice: Tensile strain and Compressive strain. 41

2.4 The strain effect on the energies of the e_g orbitals. 42

3.1 Cartoon of the possible spin and orbital order configurations considered here for half-doped manganites: FM (ferromagnetic order); A, C and CE (antiferromagnetic orderings). 46
3.2 Bulk phase diagram of Jahn-Teller coupling λ versus antiferromagnetic coupling $\mathrm{J_{AF}}$ for half-doped manganites without strain effect. 47
3.3 Bulk phase diagrams of strain e_{xy} versus antiferromagnetic coupling $\mathrm{J_{AF}}$ for half-doped manganites. 48
3.4 Phase diagram as a function of λ and $\mathrm{J_{AF}}$, with compressive and tensile strain. 49
3.5 2-dimensional (xz plane) projection of the (001) $\mathrm{AMnO_3}$ manganite ($x = 0.3$)/insulator heterostructure. 51
3.6 Average charge per plane for the three possible configurations considered at a manganite/insulator interface: FM stands for all FM Mn planes, 1CE stands for a configuration with a single CE layer at the manganite surface, and 2CE stands for two CE layers at the manganite surface. . . 52
3.7 Average charge value of the interface region for 1CE and 2CE configurations at the manganite/insulator interface, without strain. The inset shows the density of states of a perfect CE-type AF. 53
3.8 Phase diagrams of screening parameter α versus J_{AF} without strain for the manganite/insulator interface of the three configurations considered here: FM, 1CE and 2CE. 54
3.9 Phase diagram of α versus J_{AF} for the manganite/insulator interface with (tensile and compressive) and without strain of the three configurations considered here: FM, 1CE and 2CE. 56
3.10 Phase diagram λ versus J_{AF} for the manganite/insulator interface with (tensile and compressive) and without strain of the three configurations considered here: FM, 1CE and 2CE. 57
3.11 Phase diagram J_{AF} versus e_{xy} for the manganite/insulator interface with and without the e_g level splitting from the strain effect. 58
3.12 Pseudospin τ_z and $|\tau_x|$ per plane with (tensile and compressive) and without strain for FM, 1CE and 2CE electronic reconstruction at interface. 59
3.13 Density of states on each plane of the heterostructure. 61

5.1 Qubit represented by two electronic leves in an atom. 75
5.2 Bloch sphere representation of qubit 76
5.3 Moore's Law. 86
5.4 An atomic force microscope (AFM) image of an experimental device with a P donor array implanted one-by-one into the channel region of a Si transistor. 88
5.5 Silicon-Based Quantum Computer Scheme by Bruce Kane. 89
5.6 Configuration of gates (A and J gates) for Silicon Quantum Computer by Bruce Kane 92
5.7 A-gate control of the qubit 93
5.8 J-Gate: Coupling Two Qubits 93
5.9 Energy levels representation of the coupled electron-spin system as a function of the electron-spin exchange coefficient J. 95
5.10 Schematics of dopants in Si, the electron states for dopant atoms in x-, y- and z-direction confinement potentials and Si nanostructure integrated into a transport device with source, drain and gate electrodes. 98
5.11 Experimental echo decay and theory for ^{nat}Si:P at different angles of the magnetic field 100
5.12 Decoherence time T_2 of Si:P donor electron spins over varied donor concentrations C_N (for nuclear) and ^{29}Si concentration 101
5.13 A schematics of the 'top-down" fabrication strategy. 104
5.14 Transport regimes for single dopants detection in MOS-based architectures 106
5.15 Source/drain differential conductance of a dopant in a FET and simulations of the gated donor eigenstates 107
5.16 Device structure of the single donor device. 108
5.17 Current spectroscopy on the single atom transistor (SAT). 109
5.18 Scanning electron microscope and schematic of a Si devices with shallow insulated P donors in a Si gated-nanowires 109
5.19 A schematic diagram of the "bottom-up" fabrication process. 111

6.1 Silicon crystal in real and reciprocal space 114
6.2 Theoretical and experimental binding energies of donor states (A_1, T_2 y E) 117

6.3 Binding energies for the interface states as a function of the electric field applied . . . 119
6.4 Schematic of the broken degeneracy of states at the interface . . . 120
6.5 Calculated intervalley coupling as a function of applied electric field . . 122
6.6 The valley-orbit coupling at the interface with respect to barrier height 123
6.7 Intervalley coupling as a function of the conduction band offset . . . 123

7.1 Manipulation of a single electron donor close to Si/SiO_2 interface . . . 127
7.2 Typical confinement lengths of the interface states in the z direction and the xy plane. Plots of the shapes of the envelope functions at the donor and at the interface . . . 131
7.3 Symmetry of levels at the donor and at the interface. Schematic of double well potential in the z-direction formed by the Coulombic donor potential plus the triangular interface/electric field potential . . . 133

8.1 Full spectrum of eigenvalues for different distances between donor and interface, in a wide range of electric fields with different magnitudes and signs for the real valley orbit coupling. . . . 139
8.2 Evolution of the valley composition of the three lowest eigenvalues in a wide range of electric fields around the F_{ch} with different magnitudes and signs for the real valley orbit coupling. . . . 140
8.3 Zoom on the characteristic field area for different values of distance between donor and interface with a real and small value of the valley orbit coupling. . . . 142
8.4 Plot of the difference between crossing and anticrossing points versus the distance between donor and interface with a real and small value of the valley orbit coupling. . . . 142
8.5 Sketch for different scenarios of the relative positions for the anticrossing and crossing points as a function of distance between donor and interface, as well as a function of the magnitude and sing of the real valley orbit coupling. . . . 144
8.6 Full spectrum of eigenvalues in a wide range of electric fields with a complex and large value of the valley orbit coupling . . . 145

8.7 Evolution of the valley composition for the three lowest eigenvalues around the characteristic field with different values of the distance between donor and interface using a complex and real large value of the valley orbit coupling. 146
8.8 Evolution of the valley composition for the three lowest eigenvalues around the characteristic field with different values of the distance between donor and interface using a complex and real small value of the valley orbit coupling. 148
8.9 Three lowest eigenvalues around the anti-crossings region for different values of the valley orbit coupling phase. The values of the two anti-crossing gaps versus the phase of the valley orbit coupling. 149

LIST OF FIGURES

List of Tables

5.1 First rough estimates for decoherence times, operations times (seconds) and maximum number of operations, for several of the first candidates for interacting systems of quantum bits. 81

5.2 Measurements of coherence time T_2 in different systems of mobile 2D electrons as well as confined electrons. 102

8.1 Evolution of the valley composition of the three lowest states for V_{vo}^I real and negative. 150

General Introduction

Physics phenomena at surfaces and interfaces of solids have motivated intense research activity, since works such as Grove's in 1882 (1), who possibly traced the experimental beginning of "Thin Films" noting that metal films were formed by sputtering of cathodes with high energy positive ions. Also as Tamm's work in 1932 (2) with the early predictions of specific electronic surface states. This field has given as results applications that have changed our lifestyle. One of the most notable examples is the metal-oxide-semiconductor field-effect-transistor (MOSFET) which is the core of every commercial electronic device. These technological successes in semiconductor heterostructures came together with the discovery of new phenomena, such as the quantum Hall effects.

Other kind of materials which are particularly fascinating, due to an incredible variety of functional properties sometimes inaccessible for semiconductors, are the transition metal oxides which are strongly correlated electronic systems. Many oxides crystallize in simple lattice arrangements, such as the cubic perovskite structure Fig. 1.1. The chemical formula is ABO_3 with A typically a rare earth or alkaline element (Ca, Sr, Ba), B a transition-metal, and O the oxygen. Their properties result from strong interactions between spin, charge, orbital and lattice. The several competing states give rise to complex phenomena and rich phase diagrams. Representative examples are the high T_c superconductivity in Cuprates (3) or the colossal magnetoresistivity (CMR) in manganites which have been studied in this work (4). Due to the strong correlations in these systems, a small external perturbation leads to a huge response. The extreme sensitivity of these properties to structural distortions and crystal chemistry provides many ways to control and engineer new functionalities in these materials, therefore we of course could expect that interfaces between different complex oxides should give rise

to interesting and unexpected new behavior.

Thin films and multilayers may provide new degrees of freedom to control the properties and to design new ones, through strain, size and other effects at interfaces. Superconducting, ferroelectric and magnetic tunnel junctions are only a few examples of the active fields of research on perovskite heterostructures where interface effects play a crucial role. Theoretical and experimental efforts have led, for instance, to the discovery of ferromagnetic metallic states in superlattices composed of antiferromagnetic (AFM) insulators (e.g. $LaMnO_3/SrMnO_3$) (5), a superconducting electron gas between two dielectrics (6), enhanced critical temperatures in high-T_c superconductor heterostructures (7), and an unconventional type of ferroelectricity in paraelectric/ferroelectric superlattices ($PbTiO_3/SrTiO_3$), which allows the tuning of the ferroelectric properties to a very large dielectric constant, which is independent of temperature. This is different from the usual ferroelectricity in which the dielectric constant is typically large but strongly evolves around the phase transition temperature (8).

In order to fully take advantage of strain and other effects at the interface, the growth of heterostructures must be controlled at the atomic plane level. Tremendous progress has been achieved in this field. Pulsed-laser deposition, sputtering, molecular beam epitaxy (MBE), chemical vapor deposition (CVD) and atomic layer deposition are the most used techniques for the growth of functional oxides. As far as the integration of these oxides in devices (transistors, memories, sensors, actuators) is concerned, few of them have now entered mainstream production. There is much evidence showing that strain could be relevant on properties at interfaces in thin films and heterostructures. Under this perspective, we have been motivated to improve our understanding of the role of strain at interfaces and how this affects the properties of manganite systems. In the first part of this work, we have analyzed the effect of the strain on homogeneously strained epitaxially grown manganites in the (001) direction. I have focused on the strain affecting the bulk manganite ground state of a half doped (0.5 electrons per manganese) manganite and the strain influencing the electronic reconstruction at the interface between a ferromagnetic metallic manganite and an insulator.

Some complex oxide compounds have been currently proposed to replace the Si based

compounds in heterostructures for some electronic devices. For instance, recently Intel and IBM have replaced the SiO_2 gate dielectric in their latest processors with HfO_2 due to the higher dielectric constant of this transition metal oxide (9); $SrTiO_3$ has also been also considered as a potential gate oxide for the replacement of SiO_2 in transistors (10). Despite this fact, the core technological platform for computation remains based on Silicon due to the maturity of Silicon technology which has lead to an exponential progress of microelectronics. These range from quantum computers to a wide spectrum of spintronics applications.

Silicon is an excellent host material for an entirely new generation of devices based on the quantum properties of charges and spins, because Silicon is an ideal environment for spins in the solid state, due to its weak spin-orbit coupling and the existence of isotopes with zero nuclear spin. Thus, the prospect of combining quantum spin control with sophisticated fabrication technology has encouraged extensive efforts in Silicon-based quantum devices, many of them trying to design and build a Silicon based quantum computer.

The progress in deposition techniques such as ion implantation (top-down approach) to realize the new generation of Complementary metal-oxide-semiconductor (CMOS) devices and scanning probe microscopy (bottom-up approach) to place dopants in Silicon has allowed the creation of atomic-scale electronic devices in Silicon. The ability to control the matter at the atomic scale and build devices with atomic precision has lead to the fabrication of a single-atom transistor (11) and ambitions to build a functional solid-state quantum computer based in Silicon. In the design of these new devices, the choice of a suitable interface (the two most common are Si/SiGe and Si/SiO_2), as well as it growth quality, play an important role to achieve the quantum mechanical confinement of electrons in Silicon. For instance, the interface is relevant for single-electron tunneling devices operation consisting of a Silicon potential well coupled to source, drain and gate electrodes. However, the interface effects are complicated by the fact that in real devices the quantum well interface is not perfectly smooth and oriented.

Interface effects are also crucial in the proposals for the physical implementation of a Silicon based quantum computer. Among them, the 1998 original proposal by Kane

(12) consists of an array of shallow donors Phosphorous in particular in Si. The design corresponds to donor electrons in a Si host, separated by a barrier (SiO_2) from metal gates on the surface. The "A gates" control the resonance frequency of the nuclear spin qubits; the"J gates" control the electron-mediated coupling between adjacent nuclear spins. In this proposal, device parameters as the applied bias and the depth of the donor from the interface affects the electron wave function at the position of the donor, thus the hyperfine coupling. Further, the presence of the interface affects the donor orbital states: Measurements in Si devices with dopants showed a significant deviation of the donor orbital states from the expected bulk spectrum (13, 14).

It is important to highlight that Silicon has multiple degenerate valleys in its conduction band. These valleys play an important role in both dopant and quantum dot devices and they determine low-energy properties. In the second part of this work, we have focused on the role of the valleys on the control of electrons bound to a substitutional P donor nearby a Si(001)/SiO_2 interface, inspired by the Si-based proposal. Using a full six-valley model, we have analyzed the valley composition of the states involved in the donor-interface shuttling process, opening here the possibility of manipulating of the valley degree of freedom in the Si:P/barrier system.

Part I: Strained Manganites

Effect of strain on the orbital and magnetic ordering of manganite thin films and their interface with an insulator

Abstract

In this part, we have mainly studied the effect of the uniaxial strain on the ground state electronic configuration of manganite thin films. Our model Hamiltonian for manganites includes the kinetic energy, the electron lattice coupling and the nearest neighbor antiferromagnetic superexchange. We consider the uniaxial strain arising from the lattice mismatch between a manganite and a cubic and insulating substrate and assume (001) as the growth direction. In our model the strain effect on the system is twofold: The strain modifies the hopping amplitude and introduces an energy splitting between the Mn e_g levels. We focused in two cases: The effect of strain (i) on the bulk magnetic ground state of a half-doped manganite and (ii) on the electronic reconstruction of a FM-metallic manganite interface with an insulator. The results show the strain plays an important role on the properties of manganite thin films. In particular, the strain drives an orbital selection which modifies the electronic properties and the magnetic ordering of manganites and their interfaces.

Part I: Strained Manganites

This part is organized as follows:

Chapter 1 introduces this work describing the main properties of transition metal oxides and interfaces, prioritizing the manganite thin films and heterostructures, and shows some experimental and theoretical results regarding the evidence of the strain affecting the properties of manganites.

In Chapter 2 the model Hamiltonian for manganites including the relevant interactions, which are the Double exchange, Jahn Teller effect and antiferromagnetic superexchange, is described. Uniaxial strain is also included in the model.

Chapter 3 shows the results on the modifications produced by strain in the phase diagram of half-doped ($x = 0.5$) bulk manganites and in the electronic reconstruction at an interface.

We finish in Chapter 9 with a discussion on the light of reported experimental results

1

Introduction

1.1 Transition Metal Oxides: Strongly Correlated Electron Systems

The rich array of phenomena found in oxides is largely due to the oxygen. Oxygen tends to pull electrons away from other atoms in the compound resulting in strong electrical fields at the interatomic scale. These fields can give rise to substantial correlations in behavior between the electrons of one atom and those of its neighbors. And the correlations in turn can lead to effects such as ferromagnetism, in which a electrons spontaneously line up and produce a magnetic field (15).

The correlations of electrons in a solid produce a rich variety of states, typically through the interplay between magnetism and electrical conductance. That interplay has itself been a long-standing research topic among condensed matter physicists. But, since the discovery of copper-oxide high-temperature superconductors in 1986 a more general interest in the Mott transition (16) (metal-insulator transition) in correlated electron systems has been emerging. This interest led to a discovery in 1993 of the so called colossal magnetoresistance (CMR) phenomenon in which a shift in the external magnetic field causes certain oxides to undergo an orders of magnitude change in electrical resistance (17).

The transition-metal oxides are an interesting family of compounds that belongs to correlated-electron systems in which electron interactions strongly determine electronic

properties. In such systems, the dual nature of the electron and how it interacts with its neighbors dispose which aspect predominates in a solid (wavelike or particlelike). According to the Bloch theorem, for instance, an electron placed in a periodic lattice behaves like an extended plane wave. However, when the number of free electrons in a solid becomes comparable to the number of the constituent atoms and the mutual electron-electron interaction becomes strong, electrons may lose their mobility, thus they localize in sites (18). When an electron in a solid is localized it has three attributes that determine its behavior: charge (e), spin ($\pm 1/2$) and orbital symmetry. Then, the charge, spin and orbital degree of freedom and their coupling would produce complex phases, and phenomena such as electronic phase separation, among others.

Many oxides crystallize in simple lattice arrangements, such as the cubic perovskite structure Fig. 1.1. The chemical formula is ABO_3 with A typically a rare earth or alkaline element (Ca, Sr, Ba), B a transition-metal, and O the oxygen. The active electrons are usually the outer d-orbitals of the transition metals. Despite the chemical and structural simplicity, transition-metal oxides display very different physical phenomena. Consider a transition-metal atom in a crystal with perovskite structure, it is surrounded by six oxygen ions, O^{2-}, which give rise to the crystal field potential. Wave functions pointing toward O^{2-} ions (e_g orbitals $d_{x^2-y^2}$, $d_{3z^2-r^2}$) have higher energy than those pointing between them (t_{2g} orbitals d_{xy}, d_{yz}, d_{zx}). As a consequence, the d-orbitals are splitted and there is quenching of the orbital angular momentum. The orbitals are illustrated in Fig 1.2. There is an energy gap between the e_g and t_{2g} orbitals which acts like a spin or charge degree of freedom. As for spin ordering, there is an exchange interaction among the electronic orbitals (pseudo-spin) on the neighboring transition metal ions, which contributes to orbital order on the lattice sites at low temperatures.

As explained below, the transition metal in manganites parent compound is Mn^{3+} (B in the formula) with four electrons. If we start filling up orbitals from bottom up, then, one orbital of the e_g manifold will be empty. With doping the electrons may be removed from the e_g sector. On the other hand, the t_{2g} electrons are not affected by doping. Their population remains constant, and the well known Hund's rule of atomic

physics [1] enforces the alignment of the three t_{2g} spins into an $S = 3/2$ state. Then, the t_{2g} sector can be replaced by a ''localized spin" at each transition metal atom. The spin interaction between the two sectors is contained in the Hund's coupling. The total spin of the individual ions depends on the relative value of the Hund's coupling in comparison with the crystal field splitting. If the Hund'coupling dominates, the result is a maximum total spin. However, not all the transitions-metal oxides are dominated by the Hund's term, and there are cases where the minimum spin configuration is the ground state. In Fig. 1.3 a sketch representing the Hund's coupling dominated and crystal-field dominated states is provided.

The complex behavior of transition metal oxides make them potential candidates for the development of novel technologies which involve the charge, spin and orbital degrees of freedom to control and manipulate the electrical conductivity (18, 19, 20).

In the Mott-insulating state of a crystal, the d electrons are almost entirely localized on the atomic sites, which makes the spin and orbital degrees of freedom combine to produce versatile ordering patterns. Prototypical cases for perovskite oxides are shown in Fig. 1.4 for $LaVO_3$ (a t_{2g} electron system, with two localized $3d$ electrons per V) and $LaMnO_3$ (an e_g electron system). For instance, in $LaVO_3$, the spins order in the z direction as ferromagnetic chains, but in the xy plane as antiferromagnets, with neighboring spins antiparallel. That spin configuration induces an orbital ordered state: d_{yz} and d_{zx} occupy alternate lattice sites in every x,y and z direction. The spin-orbital ordering makes the electronic structure highly anisotropic despite the materials nearly cubic symmetry. On the other hand, in YVO_3, a similar perovskite with a larger lattice distortion, the staggered spin and orbital order are just the reverse of the $LaVO_3$ (Although V oxidation states are 3+ in both materials, their magnetic structures are different due to the different lattice distortion caused by the different ionic size of the A-site atoms). In the manganites, for example $LaMnO_3$, the Jahn-Teller effect (this effect is described later in section 1.3), a local deformation of the MnO_6 octahedron,

[1] Hund's Rules for a given electronic configuration: (i) The lowest electronic term has maximum spin S; (ii) The lowest term has maximum angular momentum L; (iii) The lowest term has the largest total angular momentum J if the shell is more than half full, and the smallest J if the shell is less than half full.

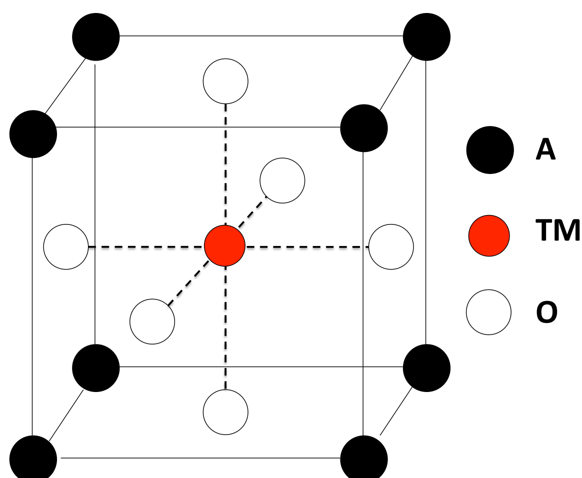

Figure 1.1: Undistorted perovskite unit cell structure. TM is a transition metal such as Mn, Cu, Ru, Ti which is in a cubic arrangement. O is oxygen, and A can be different combinations of alkaline elements, lead and rare-earth elements. The dotted lines mark the axes of a regular octahedron formed by the six oxygens.

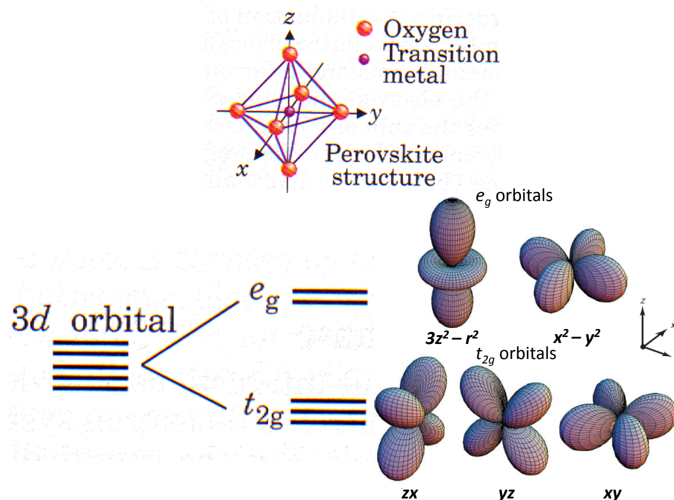

Figure 1.2: d orbitals. In the cubic crystal field, the fivefold degeneracy is lifted between the two e_g orbitals $[(x^2-y^2)$ and $(3z^2-r^2)]$ and the three t_{2g} orbitals [(xy), (yz) and (zx)]. Figures from Refs (18) and (19).

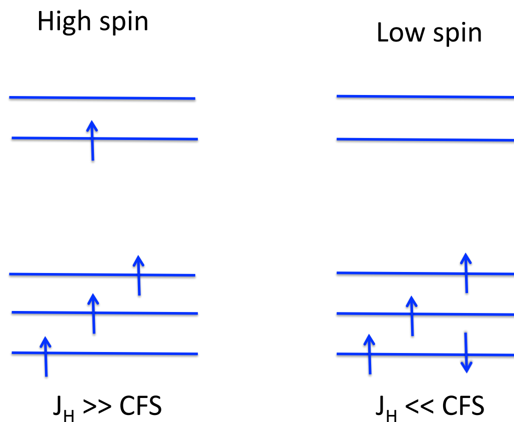

Figure 1.3: Sketch of the competition between the Hund's coupling J_H and the crystal field splitting (CFS) leading either to high-spin or low-spin configurations.

elongates the crystal in the xy plane and compresses it along the z-axis. This Jahn-Teller distortion lifts the orbital degeneracy and favors the occupation of a particular combination of the $d_{x^2-y^2}$ and $d_{3z^2-r^2}$ orbitals. Thus, in $LaMnO_3$, a local linear combination of those orbitals produces the stable states $d_{3x^2-r^2}$ and $d_{3y^2-r^2}$, alternating on the manganese sites in the xy plane. The corresponding spin-order is denoted as A-type AF, that is, ferromagnetic within the plane and AF between the planes. We will use the standard notation for the A-type AF order throughout this document.

As mentioned before, the interaction between spin, orbital and lattice is strong, producing a wide variety of complex phases. For instance $LaTiO_3$ is a Mott insulator (21). The intensively studied family of layered Cuprates, like $La_{1-x}Sr_xCuO_4$, presents antiferromagnetism, high critical temperature superconductivity, and a conducting state non-compatible with Fermi-liquid theory. Manganites, the subject of this work, show different magnetic orders, orbital and charge ordering and CMR. $TbMnO_3$ shows magnetic incommensurate phases that coexists with ferroelectricity. More exotic phases are found, for example, in Titanates and Ruthenates (22, 23).

The transition-metal oxides share another interesting characteristic: an exceptional sen-

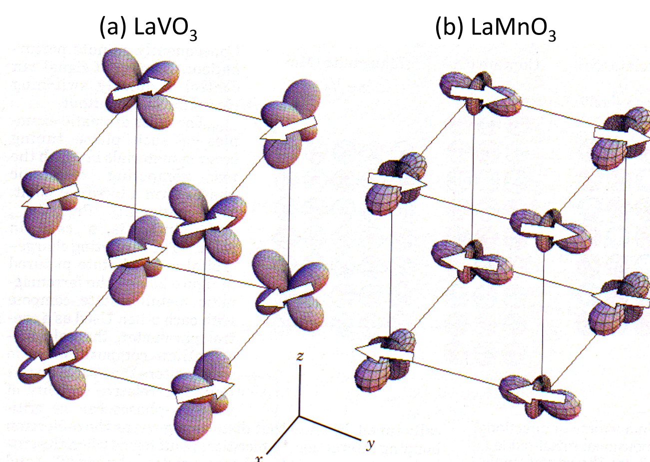

Figure 1.4: (a) The orbital spin pattern in $LaVO_3$: It consists of staggered t_{2g} orbitals (d_{yz} and d_{zx}). Here, the filled d_{xy} orbital on every vanadium site is not shown. White arrows represent the local spins at each vanadium ion. The orbital symmetry and order affects how and to which lattice sites electrons may hop. (b) The pattern in $LaMnO_3$ consisting of the e_g orbitals ($d_{3x^2-r^2}$ and $d_{3y^2-r^2}$ staggered in the xy plane). The spins couple ferromagnetically on the xy plane while stacking antiferromagnetically along the z axis. This ordering is denoted as A-type AF. Figure from Ref.(18).

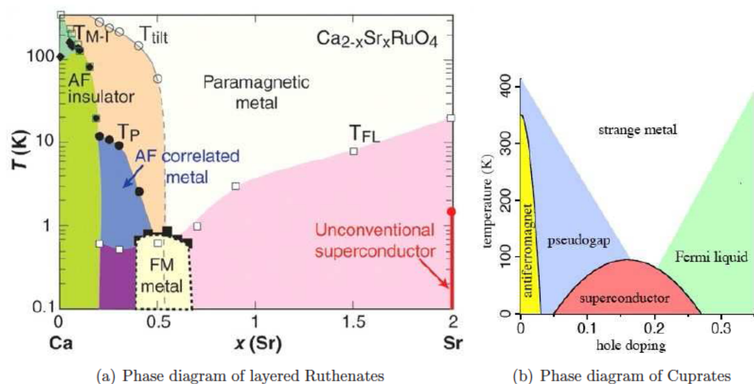

(a) Phase diagram of layered Ruthenates (b) Phase diagram of Cuprates

Figure 1.5: (a) Phase diagram of a family of layered Ruthenates, with chemical formula $Ca_{2-x}Sr_xRuO_4$. Different electronic phases, from insulating to superconducting, different magnetic orderings, and structural transitions appear. Notice that the Sr dopant is isovalent to Ca. The notation is standard, for details see (23) and (20). (b) Schematic phase diagram of Cuprates, prototype of correlated electron systems. Holes are introduced in the system by chemical doping. From Ref. (20).

sitivity to certain physical parameters, such us doping, pressure, magnetic field, or disorder. There are many published examples. In the family of Ruthenates $Ca_{2-x}Sr_xRuO_3$, the substitution of Ca by the isovalent element Sr produces a great variety of phases, despite the chemical similarity of the compounds (23). Fig. 1.5 illustrates the phase diagram of Ruthenate $CaSrRuO_3$ and cuprates (paradigm of electron correlated systems). The manganites properties are very sensitive to disorder and doping and show surprisingly large responses to magnetic fields (discussed in section below). Band theory is, in general, incapable to predict the stability of the exotic phases, and the huge responses to small or moderate stimulus. Therefore, the study of transition metal oxides constitutes a substantial and very active part of the field of *strongly correlated electrons.*

1.2 Effects of Complex Oxide Interfaces

At present, a way to perturb the strongly correlated electron systems is introducing interfaces through the nanofabrication of transition metal oxide heterostructures.

There are many works that evidence the effects of the interfaces. One of them which

provide a good example is given by the system formed by a Mott insulator $LaTiO_3$ (LTO) and a band insulator $SrTiO_3$ (STO). The results on this heterostructure indicate the presence of a bidimensional gas of electrons at the interface (24). This finding has prompted multitude of experimental and theoretical researches (25, 26, 27, 28) to clarify the origin of the novel electronic phase which does not appear in the bulk materials. In addition, this result has given rise to discuss whether the origin of the metal layer is extrinsic (oxygen vacancies) (29, 30) or intrinsic (polarity mismatch).

Okamoto and Millis (31, 32) made one of the first contributions to understand the appearance of a bidimensional electron gas at LTO/STO, which was attributed to electronic reconstruction at the interface. Their work was inspired by the striking experimental results from Ohtomo et al. (24), who fabricated atomically precise digital heterostructures by inserting a controllable number of planes of LTO into a controllable number of planes of STO, detecting the metallic interface mentioned above (heterostructure in Fig 1.6). The results of the calculations presented a leakage effect leading to electronic reconstruction, including different forms of magnetic and orbital order to those found in bulk, being the near-interface region metallic and ferromagnetic, whereas the bulk phase on either side is insulating and antiferromagnetic. Further, they showed a lattice relaxation surrounding the La ion, in which the electrostatic potential is screened, which may favor the charge transfer from LTO to STO.

The experiments reported that the metallic state also appeared at interfaces between two band insulators $LaAlO_3$ and $SrTiO_3$ (LAO/STO) (33). LAO/STO interfaces also present especially striking properties, such as electric field tunable superconductivity (6) and magnetic effects (29, 30, 34). Another example of interface effects is the combination between superconductor Cuprates ($YBa_2Cu_3O_7$) and ferromagnetic manganites ($La_{0.7}Ca_{0.3}MnO_3$) (35), where it is possible to induce ferromagnetism in the high temperature superconductor. Orbital reconstruction has also been reported in these heterostructures (36).

After more than 20 years of research on oxide thin films, the efforts are seeing results. Thin-film growth technology has been adapted for oxide compounds, desirable substrates have been developed and complex heterostructures are being studied for new

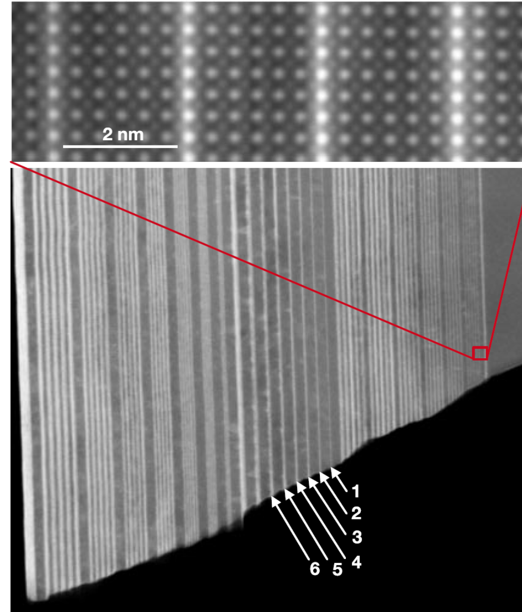

Figure 1.6: Annular dark field (ADF) image of $LaTiO_3$ layers (bright) of varying thickness spaced by $SrTiO_3$ layers. The view is down the [100] zone axis of the $SrTiO_3$ substrate, which is on the right. The numbers in the image indicate the number of $LaTiO_3$ unit cells in each layer. Field of view, 400 nm. Image from Ohtomo et al. (2002) (24).

functionality (new electronic compounds, as sensors, memory devices or solar cells) or simply for their exciting science (15). In spite of all this, the realization of high quality oxide heterostructures for applications still has some challenges to face, since they are still loaded with defects which may modify the desired properties.

1.3 Manganites

Among the transition metal oxides, I will focus on manganites. A wide range of phenomena and a variety of experimental work makes them specially attractive to the scientific community. In manganites strong coupling between charge, spin and lattice degrees of freedom produces a variety of phases in a chemically homogeneous material. In the early 1990's Jin and collaborators (37) reported a decrease of 3 orders of magnitude in the electrical resistance of a manganite thin film when a magnetic field was applied. This amazing magnetoresistance, named Colossal Magnetoresistance (CMR), raised the general interest and stimulated research on manganites for its potential for

application in commercial electronic devices.

Manganites are also half-metals (ferromagnets with only one type of conduction electron, either spin up, $\uparrow$, or spin down, $\downarrow$). This makes them good spin injectors and detectors for spintronics, an attractive, promising, and fast developing field (38).

Manganites present a rich phase diagram due to the close competition of different interactions. Charge/orbital ordering usually appears in half doped manganites (with 0.5 electrons per Mn) such as $Pr_{0.5}Ca_{0.5}MnO_3$(39), $La_{0.5}Ca_{0.5}MnO_3$(40), $Pr_{0.5}Sr_{0.5}MnO_3$ (PSMO)(41) and $Nd_{0.5}Sr_{0.5}MnO_3$(NSMO)(42). When small external perturbations, such as magnetic/electric field, strain or light are applied, drastic changes of resistivity and phase competition take place. In Fig. 1.7 the different phases arising with hole doping are shown for a family of manganites. Here, F denotes FM state. A, CE, C, and G denote A-type (FM planes coupled antiferromagnetically), C-type (FM lines in the z-direction coupled antiferromagnetically), CE-type (FM zig-zag chains coupled antiferromagnetically), and G-type (3D AF state) AFM states, respectively (19). Each of these magnetic orders are associated with a particular charge/orbital order as illustrated in Fig. 3.1. The C_xE_{1-x} state can be regarded as an extension of the CE-type charge/orbital order (43).

Before the important discovery of CMR, some works established the basic ideas and features of manganites. We will review the main characteristics, taking under consideration the main contributions to this field.

1.3.1 The first experimental works

The work of Jonker and Van Santen (44, 45) constitutes the mainspring of the field of manganites. Basically, they were interested in the properties of the transition metal oxides grown in the perovskite structure, as illustrated in Fig. 1.1. In particular, they grew different manganese oxides with a FM ground state. They called this whole family manganites.

The general chemical formula for manganites is expressed as $A_{1-x}A'_xMnO_3$, with A

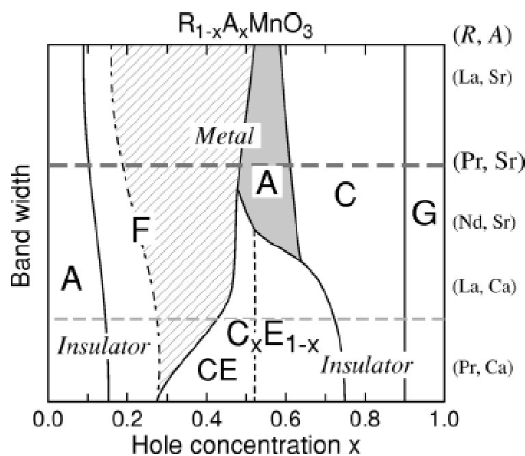

Figure 1.7: Schematic phase diagram of $R_{1-x}A_xMnO3$. F denotes FM state. A, CE, C, and G denote A-type , C-type, CE-type, and G-type AFM states, respectively. C_xE_{1-x} represents incommensurate charge/orbital ordered state. The respective orders have been illustrated in Chapter 3, Fig. 3.1. Figure taken from (43).

typically a trivalent rare-earth (e.g La or Pr) and A' a divalent cation (e.g Ca or Sr). One important aspect of the perovskite structure of these compounds is its capacity to accommodate both divalent and trivalent cations in the A position (44). When x is neither 1 nor 0, charge neutrality implies that Manganese is in a mixed valence state. $(1-x)$ is the number of electrons per Mn moving on the Mn e_g (x^2-y^2 or $3z^2-r^2$) orbital bands.

The points addressed in these first works are crucial to understand the behavior of manganites and are summarized in the following:

- the oxygen content of the sample depends closely on the preparation details, in particular on the composition of the atmosphere during preparation. They correctly realized that excess or defect of oxygen affected the average valency of the Manganese ions. This has been a subject of intense work, and, probably, a source of non exactly reproducible results until recent years.
- They found some kind of ferromagnetic interaction induced when mixed valence manganese was present in the material. They also inferred an antiferromagnetic

interaction between two Mn^{4+} ions, and discussed the nature of the interaction among Mn^{3+} ions. However, recent works indicate that the properties of manganites cannot be understood only in terms of pair like interactions: they are much better described if long range interactions, especially in the metallic regime, are considered. For instance, the long-ranged Coulomb interactions. Although these interactions can be substantially reduced in transition metal oxides by e.g. the polarization effects (particularly on the oxygen), this may affect the phase transitions (46).

- They established a correlation between the magnetic and conductivity properties: a high Curie temperature and saturation magnetization was associated to metallic-like and high conductivity in the so called optimal doping ($x \sim 0.3$).

In summary, Jonker and Van Santen established the main features of manganites and gave important indications for the growth and characterization. They started to reveal the rich phase diagram, but mainly, they demonstrated the close correlation between electronic transport and magnetism, crucially suggesting a common origin for both.

In 1995, other important contributions for the understanding of manganites were reported by Wollan and Koehler (47). They published a neutron diffraction study of the (La, Ca) manganite series. They obtained a rich and surprising phase diagram, and elucidated that despite the Manganese sites (magnetic active sites in manganites) form a simple cubic lattice, the different phases observed break this symmetry in several different ways. The competition between these phases is of great importance, and is probably responsible for the extremely large responses (Colossal) of manganites to moderate fields. They also found signatures of charge order, other important issue in manganites, which are still under discussion.

1.3.2 The first theoretical approaches

Simultaneously, in the early 1950's Zener published several theoretical papers about the magnetism of transition metals and their oxides, two of them focusing on manganites (48, 49). Zener deduced three principles in order to understand the lattice structure and magnetism of some of the transition metals, which are: *(i)* electrons in the incomplete d shells will have their spin correlated so that the total spin will be maximum.

This is equivalent to Hund's rule in atomic physics, and for manganites it implies that the Manganese ion is in a high spin state. That is, $S = 3/2$ for Mn^{4+} and $S = 2$ for Mn^{3+}; *(ii)* direct coupling between localized electrons in neighboring magnetic ions is always antiferromagnetic. Applied to the case of manganites, it explains how, in the absence of coupling mediated by conduction electrons (for insulating manganites), the ground state is antiferromagnetic; *(iii)* the conduction electrons are strongly coupled to the spin of localized electrons, and the coupling tends to align all the spins ferromagnetically.

It is important to highlight *the first principle* related with the quenching of the d orbitals momentum taking place. If the splitting of the crystal field is big compared with the dispersion of the band formed by the lowered t_{2g} orbitals, a band insulator will form for a filling of three d electrons per Manganese. Experimental measurements confirm the Hund's coupling as $1-2$eV (50), such that dominates the crystal field splitting ($\sim\rightarrow$ 1eV) (4). However, in manganites, the much used simplification is the limit $J_H = \infty$. In this case the e_g electron necessarily must have a spin perfectly parallel to that of the localized t_{2g} spin at the same site. This case corresponds to $CaMnO_3$ ($x = 1$), one end member of the family of manganites discussed by Jonker and Van Santen. In fact in manganites the three electrons in the t_{2g} orbitals form a localized 3/2 spin which is often called spin "core" (46). These localized spins are antiferromagnetically coupled via superexchange interaction, leading to G-type AF order in $CaMnO_3$. In Section 2.1.1 and section 2.1.3 we will describe the Zener mechanism, known as the Double Exchange Mechanism, and the Antiferromagnetic Superexchange interaction.

In the 1960's de Gennes considered theoretically the relative thermodynamic stability of different magnetic orders using a mean-field approximation (51). This work has mostly been cited in relation to his prediction that canted phases should appear when doping the antiferromagnetic phase (specially, the A phase in the Wollan and Koehler notation) with holes.

De Gennes's and earlier theoretical works (49, 52) neglected the twofold degeneracy of the e_g orbitals. When modern computers allowed numerical study of the double exchange model, a one orbital model was used (46, 53, 54, 55). However, the orbital

degeneracy is of crucial importance to reproduce some phases already observed by Wollan and Koehler. In particular, the A phase present in undoped manganites such as $LaMnO_3$ or the CE (56, 57, 58) phase appearing for compositions near half-doping. The one orbital model correctly reproduces some of the main features of the ferromagnetic metallic state, even the insulator-metal transition found for instance in $LaCaMnO_3$ at optimal doping (53).

De Gennes's also remarked the electron-lattice coupling. He commented that this coupling would alter the effective masses and mobility of the carriers, but it is well known that the effects are much more important. We will consider two types of distortions present in manganites. The first one is the distortion in the unit cell due to the changes in the network of the MnO_6 octahedra. The second one corresponds to symmetric distortions of the octahedra, known as Jahn-Teller distortions.

Distortions of the unit cell can be described as changes in the arrangement of the MnO_6 octahedra. If the tolerance factor Γ[1], is related to the average radius of the species occupying the different positions on the perovskite structure, depicted in Fig 1.1 is exactly one, the perovskite unit cell is ideally cubic. This only happens if the ions in the material are perfectly matching sized. If $\Gamma \neq 1$ either by ionic size mismatch or by external pressure, a distortion takes place and the Mn-O-Mn angle is less than 180°. This effect strongly affects the bandwidth of the e_g band, since it reduces the e_g hopping. The reduction of the bandwidth enhances the effects of other interactions competing with the kinetic energy, mainly the antiferromagnetic and Jahn Teller interactions (59).

The Jahn Teller distortions are very important in manganites and have been studied intensively in many works (60). According to this theorem, a system having a degenerate ground state will spontaneously distort. The distortion lowers the symmetry and removes the degeneracy, hence occupying only the lowest energy state and a new ground state with lower energy is reached. In manganites, since neighboring octahedra share corners, distortions are coupled and the Jahn Teller effect is cooperative. Kanamori studied cooperative distortions arising from the Jahn-Teller theorem in

[1] $\Gamma = (r_A + r_O)/(r_B + r_O)$, with r_i the average radius of the different species in the perovksite structure

different (undoped) compounds, such as $LaMnO_3$ (61). The Cooperative Jahn Teller general formalism is given in Section 2.1.2.

Coulomb interactions in manganites are also important to the relative stability of the different phases. Hund's rule is in fact a consequence of the Coulomb repulsion: it accounts for the strong Coulomb repulsion of electrons in the same orbital. Interorbital interactions are also significant: The inclusion of interorbital repulsion at a mean field level stabilizes the experimentally observed A order against the Ferromagnetic order in undoped manganites. As was mentioned before, long range Coulomb interactions is important for electronic phase separation. A more detailed analysis about the role of Coulomb interaction in phase separation can be found in Ref (46).

1.3.3 Colossal magnetoresistance (CMR)

Jonker and van Santen (45) found a correlation between the metallic behavior and the FM state of manganites. In 1954 Volger first reported on the negative magnetoresistence of a manganite $La_{0.8}Sr_{0.2}MnO_3$. The magnetoresistence (MR) is defined as $MR = \frac{R_H - R_0}{R_0}$ with $R_{H/0}$ the resistance with and without a magnetic field. The MR in manganites is negative due to the correlation between FM and metallicity. In the optimal doping region, the maximum MR happens at the metal insulator transition, close to the Curie Temperature. The change observed by Volger was quite small (10%), probably due to the polycrystalline nature of the sample and the method of fabrication. Only in the 1990's it was possible to improve the MR effect thanks to the development of growth techniques for high quality thin films. In 1994 Jin et. al (37) obtained 100000% value of MR (with MR defined as $\frac{R_H - R_0}{R_H}$) at low temperature in a $La_{0.67}Ca_{0.33}MnO_3$ thin film grown on $LaAlO_3$ that they called *Colossal Magnetoresistance* (CMR). This fact, together with the renewed general interest on complex oxides, the possibility of making layered heterostructures and the obtention of more and more exotic behaviors, concurred to renovate the interest in these materials.

1.4 Manganite Thin Films and Heterostructures

So far we have focused on intrinsic properties of manganites. However, not only intrinsic properties of bulk materials are interesting. Mutual influence of different compounds

and physical behavior at the reduced length scales typical in electronic devices or interfacial effects are important subjects in applied and basic condensed matter physics. This is particularly important for device engineering, because most devices involve interfaces.

Since manganites are complex systems which can display a broad range of physical phenomena, such as large spin polarization, colossal magnetoresistance, electronic phase segregation, orbital ordering, and charge ordering, they are ideal materials to develop novel concepts of oxide electronic devices (62). This fact has motivated intensive investigations of interfacial effects in manganite thin films with different complex oxides. The advantage of thin films consists in the possibility of studying crystals with high quality and a controlled amount of grain boundaries or defects. However, for instance the presence of a substrate may introduce a new degree of freedom in the already rich landscape of variables.

Much research on LSMO thin films with optimal doping ($x \sim 0.3$) indicated severe degradation of the magnetotransport properties below a critical thickness (63). The origin of this degradation has usually been attributed to the existence of phase segregation and disorder at the nanoscale motivated mainly by structural strain, oxygen stoichiometry, and variations of the chemical composition (62, 64). It is important to note that $La_{1-x}A_xMnO_3$ (A= Sr, Ca) systems at the optimal doping are very interesting from a technological point of view due to the highest magnetic transition temperature, especially LSMO with $T_C \sim 370$K.

Manganite thin films have been used to fabricate devices such as Resistance Random Access Memory (ReRAM) which work with the principle of the electrical pulse induced resistance change effect. One proposal of a resistive switching model is based on a PCMO thin film, since a report was published stating that a quite large resistance change in $Pr_{1-x}Ca_xMnO_3$ ($x = 0.3$) thin film was achieved at room temperature using an external electric pulse (65). Experimental studies suggested that the resistivity of Pt/PCMO/Pt (see illustration in Fig 1.8; Pt are the electrodes) depends mainly on the PCMO deposition temperature, which was related to the crystallinity of the thin films. In amorphous PCMO, the highest resistivity comes from the lowest deposition

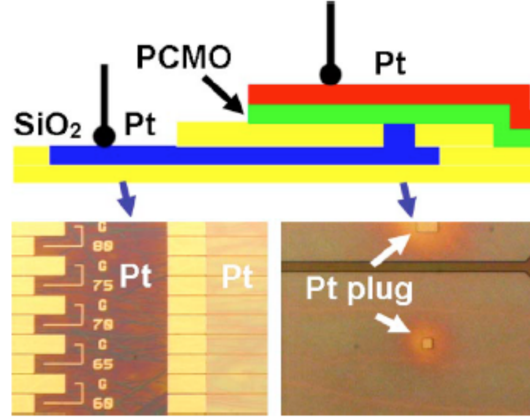

Figure 1.8: PCMO thin film based for ReRAM device. Schematic cross-sectional image of specimens. Corresponding optical microscope images of top view of real specimen is shown bottom right. Illustration taken from (66).

temperature ($\sim$ 350K) and this exhibited a resistive switching when pulses were applied (66).

Thin film studies are also relevant in multiferroic material such as $BiMnO_3$ (BMO). Multiferroic materials in bulk exhibit both ferromagnetism and ferroelectricity (FE) simultaneously, thus they are interesting for information technology. BMO thin films have been reported to be FM and FE (67). However, only few films show magnetic properties similar to bulk BMO and high enough resistivities, that is, low leakage currents to allow clear measurement of the FE properties. A possible reason suggested for the low resistivities of BMO thin films is the substrate induced strain or oxygen vacancies at interface (67, 68, 69).

Likewise, manganites heterostructures have been in the spotlight due to the appearance of new electronic phases different from bulk or thin films (electronic reconstruction, see Section 2.3).

Substantial theoretical works (32, 70, 71) have highlighted the role played by a number of interface phenomena (modified screening, band bending, polarity mismatch) in the determination of electronic parameters (bandwidth, on-site Coulomb interaction) potentially responsible for profound changes in the local charge, spin and orbital struc-

ture. In this regard, the possibility of artificially manipulating spin states at interfaces is particularly attractive in the framework of spintronics. For instance, at the interfaces between ferromagnetic (FM) metallic manganites and insulators, charge, orbital and spin ordered phases (70) appear. In heterostructures involving a band insulator ($CaMnO_3$) and a half-doped ordered manganite ($La_{0.5}Ca_{0.5}MnO_{0.3}$) in which the insulating behavior is driven by the strong correlation in the system, the formation of a metallic plane at the interface was evidenced (70). This result is similar to what has been observed in Mott/band insulator, as well as in band insulator/band insulator heterostructures (24, 33).

The adequate exploitation of the strong coupling between the electric and magnetic properties in manganite heterostructures has given rise to the most famous existing spintronic devices: spin valves. A spin valve is created by three layered devices, with a first FM (e.g LSMO with optimal doping $x = 1/3$) lead which is used as a spin polarizer, a non-ferromagnetic spacer, and a second FM lead used as spin analyzer (see example in Fig 1.9 a). The work principle of these devices is the strong dependence of the electrical resistance on the relative orientation of the spin polarized source and drain. A spin valve has an efficiency given by the tunneling magnetoresistence (TMR)(72), which is defined as the difference in the resistance R between parallel (P) and antiparallel (AP) relative orientations of the magnetization in the FM metallic electrodes[1]. Fig. 1.9 b) shows the TMR for a particular manganite based device.

A typical example of the interface effects is the striking suppression of the spin polarization at temperatures much lower than the bulk FM T_c (54, 74) leading to the so called "dead layer". This suppression is not beneficial for spin valves, due to the fact that TMR depends very strongly on the properties of the electrode/barrier interface (75). One of the reasons for the reduction of the spin polarization at the interface comes from the lack of carriers which attenuates the double exchange FM coupling between the Mn ions (70). Spin polarization can also be reduced by strain, disorder or oxygen vacancies. For instance experimental results on ferromagnetic/antiferromagnetic (FM/AFM) superlattices of five LSMO/PCMO units indicates the presence of a magnetically dead layer in the LSMO at the interface with PCMO, where the magnetization

[1] $TMR = (R_{AP} - R_P)/(R_{AP})$

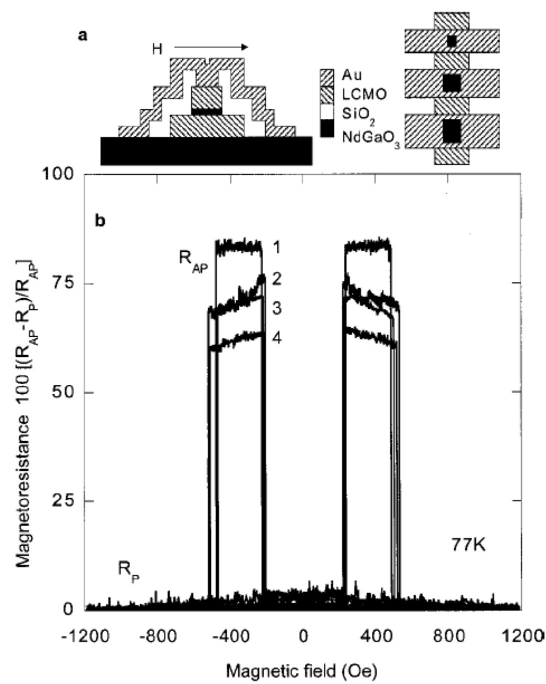

Figure 1.9: a) Schematic diagrams of the cross-section (left) of a typical device and (right) plan view of several devices on a common base electrode. b) Junction resistance versus applied magnetic field. The tunnel magnetoresistance at 77 K for four $La_{0.7}Ca_{0.3}MnO_3$ /$NdGaO_3$ /$La_{0.7}Ca_{0.3}MnO_3$ junctions. Junction areas (1) $6 \times 6\mu m^2$, (2) $8 \times 8\mu m^2$, (3) $8 \times 16\mu m^2$ and (4) $20 \times 30\mu m^2$. Results from Jon et al. (2000) (73).

is suppressed (76). However, the magnetic moment of PCMO is remarkably enhanced where nanometric FM droplets would find the optimal strain conditions to be accommodated within the AFM PCMO .

Modifications in the electronic ground state can also lead to new functionalities. One example is the FM insulating phase induced in an otherwise AF insulator $La_{0.3}Ca_{0.7}MnO_3$ due to proximity of a FM metal $La_{0.7}Ca_{0.3}MnO_3$ (77).

The evidence of surface orbital reconstruction has also been presented (78, 79), which could be promoted by the different strain or thickness patterns. The anisotropy of the d orbitals influences the electron correlation effects in an orbital direction dependent manner, thus giving rise to the anisotropy of the electron transfer and for instance destroying the DE mechanism of unstrained half-metallic LSMO. Likewise, theoretical calculations on half doped manganites $La_{0.5}A_{0.5}MnO_3$ show that the lack of cubic symmetry at surfaces, combined with the double exchange mechanism, leads to significant changes in the magnetic and transport properties. Charge is transferred from the bulk to the surface layers, and an antiferromagnetic ordering of the surface spins is favored (54).

Many works suggest that orbital order, magnetic structure, octahedral JT distortions, as well as the conduction properties change under the influence of strain. The effects of the strain on the electronic and magnetic properties was the goal of this work.

1.5 Strain Effect in Manganites

The influence of substrate strain is the main factor distinguishing manganite thin films from bulk samples. This is due to the fact that Mn e_g electrons which determine most of the physical properties are coupled to the lattice degree of freedom. In particular, strain can affect the electronic properties through orbital ordering, thus altering the magnetotransport properties of manganites thin films or heterostructures. Strain modifies both in-plane and out-of-plane lattice parameters (related to each other by the

Poisson ratio[1](80, 81, 82)), when different substrates are used.

Early works, for instance Jin et al. (1995) studied on LCMO ($x = 0.3$) films the effect of various substrates as well as film thickness on the CMR (83). They found that the strain effect, expressed through the change in the MR ratio, is most pronounced for epitaxial films. They speculated that stress is most effectively propagated through the film thickness in the absence of grain boundaries. Many other groups have investigated the strain effects by growing various films on different substrates (84, 85, 86, 87, 88).

Furthermore, theoretical and numerical studies have predicted and corroborated experimental findings on thin films and heterostructures with manganites. Millis et al. in (1998) (89) made theoretical predictions about the dependence of the ferromagnetic curie temperature T_c of the colossal magnetoresistance CMR rare earth manganese perovskites with strain. The results indicated that T_c is extremely sensitive to strain, hence exhibiting the strain as an important variable which must be considered in the design of devices based on thin films. Further, this early study of strain effects gave evidence of the relevance of the Jahn Teller electron-phonon coupling to the CMR phenomenon (89).

These results have shown the strain playing a key role in controlling the orbital ordering, magnetic structure, octahedral JT distortions, as well as the conduction properties in manganites. From the results it has been possible to predict that the effects due to strain are mainly due to the strain modification of both the in-plane and out-of-plane lattice parameters. Therefore, the reduction (increase) of the lattice parameter in a particular direction leads to an increase (reduction) of the hopping amplitude. Furthermore, the strain causes a distortion of the pseudocubic symmetry which leads to a splitting of the e_g levels which may produce orbital ordering via the Jahn-Teller coupling (19, 64, 82, 90, 91).

Taking the $Pr_{0.5}Sr_{0.5}MnO_3$ (PSMO) case, the experiments have shown a strong phase

[1]Poisson ratio (ν) is the negative ratio of transverse to axial strain. For manganites the relation between the strain in the z-direction e_z and in the xy-plane e_{xy} is given by ν as $e_z = -4\nu e_{xy}$ with $0.3 \lesssim \nu \lesssim 0.4$.

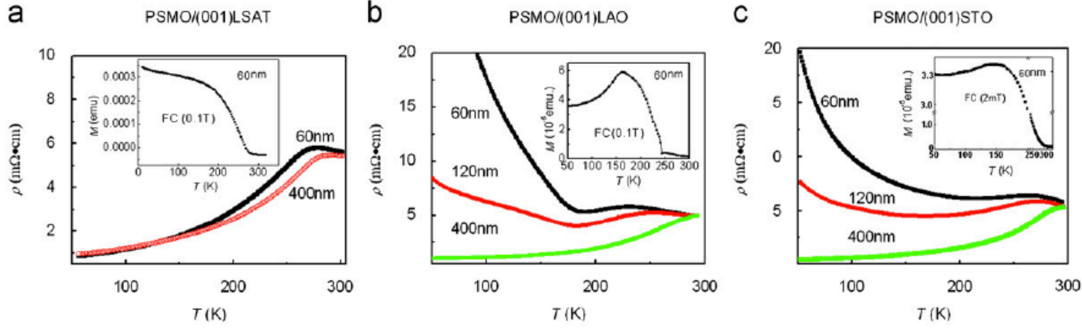

Figure 1.10: Results from Chen et al. (2012) ρ-T curves for the PSMO ($x = 0.5$) films on (001)-oriented LSAT (a), LAO (b) and STO (c).The respective inset is the Magnetization versus Temperature curve of 60 nm film. More details in Ref. (92).

competition therein yielding a ferromagnetic metal to antiferromagnetic insulator transition (FM-AF). PSMO in bulk has a stripe-type charge ordering with $d_{x^2-y^2}$ orbital state and A-type AFM spin ordering which is different from many other half-doped manganites which stabilize the CE order (43). The observations indicated that this phase transition of the PSMO films depend on several factors such as the orientation of the film growth, deposition temperature and strain. Recently, for example Chen et al. (2012) have reported a study on PSMO films with various thickness, epitaxially grown on different commercial substrates of (001)- oriented $(LaAlO_3)_{0.3}(SrAl_{0.5}Ta_{0.5}O_3)_{0.7}$(LSAT), $(LaAlO_3)$ (LAO) and $SrTiO_3$ (STO). See some results in Fig. 1.10. They found that a FM-AF transition is present in both largely compressed situations deposited on LAO ($\sim$ 1.3%) (001) and tensile cases deposited on STO ($\sim$ 1.5%) (001) but absent in little strained films grown on LSAT($\sim$ 0.8%) (001). They also observe the disappearance of the FM-AF transition with increasing thickness (due to strain relaxation) of the film (92).

There are also reports of a strong depression of the kinetic energy in thin $La_{0.7}Sr_{0.3}MnO_3$ leading to the disappearance of the metal-insulator transition when the film thickness is decreased below a specific value that strongly depends on the substrate nature and on the film preparation conditions (85, 93). For the LSMO thin films ($\sim$ 15nm) deposited onto LAO substrates, the degradation of the magnetotransport properties for very thin films has been ascribed to the epitaxial compressive strain ($\simeq$ 2.3%) induced by the substrate (opposite effect to the one presented in Fig 1.11). This in-plane compressive

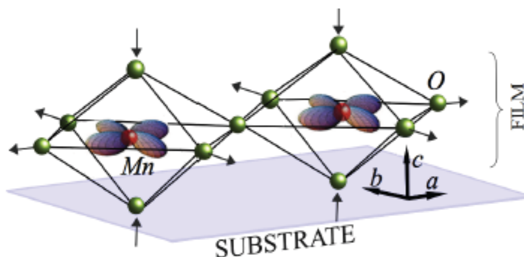

Figure 1.11: Uniform tensile strain in the a-b plane is introduced by lattice mismatch with the substrate. Volume conserving tensile strain expands the in-plane Mn-O bonds while contracting bonds in the c direction.This leads to a higher occupancy of the in-plane dx^2y^2 orbital Compressive strain, not shown, has the opposite effect. Figure from (94).

strain induced by the LAO substrate is strong enough to drive the LSMO film from the ferromagnetic DE metallic to the antiferromagnetic insulating C phase (93). This behavior may be related to the orbital ordered induced by the compressive strain.

The 3d Mn orbital occupation has been investigated by x-ray absorption linear dichroism experiments for the LSMO films deposited onto different substrates. In a cubic system, the 3d e_g orbitals are expected to be equally populated. On the contrary a preferential $d_{(3z^2-r^2)}$ orbital occupation was found so that in the case of the LSMO/LAO interface such an effect was ascribed to the compressive epitaxial strain which elongates the MnO_6 octahedra along the c axis thus lowering the energy of the of the $d_{(3z^2-r^2)}$ Mn e_g orbitals relative to (x^2-y^2) orbitals. In work done by Tebano and his collaborators, it was demonstrated that the degradation of magnetotransport properties, reported for relatively thick films, is a consequence of epitaxial strain alone and is not affected by interface chemistry (78).

It is important to highlight that both the orientation of epitaxial growth and substrate play a key role. For example, the structural and magnetic characterization of $La_{0.7}Ca_{0.3}MnO_3$ (LCMO) epitaxially grown on (110) and (001) $SrTiO_3$ substrates has shown that the (110) LCMO films relax earlier than the (001) LCMO ones and thus the (110) films display a progressively reduced strain. They also obtained evidence of strain promoting the antiferromagnetic orbital ordering. For instance, they found that tensile strain in bulk FM and metallic LCMO favors electron occupancy of the

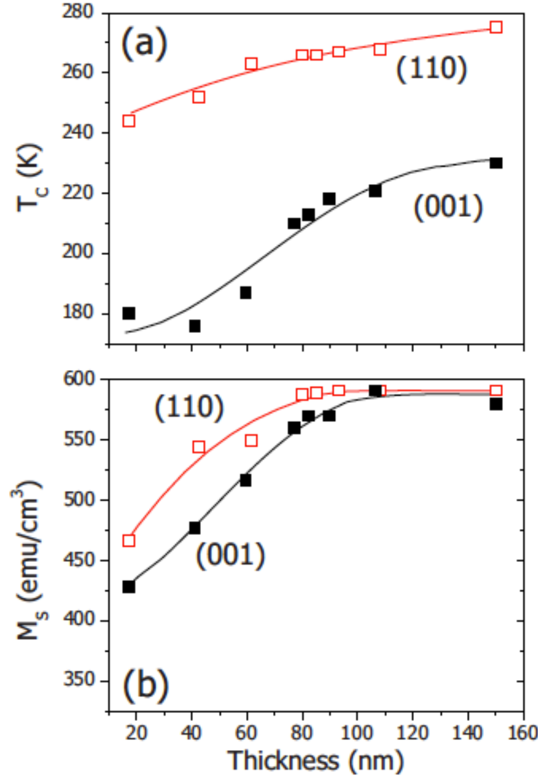

Figure 1.12: a) Curie temperature T_C and b) saturation magnetization M_S of (001) and (110) LCMO films closed and open symbols, respectively as a function of film thickness. Results from (95).

$d_{x^2-y^2}$ orbitals leading to A-type orbital ordering. However in the case of (110) growth direction, the splitting between e_g orbitals is smaller than that occurring in the (001), thus the driving force towards antiferromagnetic orbital ordering should be reduced in (110). However, in both cases the strain may contribute to depressing the magnetic properties of manganites (Curie temperature and saturation magnetization) thin films (95). Some results are shown in Fig. 1.12

In the following chapter we are going to describe the details and physical background that we use to propose a model and analyze the effect of the strain on homogeneously strained epitaxially grown manganites in the (001) direction. I will focus on two cases: The effect of the strain on

(i) The bulk magnetic ground state of a half-doped manganite and,

(ii) The electronic reconstruction of a FM-metallic manganite interface with an insulator.

2

Model

As now it is well known, manganites are specially interesting because they present a rich phase diagram as a function of composition and doping (43) due to the close competition of different interactions. Our general model includes the kinetic energy (through the double exchange (DE) interaction that results of considering an infinite Hund's coupling), the antiferromagnetic (AF) superexchange, the cooperative Jahn-Teller (JT) interaction, and the long range Coulomb interaction between the charges in the system (within a Hartree approximation). The model is solved self-consistently.

2.1 Relevant Interactions in Manganites

2.1.1 Double exchange (DE) interaction

The correlation between ferromagnetism and metallic conductivity in manganites was attributed by Zener (49) to an indirect coupling of the incomplete d-shells of the Mn via the carriers. The electrical conductivity is possible due to the mixed valency of the manganese ions. He proposed the electron transfer from one Mn ion to an adjacent Mn ion as the transfer of an electron from one Mn to the oxygen which is in the middle simultaneously with the transfer of an electron from the central oxygen to the other Mn ion. As two simultaneous processes are involved this mechanism was called double exchange. There are then two states:

$$\Psi_1 : Mn^{3+}O^{2-}Mn^{4+} \tag{2.1}$$

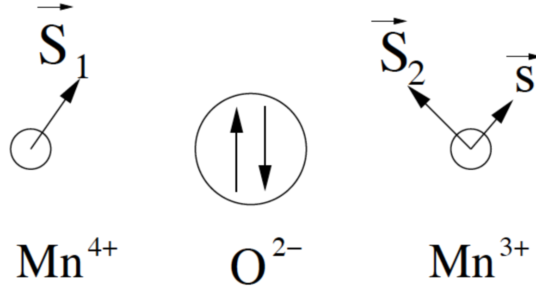

Figure 2.1: Semi-classical model for double exchange as seen by Anderson and Hasewaga (52). Spins S are considered large so they are assigned a definite direction in space, namely, they are treated as three dimensional vectors.

$$\Psi_2 : Mn^{4+}O^{2-}Mn^{3+} \tag{2.2}$$

which are degenerate in energy. A necessary condition for this degeneracy (and, hence, metallic conductivity) is that the spins of their respective d-shells point in the same direction because the carrier spin does not change in the hopping process and Hund's coupling punishes antialignment of unpaired electrons. The parallel coupling is of the order of magnitude of the hopping.

These ideas were formalized by Anderson and Hasewaga (52). They calculated the interaction for a pair of Mn ions with general spin $\overrightarrow{S}$ Fig. 2.1, transfer integral t, and internal exchange integral (Hund's coupling) J_H. In a semi-classical treatment, the electron, when transferred to a neighboring Mn ion, goes into the parallel state (in Fig 2.1 it implies that $\overrightarrow{s}$ has to be projected into the $\overrightarrow{S_2}$ direction). For $J_H >> t$, appropriate for manganites, they showed that E $\sim \cos(\frac{\Theta}{2})$ being Θ the relative angle between $\overrightarrow{S_1}$ and $\overrightarrow{S_2}$.

More recently, Mủller-Hartmann and Dagotto (96) considered the limit $J_H \to \infty$ (97) of the Kondo like Hamiltonian (98):

$$H = -t \sum_{\langle i,j \rangle} C^+_{i,\sigma} C_{j,\sigma} - J_H \sum_i \overrightarrow{\sigma_i} \overrightarrow{S_i} \tag{2.3}$$

Where, $C^{+}_{i,\sigma}(C_{j,\sigma})$ creates (annihilates) an electron at position i with spin $\sigma =\uparrow,\downarrow$ and $\overrightarrow{\sigma_i}$ is the electron spin operator $C^{+}_{i,\sigma}\overrightarrow{\sigma}_{\sigma,\sigma'}C_{i,\sigma'}$. $\sigma_x, \sigma_y, \sigma_z$ are the Pauli matrices.

Then the spin 1/2 of the carriers is rotated in each site such that their spin quantization axis is parallel to the core spin in that site. Only the spin up component matters. Hence, the $C_{i,\sigma}$ basis is substituted by a spinless d_i:

$$C_{i,\sigma} = d_i z_{i\alpha},\ z_{i\alpha} = \begin{pmatrix} cos\frac{\theta}{2} \\ sin\frac{\theta}{2}e^{i\psi_i} \end{pmatrix} \tag{2.4}$$

being θ and ψ the polar angles describing the direction of $\overrightarrow{S}_i$. Then, the Hamiltonian 2.3 can be rewritten:

$$H = -\sum_{\langle i,j\rangle} t_{ij} d^{+}_i d_j \tag{2.5}$$

where

$$t_{ij} = t^u_{\gamma,\gamma'} f(\theta_i, \psi_i, \theta_j, \psi_j) \tag{2.6}$$

$$f(\theta_i, \psi_i, \theta_j, \psi_j) = t^u_{\gamma,\gamma'}(\cos\frac{\theta_i}{2}\cos\frac{\theta_j}{2} + \sin\frac{\theta_i}{2}\sin\frac{\theta_j}{2})e^{i(\psi_i-\psi_j)} \tag{2.7}$$

where the hopping amplitude f depends on the Mn core spins orientation given by the spherical angles θ and ψ via the double-exchange mechanism, γ and γ' correspond to the e_g orbitals and u u is the direction of the hopping x, y, or z. This amplitude is considered finite only for Mn nearest neighbors.

Due to the large crystal field splitting and Hund's coupling (see Sec 1) the active

Mn orbitals are the e$_g$ ones (x^2-y^2 and $3z^2-r^2$). $t^u_{\gamma,\gamma'}$ is calculated in the Slater-Koster framework (99), which takes into account the symmetry of the orbitals (in the following $1 = x^2-y^2$ and $2 = 3z^2-r^2$) and that of the lattice. For a cubic lattice:

$$t^{\mathrm{x(y)}}_{1,1} = \pm\sqrt{3}\, t^{\mathrm{x(y)}}_{1,2} = \pm\sqrt{3} \tag{2.8}$$

$$t^{\mathrm{x(y)}}_{2,1} = 3\, t^{\mathrm{x(y)}}_{2,2} = t^{x,y}_o, \text{and} \tag{2.9}$$

$$t^{\mathrm{z}}_{2,2} = t^z_o. \tag{2.10}$$

In the absence of strain $t^{x,y}_o = t$ and $t^z_o = 4/3t$. Troughout this work t is taken as the energy unit.

2.1.2 Jahn Teller Effect

As already mentioned, manganites have the pseudocubic perovskite structure with chemical composition $A_{1-x}A'_xMnO_3$ with A typically a trivalent rare-earth (e.g. La or Pr) and A' a divalent cation (e.g. Ca or Sr). $1-x$ is the concentration of electrons moving on the Mn e_g orbital bands. Mn ions are in the center of oxygen octahedra that may undergo Jahn-Teller (JT) distortions. These lattice distortions couple to the charge and orbital degrees of freedom producing a splitting of the e_g levels sometimes associated with charge and/or orbital ordering.

In the cubic symmetry, the splitting due to the crystal-field effects leads to an e_g doublet and a t_{2g} triplet, as described in previous Chapter 1. The remaining degeneracy is usually broken by the lattice distortions. The ligand ions surrounding the transition-metal ion on consideration (in our case the oxygens around the manganese) can slightly readjust their locations, creating an asymmetry between the different directions that effectively removes the degeneracy. The lifting of degeneracy due to the orbital- lattice interaction is known as the Jahn Teller cooperative effect. This effect tends to occur due to the energy penalization of the lattice distortion growing as the square of that distortion, while the energy splitting of the otherwise degenerate orbital grows linearly.

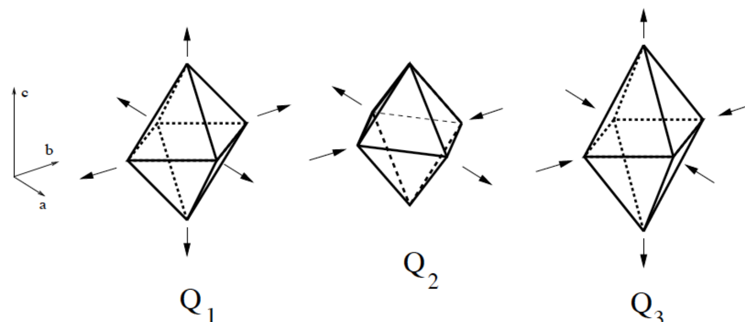

Figure 2.2: Q_2 and Q_3 are the two Jahn-Teller modes of distortion of the oxygen octahedra associated to the splitting of the e_g levels of Mn^{3+} (61) .These particular cases correspond to $Q_2 > 0$ and $Q_3 > 0$. Q_1 is the breathing distortion that occurs due to the different sizes of Mn^{4+} and Mn^{3+}.

For this reason, it is energetically favorable to spontaneously distort the lattice, thus removing the degeneracy.

Fig. 2.2 depicts the normal modes of vibration when the oxygens move along the x, y and z axis. In the case of manganites, the perpendicular modes (more details in Ref. (46)) are not important since they correspond to the displacement of the oxygens *perpendicular* to the direction of the Mn-O-Mn bond related to that oxygen. These displacements do not contribute to the splitting of the $d_{x^2-y^2}$ and $d_{3z^2-r^2}$ orbitals in which we are interested. In addition, the Q_1 mode being uniform in all directions does not contribute either to the splitting in the e_g sector. For these reasons, only Q_2 and Q_3 are needed to understand how the e_g degeneracy is removed.

The Electron-Phonon Interaction

The basic interaction between the Jahn Teller (JT) modes of the MnO_6 octahedron and the e_g electrons is given by:

$$H = \frac{1}{2}\sum_i [\beta Q_{1i}^2 + Q_{2i}^2 + Q_{3i}^2 + \lambda(Q_{1i}\rho_i + Q_{2i}\tau_i^x + Q_{3i}\tau_i^z)] \tag{2.11}$$

This term couples the e_g electrons with the three active MnO_6 octahedra distortions: The breathing mode Q_{i1}, and the JT modes Q_{i2} and Q_{i3} that have symmetry $x^2 - y^2$ and $3z^2 - r^2$ respectively. Q_{i1} couples with the charge at site i, $\rho_i = \sum_\gamma C^+_{i,\gamma} C_{i,\gamma}$, with γ the orbital index. Q_{i2} and Q_{i3} modes couple with the x and z orbital pseudospins defined as:

$$\tau_{xi} = C^+_{i1} C_{i2} + C^+_{i2} C_{i1} \qquad \text{and} \tag{2.12}$$

$$\tau_{zi} = C^+_{i1} C_{i1} - C^+_{i2} C_{i2} \tag{2.13}$$

The first term in Eq. 2.11 describes the elastic energy of the octahedra distortions, being $\beta >> 2$ the spring constant ratio for breathing and JT modes (58). The λ parameter is the Jahn-Teller coupling (electron-phonon coupling). In the perovskite structure the oxygens are shared by neighboring MnO_6 octahedra and the Q's distortions are not independent, cooperative effects being very important (53). In order to consider these collective effects we consider the position of the oxygen atoms as the independent variables of the JT distortions.

2.1.3 Antiferromagnetic AF superexchange interaction

In the limit when all the e_g electrons are removed from the system ($x = 1$) the DE model becomes trivial (the kinetic energy is zero) and the interaction between localized spins is only mediated by the t_{2g} electrons. Manganites have G-type AF state at ($x = 1$) (as occurs for instance in $CaMnO_3$). The localized spins must have an antiferromagnetic coupling among themselves to account for the G-type state. The t_{2g} electrons can induce an AF Heisenberg interaction through virtual hopping between nearest-neighbors, leading to the standard exchange mechanism. To account for this effect, the following term is introduced:

$$H_{AF} = J_{AF} \sum_{\langle i,j \rangle} \overrightarrow{S_i} \overrightarrow{S_j} \qquad (2.14)$$

Where J_{AF} is the AF coupling between nearest-neighbor $\langle i,j \rangle$ t_{2g} spins. The value of J_{AF} is usually small compared with the hopping amplitudes of e_g electrons and the Hund's coupling. However, J_{AF} plays a key role in manganites, because there are competing states with similar energies.

2.1.4 Relevant Parameters

- The crystal field that splits the five d-orbitals in three t_{2g} and two e_g has been estimated to be $\sim$ 1eV (100). It is due to Coulomb interactions between the electrons and the ionic charges. The splitting is large enough to allow the consideration of t_{2g} electrons as localized.

- The Hund's coupling J_H is the largest parameter in the problem. In a practical sense it can be considered ∞ as in the double-exchange model just introduced. Reported values are $J_H \sim 1.5 - 2$eV (98).

- The bandwidth W or, equivalently, the hopping parameter $t = \frac{W}{12}$. t has been estimated to be between 0.1eV to 0.5eV (101). The conduction band is the result of the hybridization of the outer oxygen p-levels and the e_g levels of the manganese ions. Manganites can be classified by the value of W (62). It gets smaller when lattice deformations become more important. As an example, LaSr compounds have a large W while LaCa have a small one. Large W is accompanied by a large magnetic critical temperature and large T_c is accompanied by a small magnetoresistance.

- The antiferromagnetic superexchange coupling J_{AF}. As I said above, the t_{2g} orbitals of the Mn ions are antiferromagnetically coupled. This parameter is much smaller than the hopping and it has been estimated experimentally to be around $0.1t$ (102) (we use a range of values for $J_{AF} = 0 - 0.3t$) but it has appeared

to be important when studying phase separation (55, 103) or when the double-exchange is weakened as it is for the extreme dopings $x = 0$ and $x = 1$, and also on surfaces (54).

- Jahn-Teller distortions and the electron-phonon coupling. We are considering the λ value (electron-phonon coupling) between $0 - 1.6t$. The Jahn Teller distortions split the degeneracy of the e_g orbitals.

2.2 Strain effects in Manganites

Here we will show how to include the effect of strain on homogeneously strained epitaxially grown manganites in the (001) direction. In the absence of strain, the Hamiltonian model for manganites includes all the interactions mentioned before, which are the kinetic energy, the electron-lattice Jahn-Teller coupling, and the nearest neighbor antiferromagnetic superexchange (104).

$$\begin{aligned} H &= -\sum_{i,j,\gamma,\gamma'} f_{i,j} t^{u}_{\gamma,\gamma'} C^{\dagger}_{i,\gamma} C_{j,\gamma'} \\ &+ \frac{1}{2}\sum_{i} \left[\beta Q_{1i}^2 + Q_{2i}^2 + Q_{3i}^2 + \lambda \left(Q_{1i}\rho_i + Q_{2i}\tau_i^x + Q_{3i}\tau_i^z\right)\right] \\ &+ \sum_{i,j} J^{ij}_{\mathrm{AF}} \vec{S_i}\vec{S_j} \end{aligned} \tag{2.15}$$

where $C^{\dagger}_{i,\gamma}$ creates an electron on the Mn i-site in the e_g orbital γ and $t^{u}_{\gamma,\gamma'}$ as defined in Eq 2.10. As mentioned above, here all the parameters are given in units of t which depends on the chemical composition (101). β is assumed to be very large so the Q_1 breathing mode is frozen. The other terms have already been specified in Section 2.1.

The strain is introduced uniformly in a cubic system (namely, $c/a = 1$ is assumed). We consider uniaxial strain arising from the lattice mismatch between the manganite and a cubic substrate and assume a (001) growth direction. The strain can be tensile (extension in the xy plane and compression in the z direction: $c/a < 1$) or compressive (compression in the xy plane and extension in the z direction: $c/a > 1$), as sketched in Fig. 2.3. The strain in the xy-plane e_{xy} is defined as $e_{xy} = (a_s - a)/a_s$ with a the

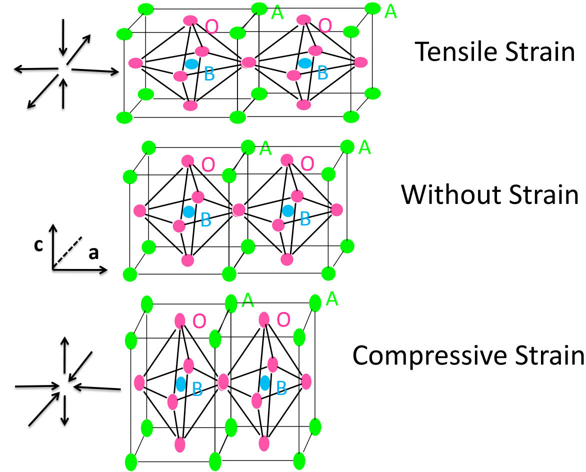

Figure 2.3: Sketch of the strain effect in a cubic lattice. (Top) Tensile strain, an extension in the xy plane and compression in the z direction, namely $c/a < 1$. (Bottom) Compressive strain, a compression in the xy plane and extension in the z direction, namely $c/a > 1$.

average lattice parameter of the manganite and a_s the in-plane lattice parameter of the substrate. See Fig. 2.4. Therefore, $e_{xy} > 0$ (< 0) corresponds to tensile (compressive) strain. The relation between the strain in the z-direction e_z and in the xy plane e_{xy} is given by the Poisson ratio ν as $e_z = -4\nu e_{xy}$ with $0.3 \lesssim \nu \lesssim 0.4$ for manganites (80, 81, 105). We choose $e_z = -\frac{3}{2}e_{xy}$ (106) and allow e_{xy} to range between -0.02 (-2%) and 0.02 (2%).

The effect of the strain on the system is twofold. On one hand, it affects the overlapping matrices and, therefore the hopping amplitudes as (107)

$$\begin{aligned} t_o^{x,y} &= t(1 - 2e_{xy}) \\ t_o^z &= 4/3t(1 - 2e_z)\,. \end{aligned} \tag{2.16}$$

The strain can also induce a splitting δ of the e_g orbitals (19, 89, 90, 105): tensile

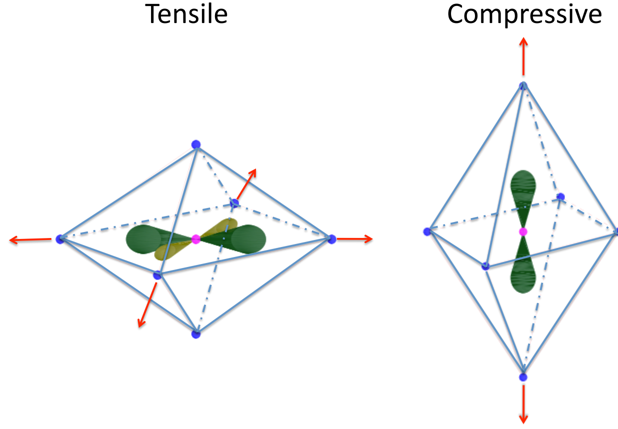

Figure 2.4: (Left) Tensile strain (namely $c/a < 1$, $\tau_z > 0$), lowers the energy of the $|x^2 - y^2\rangle$ orbital with respect to $|3z^2 - r^2\rangle$. (Right) Compressive strain (namely $c/a > 1$, $\tau_z < 0$) does the opposite.

strain lowers the energy of the $|x^2 - y^2\rangle$ orbital with respect to $|3z^2 - r^2\rangle$ ($\tau_z > 0$) while compressive strain does the opposite ($\tau_z < 0$), as illustrated in Fig. 2.4. This is introduced as an extra term in the Hamiltonian

$$H_\delta = \sum_\gamma \epsilon_\gamma \sum_i C^\dagger_{i,\gamma} C_{i,\gamma} \, , \tag{2.17}$$

with $\epsilon_{3z^2-r^2} = \delta/2$ and $\epsilon_{x^2-y^2} = -\delta/2$. We have analyzed a range of values $\delta \leq 100 e_{xy} t$ (namely $-2t \leq \delta \leq 2t$). (105)

2.3 Interface Effects in Manganites

In order to analyze the effect of the strain on the electronic reconstruction at a (001) interface in a manganite heterostructure, we have used the same Hamiltonian model

as described for the bulk case in Sec. 2.2 plus a term that takes into account the long range Coulomb interaction between all the charges in the system within a Hartree approximation. (70, 71, 108). H_{Hartree} takes the form.

$$H_{\text{Hartree}} = \frac{e^2}{\epsilon} \sum_{i \neq j} \left(\frac{1}{2} \frac{\langle n_i \rangle \langle n_j \rangle}{|\mathbf{R}_i - \mathbf{R}_j|} + \frac{1}{2} \frac{Z_i Z_j}{|\mathbf{R}_i^A - \mathbf{R}_j^A|} - \frac{Z_i \langle n_j \rangle}{|\mathbf{R}_i^A - \mathbf{R}_j|} \right) \tag{2.18}$$

with $\mathbf{R}_i$ the position of the Mn ions, $\langle n_i \rangle = \sum_\gamma \langle C^\dagger_{i,\gamma} C_{i,\gamma} \rangle$ the occupation number on the Mn i-site, eZ_i the charge of the A-cation located at $\mathbf{R}_i^A$, and ϵ the dielectric constant of the material. The relative strength of the Coulomb interaction relative to the electron hopping is given by the parameter $\alpha = e^2/a\epsilon t$, expressing the degree to which magnetic order controls electron occupation and hence hopping. The dielectric constant for a FM metallic ground state is $\epsilon = 5-10$, bringing a value of α in the range $0.7-2$ (109).

The long-range Coulomb interactions controlled by the Coulomb parameter drives the electrons to screen the charged ions. Therefore, at small α, the charge is only weakly confined, so for short period structures the charge is uniformly distributed and the system exhibits essentially the same phase as found in the randomly doped bulk material. For more model details of electronic phase behavior of correlated electrons in electrostatically defined heterostructures see Ref.(109). Experimentally, the charge transfer between different layers occurs within $2-3$ unit cells (5).

3

Results

3.1 Half-doped bulk manganites

Here we analyze the effect of homogeneous strain on half-doped ($x = 0.5$) epitaxially grown manganites in the (001) direction. Figure 3.1 depicts the spin and orbital order configurations considered. FM labels a three dimensional ferromagnet while the other three (A, C, and CE) are different antiferromagnetic orderings. We use this notation throughout this document for these different configurations. We find the ground state configuration of a half-doped manganite by solving the Hamiltonian in Eq. [2.15] plus the term in Eq. [2.17] self-consistently (at zero temperature) in a $4 \times 4 \times 4$ system with periodic boundary conditions in the three directions.

3.1.1 Without Strain

Fig. 3.2 shows the phase diagram for half-doped manganites ($x = 0.5$) as a function of λ (Jahn-Teller coupling) and J_{AF} (antiferromagnetic superexchange coupling). This phase diagram is well known from previous works (57), serving here as a reference result. It can be checked that for small values of J_{AF} and $\lambda < 1.6t$, the ground state is ferromagnetic (orbital disordered) and metallic (charge disordered) while for $\lambda > 1.6t$, the FM phase is insulating (57). As J_{AF} increases, two different antiferromagnetic phases arise, which are the A-type AF phase consisting of FM xy-planes coupled antiferromagnetically in the z-direction, and the CE-type AF. The CE order consist of FM zig-zag chains coupled AF between them. The A-type order appears only for a narrow

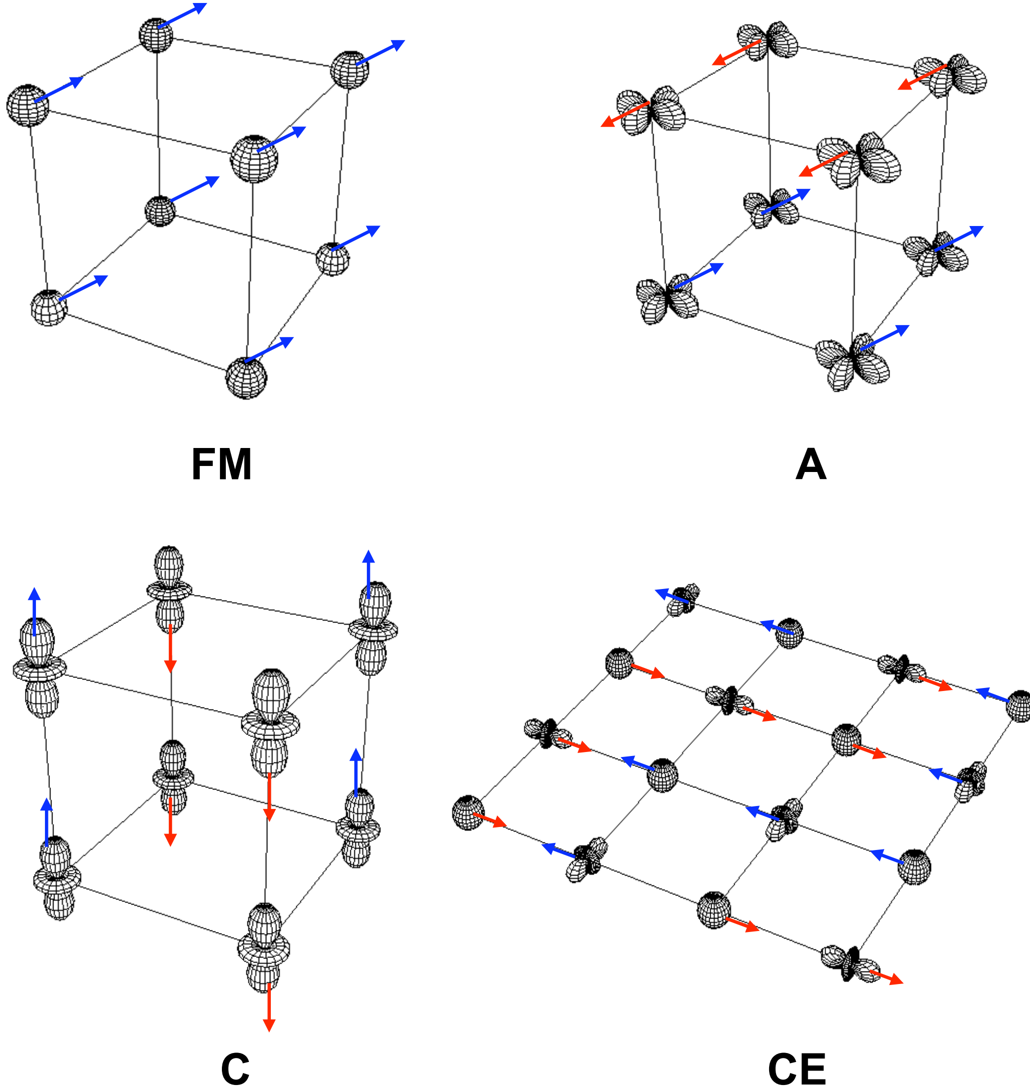

Figure 3.1: Cartoon of the possible spin and orbital order configurations considered here for half-doped manganites. FM labels a three dimensional ferromagnet while the other three (A, C, and CE) are different antiferromagnetic orderings associated with particular orbital orderings quantified by τ_x and τ_z as defined in Eq. 2.13. The FM configuration is orbital disordered (represented here by isotropic spherical orbitals), that is τ_z and τ_x = 0. The A-type, with FM planes coupled antiferromagnetically, favors the occupancy of the $x^2 - y^2$ orbitals, namely $\tau_z > 0$. The C-type, with FM lines in the z-direction coupled antiferromagnetically, favors the occupancy of the $3z^2 - r^2$ orbitals, namely $\tau_z < 0$. The CE-type ordering consists of FM zig-zag chains coupled antiferromagnetically (only one xy plane is shown here) and is associated with a peculiar orbital ordering (alternating $3x^2 - r^2$, $3y^2 - r^2$ and more isotropic orbitals) and checkerboard charge ordering, implying both τ_z and $\tau_x \neq 0$.

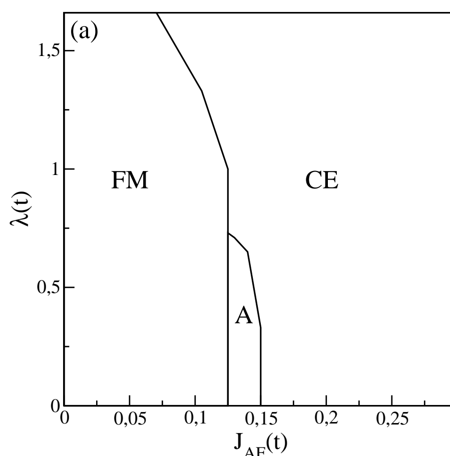

Figure 3.2: Bulk phase diagram of JT coupling λ versus antiferromagnetic coupling J_{AF} for half-doped manganites. FM, A, and CE label the different magnetic and orbital orders considered. The effect of strain is not included.

range of the J_{AF} values and $\lambda \leq 0.7t$.

3.1.2 With Strain

The effect of the strain on the ground state configurations is presented in Fig. 3.3. Fig. 3.3(a) shows the phase diagram as a function of strain (e_{xy}) and J_{AF}, for $\lambda = 1t$ and $\delta = 0$. Namely, in this figure we consider that the strain only affects the hopping amplitude, as described in Eq. 2.16. For these values of the parameters, the ground state is FM for $J_{AF} < 0.12$t and CE for $J_{AF} > 0.12$t. The effect of the strain leads to small shifts in the stability lines and to the appearance of the A phase for negative strain (compressive).

Compressive strain produces the reduction of the lattice parameter in the xy plane (namely, $e_{xy} < 0$ or c/a > 1), increasing the hopping within the xy plane and decreasing it in the z-direction. Consequently, $x^2 - y^2$ lowers its energy with respect to $3z^2 - r^2$ and the occupation of $x^2 - y^2$ is favored. Due to this orbital selection, the FM configuration loses energy with respect to the A-AF configuration. This behavior can be observed in Fig. 3.3 (a). Otherwise, tensile strain (namely $e_{xy} > 0$ or c/a < 1)

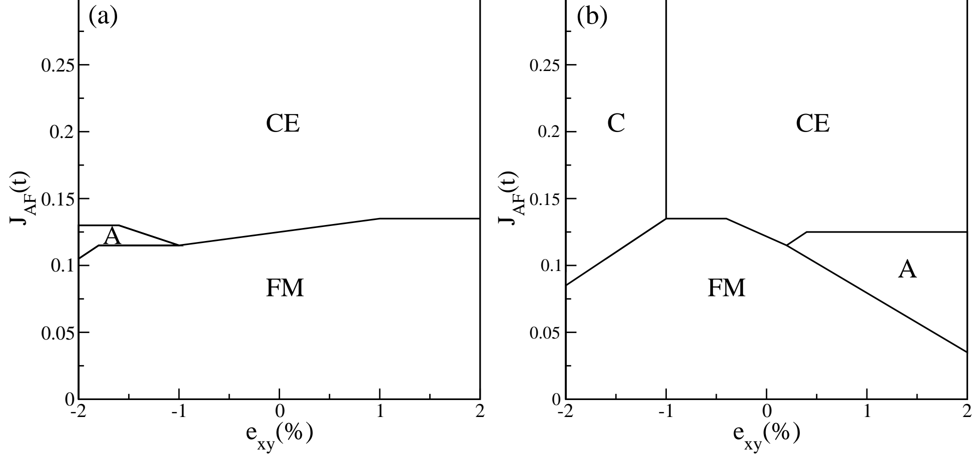

Figure 3.3: Bulk phase diagrams of strain e_{xy} versus antiferromagnetic coupling $\mathrm{J_{AF}}$ for half-doped manganites, with $\lambda = 1t$. FM, A, C and CE label the different magnetic and orbital orders considered. (a) With no splitting ($\delta = 0$) between the e_g Mn levels. (b) With a splitting $\delta = 100 e_{xy} t$ between the e_g Mn levels. The C phase appears for negative strain when $|\delta| > 50|e_{xy}|t$ if $\lambda = 0$ (not showed) and when $|\delta| > 60|e_{xy}|t$ if $\lambda = 1t$.

increases the hopping in the z-direction and lowers it in the xy-plane. In this case both AF phases (A and CE phases) lose kinetic energy with respect to the FM phase, as a result of the zero hopping in the z-direction.

In earlier experimental works (19, 64, 90, 110), it has been demonstrated that applying a compressive tetragonal distortion would produce a lowering of the $3z^2 - r^2$ orbitals with respect to the $x^2 - y^2$ ones. We include this effect through the splitting δ between the e_g levels (described in Eq. 2.17), obtaining more dramatic changes in the phase diagram, see Fig. 3.3 (b). The results can be explained in terms of the pseudospin τ_z which describes the orbital ordering related to the different AF configurations. The C-AF ordering has $\tau_z < 0$ (preferred occupation of the $3z^2 - r^2$ orbital) while both A and CE orderings have $\tau_z > 0$ (preferred occupation of the $x^2 - y^2$ orbital). The term δ tends to enforce a particular value of τ_z. Therefore, for sufficiently large values of J_{AF} the A phase becomes the ground state for tensile strain ($\delta > 0$) due to the lowering of the $x^2 - y^2$ orbital with respect to $3z^2 - r^2$ while a C phase dominates for compressive strain and $J_{\mathrm{AF}} \gtrsim 0.1t$. This C phase appears for $|\delta| > 50|e_{xy}|t$ if $\lambda = 0$

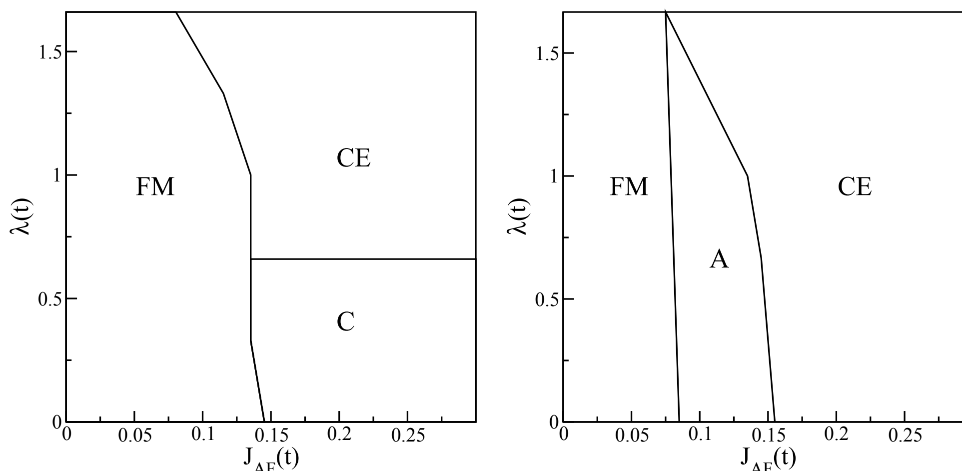

Figure 3.4: (Left) With compressive strain (c/a > 1), $e_{xy} = -2\%$. (Right) With tensile strain (c/a > 1), $e_{xy} = 2\%$ The two mechanisms of strain were taken into account in both panels, with a splitting between the e_g levels $|\delta| = 50|e_{xy}|t$ (namely, $|\delta| = t$).

and for $|\delta| > 60|e_{xy}|t$ if $\lambda = 1t$. Comparing Figs. 3.3 (a) and 3.3 (b), it is apparent that the effect of the strain on the splitting of the e_g levels clearly overcomes the effect caused by the modifications in the hopping for a sufficiently large $|\delta| > 50|e_{xy}|t$.

Fig. 3.4 describes the phase diagram as a function of λ and J_{AF}, with compressive strain ($e_{xy} = -2\%$) on the left panel and tensile strain ($e_{xy} = 2\%$) on the right panel. It is observed that the C phase arises when compressive strain is applied, while the A phase becomes more prominent with tensile strain, in accordance with Fig. 3.3 (b). It is also noticeable in Fig. 3.4 (left) that the C ordering is not favored by the JT coupling λ.

3.2 Metallic manganite/insulator interface

We will now analyze the effect of the strain in the electronic reconstruction at a (001) $AMnO_3$ manganite/insulator interface. We focus on the case of a manganite with x = 0.3, which corresponds to a ferromagnetic and metallic bulk ground state. In the (001) direction, manganites alternate MnO_2 and AO planes as shown in Fig. 3.5. The A-sites corresponds to trivalent rare-earth (e.g La or Pr) and divalent cation (e.g Ca or Sr). The AO planes give a positive background charge $1 - x$. We consider a thin manganite slab with a 4×4 cross section and $l_z = 12$ Mn planes in the z-direction. The insulator is included as a hard-wall fixing the boundary condition at $l = 1$ and $l = l_z$ to zero charge density (70). The interface layers are $l = 2$ and $l = l_z - 1$.

3.2.1 Without Strain

In Fig. 3.6 the average charge per plane in the insulator/manganite/insulator tri-layer is shown, for the three possible ground state configurations at the interface for a screening parameter $\alpha = 1$ and electron-phonon coupling $\lambda = 1t$, without strain effects ($e_{xy} = 0$). In the case of zero Coulomb interaction (namely, $\alpha = 0$, in Eq. 2.18), the electronic charges oscillate slightly around the average charge value per electronic active Mn ($\langle n_i \rangle \sim 0.7$). These fluctuations are Friedel-like oscillations and appear because of the confinement of the carriers to move into the slab (70). In the absence of Coulomb interaction, the charge of Mn ions drops abruptly to zero in just one lattice spacing (not shown here). When increasing the Coulomb interaction the electronic charge tends to screen the background of positive charge created by the counterions and approaches the bulk value $\langle n_i \rangle \sim 0.7$ at the center of the slab. Furthermore, at the interface the electronic charge drops more smoothly from $\langle n_i \rangle \sim 0.7$ to $\langle n_i \rangle \sim 0$ as the Coulomb interaction parameter increases. This is illustrated for $\alpha = 1$ on Fig. 3.6 (a) for the FM ground state configuration.

Close to $\langle n_i \rangle \sim 0.5$ manganites can be unstable toward forming a CE-type AF order due to the opening of a gap at the density of states (DOS). Therefore in the interface region where the charge drops from $\langle n_i \rangle \sim 0.7$ to $\langle n_i \rangle \sim 0$ within $2 - 3$ unit cells, it is possible that the CE order is stabilized. Fig 3.7 shows that in absence of Coulomb

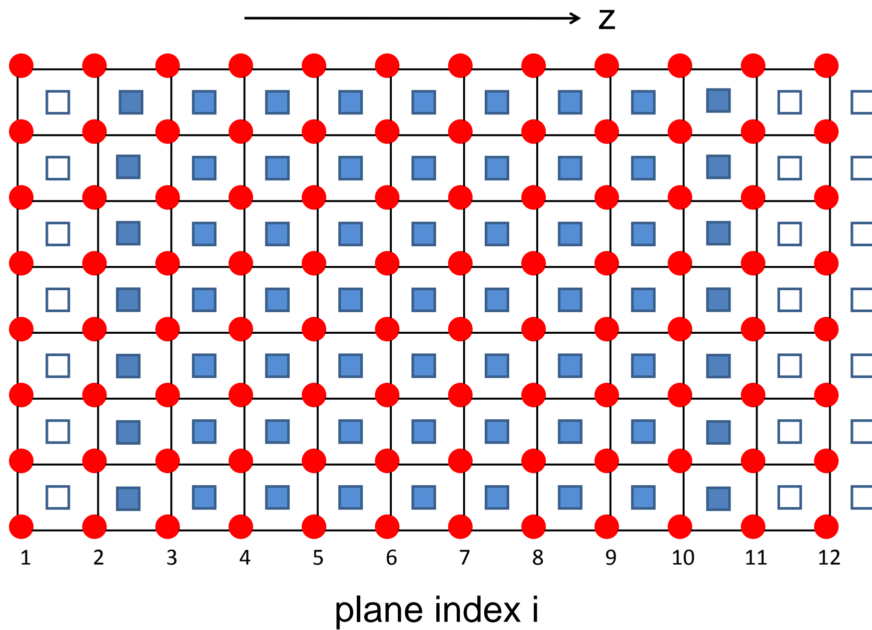

Figure 3.5: 2-dimensional (xz plane) projection of the considered heterostructure. The circles represent the Mn sites while the squares are the A-sites (La, Sr, Ca, etc) shifted by $(1,1,1)\frac{a}{2}$ with respect to the Mn. a is the lattice parameter. Full squares represent the $A^{3+}_{0.7}A'^{2+}_{0.3}O^{2-}$ plane, with a charge density of +0.7 per A atom. Empty squares correspond to the insulator planes where the charge density is zero. Periodic boundary conditions are applied in all three directions.

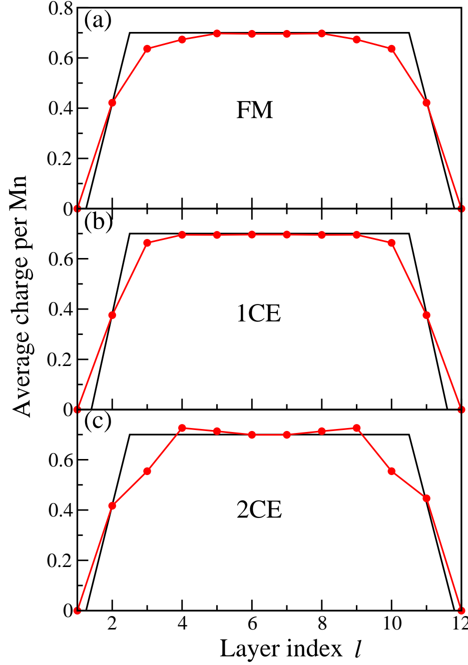

Figure 3.6: Average charge per plane for the three possible configurations considered at a manganite/insulator interface for JT coupling $\lambda = 1t$, parameter of Coulomb interaction $\alpha = 1$ and strain $e_{xy} = 0$. The continuous lines in black represent the positive background charge created by the ions located in the AO layers. The electron wave functions are forced to be zero at the first and last MnO_2 layers. (a) FM: all ferromagnetic planes, (b) 1CE: all ferromagnetic planes except for a single CE plane at each manganite/insulator interface (layers $l = 2, 11$), and (c) 2CE: two CE planes at each interface manganite insulator interface (layers $l = 2, 3, 10, 11$).

interactions $\alpha = 0$, the electronic charge in the CE layers is pinned to a value close to $\langle n_i \rangle$. As the Coulomb interaction increases, the electrons tend to follow the profile defined by the counterions. Fig. 3.7 (inset) shows the density of states of a perfect CE-type AF.

We have calculated the total energy of the system for the different Mn spin configurations at the interface as a function of α and J_{AF}. The differences in energy between the FM phase and the phases containing AF-CE ordered MnO_2 layers depend on the Coulomb interaction α and on the superexchange antiferromagnetic coupling J_{AF}. In the left side of Fig. 3.8 we plot the phase diagram $\alpha - \mathrm{J_{AF}}$ for a system with a bulk

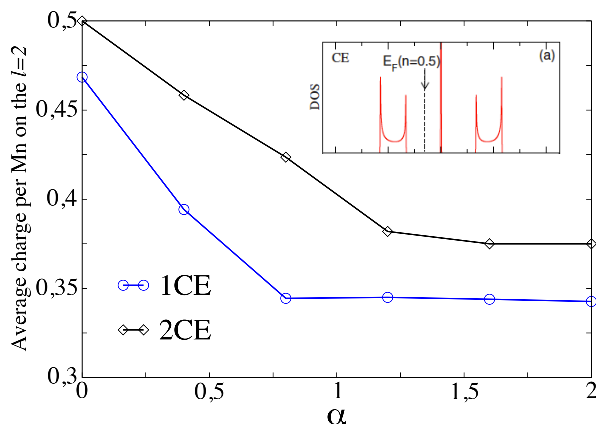

Figure 3.7: Average charge value on the $l = 2$ layer (namely, the interface layer) $\langle n_2 \rangle$ versus α, for 1CE and 2CE configurations at the manganite/insulator interface, with $e_{xy} = 0$ and $\lambda = 1t$. The inset shows the density of states of a perfect CE-type AF. The Fermi level (E_F) at half doping ($x = 0.5$) is signaled by the dashed vertical line.

hole concentration $x = 0.3$ with $\lambda = 1t$. This phase diagram was studied before in Ref. (70), presented in the right side of Fig.3.8, with a model which neglected Jahn-Teller interactions but considered instead an interorbital Hubbard term to stabilize the antiferromagnetic phases. Those results compare very well to our results.

Fig. 3.8 presents that at a fixed value α the number of CE layers in the slab near the interface increases as the AF coupling increases. In these results, it is remarkable that the critical value of the AF coupling for the appearance of an AF-CE MnO_2 layer at the manganite-insulator interface is significantly smaller than the critical value for the occurrence of the $x = 0.5$ AF-CE phase in bulk manganite. In bulk, a value of J_{AF} larger than $0.15t$ is necessary for the occurrence of the CE phase at $x = 0.5$ (70), whereas at the interface values of J_{AF} as small as $0.1t$ can stabilize an AF-CE insulating phase at the manganite-insulator interface, as can be noted in Fig. 3.8. It can also be observed that the critical J_{AF} for the appearance of a CE MnO_2 layer decreases slightly with increasing α. This is because as α increases the electron concentration in the last MnO_2 layer decreases, therefore the kinetic energy decreases and smaller AF interaction is neccesary for stabilize the CE phase.

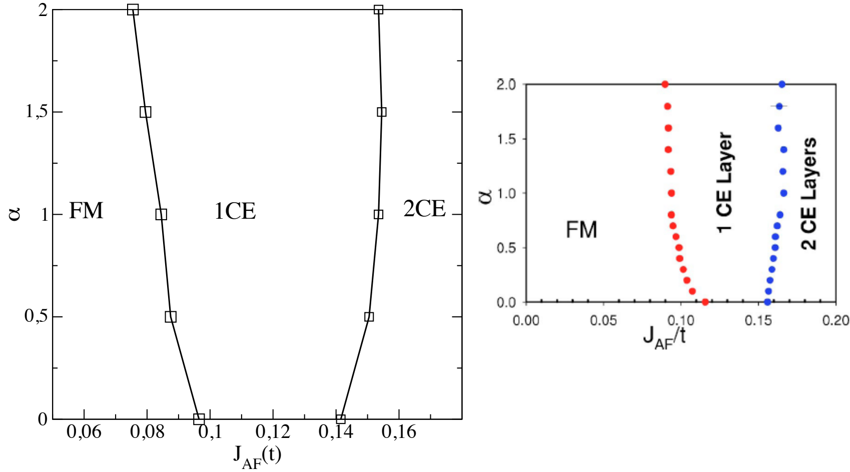

Figure 3.8: (a) Phase diagram α versus J_{AF} for the manganite/insulator interface with $\lambda = 1t$ and with $e_{xy} = 0$. FM stands for all FM Mn planes, 1CE stands for a configuration with a single CE layer at the manganite surface, and 2CE stands for two CE layers at the manganite surface. The lines represent the boundaries between the different ground state configurations. (b) Phase diagram $J_{AF} - \alpha$ for a manganite/insulator interface calculated with a different model. Reproduced from Ref. (70).

thus the critical J_{AF} also decreases (70).

3.2.2 With Strain

Our results show that the redistribution of charge in the insulator/manganite/insulator trilayer depends only very weakly on the value of the strain (not shown here). Therefore, the profile of the average charge per plane in the system is not altered very much on Fig. 3.6 when the strain is applied.

The effect of the strain on the phase diagram is shown in Fig. 3.9. We have plotted the phase diagram $\alpha - \mathrm{J_{AF}}$ for three different values of the strain $e_{xy} = 0$ (without strain as in Fig 3.8, this is used as a reference for comparison), 2% ($c/a < 1$, tensile strain) and -2% ($c/a > 1$, compressive strain) with $\lambda = 1t$ and $\delta = 50 e_{xy} t$. A compressive ($e_{xy} < 0$) strain makes the FM configuration relatively more stable (namely, a larger J_{AF} is required to produce an antiferromagnetic CE order in one or two layers) while a tensile ($e_{xy} > 0$) strain lowers the energy of the antiferromagnetic CE interface

configurations with respect to the FM. These results are consistent with the behavior observed for bulk manganites in Figs. 3.2 and 3.3 (b) and are due to the preferred occupation of the $x^2 - y^2$ orbitals in the CE order.

Similar phenomenology is observed in the phase diagram of λ versus J_{AF}, presented in Fig. 3.10, with Coulomb parameter $\alpha = 1$ and a splitting between the e_g Mn levels $\delta = 50e_{xy}t$. Here, it is also observed that tensile strain tends to favor the antiferromagnetic CE order close to the insulator while compressive strain does not seem to affect the interface ground state very strongly. As mentioned before, the occupancy of the orbital $x^2 - y^2$ favored by the tensile strain lowers the energy of the CE orders, while the compressive strain favors the occupancy of the $3z^2 - r^2$ orbitals which does not favor the CE order. The JT coupling λ also favors the CE order, in agreement with results for half-doped bulk in Section 3.1 and depicted on Figs. 3.3(b) and 3.4.

Now we turn to the antiferromagnetic coupling J_{AF} versus strain e_{xy} phase diagram in Fig. 3.11, for the three considered cases (FM, 1CE and 2CE). JT coupling $\lambda = 1t$ and Coulomb parameter $\alpha = 1$ were assumed. In Fig. 3.10 (a) $\delta = 0$, hence the only effect of the strain is on the hoppings amplitude as given in Eq. 2.16 . Compressive strain increases the hopping amplitude in the xy plane, while tensile strain produces the opposite effect. The effect of the strain is very mild for this case with only a slight gain of the configurations with CE planes for compressive strain. When the splitting in e_g levels is included ($\delta = 100e_{xy}t$, see Eq. 2.17) as illustrated in Fig. 3.10 (b), the tendency is opposite and the dependence on strain is strong. These results confirm that the effect of the strain on the splitting of the e_g levels clearly drowns the effect caused by the modifications in the hopping.

We turn now to analyzing the results in terms of the orbital occupation through the pseudospins τ_z and τ_x. As previously mentioned in bulk results, $\tau_z < 0$ means there is a preference in the $3z^2 - r^2$ orbital occupation. Whereas $\tau_z > 0$ implies a preferential occupation of $x^2 - y^2$. δ tends to enforce a particular value of τ_z. On the other hand, τ_x quantifies the mixing between the two e_g levels, therefore it decreases as τ_z increases.

Previous studies had indicated that orbital reconstruction may arise at interfaces (36,

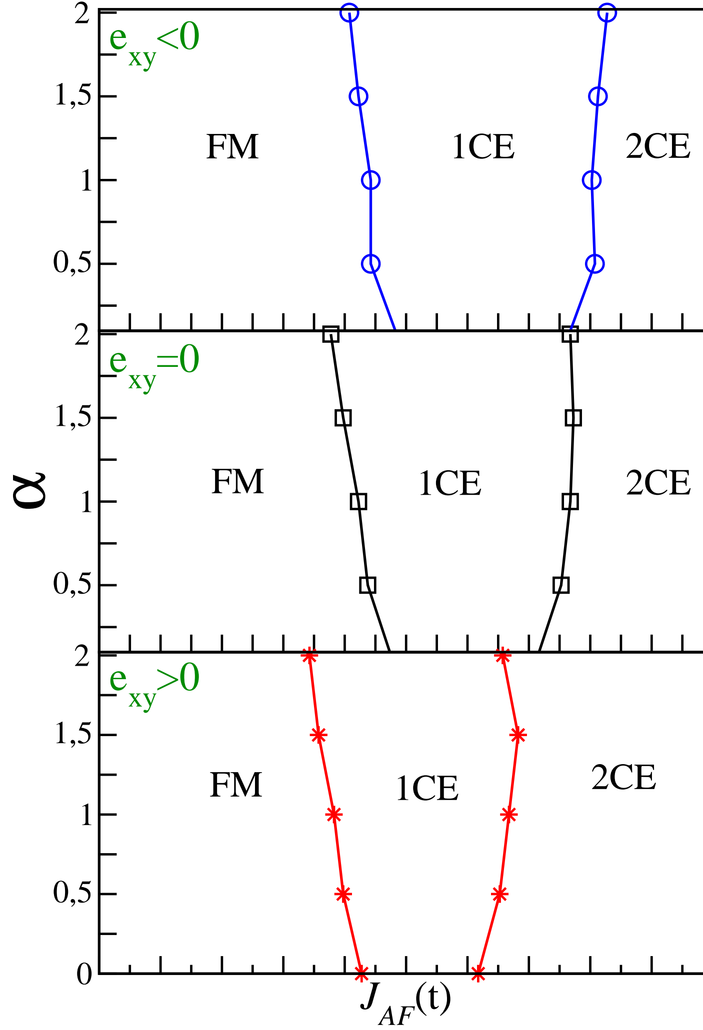

Figure 3.9: Phase diagram α versus J_{AF} for the manganite/insulator interface with $\lambda = 1t$. FM stands for all FM Mn planes, 1CE stands for a configuration with a single CE layer at the manganite interface, and 2CE stands for two CE layers at the manganite interface. The lines represent the boundaries between the different ground state configurations: (Top-panel) the blue lines (circles) for tensile strain $e_{xy} = 2\%$, (middle-panel) the black lines (squares) correspond to the results with $e_{xy} = 0$ (namely, without strain) and (bottom-panel) the red lines (stars) are for compressive strain $e_{xy} = 2\%$. $\delta = 50 e_{xy} t$ (namely, the splitting between the e_g Mn levels) is assumed.

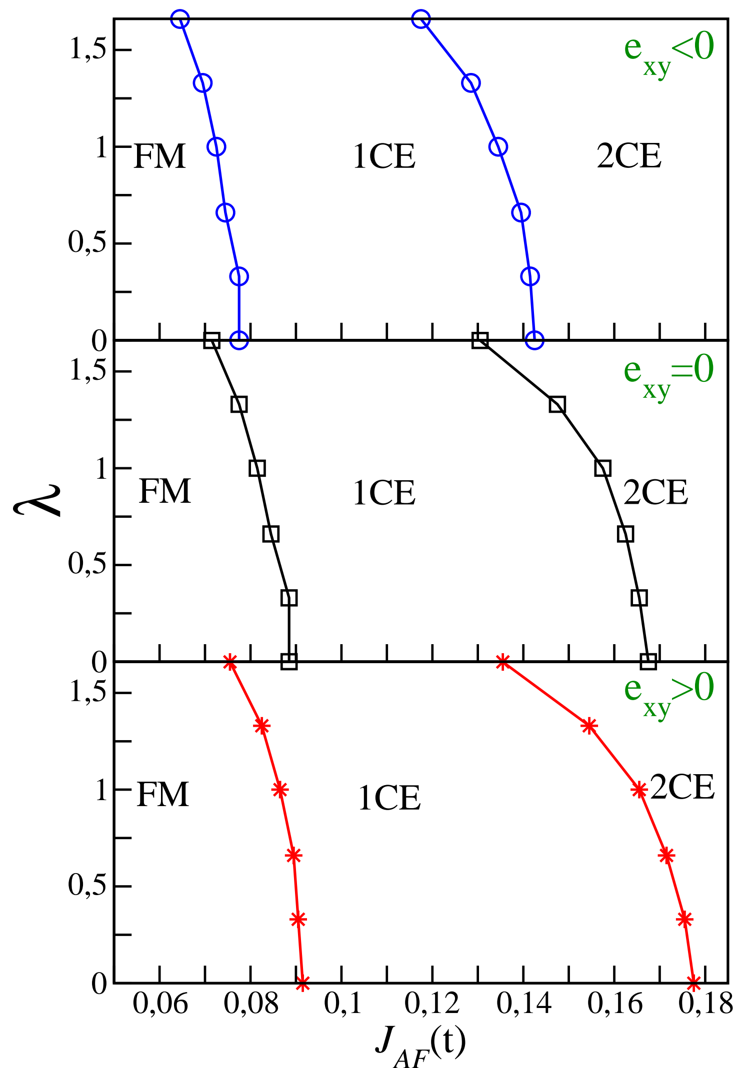

Figure 3.10: Phase diagram λ versus J_{AF} for the manganite/insulator interface with $\alpha = 1$. It was obtained for the three possible electronic reconstruction at the interface, which are FM, 1CE and 2CE. The labels are the same as in Fig. 3.9. Here, $\delta = 50e_{xy}t$ is assumed.

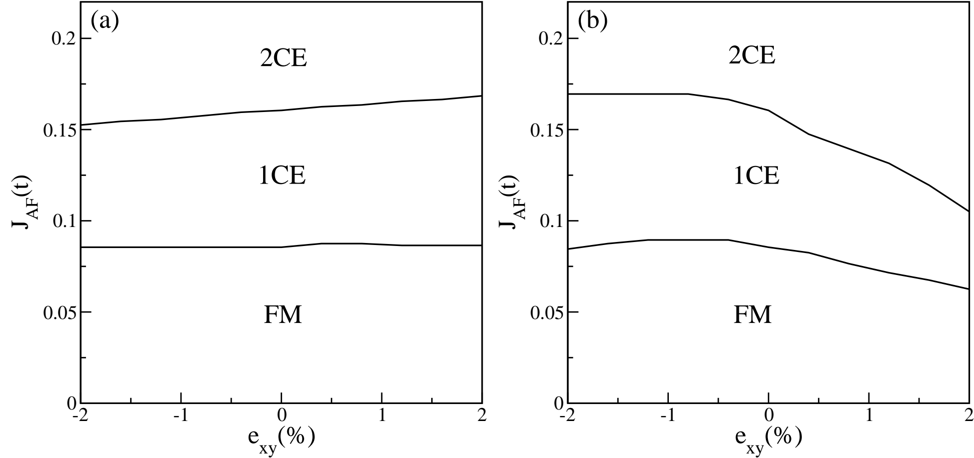

Figure 3.11: Phase diagram J_{AF} versus e_{xy} for the manganite/insulator interface with $\lambda = 1t$ and $\alpha = 1$. The strain induced e_g level splitting is $\delta = 0$ in (a) and $\delta = 100 e_{xy}$t in (b).

54, 64, 111, 112). In particular, due to the breaking of the translational symmetry in the z-direction, the $3z^2 - r^2$ orbital cannot gain much kinetic energy producing a splitting of the e_g levels which favors the occupation of the $x^2 - y^2$ orbital. This kind of ferro-orbital configuration can be observed in Fig. 3.12 (first column) for all FM layers case, in the absence of strain ($e_{xy} = 0$) corresponding to $\tau_z > 0$ at the interface layer. In Fig. 3.12, the average of τ_z and $|\tau_x|$ per plane are depicted for the different configurations at the manganite-insulator interface (FM, 1CE and 2CE). In 1CE and 2CE configurations (second and third column) τ_x is not zero at the interface, and has opposite signs on the sites with $3x^2 - r^2$ and $3y^2 - r^2$ like orbitals, characteristic of CE order. A positive strain ($e_{xy} > 0$) applied to all FM layers enhances the ferro-orbital interface ordering which also occurs in bulk, thus τ_z increases. In the same manner, on CE layers the $x^2 - y^2$ orbital occupancy increases with respect to $3z^2 - r^2$. This makes $|\tau_x|$ to decrease as τ_z to increase. On the other hand, negative strain would produce an e_g splitting opposite to the preferred $x^2 - y^2$ at an interface, leading for a sufficiently large value of the strain to a reduction and, eventually, to a sign change of τ_z.

CE layers adjacent to a FM layer, as we have in both the 1CE and the 2CE configurations, show a charge and orbital distribution which is different from the isolated

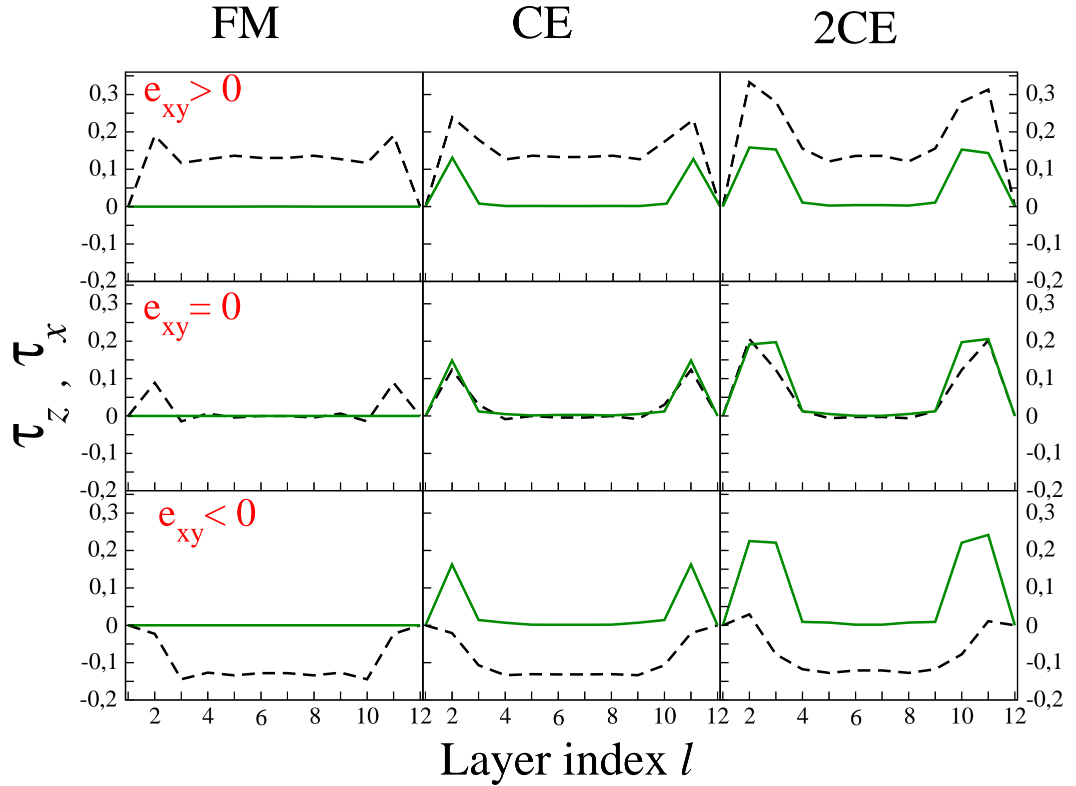

Figure 3.12: Pseudospin τ_z (Black dashed line) per plane related to the orbital e_g preference, $\tau_z > 0$ implies a preferential occupation of $x^2 - y^2$, while $\tau_z < 0$ means there is a preference in the $3z^2 - r^2$ orbital. $|\tau_x|$ per plane (Green solid line) quantifies the mixing between the two e_g levels. Results for FM, 1CE and 2CE electronic reconstruction at interface. The first row with $e_{xy} > 0$. The second row with $e_{xy} = 0$ and third row with $e_{xy} < 0$. $\delta = 100 e_{xy} t$, $\lambda = 1t$ and $\alpha = 1$ are assumed.

case. In particular, half of the spins are parallel to the spins in the nearby FM layer which produces a larger occupation on those sites (both on the CE and the FM layers) with respect to the sites with antiparallel spins (71). Moreover, the redistribution of charge at the interface controlled by the Hartree term leads, in general, to a charge density away from the 0.5 which stabilizes CE (see Fig. 3.6). As a consequence, there is a finite DOS at E_F and therefore, the CE (which is insulating in bulk at $x = 0.5$) may become metallic.

We have analyzed the possibility that insulating behavior may arise at interfacial layers due to strain. In Fig. 3.13 we present the DOS on planes $l = 1$ to $l = 6$ ($l = 7$ to $l = 12$ give symmetric figures) of the insulator/manganite/insulator trilayer with a 2CE electronic reconstruction at the interface. The 1CE interface configuration is always metallic due to the neighboring FM layers. In the 2CE case, we found that the interface CE layer becomes insulating (a gap opens at the Fermi energy) for relatively large values of tensile strain $e_{xy} \sim 2\%$ and $\delta = 2t$ if $\alpha \lesssim 0.7$, see Fig. 3.13 (Right). For larger values of α and/or smaller or negative values of the strain, the interface CE layer is always metallic. In fact, we expect that phase separation (70) or a different (maybe incommensurate with the lattice) order (113) may arise at the interface layers leading to insulating behavior. In this case, our results imply that an already existing insulating gap may be enhanced by tensile strain. On the other hand, compressive strain favors the occupation of the $3z^2 - r^2$ orbitals, which gain energy by hopping in the z-direction to the adjacent FM layer, leading to metallic behavior.

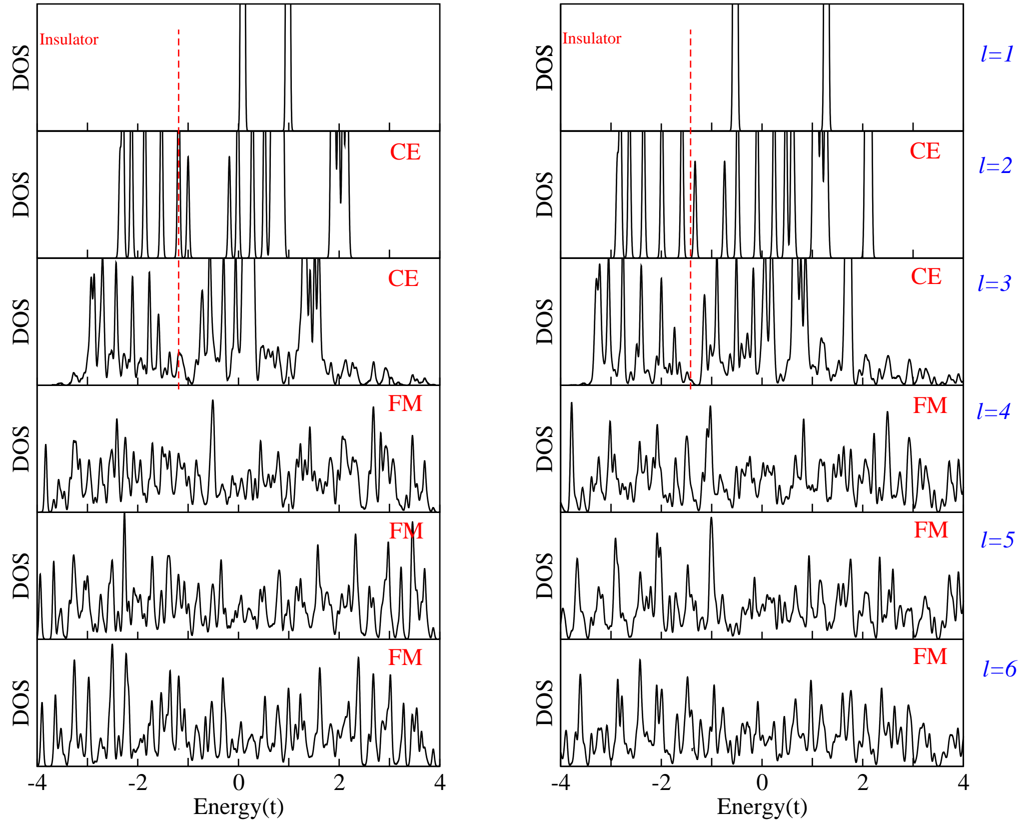

Figure 3.13: DOS on each plane of the heterostructure from $l = 1-6$, ($l = 7-12$ are symmetric) for the 2CE electronic reconstruction at a manganite/insulator interface (with $x = 0.3$). The vertical lines signal the position of the Fermi energy. (Left) Strain $e_{xy} = 2\%$, splitting between e_g levels $\delta = 2t$, JT coupling $\lambda = 1t$ and Coulomb term $\alpha = 1$. (Right) Strain $e_{xy} = 2\%$, $\delta = 2t$, JT coupling $\lambda = 1t$ and Coulomb term $\alpha = 0.5$. A gap opens at the interface layers on the case on the right.

4

Discussion and Conclusions

Substantial theoretical and experimental research shows different electric and magnetic properties of manganite thin films from those exhibited in bulk. In particular, it has been observed that the conductivity and the magnetic T_c are reduced with respect to bulk (81, 114). These differences may be due to the lattice mismatch between the manganite and the substrate throughout the whole film, and also due to modifications at the substrate/manganite interface, the effect known as electronic reconstruction. The electronic reconstruction can be most forceful in ultra thin films used in multilayers and may also be strongly affected by strain. Although the properties at the interfaces in thin films and heterostructures of manganites may also be affected by disorder, oxygen vacancies, variations of the chemical composition and others that depend mainly of growing conditions, many works suggested that the structural strain plays a key role on the electrical and magnetic properties of manganites.

Under this perspective, this work has focused on the effect of the strain on the electronic and magnetic properties of manganite thin films and manganite/insulator interfaces.

In manganites the active orbitals are the Mn e_g $3z^2 - r^2$ and $x^2 - y^2$ (as depicted in Fig 1.2). A tetragonal distortion of the (pseudo) cubic unit cell produces a preferred occupation of one of the anisotropic e_g levels or, equivalently, an energy splitting that leads to orbital ordering (19, 64, 90, 105). In turn, a particular orbital ordering is associated to a particular magnetic ordering (see Fig 3.1). Consequently, when an extension of the lattice parameter in the xy-plane takes place, which corresponds to tensile strain

(namely, $c/a < 0$; $e_{xy} > 0$), the $x^2 - y^2$ orbital is preferred. Therefore, the CE-type and A-type AFM orders are favored, because $x^2 - y^2$ is dominant in those configurations. On the other hand, compressive strain (namely, $c/a > 0$; $e_{xy} < 0$) implies the $3z^2 - r^2$ orbitals are preferred, thus the C-type AFM order is favored, because $3z^2 - r^2$ is dominant in this configuration. This is exactly what we find for bulk manganites at half-doping ($x = 0.5$) (see Figs 3.3 (b) and 3.4), if the splitting between the e_g orbitals (namely, δ defined in Eq 2.17) caused by the strain is large enough ($\delta \gtrsim 50 e_{xy} t$). This value of δ is relatively large ($\sim t$ for -2% strain) but it is comparable to typical Jahn-Teller splittings (115). This tuning of the orbital arrangement with strain has been found in experiments (19, 80, 84, 95), model calculations for $LaMnO_3$ (82), and ab-initio calculations for $La_{0.66}Sr_{0.33}MnO_3$ (116), and for $LaMnO_3/SrMnO_3$ superlattices (105).

The other system under review is the insulator/manganite ($x = 0.3$) to analyze the effect of the strain on manganite interfaces. The results are relevant for multilayered devices such as spin-valves. The general trends of the strain affecting this system are the same exhibited in the half doped bulk manganite. In this case, the bulk behavior (FM and metallic) is recovered within a few unit cells while at the interface layer a density of states close to 0.5 is expected due to the redistribution of charge. Close to $x = 0.5$ a CE-type AFM order may arise. The tensile strain favors the CE order while compressive strain disfavors it, as shown in bulk.

In manganites usually FM come hand in hand with metallicity due to Double-Exchange. Because Double-Exchange is suppressed when the degeneracy of the e_g levels is broken, it is expected that uniform strain produces a reduction of T_c. This fact has been corroborated by some experimental and theoretical research (85, 89, 93). The compressive strain does not affect very strongly the interface ground state. Despite this fact, the splitting of the e_g levels is enhanced ($\delta > 0$), which may lead to reduced conductance at interfaces with respect to bulk.

The results also evidence an orbital reconstruction at the interface, even without strain: the occupation of $x^2 - y^2$ is preferred in the FM interface configuration. This ferro-orbital ordering is reinforced by tensile strain, both for the FM and CE interface orders.

The behaviour at surfaces may be qualitatively different when the oxygen octahedra which surround the Mn ions are incomplete. In this case, the $3z^2 - r^2$ orbital, which points towards the surface, is shifted in energy downwards with respect to $x^2 - y^2$ orbital, which is more localized around the ion (54). Also, hybridization across an interface could lead to a preferential occupation of $3z^2 - r^2$ (111).

When the CE order is favored at a manganite-insulator interface, we find that in most cases the interface shows metallic conduction (there is not gap at the Fermi energy). Only tensile strain together with a relatively small α parameter ($\alpha \lesssim 0.7$) may lead to insulating behavior at the interface.

Summarizing:

- The effect of the strain on the manganite system is twofold. On one hand, it affects the overlapping matrices and, therefore the hopping amplitudes. On the other hand, the strain can also induce a splitting δ of the e_g orbitals. Comparison with the experimental results indicates that the splitting of the e_g orbitals induced by the strain dominates over the modification of the hopping amplitudes. This implies that δ has to be sufficiently large $\delta \gtrsim 50e_{xy}t$.

- In half-doped ($x = 0.5$) bulk manganite system, tensile strain (extension in the xy-plane) promotes an orbital selection: the x^2-y^2 orbital is preferred. Therefore, the CE-type and A-type AFM orders are favored, because $x^2 - y^2$ is dominant in those configurations. Otherwise, compressive strain produces an orbital selection where the $3z^2 - r^2$ orbitals are preferred, thus the C-type AFM order is favored, because $3z^2 - r^2$ is dominant in this configuration.

- In an insulator/manganite ($x = 0.3$)/insulator heterostructure, the effect of the strain on the electronic reconstruction at interface is consistent with the behavior observed for bulk in manganites. Here, the CE configuration at the interface is favored by tensile strain due to the preferred occupation of the x^2-y^2 orbital. On the other hand, FM becomes more stable with respect to CE when compressive

strain is applied. However, the conductance at an interface with respect to bulk may be reduced due to the degeneracy breaking of the e_g levels. Large values of strain also may induce an insulating behavior at the interfacial layer (a gap opens at the Fermi energy).

- The main consequence of the strain is the occurrence of an orbital selection which is intimately related to the spin degree of freedom and the transport properties. In this way, strain provides with a way to tune the ground state configuration on manganites and, therefore, control the performance of manganite based electronic devices. Recent calculations (94) show an enhancement of the magnetoresistence in a half-doped thin-film under tensile strain.

In this work we considered a uniform strain and a uniform Poisson ration ν. However, even a uniform in-plane strain can by accompanied by non-uniform strain in the z-direction (90). Therefore, in this case δ may have different signs at different atomic planes and lead to more complex orbital arrangements than ones reported here. This is the case reported in Ref (90), for a multilayer $(La_{0.7}Sr_{0.3}MnO_3)_3/(BaTiO_3)_3$ deposited on a lattice matched STO(001).

Our findings show that strain produce a kind of orbital ordering in accordance with many experimental and theoretical works (19, 80, 84, 94, 95). For instance, compressive strain on LSMO thin films produces a phase change from FM and metallic to C-type AFM (93). Also, tensile strain in bulk FM and metallic LCMO favors electron occupancy of the $x^2 - y^2$ orbitals leading to A-type orbital ordering (95). In addition, our results become more close to the experimental ones, when we take the splitting of the e_g levels as the more dominant effect of the strain in comparison with the change in the hoppings amplitude. These predictions are also in accordance with some theoretical and experimental works (19, 64, 82, 89, 90, 91).

The strain effects continue to be a focus for study on manganite systems, with the goal of improving the knowledge of the tuning of the electrical and magnetic properties (117, 118). The implications of strain that we have proposed in this work, as well as

our results, may be useful for the tuning of the desired properties of novel thin films and heterostructures conceived for the new spintronics devices.

Part II: Silicon for Quantum Computing

Impact of the valley degree of freedom on the control of donor electrons near a Si/SiO_2 interface

Abstract

In this part, we have analyzed the valley composition of one electron bound to a shallow donor, more specifically a substitutional Phosphorous (P) donor in Silicon close to a (001) Si/barrier. A full six-valley effective mass model Hamiltonian is adopted, where the valleys correspond to the minima of the Si conduction band along the x, y and z crystallographic directions. An electric field perpendicular to the barrier is applied in order to manipulate the band electron. For low electric fields, the electron ground state is essentially confined at the donor, where the lowest energy manifold is split by the tetrahedral crystal field environment into states with distinct contributions from the six valleys. At high enough fields, the donor is ionized, and its electron is shuttled to the interface, where the valley levels split into a four-fold degenerate excited state, consisting of $\pm x$ and $\pm y$ valleys, and a lower manifold spanned by the $\pm z$ valleys. Valley splitting at the interface separates slightly the two valley ground state due to the valley-orbit coupling, V_{vo}^{I}. At intermediate electric fields, close to a characteristic shuttling field, the electron states may constitute hybridized states with valley

compositions different from the donor and the interface ground states. The degree of level repulsion, thus the width of the anti-crossing gap, depends on the relative valley compositions, which vary with the valley orbit-coupling modulus and phase and the interface-donor distance. We focus on the valley configurations of the states involved in the donor-interface tunneling process, given by the anti-crossing of the three lowest eigenstates. A sequence of two anti-crossings takes place and the complex phase affects the symmetries of the eigenstates and level anti-crossing gaps. Our results contribute to a better understanding of controlled valley manipulations, relevant for the practical manipulation of donor electrons in Si nanostructures, which is crucial for some Si-based Quantum Computer proposals.

This part is organized as follows:

Chapter 5 presents an overview of the relevant concepts related with quantum computation, mentioning some quantum computer proposals and its operating principles. Here, we introduce the features and the fundamental aspects for the doped-Si based Quantum computer implementation.

In Chapter 6 the relevant Silicon features for quantum computing are described. Particularly, the peculiarities of the Si band conduction minima (valleys) and their key role in the spin manipulation and coherence. Likewise, the effects of valleys at the donor and at the interface are reviewed.

The full-valley effective mass model Hamiltonian is defined in Chapter 7. We model the system by the combination of two potential wells: one that binds the electron to the donor (at low fields) and another binding the electron at the interface (at high fields). The ground states of the electron at the donor and at the interface define the envelope functions in the basis for the full six valley problem.

Our results for the electric field dependence of the low-lying electronic ground states and valley composition are presented in Chapter 8.

Finally, we conclude in Chapter 9 with a discussion of the implications of these results on the practical manipulation of donor electrons in Si nanostructures, as well as with a description of the different scenarios for quantum computing applications.

5

Introduction

5.1 Quantum Computing

The field of quantum computation is one of the newest branches of theoretical physics. Its emergence in the early part of the 1980's was inspired in part by a speech by Richard Feynman on the simulation of quantum mechanical systems (119):

Nature is not classical...and if you want to make a simulation of Nature, you would better make it quantum mechanical, and by golly it is a wonderful problem, because it does not look so easy.

Feynman got the interest of a large group of physicists and chemists, that wished in harnessing the power of modern computers to simulate the behavior of elementary particles, atoms, and molecules. Systems containing more than a few particles are very difficult to solve. This led Feynman and other physicists to wonder whether a computer could exploit the physics of quantum mechanics to simulate these systems in an efficient manner. Simultaneously, another group of researchers were becoming interested in quantum computing in connection with determining the most efficient computer permitted by the laws of physics. Since nature is ultimately based on quantum mechanics, it would be expected to be able to generalize the ideas of information theory to create a quantum notion of information. One could then use the laws of quantum physics to arrive at the true limit for computational efficiency.

Despite these interests, quantum computing did not gain much attention until the discovery of Shor's factoring algorithm and Grover' search algorithm in the middle of 1990's. Both of these algorithms have real world applications beyond quantum simulation, and both offer a significant speed up over their classical analogues.

For example, the most common method of encryption used to secure financial transactions and secure communications over the Internet relies on the classical infeasibility of factoring the product of two very large prime numbers. Shor's factoring algorithm would enable someone with a quantum computer to break the encryption scheme in a very short amount of time immediately grabbing the attention of organizations like the National Security Agency (NSA). See below in Section 5.4.

Thus, there are physicists looking to apply computer science to physics or computer scientists seeking to apply physics to computer science. There is considerable interest in creating some sort of computing device that can take advantage of the laws of quantum mechanics to perform calculations.

Under this perspective, Quantum Computing involves quantum information and quantum computation concepts based on the study of the information processing tasks that can be accomplished using quantum mechanical systems.

5.2 Quantum bits

The bit is a fundamental concept of classical computation and classical information. Quantum computing is built upon an analogous concept, the *quantum bit*, or *qubit* for short. A classical bit has a state either 0 or 1. The difference between bits and qubits is that a qubit can be in a state other than $|0\rangle$ or $|1\rangle$. It is also possible to form linear combinations of states as:

$$|\psi >= \alpha|0\rangle + \beta|1\rangle. \tag{5.1}$$

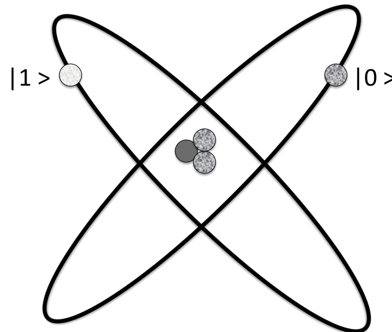

Figure 5.1: Qubit represented by two electronic leves in an atom.

The state of a qubit is a vector in a two-dimensional complex vector space. The special states $|0\rangle$ and $|1\rangle$ are computational basis states, and form an orthonormal basis for this vector space. The measurement of a qubit gives either result 0, with a probability $|\alpha|^2$, or the result 1, with probability $|\beta|^2$. Naturally, $|\alpha|^2 + |\beta|^2 = 1$.

To define a qubit it is precise to have two states separated from the rest: the two different polarizations of a photon, the alignment of a nuclear spin in a uniform magnetic field, or two states of an electron orbiting a single atom such as shown in Fig. 5.1. In the atom model, the electron can exist in either the ground state $|0\rangle$ or the "excited" state $|1\rangle$. Transitions between the 2 states can be produced by shinning light on the atom: with an appropriate energy and for an appropriate length of time, it is possible to move the electron from the $|0\rangle$ state to the $|1\rangle$ state and vice versa. However, reducing the time of exposure to the light, an electron initially in the state $|0\rangle$ can be moved "halfway" between $|0\rangle$ and $|1\rangle$, into the $|+\rangle$ state, which often denotes the state $(\frac{1}{\sqrt{2}}|0\rangle + \frac{1}{\sqrt{2}}|1\rangle)$, when measured gives the results "0" fifty percent of the time, and the result "1" fifty percent of the time. Then, a qubit can be $|0\rangle$, $|1\rangle$, or a superposition of both. A pure qubit state is a linear superposition of the basis states represented as a linear combination of $|0\rangle$ and $|1\rangle$, Eq. 5.1.

The qubit has the following geometric representation. We may rewrite Eq. 5.1 as:

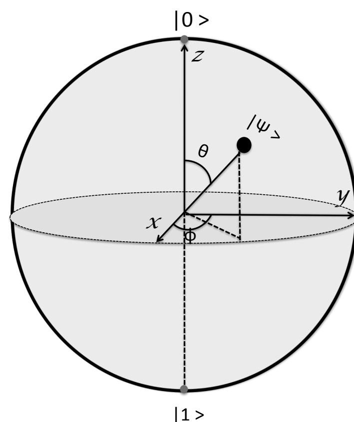

Figure 5.2: Bloch sphere representation of qubit

$$|\psi\rangle = e^{i\gamma}(cos\frac{\theta}{2}|0\rangle + e^{i\phi}sin\frac{\theta}{2}|1\rangle) \tag{5.2}$$

Where γ, θ, ϕ are real numbers. We can ignore the factor of $e^{i\gamma}$, because it has no observable effects and rewrite Eq .5.2:

$$|\psi\rangle = (cos\frac{\theta}{2}|0\rangle + e^{i\phi}sin\frac{\theta}{2}|1\rangle) \tag{5.3}$$

The numbers θ, ϕ define a point on the unit three-dimensional sphere, as shown in Fig 5.2. This sphere is often called the *Bloch sphere*; it provides a useful means of visualizing the state of a single qubit.

An important two qubit state is the *Bell state*

$$\frac{|00\rangle + |11\rangle}{\sqrt{2}} \tag{5.4}$$

The Bell state has the property that upon measuring the first qubit, one obtains two possible results: 0 with probability 1/2, leaving the post-measuring state $|\phi^{'}\rangle = |00\rangle$, and 1 with probability 1/2, leaving $|\phi^{'}\rangle = |11\rangle$. As a result, a measurement of the second qubit always gives the same result as the measurement of the first qubit. That is, the measurements outcomes are *correlated*. This is the key ingredient in quantum teleportation [1](120) and superdense coding [2] (121), and the prototype for many other quantum states.

More generally, we may consider a system of n qubits. The computational basis states of this system are of the form $|\mathrm{x_1, x_2 ... x_n}\rangle$. The quantum state has an amplitude 2^n. For instance, with $n = 600$ this number is huge and it would not be possible to store on any classical computer. This problem could be solved using the quantum mechanics as computation, where the manipulation of such enormous quantities of data is possible, even for systems containing only a few hundred of atoms. It is as if Nature were keeping 2^{600} hidden pieces of scratch paper on the side, on which she performs her calculations as the system evolves.

Changes occurring to a quantum state can be described using the language of *quantum computation*. Analogous to the way a classical computer is built from an electrical circuit containing wires and logic gates, a quantum computer is built from a *quantum circuit* containing wires and elementary *quantum gates* to carry around and manipulate the quantum information (122).

5.3 Quantum Operations

Similar to the classical case where computation can be decomposed into a sequence of elementary logical gates like AND or NOT, the evolution of quantum bits is described

[1]Quantum teleportation, or entanglement-assisted teleportation, is a process by which a qubit (the basic unit of quantum information) can be transmitted exactly (in principle) from one location to another, without the qubit being transmitted through the intervening space

[2]Superdense coding is a technique used to send two bits of classical information using only one qubit, with the aid of entanglement.

by the successive application of quantum gates. These are composed out of unitary transformations and are therefore reversible. As for classical logic networks, there exist universal sets of quantum gates: any logic quantum gate, i.e. any unitary action on arbitrary many quantum bits, can be composed out of an entangling two-qubit gate, together with the arbitrary operations on single qubits (single-qubit gates) (122).

The single qubit gate corresponds to a rotation in the Hilbert space (the simplest nontrivial Hilbert space is of dimension 2). The generators of rotations in the two-dimensional Hilbert space are the Pauli matrices

$$\sigma_x = \begin{pmatrix} 0 & 1 \\ 1 & 0 \end{pmatrix}, \sigma_y = \begin{pmatrix} 0 & -i \\ i & 0 \end{pmatrix}, \sigma_z = \begin{pmatrix} 1 & 0 \\ 0 & -1 \end{pmatrix} \tag{5.5}$$

These matrices generates a rotation about the x, y, z axis of the Bloch sphere, respectively. Hence, each single-qubit gate can be described by a rotation of the Bloch vector about a normalized axis $\overrightarrow{n}$ by an angle θ

$$R_{\overrightarrow{n}}(\theta) = e^{-i\frac{\theta}{2}\overrightarrow{n}\overrightarrow{\sigma}} = cos\frac{\theta}{2}\mathrm{I} - isin\frac{\theta}{2}(\overrightarrow{n}\overrightarrow{\sigma}) \tag{5.6}$$

Where I is the identity matrix. Furthermore, each rotation within a two-dimensional unit sphere can be decomposed into successive rotations about two fixed non parallel axes. Therefore, for an arbitrary transformation of the state of one qubit, it is sufficient to possess two sets of single-qubit gates corresponding to rotations about two different axes (122).

Two examples of single qubit gates that directly follow from a rotation generated by one of the Pauli matrices Eq. 5.5, are the NOT gate (negating the state of the qubit) and the phase-gate (where the state $|1\rangle$ acquires a relative phase ϕ). They are represented by

$$\begin{pmatrix} 0 & 1 \\ 1 & 0 \end{pmatrix} and \begin{pmatrix} 1 & 0 \\ 0 & e^{i\phi} \end{pmatrix}, \tag{5.7}$$

and result from a rotation about the x and the z-axis, respectively.

The most famous example of a "universal" two-qubit gate is the controlled NOT gate. It negates the state of the second qubit if, and only if, the first qubit is in the state $|1\rangle$. However, any two-qubit gate producing entanglement out of an unentangled two-qubit state is universal (123).

5.4 Advantages of building a Quantum Computer

It has been shown in theory that a quantum computer will be able to perform any task that a classical computer can. If we use the classical algorithms on a quantum computer, it will simply perform the calculation in a similar manner to a classical computer. In order for a quantum computer to show its superiority it needs to use new algorithms which can exploit the phenomenon of quantum parallelism. Such algorithms are not easy to formulate, but once discovered they yield spectacular results. These include:

- The quantum factorization algorithm created by Peter Shor of $AT\&T$ Bell laboratories. The algorithm tackles the problem of factorising large numbers into its prime factors. This task is classically very difficult to solve; in fact it is so difficult that it forms the basis of RSA (Ryvest, Shamir y Adleman) encryption[1](124), probably the most popular method of encryption used today. Shor's algorithm cleverly uses the effects of quantum parallelism to give the results of the prime factorization problem in a matter of seconds whereas a classical computer would

[1] RSA is an algorithm for public-key cryptography that is based on the presumed difficulty of factoring large integers. Anyone can use the public key to encrypt a message, but with currently published methods, if the public key is large enough, only someone with knowledge of the prime factors can feasibly decode the message

take, in some cases, more than the age of the universe to produce a result (125).

- Grover's algorithm is a quantum algorithm for searching an unsorted database with N entries in $O(N^{1/2})$ time and using O(log N) storage space. It was discovered by Lov Grover in 1996. In models of classical computation, searching an unsorted database cannot be done in less than linear time. Grover's algorithm illustrates that in the quantum model searching can be done faster than this; in fact its time complexity $O(N^{1/2})$ is asymptotically the fastest possible for searching an unsorted database in the quantum model. It provides a quadratic speedup, unlike other quantum algorithms, which may provide exponential speedup over their classical counterparts. However, even quadratic speedup is considerable when N is large (126).

- The universal quantum simulator as a quantum computer proposed by Richard Feynman in (1982) (119). Feynman showed that a classical Turing machine (127) would presumably experience an exponential slowdown when simulating quantum phenomena, while his hypothetical universal quantum simulator would not. He conjectured that if one builds a machine that can perform computations using quantum mechanics elements, any quantum mechanical system including the physical world could be probably simulated.

5.5 Experimental Requirements for a Quantum Computer

To realize a quantum computer, we should not only give qubits some robust physical representation (in which the qubits retain their quantum properties), but also select a system in which they can be made to evolve as desired. Furthermore, it should be possible to prepare qubits in some specified set of initial states, and to measure the final output state of the system.

The challenge of the experimental realization is that these basic requirements can often only be partially met. A single nuclear spin can be a very good qubit, because the superposition state of being aligned with or against an external field can last a long

time, even for days. But it can be difficult to build a quantum computer from nuclear spins because the coupling to the environment is so small that it is hard to measure the single nuclei. The observation that the constraints are opposing is general: a quantum computer has to be well isolated in order to retain its quantum properties, but at the same time its qubits have to be accessible so that they can be manipulated to perform a computation and to read out the results. A key concept in understanding the suitability of a particular quantum computer realization is the notion of *decoherence* (quantum noise). This is because the length of the longest possible quantum computation is rigorously given by the ratio τ_Q, the time for which a system remains quantum-mechanically coherent, to τ_{op} the time it takes to perform elementary unitary transformations (which involve at least two qubits). These two times are actually related to each other in many systems, since they are both determined by the strength of coupling of the system to the external environment. Nevertheless, $\lambda = \tau_Q/\tau_{op}$ can vary over a surprisingly wide range (see Table 5.1).

Table 5.1: First rough estimates for decoherence times τ_Q (seconds), τ_{op} operations times (seconds), and maximum number of operations $\eta_{op} = \lambda^{-1} = \tau_Q/\tau_{op}$, for several of the first candidates for interacting systems of quantum bits. Table taken from Nielsen and Chuang (2001) Ref. (122).

System	τ_Q	τ_{op}	$\eta_{op} = \lambda^{-1}$
Nuclear Spin	$10^{-2} - 10^{8}$	$10^{-3} - 10^{6}$	$10^{5} - 10^{14}$
Electron Spin	10^{-3}	10^{-7}	10^{4}
Ion Trap ($In^{(+)}$)	10^{-1}	10^{-14}	10^{13}
Electron-Au	10^{-8}	10^{-14}	10^{6}
Electron-GaAs	10^{-10}	10^{-13}	10^{3}
Quantum dot	10^{-6}	10^{-9}	10^{3}
Optical Cavity	10^{-5}	10^{-14}	10^{9}
Microwave Cavity	10^{0}	10^{-4}	10^{4}

These estimates give some insight into the basis and merits of different possible physical realizations of a quantum information processing machine, but many other important sources of noise and imperfections arise in the implementation. For instance, manipulation of a qubit represented by two electronic levels on an atom by using light to cause transitions between levels would also cause transitions to other electronic levels

with some probability. These would also be considered noise processes, since they take a system out of the two states that define the qubit. In general, anything which causes a loss of quantum information is a noise process (122).

As discussed later in Section 5.8.1, the property of a physical system to encode and preserve quantum information could be quantified through parameters such as the relaxation time called T_1 and the coherence time T_2 (related to τ_Q). The first describes the timescale over which an energy excited state decays to the ground state and the second one describes the timescale over which the phase coherence between different branches of the quantum superposition can be preserved. In real systems usually $T_2 << T_1$.

5.5.1 Conditions for a quantum computation

There are four basic requirements for quantum computation. These consist in the capacities to (122):

1. Robustly represent quantum information.
2. Perform a universal family of unitary transformations
3. Prepare a fiducial initial state
4. Measure the output result.

David DiVicenzo developed a set of five specific and technological criteria that have been very useful in guiding the search for a feasible quantum computing architecture. These five criteria say that for a system to be candidate for an implementation of quantum computation, it should (128):

1. Be a scalable physical system with well-defined qubits.
2. Be initializable to a simple fidutial state such as $|000...\rangle$.
3. Have quantum gates faster than decoherence times.
4. Have a universal set of quantum gates.
5. Permit high quantum efficiency, qubit specific measurements.

5.6 Quantum Computer Proposals

Many different candidates for quantum computers are now being investigated which are distinguished by the physical system used to realize the qubits. Some of the physical implementations proposals are:

- Trapped ion quantum computer: Ions, or charged atomic particles, can be confined and suspended in free space using electromagnetic fields. Qubits are stored in stable electronic states of each ion, and quantum information could be processed and transferred through the collective quantized motion of the ions in the trap which interact through the Coulomb force. Lasers are applied to induce coupling between the qubit states (for single qubit operations) or coupling between the internal qubit states and the external motional states (for entanglement between qubits). In 2011 the largest number of particles controllably entangled was 14 trapped ions. More details in Ref. (129)

- Nuclear magnetic resonance quantum computer (NMR) uses the spin states of molecules as qubits. NMR differs from other implementations of quantum computers in that it uses an ensemble of systems, in this case molecules. The ensemble is initialized to be the thermal equilibrium state. Operations are performed on the ensemble through RF (radiofrequency) pulses applied perpendicular to a strong, static field, created by a very large magnet. In 2001 researchers at IBM reported an implementation of the simplest instance of Shor's algorithm: factorization of N= 15, using a 7-qubit NMR quantum computer (130).

- Optics-based quantum computer (Quantum optics). The qubits are states of different modes of the electromagnetic field. For instance in Ref. (131) it has been proposed the utilization of linear optics for quantum information processing requiring single photon sources, beam splitters, phase shifters, photo-detectors, and feedback from photo-detector outputs. Here, a qubit is realized by one photon in two optical modes (such as horizontal or vertical polarization).

- Superconductor-based quantum computers: QC based on nanofabricated superconducting circuits coupled through Josephson junctions. There exists three families of superconducting qubits which are the charge qubits, flux qubits, and hybrid qubits. Their quantum state is manipulated by using electromagnetic pulses to control the magnetic flux, the electric charge or the phase difference across a Josephson junction (132).

- Nitrogen-Vacancy Centers in Diamond: This proposal uses a diamond's impurity, called the nitrogen-vacancy NV. It consists of a nearest-neighbor pair of a nitrogen atom, which substitutes for a carbon atom, and a lattice vacancy. The spin in a nitrogen nucleus became the first qubit, with an electron in a second one forming the second. These qubits can be manipulated at room temperature by applying a magnetic field, electric field, microwave radiation or light, or a combination, resulting in sharp resonances in the intensity and wavelength of the photoluminescence. Although NV may be a good candidate for qubits, this is just one of an enormous number of crystalline defects found and characterized to high degree (133).

- Loss-DiVincenzo quantum computer: The proposal was to use as qubits the intrinsic spin 1/2 degree of freedom of individual electrons confined in quantum dots. The computer operates, basically, using inter-dot gate voltage for implementing swap operations and local magnetic fields (or any other local spin manipulation) for implementing the Controlled NOT gate (128, 134).

- Kane quantum computer: Solid state QC based on an array of individual phosphorus donor atoms embedded in a pure silicon lattice. Both the nuclear spins of the donors and the spins of the donor electrons participate in the computation. Quantum operations on the spins are performed using a combination of voltages applied to gates adjacent to the spins and radio frequency magnetic fields applied resonant with spin transitions. Initialization and measurement of the electron spins is made by electrostatic probing of a two electron system, whose orbital

configuration must depend on the spin states of the electron because of the Pauli Principle (12). This proposal is the focus of this work. In the following section, we are going to discuss why doped Si is a promising candidate for quantum computing.

There are also other QC proposals such as charge manipulation in quantum dots (135) or single donors (136), Bose-Einstein condensate-based, Cavity quantum electrodynamics (CQED) (137), Rare-earth-metal-ion-doped inorganic crystal-based (138), Fullerene-based on Electron Spin Resonance (ESR) (139), among others. They have an operating principle similar to some described above.

5.7 Silicon for Quantum Computation

In the last few decades, the density of transistors in a chip has been consistently duplicated every eighteen months, as given by Moore's law (see scheme in Fig 5.3). The exponential progress of microelectronics has been based on silicon technology. Silicon is an ideal environment for spins in the solid state, due to its weak spin-orbit coupling and the existence of isotopes with zero nuclear spin. The prospect of combining quantum spin control with the exquisite fabrication technology already in place for classical computers has encouraged extensive effort in silicon based quantum devices over the past decade.

As seen in section 5.6 , there are many proposed physical realizations for quantum information processors, some of which are semiconductor-based because of their commonalities with classical electronics (Kane, 1998 (12), Loss & DiVicenzo, 1998 (128)). Initially, the Loss and Di Vicenzo original proposal generated special interest on the electron spins in quantum dots. Despite the Si technological great maturity for classical field transistors, GaAs quantum dots were historically more advanced, due to the very early work in the epitaxial growth in lattice-matched III-V material. Consequently, experiments on lithographically defined quantum dots in GaAs/AlGaAs heterostructures demonstrated qubit initialization, single-shot single-electron spin readout (140), and coherent control of single-spin and two spin states (141, 142). In this way, the GaAs system fulfilled the DiVincenzo criteria for quantum computation, described above in

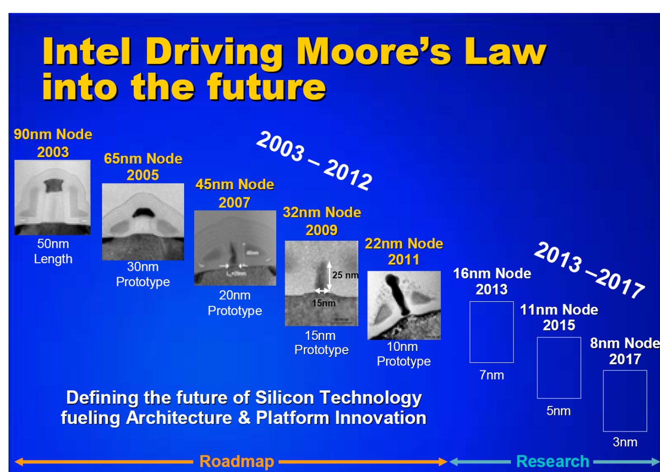

Figure 5.3: Moore's law, defining the future of the Silicon Technology fueling architecture and Platform innovation. The channel of 15nm in 32nm mode has less than 100 Si atoms across. Scheme from Intel (9).

the section5.5.1(143).

However, GaAs has relevant issues related to the inevitable presence of nuclear spins in the host material. For instance, in AlGaAs/GaAs heterostructures, Al, Ga and As all have non-zero nuclear spin, which causes that an electron spin in a QD interacts with many (10^6) nuclear spins in the host material by the hyperfine coupling. This coupling has three disadvantageous effects: (i) electron spin decoherence resulting from the random effective magnetic field caused by nuclear spin fluctuations, (ii) direct electron-nuclear spin flip-flops (for energetically similar electron spin states) (144) and (iii) admixing between the electron orbital and electron spin states by the orbital dependence with magnetic field. Transitions between perturbed states might occur with assistance of phonons (145). The randomness in the nuclear field leads to high decoherence, with a T_2 measured by spin echo $\sim 1\mu$s at 0.1T (142).

On the other hand, natural Silicon consists of 95% non-magnetic nuclei (^{28}Si). Furthermore, Si may be purified to nearly 100% zero-nuclear spin isotopes. Si is a much lighter element than Ga and As, reducing the spin-orbit coupling. For these reasons, various proposals have been made for Si-based electron spin qubits on quantum dots (146), and donors (147, 148). The ESR experiments of donors in Si demonstrated much

longer coherence times than GaAs, with an order of magnitude of seconds (149). The spin decoherence in Si will be described later in section 5.8.

A major focus is to project the achievements in integrated-circuit technology onto a supposed scalability of quantum bits in silicon. Despite the current silicon industry standards, with 22 nm features, have higher resolution than typical quantum devices, there is no guarantee of any kind of "quantum CMOS". One of the relevant inconveniences, and thus a challenge, is the variability increasing as CMOS transistors are scaled to nanometer feature sizes. However, many groups are working to minimize this voltage threshold variation through technology optimization and ensuring robust product functionality and performance (150). For instance, Shinada et al. (2005) reported the fabrication of semiconductor devices in which both the number and position of the dopant atoms are precisely controlled using single-ion implantation techniques (see Fig 5.4). Their results showed the threshold voltage V_{th} variability is less important for those structures with ordered dopant arrays than for those with conventional random doping, attributing this to the uniformity of electrostatic potential in the conducting channel region due to the ordered distribution of dopant atoms. These results serve to highlight the improvements in device performance that can be achieved through atomic-scale control of the doping process, thus enhancing the prospects for realizing silicon-based solid-state quantum computers (151).

5.7.1 Features of the Silicon-Based Computer with Dopants: Kane Proposal

The main theme of electronics applications using single dopants is the ability to modify the dopant electron wave function using external electric fields and/or to manipulate the spin degrees of freedom using magnetic fields. In many proposals for dopant based qubits using either electron or nuclear spin as qubits, as well as the recent valley-based qubit (initially in QD (152)), dopant electron wave function engineering is critical to realize single and two qubit gates. The original idea comes from the Kane proposal for a nuclear-spin based quantum computer in Silicon (12).

The Kane computer architecture consists of a linear array of Phosphorus atoms (shal-

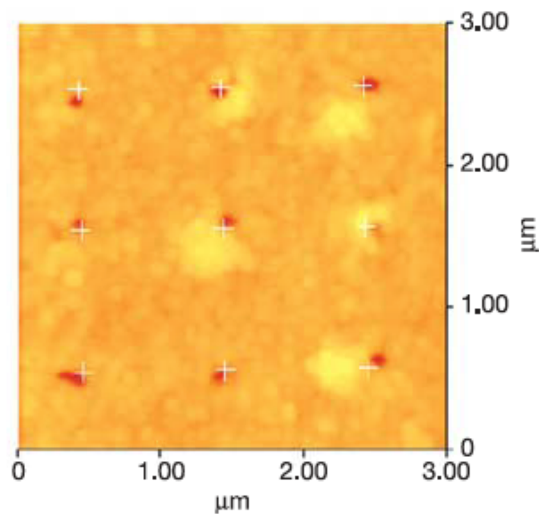

Figure 5.4: An atomic force microscope (AFM) image of an experimental device with a P donor array implanted one-by-one at 30 kV into the channel region of a Si transistor. Image from Ref. (151).

low donors)[1](153)(P) embedded underneath the surface of a pure silicon wafer. Each P nuclear spin serves as a qubit, and the linear array forms the computer quantum register. The entire wafer is placed in a strong, static magnetic field B_0 at sub-Kelvin temperatures ($B_0 \gtrsim 2$T), and alignment of the P atoms nuclear spin as parallel or antiparallel to B_0 corresponds to the $|0\rangle$ and $|1\rangle$ states of the qubit, respectively. In order to execute a quantum algorithm, it is needed to rotate individual qubits in Hilbert space and couple two qubits together. Both operations can be reached with an array of gate electrodes. Here the gates are used for controlling charge motion. These gates lie on top of the wafer but are isolated from the pure silicon by a thin insulating layer of silicon dioxide SiO_2, see Fig. 5.5. Note that each A-gate is located precisely above a P atom and each J-gate lies between adjacent atoms. As discussed later, a small positive voltage applied to the A-gate gives independent control of the qubit directly under the gate, while voltage applied to the J-gate allows coupling two qubits together through an electron-mediated interaction.

To design the Silicon-based computer individual P atoms are embedded in Silicon.

[1]Shallow donor refers to a donor with energy states equivalent to atomic hydrogen with an altered expected mass.

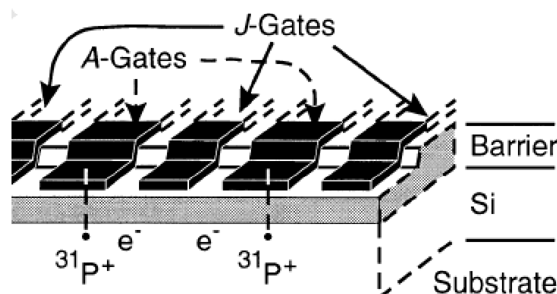

Figure 5.5: Silicon-Based Quantum Computer Scheme. The Kane's solid-state quantum computer is constituted by a linear array of P donor atoms in a pure silicon wafer, with an interdonor spacing of about 20nm. In the presence of a large magnetic field and at sub-Kelvin temperatures, the nuclear spins of the donor atoms can be aligned either parallel or antiparallel with the field, corresponding to the $|0\rangle$ and $|1\rangle$ qubit states, respectively. An array of metal gates lies on the surface, isolated from the silicon by a barrier layer of SiO_2. The A-gates lie directly above the donor atoms and permit individual control of single qubits. The J-gates lie between the donors and control an electron-mediated coupling between adjacent nuclear spins, then allowing for two-qubit operations. Figure from B. E. Kane (1998)

These two elements are chosen for several reasons, one of these is the fact that P is the standard dopant for conventional Silicon-based semiconductor devices and there is enormous working knowledge of P and Silicon from the conventional computing industry. Another reason comes from the need to control the spin environment. It is required for the qubits to have a nuclear spin I = 1/2, but also the surrounding environment to be spin free. Undesirable spin-spin interactions between the qubit and any nearby nuclear spins would compromise the coherent states needed for quantum computation. The only stable P isotope, ^{31}P, is a spin 1/2 nucleus, so nature has automatically satisfied the qubit criterion. Natural silicon contains a mixture of three isotopes: ^{28}Si (the most abundant corresponding to 92.23%), ^{29}Si (4.67%), and ^{30}Si (3.1%). Whereas the even-numbered isotopes are spin free, ^{29}Si has a spin of I = 1/2. The presence of ^{29}Si is a problem to obtain the spin-free environment required, but currently available isotopic purification techniques can significantly reduce the presence of ^{29}Si (154) to achieve isotopically pure silicon (99.9% ^{28}Si). Using the spin-lattice relaxation time T_1 and the phase coherence time T_2 is one way to infer the stability of the nuclear P spin, which characterizes the time it takes for a spin system with a net alignment (a net magnetization) to return to its thermally equilibrated magnetization. The nuclear spin

qubits interact with the environment through their donor electrons, this means that the electron spin stability called the electron-spin relaxation is also important, particularly for qubit readout. The phase coherence time of the electron spin, as measured by the spin-spin relaxation time T_2, is shorter than T_1 . However, this value for T_2 should be long enough to perform a quantum computation and read out the result (see section 5.8.1).

5.7.1.1 Single Qubit Operation: Nuclear qubit

P has one more electron in its outer electron shell than silicon. When it is placed into a silicon crystal lattice, P acts as a surrogate silicon atom and still has one electron left over. At very low temperatures, that donor electron remains bound to the P nucleus. The electron feels the nucleus primarily through the charge (Coulomb) interaction and to a lesser extent through the hyperfine interaction between the electron spin and the nuclear spin.

The effective low-energy, low-temperature Hamiltonian for the spin interactions for the electron spin and the nuclear spin of an atom in the presence of a static magnetic field $\mathrm{B_0}$ is given by:

$$H = \mu_B B_0 \sigma_z^e - \mathrm{g_n} \mu_\mathrm{n} \mathrm{B_0} \sigma_\mathrm{z}^\mathrm{n} + \mathrm{A} \sigma^\mathrm{e} \cdot \sigma^\mathrm{n} \tag{5.8}$$

where μ_B and μ_n are the Bohr and nuclear magnetons, respectively. σ_z^n and σ_z^e are Pauli spin matrices, and $\mathrm{g_n}$ is the nuclear g-factor. The hyperfine interaction is described by the term $A\sigma^e \cdot \sigma^n$.

The $|\uparrow\downarrow\rangle$ notation is used here to represent the electron spin state and the $|01\rangle$ notation the nuclear state. Hence, for large values of $\mathrm{B_0}$, the Hamiltonian in Eq. 5.8 leads to a set of energy levels that correspond to the four hyperfine levels, $|0\downarrow\rangle$, $|1\downarrow\rangle$, $|0\uparrow\rangle$, $|1\uparrow\rangle$. At the sub-Kelvin operating temperature of the computer, however, the electron spins are completely spin polarized in the lower-energy state $|\downarrow\rangle$.

Thus, for one-qubit operations, the electron spin polarization may be ignored. It is a good approximation to consider only the two nuclear states $|0\rangle$ and $|1\rangle$. The energy difference between those states is:

$$\Delta E_0 = \hbar\omega_0 \cong 2g_n\mu_n B_0 + 2A^2/\mu B B_0 \tag{5.9}$$

Where ω_0 is the nuclear resonance frequency. The resonance frequency, which is typically in the radio-frequency (rf) range is the rate at which the nuclear spins precess about the magnetic-field lines (known as Lamour frequency). Assume B_0 is aligned along the z-axis, and the nuclear spin is initially in the $|0\rangle$ state. Exposing the spins to a secondary magnetic field that is oscillating in the x-direction at the nuclear resonance frequency, labeled by $\mathrm{B_1 = B_1 cos(\omega_0 t)\hat{x}}$, the nuclear spins will begin to rotate toward the z-axis, or from the parallel to the antiparallel alignment. The spin rotation is equivalent to rotating a qubit in Hilbert space from the $|0\rangle$ state to some superposition of the $|0\rangle$ and $|1\rangle$ states. As mentioned, the B_1 field is affecting all spins simultaneously. The A-gates are used to control a particular spin modifying the donor atom's hyperfine coupling. The parameter A in Eq.5.8 is proportional to the magnitude of the electron probability density at the site of the nucleus, $\Psi_e(0)$.

$$A = 8/3\pi\mu_B \mathrm{g_n}\mu_\mathrm{n}|\Psi_\mathrm{e}(0)|^2 \tag{5.10}$$

As shown in Figure 5.6(b), placing a positive voltage on the A-gate above the P atom attracts the electron cloud toward the surface and away from the nucleus, therefore reducing the magnitude of $\Psi_e(0)$. The hyperfine energy levels of that one atom change slightly, and the resonance frequency needed to rotate the nuclear spin is reduced from ω_0 to ω. If the frequency of the B_1 field is stablished to ω, being $\mathrm{B_1} = B_1 cos(\omega t)\hat{x}$, then only the spin directly under the A-gate will be in resonance and it will begin to

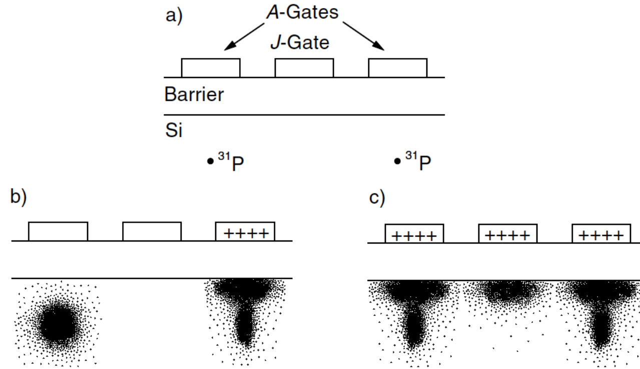

Figure 5.6: (a) Configuration of gates and two donor to make one and two logical operations. A gates are above the donors and J gates lies between the donors sites. (b) The A gates perform one qubit operations, which carry a selected spin into resonance with an external field (rf) magnetic field. (c) The J-gates perform the two qubit operations, lowering the potential barrier between donor sites and turning on the exchange coupling between the donors. In this way the electron mediated nuclear spin exchange will then occur between the donor nuclei.

rotate. By removing the voltage on the A-gate, the rotation is interrupted.

As a consequence, a one-qubit gate operation is implemented if the silicon wafer is exposed to a transverse oscillating B-field of frequency ω and if the A-gate above a qubit is pulsed for a defined period. All over the duration of the pulse, the qubit is in resonance with the secondary magnetic field and rotates through some angle in Hilbert space. If the voltage is eliminated at the end of the pulse, the qubit is left in the desired superposition of the $|0\rangle$ and $|1\rangle$ states.

5.7.1.2 Two-Qubit Operations: Spin Qubit

To select adjacent pairs of qubits for two-qubit operations you need to apply a positive voltage to the J-gate between them. As seen in Fig. 5.6 (c), thus the electron wave functions of the two donor atoms overlap and the electron spins couple together through the electron-spin exchange interaction. Due to each electron's coupling to their nucleus through the hyperfine interaction, the electron-spin exchange interaction also couples the nuclear spins together.

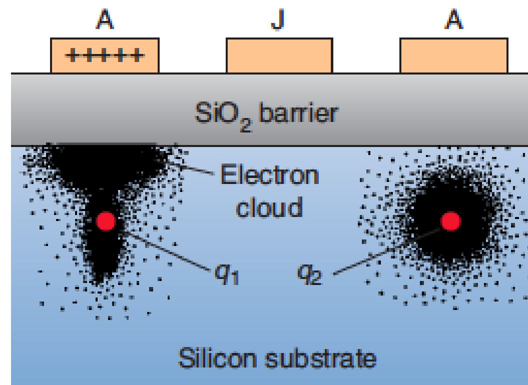

Figure 5.7: A-gate control of the qubit. Here is a representation when a small voltage is applied to the A-gate directly above a qubit. The donor electron moves away from the ^{31}P nucleus. q_1 and q_2 are neighboring nuclei. Figure from (155).

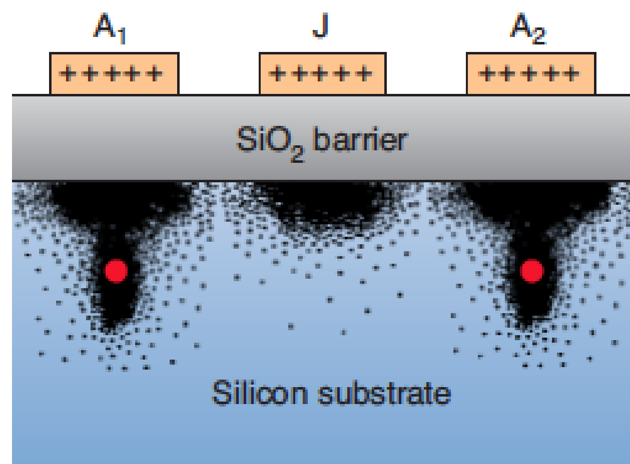

Figure 5.8: J-Gate: Coupling Two Qubits. In case that the gates A_1 and A_2 are properly biased, when a small positive voltage is applied to the J-gate, the potential barrier between adjacent donor sites is lowered and turns on an electron-spin exchange interaction between qubits. The electrons interact with the nuclei through the hyperfine interaction. Therefore, the two nuclear spins become coupled to each other. Figure from (155).

The effective Hamiltonian for the coupled nuclear-electron spin system is:

$$H_{coupled} = H^1 + H^2 + J\sigma^{1e} \cdot \sigma^{2e} \tag{5.11}$$

The first two terms correspond to the hyperfine Hamiltonian of each donor in Eq 5.8 and the last term corresponds to the spin exchange. This Hamiltonian is valid at energy scales that are small compared with the electron-binding energies of the donor atoms. The exchange coupling coefficient J is proportional to the overlap between the wave functions of the two donor electrons, its strength is a function of the J-gate voltage.

The effect of the spin exchange interaction is to create coupled electron-spin states, three with total spin S = 1 and one with total spin S = 0. The respective wave functions are:

$$\begin{array}{rc} \mathrm{S} = 1 & |\uparrow\uparrow\rangle \\ & 1/\sqrt{2}|\uparrow\downarrow + \downarrow\uparrow\rangle \\ & |\downarrow\downarrow\rangle \\ \mathrm{S} = 0 & 1/\sqrt{2}|\uparrow\downarrow - \downarrow\uparrow\rangle \end{array}$$

When B is not present, the energy difference between the states with S = 1 and S = 0 is 4J, known as the exchange energy. When the magnetic field B_0 is applied, the $|\uparrow\uparrow\rangle$ and $|\downarrow\downarrow\rangle$ states are Zeeman-split around zero by an amount $\pm 2\mu_B \mathrm{B}_0$ and the energies of the coupled electron-spin states vary as a function of J, as seen in Fig. 5.9. It is important to note that when the exchange energy becomes equal to the Zeeman splitting, namely $4\mathrm{J} = 2\mu_\mathrm{B}\mathrm{B}_0$, thus the lowest-energy S = 1 state and the S = 0 state cross.

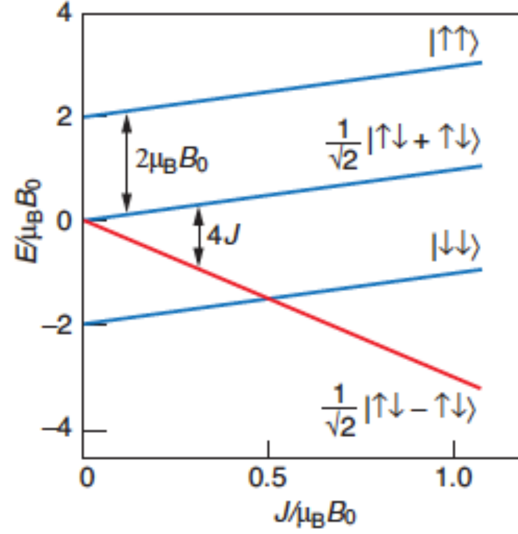

Figure 5.9: Energy levels representation of the coupled electron-spin system as a function of the electron-spin exchange coefficient J. They may be modified by voltage applied to the J-gate. The electrons couple their spins to form three states with S = 1 (blue) and one with S = 0 (red). For $J/\mu_B \mathrm{B}_0 < 0.5$, the electrons occupy the lowest energy S = 1 state $|\downarrow\downarrow\rangle$. Two-qubit operations are achieved in this low J regime. Reproduced by (12).

For every coupled electron-spin state, there are four possible orientations of the two nuclear spins, corresponding to the uncoupled (J = 0) nuclear states $|00\rangle$, $|01\rangle$, $|10\rangle$, and $|11\rangle$. Thus, there are sixteen electron spin-nuclear spin states in all. Focusing only on those states associated with the electron ground state $|\downarrow\downarrow\rangle$ and assuming that $4\mathrm{J} < 2\mu_\mathrm{B}\mathrm{B}_0$, then in order of decreasing energy, the coupled nuclear-spin states are the following:

$$\begin{aligned} &|11\rangle \\ |\Phi_+\rangle &= 1/\sqrt{2}|10+01\rangle, \\ |\Phi_-\rangle &= 1/\sqrt{2}|10-01\rangle, \\ &|00\rangle \end{aligned}$$

The electron-spin exchange interaction shifts the energy of the $|\Phi_-\rangle$ state below $|\Phi_+\rangle$

by an amount

$$\Delta E_{\mathrm{J}} = \hbar\omega_{\mathrm{J}} = 2A^2\left(\frac{1}{\mu_B \mathrm{B}_0 - 2\mathrm{J}} - \frac{1}{\mu_B \mathrm{B}_0}\right) \tag{5.12}$$

The most popular two-qubit gate is the controlled-NOT (C-NOT), also known as the XOR or the measurement gate. This flips the second (target) qubit if the first (control) qubit is $|1\rangle$, which along with single-qubit operations form a universal set of gates from which any quantum algorithm can be executed. In the Kane system, the CNOT corresponds to the conditional rotation of a target spin by 180° , provided the control spin is in the state $|1\rangle$. In principle, it can be realized by subjecting the wafer to a transverse magnetic field B_1 and applying voltages to the A- and J-gates.

Taking two electron spins initially uncoupled ($\mathrm{J} = 0$) the hyperfine coupling constants A_1 and A_2 of the two donor atoms are equal ($\mathrm{A}_1 = \mathrm{A}_2$). If we apply bias to the A-gates such that $\mathrm{A}_1 > \mathrm{A}_2$ the control qubit and the target, can be distinguished. Then, we turn on the spin exchange interaction such that ($\mathrm{J} > 0$) and slowly make $\mathrm{A}_1 = \mathrm{A}_2$. As a result, we would obtain that the uncoupled qubit state $|10\rangle$ evolves adiabatically into the state $|\Phi_+\rangle = 1/\sqrt{2}|10 + 01\rangle$, and $|01\rangle$ evolves into $|\Phi_-\rangle = 1/\sqrt{2}|10 - 01\rangle$. The energy splitting between the two states is given by Eq. 5.12. During this procedure the states $|11\rangle$ and $|00\rangle$ are not modified.

Consequently, we apply a linearly polarized oscillating field B_1 with frequency such that is resonant with the $|11\rangle$ to $|\Phi_+\rangle$ energy difference. The field is left applied on until the $|11\rangle$ state has rotated into the $|\Phi_+\rangle$ state and vice versa. By executing a reverse of the sequence of steps performed at the beginning of the operation, we make an adiabatic transformation of the $|\Phi_+\rangle$ and $|\Phi_-\rangle$ states back into $|10\rangle$ and $|01\rangle$, respectively. The change effected is:

$$|00\rangle \longrightarrow |00\rangle$$

$$
\begin{aligned}
|01\rangle &\longrightarrow |01\rangle \\
|10\rangle &\longrightarrow |11\rangle \\
|11\rangle &\longrightarrow |10\rangle
\end{aligned}
$$

That is that the only qubits that are flipped are those in which the control qubit is in the state $|1\rangle$. This is precisely the definition of a CNOT operation.

5.8 Quantum Confinement in Si Nanostructures: Dopants

The electrons can be confined in Si nanostructures using a combination of material and electrostatic confinements. The shape and size of nanostructured materials provide natural confinement of electrons to 0, 1 or 2 dimensions. The exact confinement potential of the structure in x, y and z directions sets the additional requirements in terms of additional electric fields.

In a single dopant atom the electrostatic potential is radially symmetric, resulting in the same sharp potential well in all directions, as shown in the first column and second column of Fig 5.10. The Bohr radius a_B is the mean radius of the orbit of an electron around the nucleus of an atom in its ground state, and equals for example 2.5 nm for Phosphorus in Silicon. A dopant atom has three charge states: the ionized D^+ state, the neutral D^0 state (one electron bound to the dopant) and the negatively charged D^- state (two electrons bound to the dopant).

Depending on the architecture, the source and drain reservoirs can be constituted of highly-doped Si (157),(158),(11), or of a two-dimensional electron gas (159). The same applies for the gates, but they can also be metals (159). The result is a single-electron transistor that consist of a sharp dopant potential well connected to source and drain reservoirs.

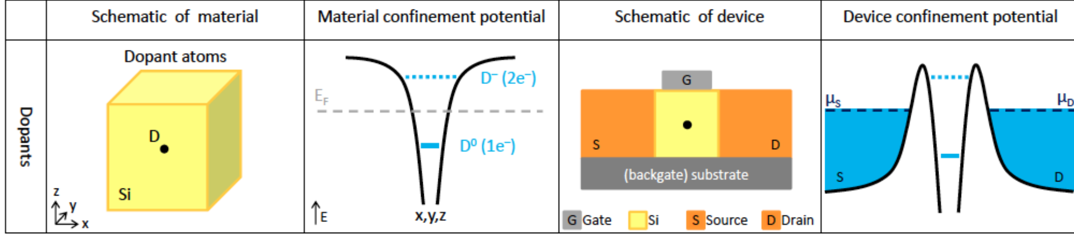

Figure 5.10: First column: schematic of dopants in Si. Second column: The electron states for dopant atoms in x-, y- and z-direction confinement potentials, which are occupied up to the Fermi energy E_f (dashed grey line). Occupied and unoccupied electron states are indicated as straight and dashed lines respectively. Third column: Schematic of the silicon nanostructure integrated into a transport device with source, drain and gate electrodes. Fourth column: The potential landscape of the single-electron transistor is made up of the steep dopant potential well which is tunnel-coupled to source and drain reservoirs and electrostatically coupled to gates which can move the ladder of electrochemical potentials. Figures from Reference (156).

5.8.1 Spin Relaxation and Decoherence

The measurements of T_1 in bulk samples are performed obtaining the timescale over which the thermal equilibrium is recovered after either an inversion pulse[1], which changes the populations of the ground state and excited spin state, or a saturation comb [2](160) which equalizes the populations.

The coherence time T_2 for electron spins in a solid state is determined by the hyperfine coupling between the electron and the surrounding nuclear spins. The nuclear spins exhibit a complicated dynamics, driven by the interplay of their mutual interactions and the coupling with the electron. The time fluctuations of the hyperfine field randomize the electron spin precession frequency and destroy its coherence. Even in the presence of a perfectly static nuclear spin bath, a macroscopic ensemble of spins

[1]The inversion recovered method is popular to measure the T_1, where the magnetization is inverted with a π pulse, then a time τ allowed to relax along the $+z$-axis. The magnetization after time τ is measured applying a $\frac{\pi}{2}$ pulse and then measuring the Nuclear Magnetic Resonance (NMR) signal.

[2]Saturation comb pulses is another method to measure T_1 with special NMR pulse sequences. When $\pi/2$ pulse sequences are irradiated to a system with an interval of time sufficiently longer than the time T_2 of nuclear spins, a completely mixed state in which the nuclear spin in the ground state and excited state are equally mixed is formed in short time. When the system is allowed to freely evolve from this mixed state as the initial state, the nuclear spins are relaxed to the thermal equilibrium state in a time scale T_1.

would exhibit a spread of precession frequencies as a consequence of inhomogeneity in the local magnetic field, caused e.g. by the difference in the instantaneous value of the local hyperfine field at every electron site. The resulting dephasing time T_2^* represents the timescale over which a free induction decay occurs. T_2^* process arises when the quasi-static value of the local magnetic field changes from one repetition to the next. The 'true' decoherence time T_2 is obtained in the experiments by 'refocusing' the quasi-static inhomogeneity of the magnetic field through a Hahn echo technique (161).

5.8.1.1 Spin Decoherence

The theory of electron spin decoherence arising from nuclear spins in Si is well understood. The correct order of magnitude of the decoherence time T_2 was already predicted by early studies, initially neglecting time correlations (162). Later, using fully quantum mechanical solutions of the dynamics of electron spins in a nuclear bath included nuclear spin pair correlations yielded accurate matching between theory (163) and experimental data on the electron spin echo decay of P donors in natural silicon (164), see Fig. 5.11.

The echo decay to determine the T_2 decoherence adopt the form (163):

$$V2\tau \propto ESEEM \times exp[-2\tau/T_{\mathrm{R}}] \times exp[-(2\tau/T_{\mathrm{SD}})^{\alpha}] \tag{5.13}$$

Here $V2\tau$ is the amplitude of spin echo signal, ESEEM means the electron spin echo envelope modulation, τ is the time interval before and after the refocusing π pulse in the Hahn-echo sequence, T_{R} is a relaxation time that accounts for both instantaneous diffusion and T_1 processes, T_{SD} is the spectral diffusion time, which depends on the internal dynamics of the nuclear bath, and the exponent α takes the value 2.3 (163). ESEEM arises from the anisotropic component of the hyperfine coupling to the ^{29}Si nuclei.

Theoretical results have been extended to the study of decoherence on isotopically

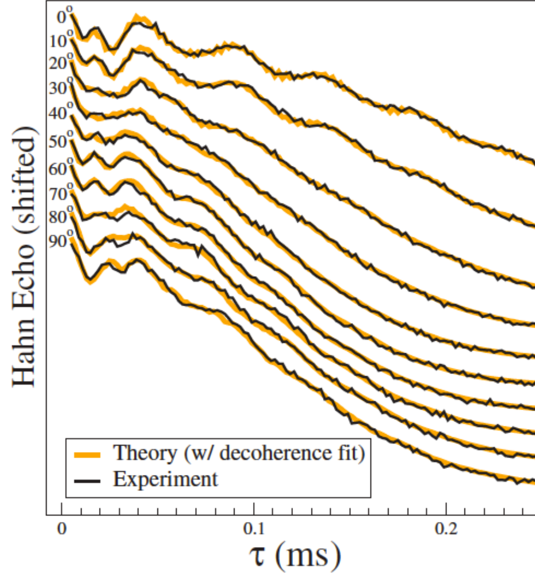

Figure 5.11: Experimental echo decay (black) and theory (orange) for ^{nat}Si:P at different angles of the magnetic field with respect to the crystallographic [001] axis. Notice the echo envelope modulation arising from anisotropic hyperfine coupling between donor electron and ^{29}Si nuclei. From Ref. (163).

purified samples (165). The theoretical results to match with Si:P bulk data involve the interplay between ^{29}Si spectral diffusion and dipole-dipole coupling among electron spins, see Fig 5.12. The latter allow the excitation of spin 1 and de-excitation of spin 2 or vice versa ("flip flop" process) while conserving total energy to within the strength of the coupling term. This process produces additional magnetic noise on a spin qubit. With this basic understanding, recently Tyryshkin et al. (149) have measured $T_2 > 10$s, using a highly purified ^{28}Si:P crystal, and deliberately introducing a magnetic field gradient across the sample to prevent neighboring spin undergoing energy-conserving flip flop processes. We can also suppress flip-flop lowering the temperature such that $g\mu B >> k_{\rm B}T$, then polarizing the electron spins. This would lead to an exponential suppression of the dipolar decoherence channel (159, 165, 166) because of the deficiency of spins in an excited state.

5.8.1.2 Observed Coherence T_2 in Si

- Electrons bound to donors in highly purified bulk in Si: 10s at 1.8 K (149). The long time is achieved by the suppression of flip-flop processes.

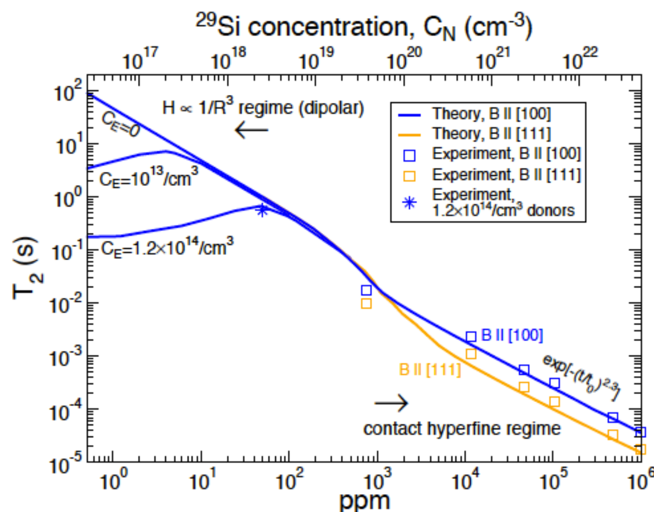

Figure 5.12: Decoherence time T_2 of Si:P donor electron spins over varied donor concentrations C_N (for nuclear) and ^{29}Si concentration, using ppm (namely, parts per million) of lattice sites. At high C_N, contact hyperfine interactions dominate and T_2 is dependent upon the magnetic field direction relative to the lattice orientation. At low C_N, T_2 is dependent upon C_E (for electron), and eventually dominated only by dipolar interactions. Experimental results are shown as square and star symbols. Results taken from (165).

- Electrons bound to donors 50 nm below a Si surface: 0.3 ms at 5.2 K (0.75 ms for hydrogen passivated surface) (167).
- Electron bound to donors in CMOS (natural Silicon): 200μs at 300mK (166).
- 2D electrons at the Si/SiO_2 interface (natural Silicon): 0.3 ms at 5 K (168).
- Electrons at natural Si quantum dots: 20 ms at 1 K (168).

Table 5.2 shows some experimental measurements concerning T_2 on different systems. One can observe that T_2 depends on the density of confined electrons, with shorter T_2 observed for higher dot densities.

5.8.2 Orbital and valley relaxation

Excited orbital or valley states act as intermediate states for perturbations involving lattice phonons and spin-orbit coupling causing spin relaxation. However, the orbital

Table 5.2: Measurements of T_2 in different systems of mobile 2D electrons as well as confined electrons. Data from Ref. (168).

System	Confined Electrons	Mobile Electrons
^{28}Si accumulation Field Effect Transistor (FET) ($\mu = 14000\text{cm}^2/\text{Vs}$)	$T_2 = 2\mu s$	$T_2 = 0.39\mu s$
Natural Si Inversion FET ($\mu = 2000\text{cm}^2/\text{Vs}$)	$T_2 = 0.54\mu s$	$T_2 = 0.11\mu s$
Si/SiGe ($\mu = 10^5\text{cm}^2/\text{Vs}$)		$T_2 = 3\mu s$

and valley excited states may also be used, for instance to mediate strong interaction between nearby donors. One early proposal suggested the use of the excited $2p$ orbital states of a deep donor to induce a superexchange interaction between pairs of shallow donors placed on either sides of the central one (169). This involves the coherent manipulation of hydrogenic Rydberg states[1] (170). The 2p Rydberg state lifetime for P donors in Si was found to be $T_1 \approx 200$ps attributed to the spontaneous emission of phonons (171). Coherent control of the Rydberg states has also been achieved, with an orbital coherence time $T_2 \approx 28$ps (170).

Valley states are expected to have much longer lifetimes and coherence, due to the unlikelihood of processes that cause inter-valley transitions. A recent proposal describes the use of singlet and triplet valley states of a double quantum dot to encode and manipulate quantum information with reduced sensitivity to noise (152). See Chapter 6 in section 6.4. Recent experiments have given evidence of the valley physics and its effect on electronic states. Through transport spectroscopy measurements of donor states in FinFETs, Lansbergen et al. (172) showed that under certain conditions relaxation of excited states into lower manifolds is suppressed due to a combination of both spin and valley blockade. The phenomena due to 'lifetime enhanced transport' (LET) was first observed in a silicon double quantum dot. In the experiment, LET enabled to identify a blocked transition between states that have different valley symmetries.

[1] The Rydberg states of an atom are electronically excited states with energies that follow the Rydberg formula as they converge on an ionic state with an ionization energy. The wavefunctions are expanded from their ground-state extents of less than 0.1nm to several nanometres and even beyond. This allows atoms far enough apart to be non-interacting in their ground states to strongly interact in their excited states.

As noted above, the multiple conduction band valleys in silicon can be a useful ingredient for a QC. This feature (as described in next Chapter 6) may impose limitations on spin manipulation and coherence but, on the other hand, it may be used for encoding quantum information mediating relevant transition between neighbor donors. Consequently, the interest in valley physics applied to QC has been raised recently to explore issues such as how to promote controlled inter-valley transitions, to what extent valley degeneracy can be lifted and how sensitive such operations are to fabrication-related parameters. The valley degree of freedom in the manipulation of donor electrons is the focus of this part of the thesis.

5.9 Silicon Based Quantum Computer Fabrication

The use of single donor atoms in Silicon as qubits has demanded tremendous advances in single atom fabrication and engineering. Donor separations of order $\sim 10 - 20$ nm as in Kane's proposal are required to ensure significant coupling between neighboring spins. Currently this is at the limit of what is technologically achievable. Despite these concerns there have been concentrated efforts internationally to realize a donor-based qubit architecture resulting in a deluge of experiments of transport in nano-scale doped quantum dots and donors. Significant to these results has been the different technologies developed to fabricate donor-based devices, which are briefly discussed as follows.

5.9.1 Single dopants in MOS-based architectures: Top-down approach

Single dopant transport in ultra-scaled Metal-oxide-semiconductor Field-effect (MOSFET) transistor structures is based on randomly and deterministically doped devices. The newer generations of CMOS devices are using an undoped channel to evade the issues related to random device fluctuations. However some dopant atoms diffuse in the nano-scale transistors from the source and drain regions into the channel. In this case, devices with a small number of dopant atoms in the channel can be studied (157, 173). These experiments have showed that the number of electrons bound to the dopant atom could be controlled by the gate electrode. Such spectroscopic transport experiments reveal relevant information on the orbital levels, the charging energy and the

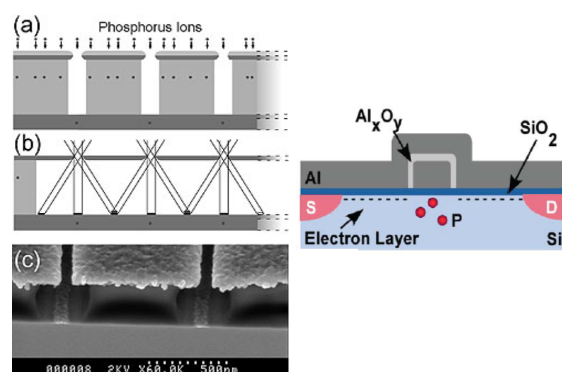

Figure 5.13: (Left)A schematic of the 'top-down" fabrication strategy. Holes are formed in a trilayer resist structure through which P ions are implanted. (b) After removal of the top layer of resist and chemical development, a triple angle evaporation process is used to form the SETs and control electrodes. (c) SEM images showing a 250 nm wide cavity below an overhanging Poly Methyl Methacrylate (PMMA) resist layer with Al deposited through a 50nm gap. Courtesy by (176). (Right) Schematic of a nanoFET where roughly 3 donors have been implanted into the 50 × 30nm active area of the device. From Ref. (177)

binding energy of the dopant atom and the spin configuration of the bound electron(s) (172, 173). Other groups have concentrated on adjusting the industry standard technique of ion implantation (namely, top down technique sketched in (Left) Fig 5.13) to implant single dopants into a silicon device in a controlled manner (174, 175). Nevertheless, there are three main limitations to applying the technique to scalable single atom architectures: the capability to register individual ions, the overall spatial registration of the ion implant site and subsequent straggling of the ion. When the dopants are implanted a rapid thermal annealing at high temperature is needed to repair the damage and activate the donors, causing diffusion and segregation of dopants.

Despite these inconvenients, silicon nanoscale transistors were fabricated with a low density of local area implants where it was possible to tune individual dopants into resonance and observe transport spectroscopy through a single dopant, such as a P donor. A schematic drawing is shown in Fig 5.13 (right). More recently single dopant implantation has been demonstrated into the channel of a silicon nanoscale metal-oxide-

semiconductor field-effect transistor (178).

There are 3 different modes to realize transport experiments for single dopants:

1. The channel current is influenced by the presence of a neutral or charged dopant. For instance, in Ref (179) was identified a single acceptor that modified the current through a FET depending on its charge state. For this regime single dopants can be detected by their electrostatic coupling to free electrons in the channel.

2. Direct transport through a dopant in the access region of an FET channel. The access region depends on both the device design and the doping level. This region is constituted by the part of the channel that has a weaker coupling to the gate which leads to a barrier in the band structure and the electron pass through this access region by transport via dopant states. (180). This allowed the study of electric field and strain effects on the acceptor and the Zeeman splitting.

3. Direct transport through the dopant states in the sub-threshold regime of a transistor. Due to the progress in device scaling this was recently realized in ultra-scaled MOSFET (157). This represents the most direct way to access information about the properties of a dopant and its environment.

All three transport regimes are illustrated in Fig 5.14.

The transport measurements have shown that the environment, such as the presence of the leads, an interface to a gate, or an electric field in a Si nanostructure may alter the states of a dopant in comparison to the unperturbed bulk. This could be observed in Ref (173), where the energy spectrum of single donors located in the channel of FinFETs was measured by transport spectroscopy, see Fig. 5.15 (a) . Here theoretical analysis together with the data, allowed to identify the donors (As in this case) and gave a determination of the degree of gate-controlled quantum confinement in each device. Fig 5.15 (b) shows the three confinement regimes that could be distinguished: At low electric fields the electron is located at the donor site and its ground state corresponds to a donor in bulk. At high electric fields the electron is pulled inside the triangular potential well at the interface. The electron is still localized near the donor site, in correspondence with the results of (182). At the crossover between these regimes, the

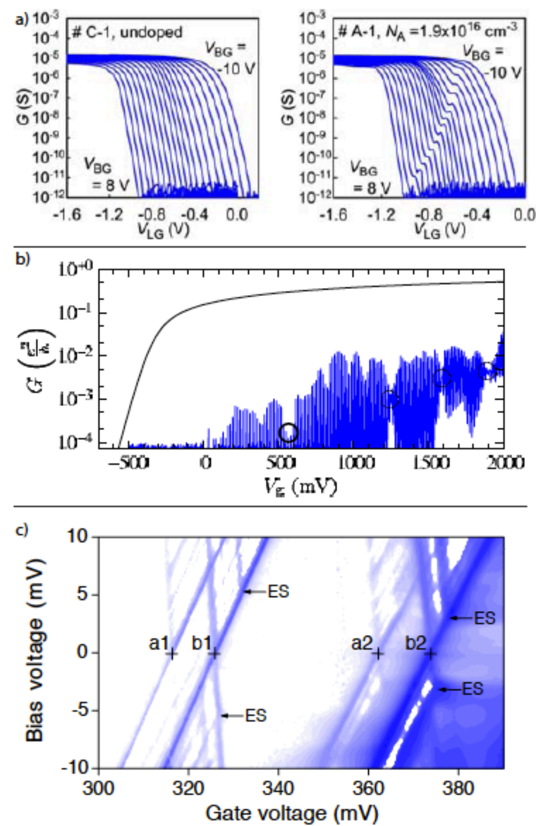

Figure 5.14: An example of the dopant detection regime based on the capacitive coupling the channel is shown in a) for an undoped (left) and doped (right) MOSFETs. An example of the second regime where the dopant is in the barrier of the access region in series with a quantum dot is shown in b) (the thick black line represents the room temperature FET characteristics and the line below the low temperature Coulomb blockade). The third regime with direct transport through a dopant in the sub-threshold limit is shown in c). From a) (179), b) (180) and c) (181)

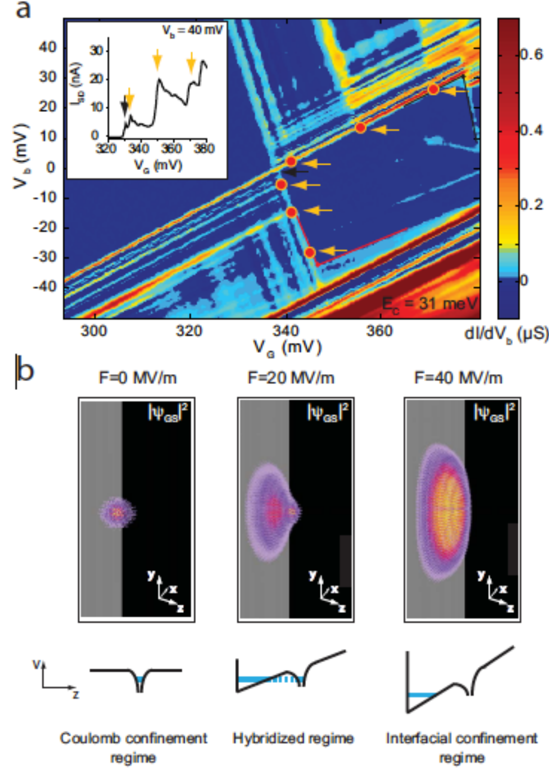

Figure 5.15: a) Source/drain differential conductance of a dopant in a FET. Excited states are indicated by the red dots and yellow arrows. Inset in (a) shows source/drain current as a function of gate voltage. b) Simulations of the gated donors eigenstates: wave function density of the (D^0) ground state located 4.3 nm below the interface in the three different electric field regimes. Figure from Ref. (173).

electron is delocalized over the donor and well sites. In this work the ground state of a neutral (D^0) and negatively charged donors (D^-) hybridized with the interface was measured.

Very recently transport measurements have demonstrated the ability to manipulate the wave function of a single donor electron with an electric field. The experiment used a Nano-wire FET with a small number of randomly placed P donors in the channel (also called single atom transistor (SAT)) as a platform to study single dopants. Due to fact that the position of the donors is random, the tunnel coupling to the source and drain contacts is different for each donor. This allowed to select a device with a dopant in a favorable location in the channel. The device is depicted in Fig. 5.16. This design

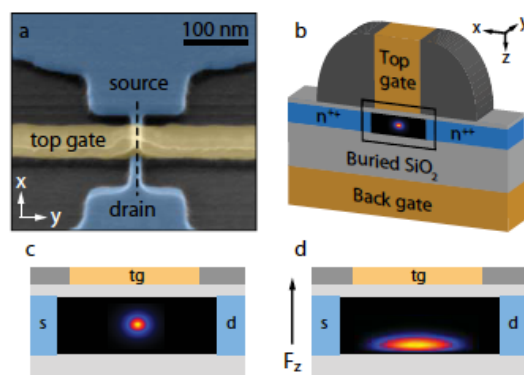

Figure 5.16: a) Scanning electron micrograph of the single donor device. b) A schematic cross-section of the device across the dashed line. c) and d) show the simulated wave function of an electron bound to a single phosphorus donor in the center of the channel. By inducing an electric field in the z-direction, the one-electron electron wave function is deformed in a controlled way. Courtesy from (183).

provided a high degree of tunability to control the wave function of single donors.

In the experiment described above, they performed single donor current spectroscopy on the SAT keeping the source/drain bias small ($\mu_{s,d} \approx eV_s \approx eV_d$)$< k_BT$ (k_B is the Boltzmann constant) and thus only the ground state is probed. At low gate voltages the current is blocked. As the gate voltages are increased, a localized state in the channel moves into resonance with the source and drain chemical potentials and the current can flow. When the localized state is situated below the source/drain chemical potential the current is blocked again. From the resonant current signal they identified three important regions labeled as A, B, C as depicted in Fig. 5.17. In region B the current flow is mediated by a bulk like wave function localized at the donor nucleus. In regions A and C the current is mediated by the wave function localized in an interface well that is induced by the electric field. Thus, by changing the frontgate and backgate voltage the local electric field can be tuned, while maintaining the donor in resonance with the source/drain chemical potential.

Other recent transport experiments on the characterization of donor states in Silicon devices (design depicted in Fig. 5.18) (184) have permitted the measurement of the energy separation of the ground and first excited state of a donor 'valley orbit-splitting' '

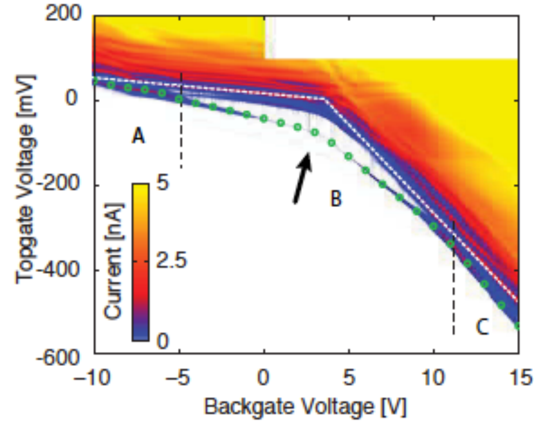

Figure 5.17: The drain current as a function of backgate and topgate voltage at a source/drain bias of 0.2 meV at 4.2 K. The white dashed line indicates the intrinsic device threshold voltage and the green circles a single donor resonance. In region B, between the black vertical dashed lines, the resonance is induced by a bulk-like donor state and in the regions A and C an interface-well-like one. Courtesy from (183).

(VOS) for shallow isolated P donors in silicon gated-nanowires. The VOS was determing using a double dopant transport spectroscopy using a compact 3-gate design, where the ground level of one donor atom acts as an energy filter, which probes the levels of the other. The VOS results are found to be close to its bulk value.

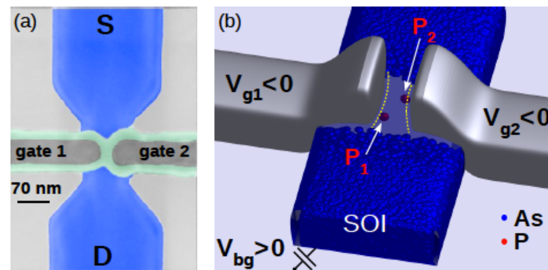

Figure 5.18: a) View of the sample (scanning electron microscope). Two gates (gray) surrounded by nitride spacers (green) partially cover the silicon-on-insulator (SOI) channel between the source (S) and drain (D). (b) Schematic of the sample with As dopants in the source and drain. Figure from Ref. (184).

5.9.2 Single dopants in crystalline silicon: Bottom-up approach

An alternative technology has been developed to place dopants in Silicon with atomic precision using a scanning probe microscope. However this technology to manipulate atoms in silicon was not simple due to the strong, covalent nature of silicon bonds. To position atoms in silicon it was necessary to use a lithographic process, analogous to conventional optical/e-beam lithography. Here a monolayer of hydrogen resist is patterned using the tip of the STM to create an atomic-scale template, described in Fig 5.19. The process of STM hydrogen lithography has since been adapted to realize a complete fabrication strategy for atomic-scale Silicon device fabrication (185). The important feature of these devices is that, in contrast to modern CMOS devices and almost all quantum semiconductor devices, which use many materials and have heterogeneous interfaces, STM-patterned devices are formed in single crystal silicon, thus the confinement of electrons is achieved by atomically abrupt changes in the density of dopant atoms within the silicon crystal. The doped regions can have very high planar electron densities in the range $n_{2D} \approx 2.5 \times 10^{-14}\mathrm{cm}^{-2}$. At these high carrier densities, it has been possible to realize electron transport studies in these highly doped single crystal donor-based quantum wires, and recently this technique has been used to realize conducting wires in silicon with Ohmic behavior down to the atomic-scale (186).

It is also possible to pattern more complex devices, such as atomically abrupt, epitaxial quantum dots with 1D source and drain leads. These studies have allowed the impact of vertical and lateral confinement on silicon quantum dots to be investigated. Using such a technology it is also possible to pattern individual dopants in silicon with atomic precision to realize single dopant atom transistors (see bottom of Fig. 5.19) (11, 187). These transport devices also contain electrodes, and these electrodes are known to have profound effects on the energetics of the single dopant atom. In these epitaxial architectures the electrostatic potential at the dopant could be tuned using two in-plane gates G1 and G2 patterned at either side of the transport channel defined by the S and D leads (see the device in Fig. 5.19 at bottom right corner). In Fig5.19 at bottom left corner, the measured stability diagram of the single donor is presented, in which the three charge states of the donor can easily be identified: the ionized D^+ state, the neutral D^0 state and the negatively charged D^- state.

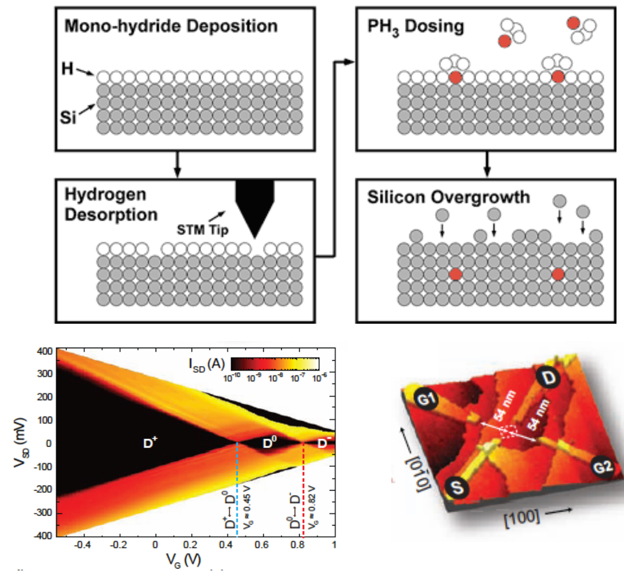

Figure 5.19: (Top) A schematic diagram of the "bottom-up" fabrication process. A low defect density Si (001) 2x1 surface is passivated with a monolayer of hydrogen. An STM tip is used to selectively desorb hydrogen, exposing silicon at the atomic scale to allow one phosphine molecule to adsorb at each of the required sites. Low temperature silicon MBE overgrowth encapsulates the phosphorus array. (Bottom right corner) the source (S), drain (D) and two gate leads (G1, G2) to the central donor, which is incorporated into the dotted square region. (Bottom left corner) The electronic spectrum of the single-atom transistor, showing the stability diagram with the drain current I_{SD} (on a logarithmic scale) as a function of source-drain bias V_{SD} and gate voltage V_G (applied to both gates). Courtesy from (11).

Transport in these devices and the manipulation of the donor electrons for quantum computing are affected by the Si band structure. In chapter 6, we will examine the singular features of silicon conduction bands as well as the implications for QC.

6

Relevant Silicon Features For Quantum Computing

6.1 Bulk silicon: valley degeneracy

Here we review aspects of silicon that will be critical in understanding the challenges that arise in describing Si-based nanoscale devices with the desired properties. One such aspect is how the effects of multiple valleys present in the conduction band in bulk silicon appear in particular silicon nanodevices. The manifestations of valley physics are crucial for manipulating the spin degrees of freedom of electrons in dopant-based devices. In the following sections we are going to discuss the conduction band valleys in bulk silicon, the valley coupling and the related splitting in dopant devices, and the consequences of valley physics in Quantum Computing (QC).

Crystalline silicon is a covalently bonded crystal with a diamond lattice structure, see Fig 6.1(a) and (b). Fig 6.1(c) shows the band structure of Si. The conduction band has its minima away from the Brillouin zone center, close to the X points with $k_0 = 0.85\frac{2\pi}{a}$, with a the lattice parameter. Due to the cubic symmetry, these are 6 equivalent valleys as sketched in Fig. 6.1(d).

In traditional electronic devices, the presence of multiple valleys typically does not affect transport properties. However, valley physics plays a critical role in quantum electronics due to the interference between different valleys arising when the electronic

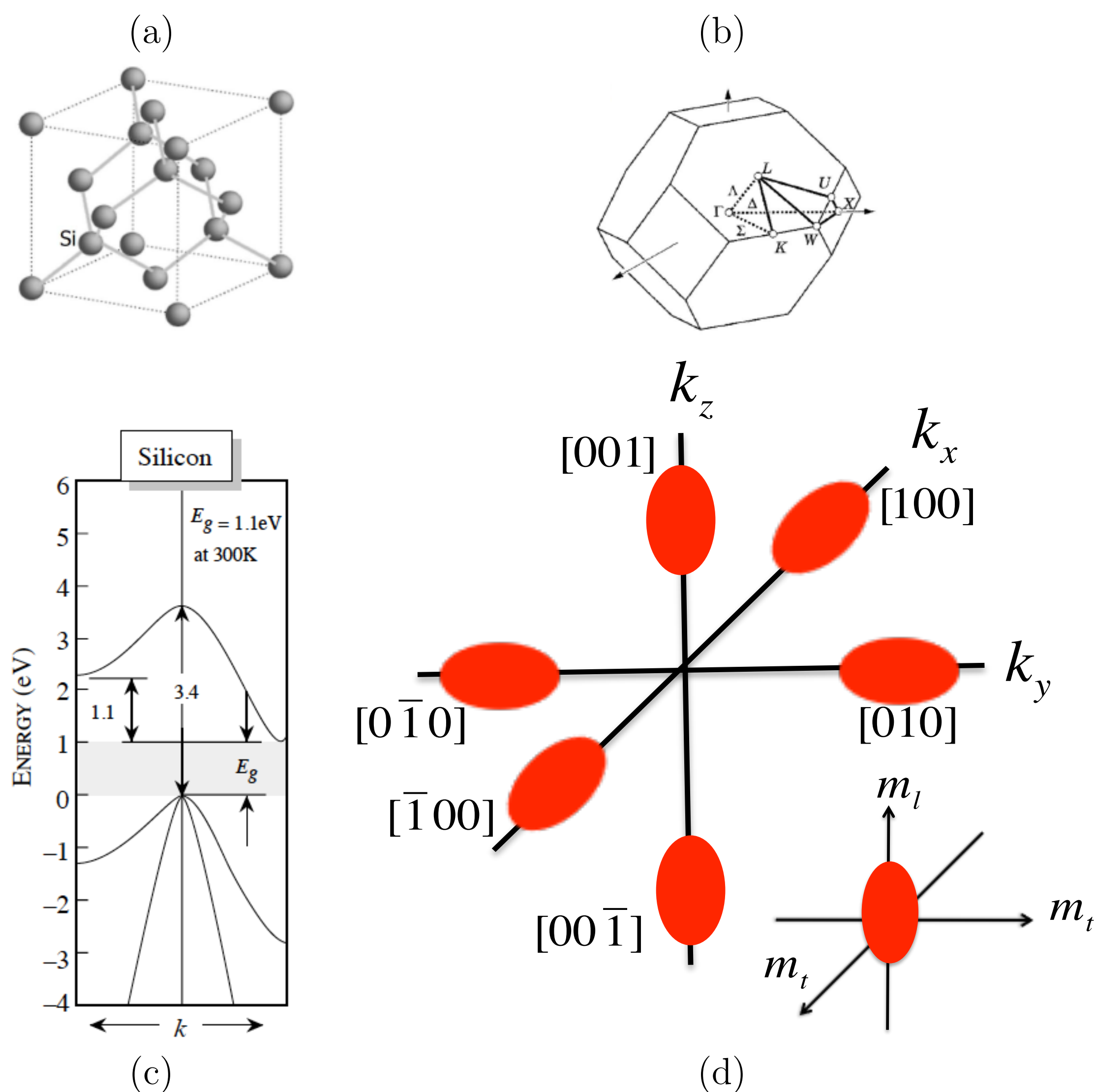

Figure 6.1: Silicon crystal in real and reciprocal space. (a) 3D plot of the unit cell of the bulk silicon crystal in real space, showing the diamond or Face-Centered Cubic (FCC) lattice, which has cubic symmetry. (b) Silicon crystal in reciprocal space. Brillouin zone of the silicon crystal lattice. It is the Wigner-Seitz cell of the BCC lattice. Γ is the center of the polyhedron. (c) Band structure of bulk silicon. Figures from Ref. (156). (d) The conduction band has its minima away from the zone center (188), close to the X points with $\mathrm{k}_0 = 0.85\frac{2\pi}{a}$, with a the lattice parameter. Due to the cubic symmetry there are 6 equivalent valleys.

transport is fundamentally quantum. For example, the presence of additional valleys greatly complicates spin manipulation because it can lift Pauli spin blockade, which is fundamental for many strategies for spin manipulation in quantum dot nanodevices (141, 189).

The valleys are degenerate which means that the energies of the six states related by the cubic symmetry are the same. The ground state for a donor electron is labeled by the reciprocal-space points k_μ at which the valley minima occur, being $\mu = x, -x, y, -y, z, -z$. The effective mass of these anisotropic minima is characterized by a longitudinal mass along the corresponding equivalent (100) direction and the two transverse masses in the plane perpendicular to the longitudinal direction. In silicon the longitudinal electron mass is $m_l = 0.91 m_e$ and the transverse electron masses are $m_t = 0.19 m_e$, where m_e is the free electron mass. Accordingly, the low energy donor electron wave functions can be expanded in the basis spanned by the six valleys, see Eq 7.2. Nevertheless, in nanodevices this degeneracy of states may be and usually is broken by various effects, basically due to the mass anisotropy, as well as strain, confinement, and electric fields effects. When the valley degeneracy is lifted, at low temperatures the carriers populate only the lowest-energy valley, thus eliminating some of the quantum effects that arise when the valleys are degenerate.

6.2 Valley Effects At The Donor

The existence of six equivalent conduction-band minima along the [100] directions in silicon has a profound influence on the energy states of donors. The central-cell potentials of donor atoms occupying tetrahedral lattice sites, either substitutional or interstitial, will split a sixfold-degenerate s state into a singlet (A_1), a triplet (T_2) and a doublet (E), with the ground state being a non-degenerate state. This splitting is usually referred to as valley-orbit splitting. Since the central-cell potential is very localized, the splitting is much less for excited s states than for the $1s$ state and negligible for $p, d, ...$ states. In Ref (190), the valley-orbit splitting and binding energies for shallow level group-V donors (hydrogenic donors, as P, As, Sb and Bi) have been calculated in silicon, using a model impurity potential with central cell corrections and intervalley overlaps of the wave function components. This model may be scaled to give the model

impurity potentials of the deep-level group-VI donors (as S, Se, Te and Po) of the same row in the Periodic Table, Ref (191).

The valley orbit interactions (192, 193), which account for intervalley scattering effects, may be included in an effective way as perturbations to determine the binding energies and the donor electron wave function. These valley-orbit effects are conveniently represented by two types of intervalley couplings for valleys on perpendicular symmetry directions (e.g. x, z) and for those on opposite symmetry directions (e.g. z, z) (194). Here, these couplings have been represented by Δ_c and $\Delta_c(1+\delta)$ respectively, which have been included in the model Hamiltonian in Chapter 7, Eq 7.27. Taking into consideration the valley-orbit scattering through $\Delta_c = 2.16$meV and $\delta = -0.3$ (195) parameters, it is possible to reproduce correctly the ordering and relative splittings of the lowest energy states manifold for P donors in Si: A ground state A_1 followed by a triplet T_2 and by a doublet E with a binding energy of 41.15 meV for the ground state, 29.57 meV for the triplet and 28.37 meV for the doublet. These numbers are in a good agreement with the experimental values of 45.46 meV, 33.74 and 32.37 meV, respectively (190). Another accurate estimates of the binding energy were obtained through non-perturbative variational treatments, within the multivalley effective mass spherical band approximation (190). A straightforward sketch of the binding energies of the states and the splitting among them is presented in Fig 6.2 (a). The valley compositions of these states show that the ground singlet A_1 is a symmetric superposition of all six valleys: $1/\sqrt{6}(1,1,1,1,1,1)$, while the triplet T_2 has $[1/2(1,\bar{1},0,0,0,0), 1/2(0,0,1,\bar{1},0,0), 1/2(0,0,0,0,1,\bar{1})]$ symmetries and the doublet E has $[1/\sqrt{2}(1,1,\bar{1},\bar{1},0,0), 1/\sqrt{12}(1,1,1,1,\bar{2},\bar{2})]$ symmetries, as depicted in Chapter 7, Fig 7.3. Thus, for P dopants, strong central-cell corrections near the dopant break the six-fold valley degeneracy of bulk silicon so that the lowest energy state is non-degenerate (except for spin degeneracy), lowered by an energy $E_{GS} = E_{SV} - (5-\delta)\Delta$. We use the value of single valley (namely, no valley orbit interaction) energy as $E_{SV} \sim 31$ meV (196). The degeneracies of higher-energy levels (namely, T_2 and E) are broken by lattice strain and by electric fields.

Another physical effect for donor in bulk Si, and surely important for quantum electronic devices, is the inter-valley interference between the conduction-band-edge states

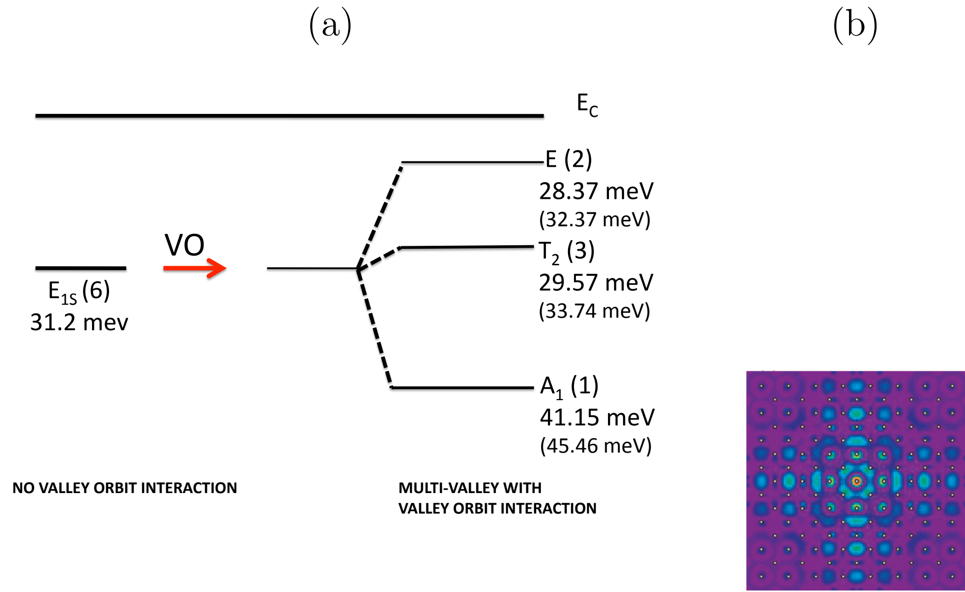

Figure 6.2: (a) Binding energies of the singlet (A_1) (ground state), triplet (T_2) and doublet (E) levels. In parentheses are the binding energies obtained experimentally, presented in Ref (190). (b) Charge density $|\psi_{R_0}(r)|^2$ for the donor state. The impurity site R_0, corresponding to the higher charge density, is at the center. Except for this central site, regions of high charge concentration and atomic sites (white dots) do not necessarily coincide, because the charge distribution periodicity imposed by the plane-wave part of the Bloch functions is incommensurate with the lattice period. Courtesy of Koiller et al (196).

of Si. This effect leads to oscillatory behavior in the charge distribution of one-electron bound states and in the exchange coupling in two-electron states. These interesting oscillatory patterns result from interference between the different plane wave components of the Bloch functions. Thus, the charge distribution periodicity imposed by the plane-wave part of the Bloch functions is incommensurate with the lattice period (196), see Fig 6.2 (b).

6.3 Valley Effects on the Interface V_{VO}^{I}

Several quantum computer architectures under investigation involve manipulation of the electronic spin at an interface between Si and some barrier material, by local surface gates. The most commonly used barriers are SiGe alloys (146) and SiO_2 (12). In these systems, the conduction band degeneracy in Si is lifted at the interface as the spatially abrupt change in the conduction band minimum leads to intervalley scattering.

The confining electric field (generated by external electrostatic gates and/or depletion layers) generates a quasi triangular potential well at the interface, perpendicular to the z direction [(001) interface]. Thus, the ground state energy of such triangular potential well depends on the effective mass in the z direction. The effective masses at the conduction band minima of Si are anisotropic, with the longitudinal effective mass more than 4 times larger than the transversal. This shifts the minima along the x and y directions well above the minima in the z direction. As shown by Fig 6.3 the six-fold degeneracy is breaking into a 2-fold degenerate ground state and a 4-fold degenerate excited state (197) [1]. For instance, the splitting due the anisotropy effective masses

[1] In the effective-mass approximation EMA, the electrons are considered having masses characteristic of the conduction-band minimum. Because of the kinetic energy term in the Hamiltonian the valleys giving the largest effective mass m_z for motion perpendicular to the surface will have the lowest energy. Using a triangular potential approximation to describe a potential well bound on one side by the infinite vertical barrier that keeps electrons out of the insulator and on the other side by the electric field linearly rising potential, the binding energies are obtained as $E_\mu = \langle f_\mu(z)|H|f_\mu(z)\rangle$, $\mu = x, y, z$, with $H = T - keFz$, where T is the kinetic energy and $keFz$ is related to the triangular potential. Then, the eigenstates energies are:

$$E_x = E_y = (\hbar/2m_\perp)^{1/3}[\frac{3}{2}\pi eF(\frac{3}{4})]^{2/3}; E_z = (\hbar/2m_z)^{1/3}[\frac{3}{2}\pi eF(\frac{3}{4})]^{2/3};$$

$m_x = m_y = m_\perp$ and $m_z = m_\parallel$, with $\gamma = \frac{m_\perp}{m_\parallel}$. The splitting at the triangular potential and binding energies depend on the electric field applied along z direction (182, 197)

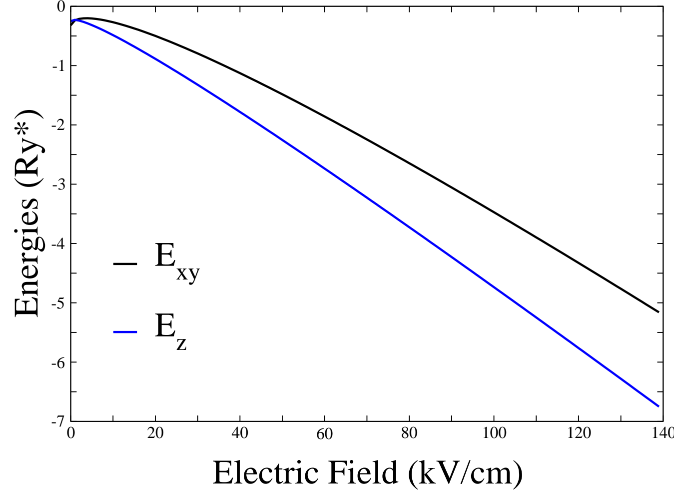

Figure 6.3: Binding energies for the interface state with respect to electric field applied. These are calculated using a triangular potential approximation. E_z (blue solid line) corresponds to the 2-fold degenerate ground state. E_{xy} (black solid line) corresponds to the 4-fold degenerate ground state.

is $\sim 1.13Ry^*$ for $F = 80$ kV/cm. The splitting is further enhanced if tensile strain is applied to the Si crystal (e.g. in Si quantum wells grown over relaxed SiGe substrates) (198).

The 2-fold degeneracy remaining in the ground state of the electron at the interface is an important spin decoherence source. However, this effect can be overcome close to an interface that can efficiently scatter carriers between the two degenerate valleys that are near opposite ends of the Brillouin zone. Therefore, the degeneracy in the two-dimensional $\{k_z, k_{-z}\}$ subspace is lifted in the presence of a sufficiently singular perturbation potential, as long as the interface is sharp enough (199). The coupling due to the perturbation lifts the degeneracy leading to the valley splitting $2|V_{VO}^{I}|$. Then, the quantity of interest to determine the splitting is V_{VO}^{I}, also called valley-orbit coupling at the interface, see Fig 6.4.

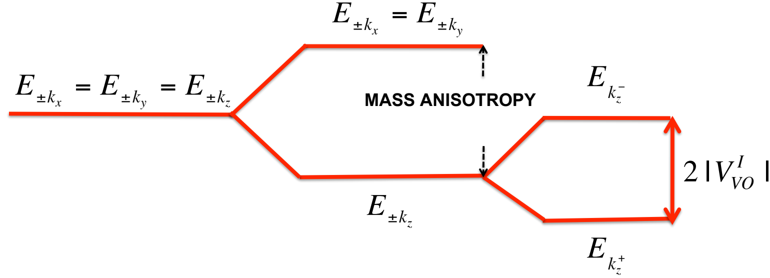

Figure 6.4: The energy states at the interface. At the interface the mass anisotropy breaks the valley degeneracy in a doublet $(z, -z)$ and a quadruplet $(x, -x, y, -y)$. The doublet degeneracy is lifted due to the valley orbit coupling ($V_{VO}^I = |V_{VO}^I|e^{i\theta}$) arising in a sharp (001) interface. k_z^+ and k_z^- denote the symmetric and anti-symmetric combination of the z valleys.

6.3.1 Valley Orbit Coupling at Interface V_{VO}^I

In a junction of a semiconductor with another material, such as an oxide or another semiconductor, the electron motion in the presence of an external potential can be treated in the effective mass approximation (EMA), in which the effective potential is taken to include the jump at the interface. The electric field normal to the semiconductor-oxide interface draws the electrons from the bulk of the semiconductor to the interface where they are prevented from entering the oxide by a large work function. Then, the interface determines the strength of the coupling between the two initially degenerate valleys $[(0, 0, \pm k_0)$, where $k_0 = 0.85\frac{2\pi}{a}]$, as well as the valley splitting, providing a unique ground state. The usual EMA calculations furnishes the energies and the wave functions in the inversion layer [1] (200) of the (001) surface.

Early theoretical studies on valley splitting $2|V_{VO}^I|$ in the framework of the EMA were performed more than 30 years ago by Sham and Nakayama (201), guided about the profound effects of the interface on the electron dynamics in the inversion layer, giving a valley splitting $2|V_{VO}^I|$ linear in the electric field, $\Delta E = 2|V_{VO}^I| = \lambda F$. The parameter λ is a characteristic length. More recent works (199, 202, 203) have proposed more complete models than the conventional EMA giving different values of λ. For example,

[1] When an electric field is applied normal to a semiconductor surface the energy bands are bent and, when this bending is sufficiently large, a roughly triangular potential well is formed at the surface in which carriers can be bound. This surface is then said to be *inverted*.

an enhancement in the λ parameter has been reported in (202) as a result of the inclusion of the effect of the indirect gap and the localization of carriers in the quantum dots. Another sophisticated EMA results focused in the relevance of the barrier height and the interface width, showing an intervalley coupling with a nonlinear behavior at low electric fields recovering a more familiar linear field dependence at higher fields (203). They also found that the valley-orbit coupling does not increase steadily with the barrier height, while it is always suppressed for a finite width interface profile.

Fig. 6.5 exhibits the response of the valley splitting $|V_{VO}^I|$ to a wide range of external electric fields. The solid straight line is a possible prediction from Sham and Nakayama (201) with $\lambda = 0.215\mathring{A}$. Data points give the calculated results from Saraiva et. al (203). The dashed vertical lines correspond to the experimental values of the breakdown field for SiGe and SiO_2. In Fig 6.5 there is also a results reference (dotted horizontal) of the unexpected result reported by Takashina et al. (204), who measured a giant splitting of 23 meV on a Si/SiO_2 interface in a SIMOX (separation by implantation of oxygen) structure, while the majority of experimental values have been reported in the 0.1 to 1 meV range (197, 205).

For a sharp interface, two main contributions to the valley splitting have been identified: the electron wave function at the interface and the wave function gradient for the evanescent wave in the barrier material. The results have shown that the external electric field (which increases the wave function at the interface), the appropriate barrier potential height and the proper choice of barrier material can help maximize the valley splitting (199). It has been seen, that the presence of miscuts [1] in quantum well interfaces suppresses the valley splitting, hence a flat interface as well as electronic confinement in nanostructures may enhance it (205). From Ref. (199), one can observe a general behavior of V_{VO}^I with the barrier height U_0 in Fig. 6.6 (solid line) for $F = 150$ kV/cm, where one sees that very low or very high barriers tend to suppress the valley coupling. Tuning U_0 involves changing the alloy composition or the material in the barrier. Also it can be observed that the interface width suppresses the intervalley coupling, as illustrated by the dashed lines in Fig. 6.6.

[1] Related to the step density in quantum wells

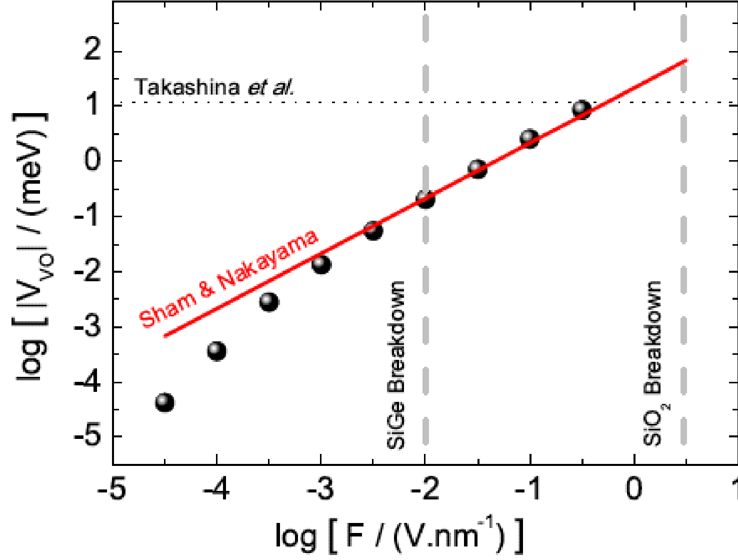

Figure 6.5: Data points give the calculated intervalley coupling as a function of applied electric field, both given in a log scale by Saraiva et al. Ref (203). The barrier height is set to $U_0 = 3$ eV. The dashed vertical lines correspond to the experimental values of the breakdown field for SiGe and SiO_2. The dotted horizontal line represents the measured valley coupling (or half the splitting) reported in Ref (204). The solid straight line is a possible prediction from the model by Sham and Nakayama. Courtesy from Saraiva et al. (2011) (203).

Additionally, research reports that the valley orbit coupling V_{VO}^I is a complex number, and hence $V_{VO}^I = |V_{VO}^I|e^{i\theta}$. One can observe this property in the results acquired from Ref (203). Here, the valley orbit coupling is shown as a function of the barrier height (See Fig. 6.7). Analyzing the graph and locating the barrier height $U_0 = 3eV$ which corresponds to an abrupt Si/SiO_2 interface, it is possible to check that the value of the valley orbit coupling corresponds to a complex quantity $V_{VO}^I = (-0.100 + i0.158)$, namely $\theta \sim \frac{\pi}{3}$. In this work, it will be shown how both the modulus and the phase of the V_{VO}^I affect the quantum behavior of donor electrons in Si near an interface. Our results have been obtained using the V_{VO}^I coupling calculated by Friesen et. al (202) and Sham and Nakayama (201).

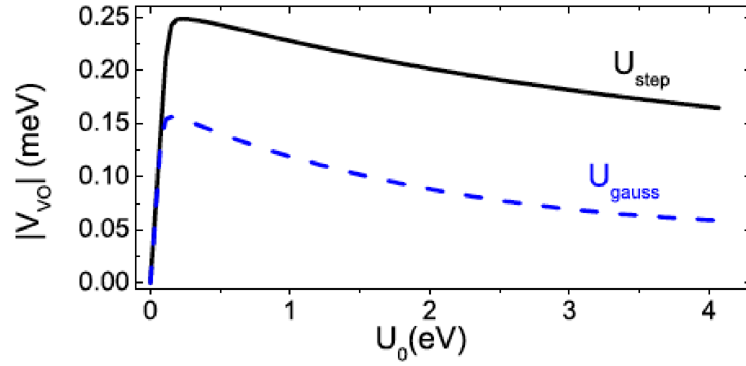

Figure 6.6: Variation in the absolute value of the valley-orbit coupling at the interface with barrier height for $F = 150$ kV/cm. The solid line corresponds to a step model potential at the interface, while the dashed line corresponds to a gaussian smooth profile with a width of one monolayer. Both present a maximum for $U_0 = 200$ meV. From Saraiva et al. (2009) (199).

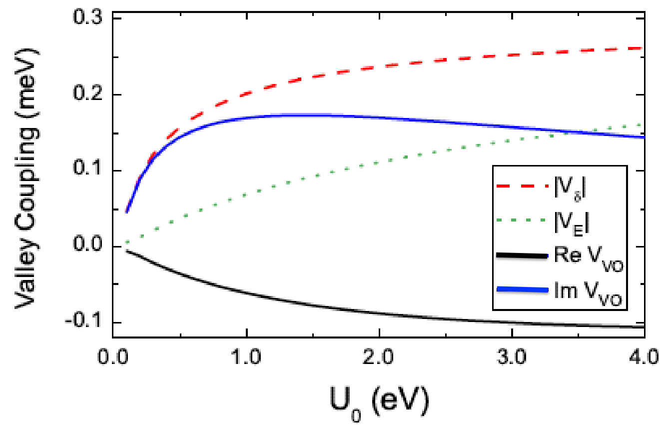

Figure 6.7: (Reproduced from Fig 2 on Ref.(203)) Intervalley coupling as a function of the conduction band offset U_0. All data correspond to an external field of 100 kV/cm. The delta function contribution $|V_\delta|$ which is related to the role of the electronic density at the interface, and the evanescent tail of the electronic envelope function into the barrier material contribution $|V_E|$, are depicted separately. The offset for Si/SiGe interfaces is $0.1 - 0.2$ eV and for Si/SiO_2 interfaces is 3 eV.

6.4 Valley Qubits Proposal

As it was explained before, one obstacle identified in Si Quantum Computing QC is the orbital multiplicity due to the valley degree of freedom, since the conduction band of bulk Si consists of six equivalent valleys. However, recently, a new QC platform in isotopically purified ^{28}Si quantum dots (QDs) has been presented in Ref (152) by D. Culcer et al. (2011). The scheme explores the closeness in energy of two polarized spin-triplet states with different valley compositions. The tunneling between valley eigenstates is induced through the top gate, which tunes the magnitude of the valley-orbit coupling in each of the two quantum dots (QD). The decoherence times are set by intervalley transitions, which occur on longer time scales than intravalley transitions, permitting long coherence times.

The task of this valley-based QC is to find two states with different valley compositions which can be rotated into each other by a tunable interaction. This proposal focused on a double quantum dot (DQD), which should have identical valley eigenstates as long as the interface is sharp along the growth direction and perpendicular to it, or if the interface roughness is correlated over distances much different than the size of the QD. The valley degree of freedom is expected to be resistant to charge noise, since different valley states with identical envelope functions are affected identically by low frequency charge noise, so that no dephasing occurs. This proposal is a new valley-based QC platform in Si QDs that offers electrical control of quantum information and can be achieved with currently available technology.

7

Model

In this work we consider the minimal unit for the kane''s computer proposal: a single electron bound to a substitutional P donor at $z = 0$ near a Si(001) / SiO_2 interface at $z = d$ has been considered. The system is under an applied uniform electric field perpendicular to the interface $\vec{F} = F\hat{z}$ pointing from the barrier to Si, thus pushing the electron away from the donor and towards the interface (see Fig. 7.1).

This study applies when d is larger than the Bohr radii of the electron bound to the donor. When no external fields are applied, the only attractive potential felt by the electron is the donor Coulomb potential and, at the low temperatures relevant here, the electron remains bound to the donor (See Fig 7.1(a)). Under an electric field F applied perpendicular to the interface, a triangular potential well is formed at the interface as shown in Fig 7.1(b). When F reaches a characteristic value F_c such that the bound state at the interface is degenerate in energy with the bound state at the donor, tunneling between the two wells (the attractive donor Coulomb potential, and the triangular well at the interface) is possible. In this way, we can reversibly manipulate the position of the electron between the donor and the interface by oscillating the electric field around F_c [namely, going back and forth from the situation in Fig 7.1(b) to the situation in Fig 7.1(c)]. Note that the electron, when at the interface, may still remain bound to the donor along the xy-plane, and hence, the electron may be confined in all three space directions upon certain conditions that will be described below. At the characteristic field F_c, the electron is in a hybridized donor-interface state (206).

The problem can be simplified assuming that the SiO_2 barrier is infinite. In effective "atomic" units for Si, $Ry^* = m_\perp e^4/2\hbar^2\epsilon_{\rm Si}^2 = 19.98$ meV and $a^* = \hbar^2\epsilon_{\rm Si}/m_\perp e^2 = 3.157$ nm, the Hamiltonian is written as (207, 208).

$$H = -\frac{\partial^2}{\partial x^2} - \frac{\partial^2}{\partial y^2} - \gamma\frac{\partial^2}{\partial z^2} - \frac{2}{r} + keFz + H_{vo} \tag{7.1}$$

with $\gamma = m_\perp/m_\parallel$ as the ratio between the transverse ($m_\perp = 0.191m$) and longitudinal ($m_\parallel = 0.916m$) effective masses, $\epsilon_{Si} = 11.4$, $k = 3.89\cdot 10^{-7}\epsilon_{Si}^3(m/m_\perp)$cm/kV, and the electric field F is given in kV/cm. In Eq.(7.1), the kinetic energy is $(-\frac{\partial^2}{\partial x^2} - \frac{\partial^2}{\partial y^2} - \gamma\frac{\partial^2}{\partial z^2})$, the next two terms are the attractive donor Coulomb potential and the electric-field linear potential, respectively. The last term describes the valley-orbit effects, namely the coupling between different valleys due to the singular nature of both the donor (D) and the interface (I) potentials, as described below.

The problem will be solved in the non-orthogonal basis formed by the states bound to the donor potential (D) and to the interface potential (I). We first discuss the donor and interface states separately.

7.1 Donor States

As previously discussed, the conduction band of Si has six degenerate minima (valleys) in the $\langle 100\rangle$ directions at a distance $k_0 = 2\pi\frac{0.85}{a_{Si}}$ from the Γ point, where $a_{Si} = 5.4$ Å is the lattice parameter of Si. In the simplest effective mass approximation, only the Bloch functions at the positions of the six conduction band minima are considered, and the ground state of the electron at the donor is written (209):

$$\Psi_D = \sum_{\mu=\pm x,\pm y,\pm z} C_D^\mu F_D^\mu(\mathbf{r})\phi_\mu(\mathbf{r})\,, \tag{7.2}$$

where $F_D^\mu(\mathbf{r}) = F_D^{-\mu}(\mathbf{r})$ are envelope functions and $\phi_\mu(\mathbf{r}) = u_\mu(\mathbf{r})e^{i\mathbf{k}_\mu\cdot\mathbf{r}}$ are the six Bloch eigenstates at the conduction band minima and μ is the valley index [1] (71). We

[1] In Eqs.(7.2) and (7.9) we do not include explicitly the pinning point for the plane-wave part of the Bloch functions at the donor and interface potentials. The general functions of the ground state of the electron at the donor and at the interface are defined by: $\Psi_D = \sum_\mu C_D^\mu F_D^\mu(\mathbf{r})\phi_\mu(r, r_D)$ and

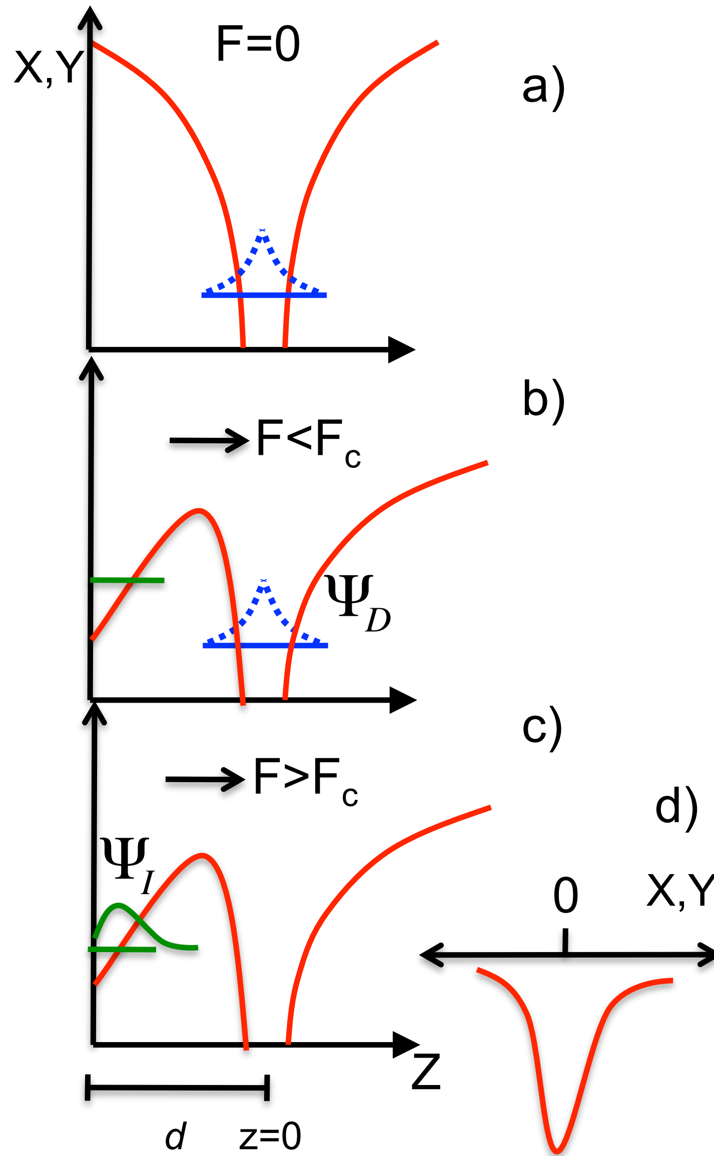

Figure 7.1: Manipulation of a single electron donor close to Si/SiO$_2$ interface. (a) If no electric field is applied the electron only feels the donor potential and is bound to it. (b) When an electric field F, perpendicular to the interface, is applied, a triangular shaped potential forms at the interface. For a certain value of F a bound state exists at the interface. (c) When $F > F_c$ the electron is at the interface (d) Donor potential at the interface along the xy-plane $V(x, y) = -\frac{2}{\sqrt{\rho^2+d^2}}$. This attractive potential causes the electron not to spread along the interface when it is ionized from the donor.

take the variational donor envelope functions $F_D^\nu(\mathbf{r})$, where $\nu = |\mu|$, centered at $r = 0$, following the form introduced in (209).

$$F_D^x = N_D^x \, e^{-\sqrt{\frac{y^2+z^2}{a^2}+\frac{x^2}{b^2}}} \,, \tag{7.3}$$

$$F_D^y = N_D^y \, e^{-\sqrt{\frac{x^2+z^2}{a^2}+\frac{y^2}{b^2}}} \,, \tag{7.4}$$

$$F_D^z = N_D^z \, e^{-\sqrt{\frac{x^2+y^2}{a^2}+\frac{z^2}{b^2}}} \,. \tag{7.5}$$

These are normalized hydrogenic 1s envelopes, distorted due to the Si conduction band effective mass anisotropy, and $\{N_D^\nu\}$ are normalization factors

$$N_D^\nu = \frac{1}{\sqrt{< F_D^\nu | F_D^\nu >}} \tag{7.6}$$

For $d \gg a, b$, the donor wave functions reduces to the bulk limit. Hence the normalization factors have the simple form $1/\sqrt{\pi a^2 b}$. This approximation is used here. The effective Bohr radii a and b are variational parameters chosen to minimize the ground state energy,

$$< \psi_D^\nu | H_D | \psi_D^\nu > \tag{7.7}$$

with

$$H_D = T - \frac{2}{r} \tag{7.8}$$

T is the kinetic energy term as defined in Eq. 7.1. The second term is the isolated impurity Coulomb donor potential. For the distances used here ($d \gtrsim 2a^* \approx 6$ nm), it is a good approximation to use the Kohn and Luttinger's bulk values for the Bohr radii a and b (209) ($d \to \infty$), namely, $a = 2.365$ nm and $b = 1.36$ nm (182).

7.2 Interface States

Following Eq. (7.2), we take the lowest states at the interface as

$$\Psi_I = \sum_{\mu=\pm x, \pm y, \pm z} C_I^\mu F_I^\mu(\mathbf{r}) \phi_\mu(\mathbf{r}) \,. \tag{7.9}$$

$\Psi_I = \sum_\mu C_I^\mu F_I^\mu(\mathbf{r}) \phi_\mu(r, r_I)$, in which r_D and r_I represent a pinning site for the Bloch waves in the superposition state and could be calculated variationally. Here we assume r_D would be the position at the donor $r_D = 0$ for an isolated impurity (209). In the same way, for isolated interface, we assume r_I is exactly at the interface. The pinning points could be incorporated as a phase in V_{vo}^I. A full variational calculation including the pinning points would cause oscillations on the gap at anticrossing as a function of d.

The envelope functions $F_I^\nu(\mathbf{r})$, with $\nu = |\mu|$, are taken in the variational form (182)

$$F_I^x = N_I^x(z+d)^2 e^{-\alpha_{xy}(z+d)/2} e^{-(\beta_1^2 x^2 + \beta_2^2 y^2)/2}\,, \tag{7.10}$$

$$F_I^y = N_I^y(z+d)^2 e^{-\alpha_{xy}(z+d)/2} e^{-(\beta_2^2 x^2 + \beta_1^2 y^2)/2}\,, \tag{7.11}$$

$$F_I^z = N_I^z(z+d)^2 e^{-\alpha_z(z+d)/2} e^{-\beta^2\rho^2/2}\,, \tag{7.12}$$

$\{N_I^\nu\}$ are normalization factors, calculated by

$$N_I^\nu = \frac{1}{\sqrt{< F_I^\nu | F_I^\nu >}} \tag{7.13}$$

The normalization constants are calculated to be:

$$|N_I^x| = |N_I^y| = \frac{\alpha^{5/2}}{\sqrt{4!}}\sqrt{\frac{\beta_1\beta_2}{\pi}}\quad , \tag{7.14}$$

$$|N_I^z| = \frac{\alpha^{5/2}}{\sqrt{4!}}\frac{\beta}{\sqrt{\pi}}\quad . \tag{7.15}$$

Here, the penetration into the barrier is considered to be negligibly small as we are considering the SiO_2 barrier to be infinite. $\rho^2 = x^2 + y^2$, and α, α_{xy}, β, β_1 and β_2 are variational parameters from minimizing Eq. 7.16:

$$< \psi_I^\nu | H_I | \psi_I^\nu > \tag{7.16}$$

with

$$H_I = T - \frac{2}{\sqrt{\rho^2 + d^2}} + keFz \tag{7.17}$$

The first term is the kinetic energy term as defined in Eq. 7.1. The second term is the impurity potential at the interface, while the last term is the electric field linear potential. The variational parameters can be calculated analytically:

$$\alpha = \sqrt[3]{30Fk\gamma} \tag{7.18}$$

$$\alpha_{xy} = \sqrt[3]{30Fk} \tag{7.19}$$

$$\beta = \frac{1}{d^{\frac{3}{4}}} \tag{7.20}$$

$$\beta_1 = \frac{1}{d^{\frac{3}{4}}\gamma^{\frac{1}{4}}} \tag{7.21}$$

$$\beta_2 = \frac{1}{d^{\frac{3}{4}}} \tag{7.22}$$

The α and α_{xy} variational parameters of the envelope functions at the interface are related to the width of the wave functions along the z-direction, and depend on the value of the applied electric field; β, β_1 and β_2 correspond to the confinement in the xy plane, which is controlled by the attractive potential of the donor. Hence the β, β_1 and β_2 parameters depend on the distance d (182). Fig. 7.2 shows the plots of $1/\alpha$ and $1/\alpha_{xy}$ variational parameters as a function of F, and $1/\beta$, $1/\beta_1$ and $1/\beta_2$ as a function of d. The reversible manipulation of the electrons, from donor to interface and viceversa, requires that the electron is confined in the xy plane when at the interface. Therefore, $1/\beta$, $1/\beta_1$ and $1/\beta_2$ give an estimation of the minimum distance required between donors in a Si quantum computer. From this distance we get a maximum planar density $\sim 10^{10}\text{cm}^{-2}$ (182, 208) in order to avoid the formation of a two-dimensional electron gas (208) at the interface.

7.3 Full-Multivalley Hamiltonian

We solve for the lowest states of the full potential (donor, electric field and interface) by obtaining the spectrum of H in the combined basis of the lowest D and I envelopes as determined variationally, each multiplied by the respective Bloch functions. This defines the Hilbert space for our model calculation. Hence, the Hamiltonian is represented by a 12×12 matrix, written formally as four 6×6 blocks

$$H = \begin{bmatrix} H_{DD} & H_{ID} \\ H_{DI} & H_{II} \end{bmatrix}. \tag{7.23}$$

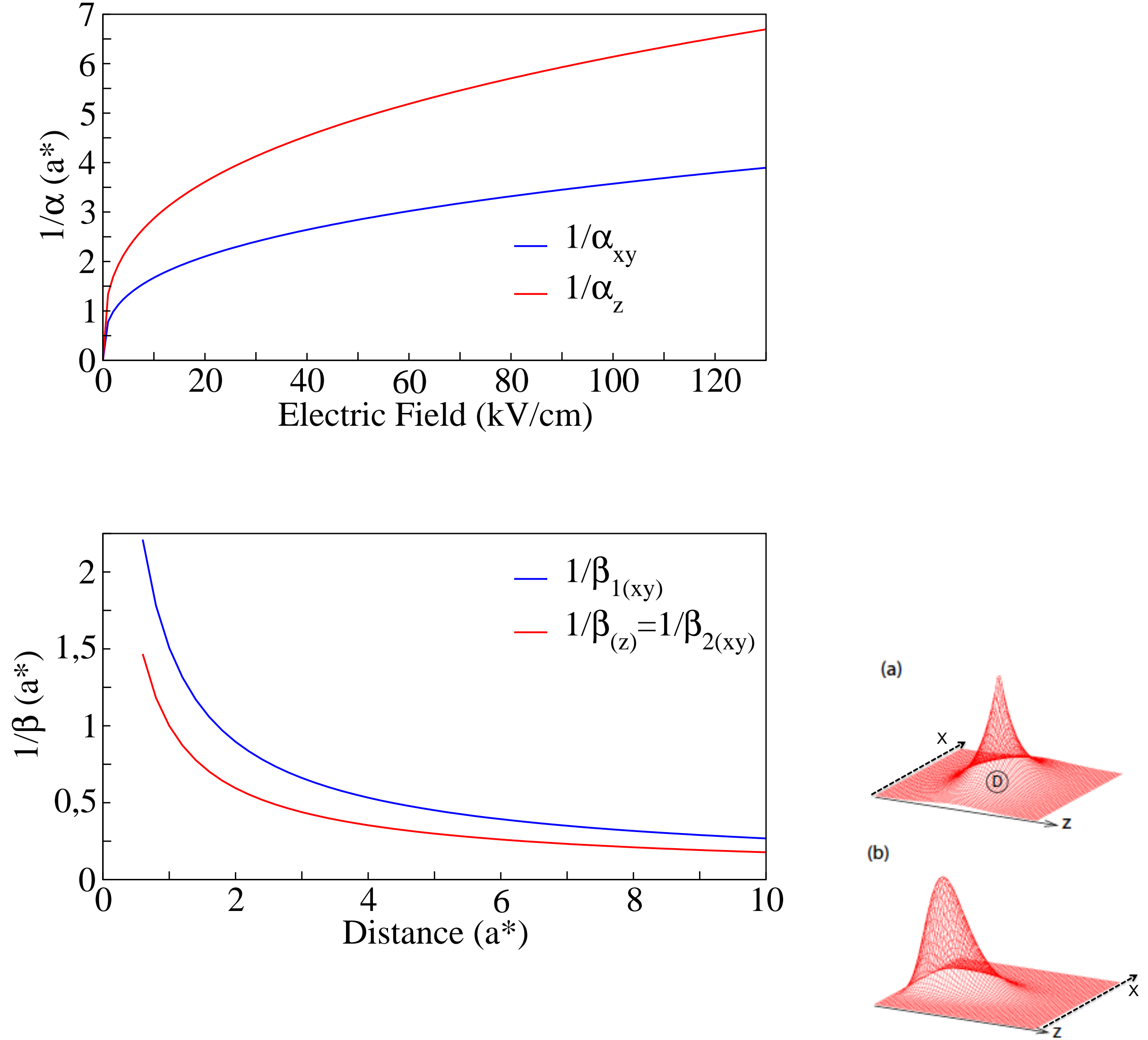

Figure 7.2: (Main panel) Typical confinement lengths of the interface states in the z direction $1/\alpha_z$ and $1/\alpha_{xy}$. Likewise, the xy plane confinement lenghts described by $(1/\beta)$ in the z valleys, $(1/\beta_1)$ and $(1/\beta_2)$ in the x and y valleys. (a) Typical plots of the shapes of the envelope functions at the donor given by F_D^z in Eq (7.5) and at the interface (b) given by F_I^z in Eq(7.12).

The equation giving the spectrum takes into account the non-orthogonality of our basis, *i.e.*, we solve for $H\Psi_i = E_i S \Psi_i$, where S is the 12×12 overlap matrix so that $S_{DD}^{\mu,\nu} = S_{II}^{\mu,\nu} = \delta_{\mu\nu}$ and $S_{DI}^{\mu,\nu} = S_{ID}^{\mu,\nu} = \delta_{\mu\nu} \left\langle F_D^{\mu} \mid F_I^{\mu} \right\rangle$. Here, $\left\langle F_D^{\mu} \mid F_I^{\mu} \right\rangle$ is the overlap between the interface and the donor envelope functions, an exponentially decreasing function of d. S is calculated numerically, its matrix form is:

$$S = \begin{bmatrix} S_{DD} & S_{ID} \\ S_{DI} & S_{II} \end{bmatrix} \quad , \tag{7.24}$$

$$[S_{DD}] = [S_{II}] = \begin{pmatrix} 1 & 0 & 0 & 0 & 0 & 0 \\ 0 & 1 & 0 & 0 & 0 & 0 \\ 0 & 0 & 1 & 0 & 0 & 0 \\ 0 & 0 & 0 & 1 & 0 & 0 \\ 0 & 0 & 0 & 0 & 1 & 0 \\ 0 & 0 & 0 & 0 & 0 & 1 \end{pmatrix} \quad , \tag{7.25}$$

$$[S_{DI}] = \begin{pmatrix} \langle F_D^x | F_I^x \rangle & 0 & 0 & 0 & 0 & 0 \\ 0 & \langle F_D^{-x} | F_I^{-x} \rangle & 0 & 0 & 0 & 0 \\ 0 & 0 & \langle F_D^y | F_I^y \rangle & 0 & 0 & 0 \\ 0 & 0 & 0 & \langle F_D^{-y} | F_I^{-y} \rangle & 0 & 0 \\ 0 & 0 & 0 & 0 & \langle F_D^z | F_I^z \rangle & 0 \\ 0 & 0 & 0 & 0 & 0 & \langle F_D^{-z} | F_I^{-z} \rangle \end{pmatrix} \tag{7.26}$$

and

$$[S_{DI}] = [S_{ID}]$$

As already explained in Section 6.2, the six-fold degeneracy of the ground state is lifted at a substitutional impurity because the translational symmetry of the host crystal is broken, leading to intervalley scattering effects known as the valley-orbit interaction (192, 193). This effect can be accounted for phenomenologically, introducing a coupling between valleys in perpendicular directions (e.g. x, z) $-\Delta_c$ and in parallel directions (e.g. $z, -z$) $-\Delta_c(1 + \delta_c)$ (194). This splits the unperturbed six-fold-degenerate donor electron ground state into a singlet (A_1 symmetry), a triplet (T_2 symmetry) and a doublet (E symmetry), as depicted in Fig 6.2. For P in Si, the relative splittings between the different symmetry levels are reproduced taking $\Delta_c = 2.16$ meV and $\delta = -0.3$ (194).

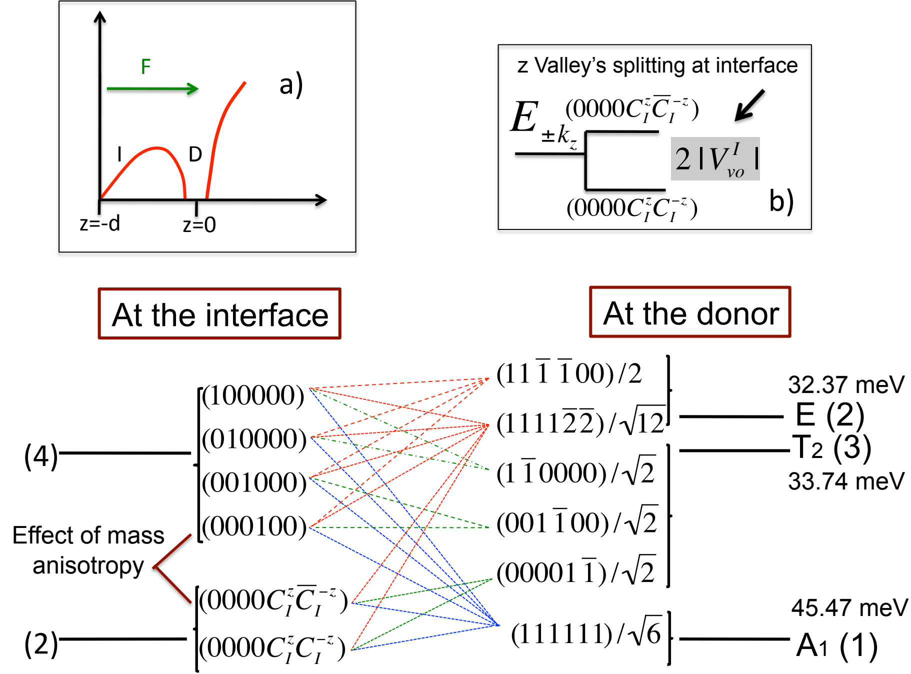

Figure 7.3: (a) Double well potential in the z-direction formed by the Coulombic donor potential plus the triangular interface/electric field potential. d is the distance between the donor and interface. (Main panel) Symmetry of levels at the donor and at the interface. Every level is described by six coefficients corresponding to the six valleys of Si conduction band: $(x, -x, y, -y, z, -z)$. This defines the valley composition of each state. At the interface, the mass anisotropy breaks the valleys degeneracy in a doublet $(z, -z)$ and a quadruplet $(x, -x, y, -y)$. The doublet degeneracy is lifted due to the valley orbit coupling ($V^I_{\rm vo} = -|V^I_{\rm vo}|e^{i\theta}$) arising in a sharp (001) interface (199, 201, 203) as shown in (b). C^z_I and C^{-z}_I are defined in Eq. (7.9), and $\bar{C}^{-z}_I = -C^{-z}_I$. At an isolated donor, the valley orbit coupling leaves a non-degenerate ground state with A_1 symmetry, well separated (splitting ~ 12 meV) from the other five levels (190, 209, 210) The binding energies are experimental values for bulk P donors (190).

Likewise, in Chapter 6, section 6.3 the lifting of degeneracy at (001) interface has been described (197, 211). Thus at the interface due to the mass anisotropy, the z and $-z$ perpendicular valleys are lower in energy than the ones parallel to the interface. The two lowest energy states are combinations of the z and $-z$ valleys, whose double degeneracy is lifted due to the valley-orbit coupling V_{vo}^{I} which is proportional to the electric field and dependent on the barrier height and abruptness. This parameter has been described in Section 6.3.1. We will show results for two different values of λ estimated in the literature: (i) The large value $\lambda = 1.36$ Å , has been estimated by M. Friesen et al. in Ref (202). (ii) The smaller value $\lambda = 0.215$Å was estimated by Sham and Nakayama in Ref (201). In both cases we discuss the qualitative changes that occur in the spectrum. H_{vo} in Eq. (7.1) takes into account all these valley-orbit interactions, both at the donor (D) and at the interface (I). Its form (in a basis set defined next) is described as

$$[H_{\text{vo}}]_{DD} = \begin{pmatrix} 0 & \Delta_{\parallel} & \Delta_{\perp} & \Delta_{\perp} & \Delta_{\perp} & \Delta_{\perp} \\ \Delta_{\parallel} & 0 & \Delta_{\perp} & \Delta_{\perp} & \Delta_{\perp} & \Delta_{\perp} \\ \Delta_{\perp} & \Delta_{\perp} & 0 & \Delta_{\parallel} & \Delta_{\perp} & \Delta_{\perp} \\ \Delta_{\perp} & \Delta_{\perp} & \Delta_{\parallel} & 0 & \Delta_{\perp} & \Delta_{\perp} \\ \Delta_{\perp} & \Delta_{\perp} & \Delta_{\perp} & \Delta_{\perp} & 0 & \Delta_{\parallel} \\ \Delta_{\perp} & \Delta_{\perp} & \Delta_{\perp} & \Delta_{\perp} & \Delta_{\parallel} & 0 \end{pmatrix} \tag{7.27}$$

$$[H_{\text{vo}}]_{II} = \begin{pmatrix} 0 & 0 & 0 & 0 & 0 & 0 \\ 0 & 0 & 0 & 0 & 0 & 0 \\ 0 & 0 & 0 & 0 & 0 & 0 \\ 0 & 0 & 0 & 0 & 0 & -|V_{\text{vo}}^{I}|e^{i\theta} \\ 0 & 0 & 0 & 0 & -|V_{\text{vo}}^{I}|e^{-i\theta} & 0 \end{pmatrix} \tag{7.28}$$

and

$$[H_{\text{vo}}]_{ID} = [H_{\text{vo}}]_{DI} = 0 \quad . \tag{7.29}$$

States with different Bloch indices $\mu \neq \nu$ are not coupled unless there is a non-zero contribution from H_{vo} (see Eq .7.28).

A general state in the double well system is written as:

$$\Psi = \sum_{\mu=\pm x,\pm y,\pm z} \sum_{L=I,D} C_L^{\mu} F_L^{\mu}(\mathbf{r}) \phi_{\mu}(\mathbf{r}) \, . \tag{7.30}$$

The complex coefficients $\{C_L^\mu\}$ give the contributions to the state Ψ of each valley μ at the interface or donor ($L = I, D$). Also, they define the symmetry of the state, and are referred to here as "valley coefficients". The normalization condition reads

$$\sum_{\mu,\nu,L,L'} C_L^{\mu *} S_{\mu,\nu} C_{L'}^{\nu} = \sum_L |C_L^\mu|^2 + \text{cross terms} = 1, \tag{7.31}$$

where the cross terms are zero for $L = L'$ and/or for $\mu \neq \nu$. For $d = 4a^*$ the cross terms due to the finite overlap between donor and interface envelopes are less than 5% in the electric field range of interest. The overlap S_{ID} is negligible for $d = 5a^*$ and larger.

In Fig. 7.3, we show the valley coefficients of the states at an isolated donor (just the $\{C_D^\mu\}$ are given since $C_I^\mu = 0$ for all μ) and at an interface under a perpendicular electric field (just the $\{C_I^\mu\}$ are given since $C_D^\mu = 0$ for all μ). The valley coefficients are perturbed when the impurity is located at a distance d from the interface, and hybrid states may be formed (206, 208) where both D and I coefficients contribute. The lines in Fig. 7.3 indicate schematically symmetry-allowed paths connecting the initial (for low F) donor and final (for strong enough F) interface levels.

8

Results

8.1 Full Spectrum of Eigenvalues of the 6-Valley Model

Previous theoretical and experimental studies (173, 206, 208) identified and analyzed a characteristic field F_{ch} at which the electron ground state crosses over from being bound mainly around the donor (D-like) into being bound mostly near the interface (I-like). These results are reproduced with the 6-valley model studied in this work (see Fig. 8.1). Here, we explore the valley degrees of freedom, mainly close to the characteristic field, and analyze how the applied field changes the valley composition of the main electronic states involved in the donor-interface shuttling.

The electric-field dependence of the complete spectrum of the Hamiltonian in Eq. (7.23), for $d = 4a^*$, $d = 5a^*$ and $d = 8a^*$, is shown in Fig. 8.1. The results in the left column correspond to a relatively large value of the valley orbit coupling at the interface $|V_{\text{vo}}^I| = \lambda F$ with prefactor $\lambda = 1.36$Å (202), while the right column shows the results for $\lambda = 0.215$Å (201). The overall level structure here is similar to the one presented in Ref. (212), which corresponds to a Stark shifted spectrum of P donors in bulk Si (namely, no barrier is present). In Ref. (212) the spectrum has been obtained using the effective mass approach and the envelope functions are expressed as a combination of atomic-like orbitals.

In this work, at small fields (for instance, $F < 32$ kV/cm for $d = 4a^*$), the six lowest eigenstates are donor bound. The degeneracies of the T_2 triplet and the E doublet are lifted (with a very small splitting) due to the perturbation by the interface. At large fields ($F \gtrsim 70$ kV/cm for $d = 4a^*$), the six lowest eigenstates are interface-bound states. The two lowest eigenstates, which are combinations of the z and $-z$ valleys, are split by $2|V_{VO}^I|$, that is a small quantity in the scale of the plot. Different eigenvalues cross or anti-cross over each other as F changes. The general level scheme is qualitatively similar for different values of the distance as illustrated in Fig. 8.1 for d=$4a^*$, $5a^*$, and $8a^*$. Nevertheless, the distance between donor and interface affects both the size of the gap at the anticrossings and the value of the characteristic field required to

ionize the donor.

At low temperature, only the three lowest eigenvalues are required to describe the shuttling of the electron from donor to interface. The gap at the lowest anticrossing is inversely related to the tunneling time involved in the shuttling between donor and interface, which increases exponentially with distance. On the other hand, the characteristic field decreases with d as $1/d$ (208).

8.2 Evolution of Valley Composition of the Three Lowest States

Current experiments are performed at temperatures of the order of 0.1K, hence we are interested in the lowest energy states. Moreover those are the relevant ones for quantum computing. In the following, we will analyze the evolution of the valley populations and symmetry of the three lowest eigenstates, which, via mutual energies crossing over, "become" or contribute to the ground state for some range of field values. Because of time-reversal symmetry, valleys μ and $-\mu$ are equally populated, so the population of each direction $\nu = x,\ y,\ z$ is defined by

$$P_\nu = \sum_{\mu=\pm\nu} \sum_{L=I,D} |C_L^\mu|^2 \tag{8.1}$$

Due to the cylindrical symmetry of the system, P_z is in general different from P_x and P_y, while the two latter are equivalent. Therefore, the results are presented in terms of P_z and

$$P_{xy} = (P_x + P_y)/2 = \frac{1}{2} \sum_{\mu=\pm x,\pm y} \sum_{L=I,D} |C_L^\mu|^2. \tag{8.2}$$

This definition does not take the cross terms from Eq. (7.31) into account, so normalization gives $2P_{xy} + P_z \approx 1$, allowing P_z and P_{xy} to be directly compared to each other, giving the relative weight of the z and the average x and y populations.

We turn now to analyze the valley quantum number as a function of electric field in the range where the hybridization between donor and interface states takes place. We wish to get a clear description of the changes in symmetry and valley composition of the states involved in the donor-interface electron shuttling problem.

8.2.1 Real V_{VO}^I

In Fig. 8.2 we start analyzing straightforward cases of the evolution of the valleys population as a function of F for the three lowest states, using a real value of the valley orbit coupling at interface and $d = 4a^*$ ($\sim$ 12nm donor-interface distance). Since $V_{\rm vo}^I = -|V_{\rm vo}^I|e^{i\theta}$, V_{VO}^I is negative for $\theta = 0$ and positive for $\theta = \pi$. The spectrum in the area close to the lowest energy

$d = 4a^*$ $\lambda = 1.36\text{Å}$ $\lambda = 0.215\text{Å}$

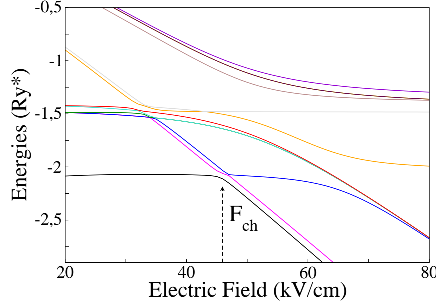

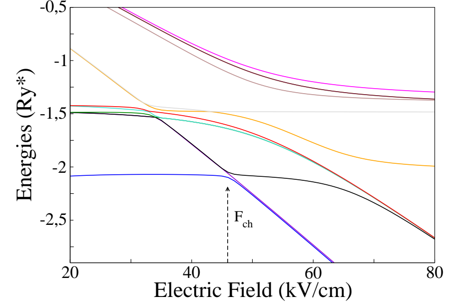

$d = 5a^*$

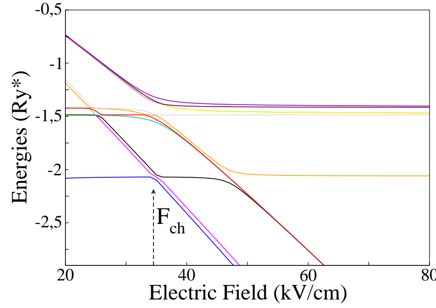

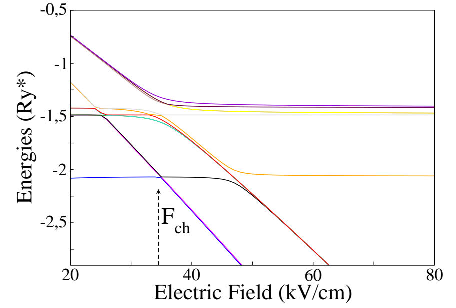

$d = 8a^*$

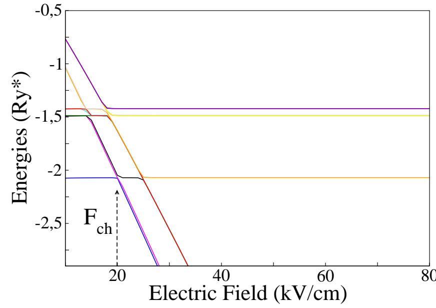

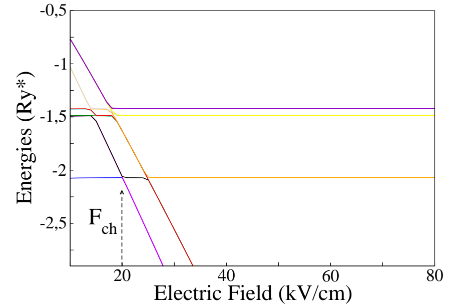

Figure 8.1: Full spectrum of eigenvalues for $d = 4a^*$, $d = 5a^*$ and $d = 8a^*$, in a wide range of electric fields. For small values of the electric field, the first six eigenvalues correspond to the donor states and the highest six to interface states. The valley orbit coupling between z and $-z$ valleys at the interface V^I_{VO} considered here is real, negative, and a function of F and defined as $V^I_{\text{vo}} = -|V^I_{\text{vo}}|e^{i\theta}$ with $|V^I_{\text{vo}}| = \lambda F$, $\theta = 0$. In the left column $\lambda = 1.36$ Å (202), whereas in the right column $\lambda = 0.215$Å (201). Note that an increasing d implies a decreasing F_{ch} and a smaller gap at anticrossing (equivalent to a larger donor-interface shuttling time).

V_{VO}^I **real and positive** $(\theta = \pi)$

V_{VO}^I **real and negative** $(\theta = 0)$

$\lambda = 1.36\text{Å}$

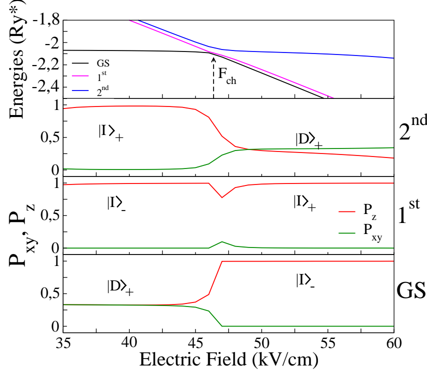

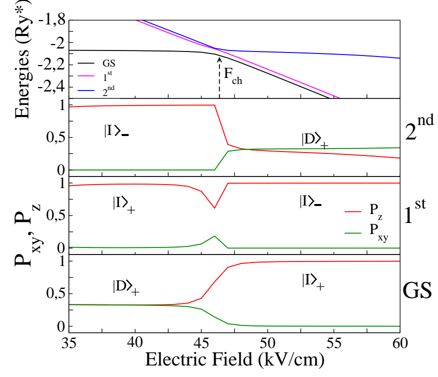

$\lambda = 0.215\text{Å}$

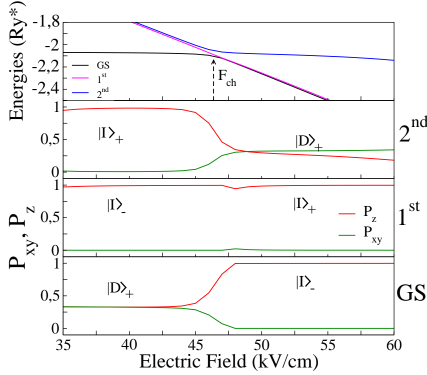

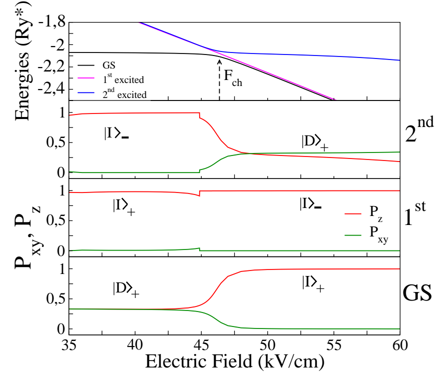

Figure 8.2: Evolution of the valley composition, for $d = 4a^*$. The three lowest eigenvalues in a wide range of electric fields around the F_{ch}. Here, the results have been acquired with different magnitudes and signs for the real valley orbit coupling. The left column correspond to real and positive V_{VO}^I, whereas the right column to a real and negative V_{VO}^I. Each case shows in the first frame the three eigenvalues involved in the lowest energy anticrossing; the other three panels show the valley composition in the second excited state, the first excited state, and the ground state GS, respectively. The red curves correspond to the weight of the $\pm z$ valleys or longitudinal weight (at donor and interface), and the green curves are the weight of the $\pm x$ and $\pm y$ valleys or transversal weight (at donor and interface). The states are labeled by their location, donor **(D)** or interface **(I)**, and by their symmetry, symmetric (+) or antisymmetric (-).

anticrossing is shown in Fig. 8.2 for $\theta = 0$ **(right panels)** and $\theta = \pi$ **(left panels)**. Four cases are presented corresponding to different magnitudes and signs of the valley orbit coupling at the interface. The lower frames give the corresponding valley populations. Below F_{ch} the ground state (GS) is a symmetric combination of the six valleys, thus $P_{xy} = P_z$. Since negligible contributions come from the C_I^μ coefficients, this configuration is called $|D\rangle_+$. Above F_{ch}, the ground state tends asymptotically to a symmetric $|I\rangle_+$ **(right panels)** or anti-symmetric combination $|I\rangle_-$ **(left panels)** of the z and $-z$ valleys at the interface, therefore the population $P_{xy} \to 0$. The first excited state changes from predominantly $|I\rangle_+$ and tends to $|I\rangle_-$ **(right panels)** or from $|I\rangle_-$ to $|I\rangle_+$ **(left panels)**. The second excited state changes from predominantly $|I\rangle_-$ **(right panels)** or $|I\rangle_+$ **(left panels)** well below F_{ch} and tends to $|D\rangle_+$ well above F_{ch}, up to ~ 60 kV/cm, in all cases presented.

In addition, Fig. 8.2 shows the effect of the valley orbit coupling magnitude. The upper panels show the results for a large value of the $\lambda = 1.36$Å, while the lower panels show the results for a smaller value $\lambda = 0.215$Å. It will be shown below, in more detailed results, that the splitting between the z valleys interface states, defined by $2|V_{\text{vo}}^I|$, takes a key role in the nature of the anti-crossing between the three lowest states.

Fig. 8.2 also provides evidence of small discontinuities in the valley populations of the first and second excited states. We will now zoom in the region around F_{ch} to look into the details.

8.2.2 Area around F_{ch}

If we zoom in the region around F_{ch}, we can see that the apparent anticrossing at F_{ch} consists in fact of a series of a crossing F_{c} and an anticrossing F_{a}. The discontinuities in the valley populations happen at the crossing. This is shown in Fig. 8.3 for two different values of d ($d = 4a^*$ in the left panels and $d = 8a^*$ in the right panels) and for a real and negative value of V_{vo}^I corresponding to $\lambda = 0.215$ Å. For a negative real V_{vo}^I the interface eigenstates involving z and $-z$ valleys are $|I+\rangle$ and $|I-\rangle$ with energies $E_I - |V_{\text{vo}}^I|$ and $E_I + |V_{\text{vo}}^I|$, respectively. As explained below, whether we have a crossing or an anticrossing depends on the symmetry of the wave-functions involved.

Two main differences are apparent between $d = 4a^*$ and $d = 8a^*$: (i) the order of the anticrossing (F_a) and the crossing (F_c) fields is switched; and (ii) for $d = 8a^*$ the transition is much sharper and the valley populations are either pure-donor or pure-interface states in the whole fields range, with negligible mixing regions. In contrast, for $d = 4a^*$ the larger hybridization leads to a smooth transition between the donor and interface states, consistent with previous works (206, 208). In Fig. 8.3 it can also be seen in the region around F_{ch} that the 1st excited state is donor-like for $8a^*$, while it is an interface donor hybrid for $d = 4a^*$ due to the larger donor-interface overlap.

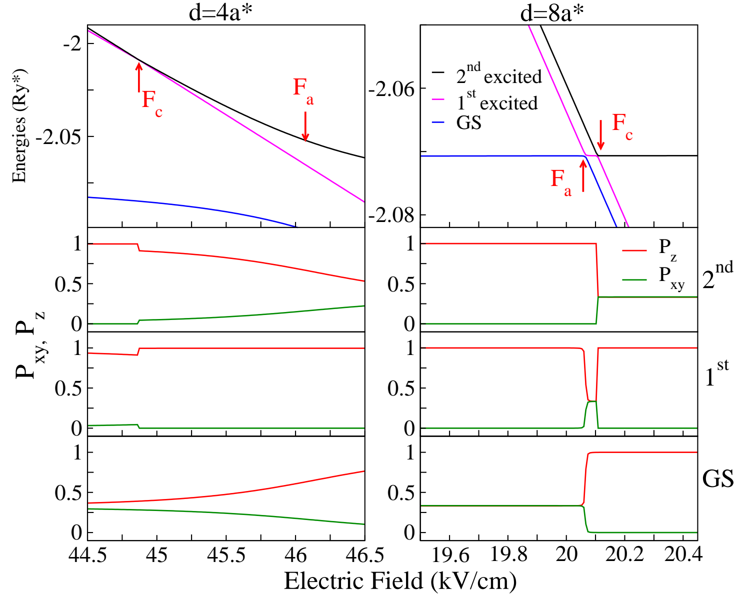

Figure 8.3: Zoom on the characteristic field area for two different values of d: $d = 4a^*$ (left) and $d = 8a^*$ (right), for a real and negative value of V_{vo}^I with $\lambda = 0.215$Å. At the characteristic field a crossing and an anticrossing take place with a relative order dependent on d. Top: eigenvalues showing both the crossing F_c and anticrossing F_a points. The three bottom rows show the valley composition of the second excited state, first excited state, and ground state, respectively.

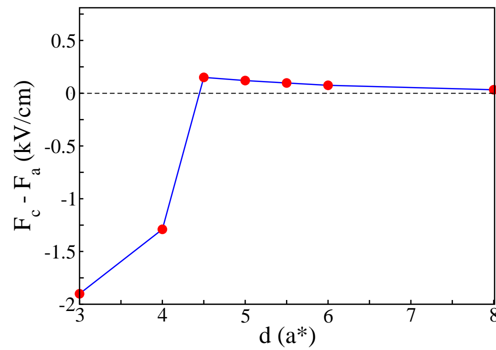

Figure 8.4: Plot of the difference $F_c - F_a$ (crossing minus anticrossing points) versus d (distance from donor to interface) for a real and negative value of V_{vo}^I with $\lambda = 0.215$Å. There is a change of sign of this difference at $4a^* < d_0 < 4.5a^*$.

In the case plotted in Fig. 8.3, the relative position of F_c and F_a is a function of d, as shown in Fig. 8.4: F_c is larger (smaller) than F_a for $d > d_0$ ($d < d_0$) with $4a^* \lesssim d_0 \lesssim 4.5a^*$. The two crossover fields get closer as d increases above d_0. The symmetry and the valley compositions of the crossing and anticrossing states depend on the relative position of F_c and F_a. A comparison is summarized schematically in table 8.1. The crossing states are always the 1st and 2st excited states, which do not couple because one of the eigenvectors is symmetric while the other is anti-symmetric. The anticrossing happens between $|D\rangle_+$, the symmetric combination at the donor (A_1 symmetry) and the symmetric combination $|I\rangle_+$ of the z and $-z$ valleys at the interface.

If the sign of the valley orbit coupling is positive ($\theta = \pi$), the relative position of F_c and F_a is exchanged. This position not only depends on the sign of V^I_{VO}, it is also affected by its magnitude. When a large value of V^I_{VO} ($\lambda = 1.36$Å) is imposed, $F_c - F_a$ is always negative (positive) with $\theta = 0$ ($\theta = \pi$) for all values of d. The different scenarios as a function of d and λ can be understood using the sketches in Fig. 8.5. For instance for $d = 4a^*$ with $\theta = 0$, due to the fact that the value of valley orbit splitting between the interface states is slightly larger than the gap at anti-crossing, the symmetric combination at the donor (A_1 symmetry) and the symmetric combination $|I\rangle_+$ of z and $-z$ valleys at the interface, feel each other (namely, they anticross) before the symmetric combination $|I\rangle_+$ and antisymmetric combination $|I\rangle_-$ of z and $-z$ valleys at the interface cross. Such behavior still remains for larger values of d, then $F_c - F_a$ continues to be negative as has been illustrated in Fig. 8.5 (a) and (e). On the contrary, when the sign of valley orbit coupling is positive (namely, $\theta = \pi$), the symmetric combination at the donor (A_1 symmetry) and the antisymmetric combination $|I\rangle_-$ of z and $-z$ valleys at the interface feel each other (cross) before the antisymmetric combination $|I\rangle_-$ and symmetric combination anticross. Therefore, $F_c - F_a$ is positive for all values of d, as further illustrated in Fig. 8.5 (c) and (f). As a basis for comparison, the case explained before with small value of λ is presented in Fig. 8.5 (b) for negative and Fig. 8.5 (d) for positive V^I_{VO}.

The results presented so far have been obtained considering the extreme cases of real negative and real positive values for valley orbit coupling at interface V^I_{VO}. From these results we can infer that the valley compositions of the states involved in the lowest energy anticrossing depend on both the modulus and phase of V^I_{VO} as well and on the distance between donor and interface.

8.2.3 Complex V^I_{VO}

Now we explore the effect of a more realistic general phase on the valley-orbit coupling at the interface. For a complex V^I_{VO}, the two lowest eigenstates at the interface are complex combinations of the $+z$ and $-z$ valleys with a relative phase θ. This form of the interface eigenstates

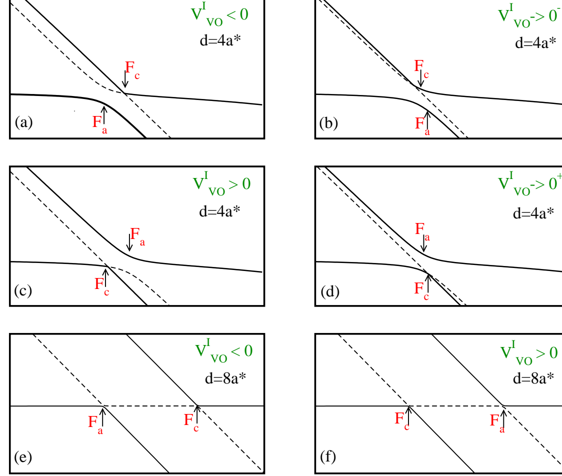

Figure 8.5: Sketch for different scenarios as a function of d and λ. Real V^I_{VO}.

.

affects the valley composition and the details in the $F_{\rm ch}$ area.

Fig. 8.6 shows the complete spectrum of the Hamiltonian in Eq. (7.23), for $d = 4a^*$, using a complex $V^I_{\rm vo}$, with $\theta = \pi/3$ and prefactor $\lambda = 1.36$Å (the largest value presented here). As a whole the level structure in Fig. 8.6 is similar to the one presented in Fig. 8.1, where $V^I_{\rm vo}$ is real with $\theta = 0$ or $\theta = \pi$. The difference between both cases is essentially on the nature of the anticrossing given by the symmetries of the z lowest states at interface. Here, there are two anticrossings at F_{ch}.

In Fig. 8.7 the evolution of valley composition of the three lowest eigenstates is presented for a reduced range of fields around the characteristic field for $d = 4a^*$ ($F_{\rm ch} \sim 46$ kV/cm), $d = 5a^*$ ($F_{\rm ch} \sim 35$ kV/cm) and $d = 8a^*$ ($F_{\rm ch} \sim 20.2$ kV/cm). The upper panels show the results for a complex $V^I_{\rm vo}$ with phase $\theta = \pi/3$ (similar to the one estimated for an abrupt Si/SiO$_2$ interface (199)) . The lower panels reproduce the results for a real and positive $V^I_{\rm vo}$. The magnitude is determined by $\lambda = 1.36$ Å. In all cases **(upper frames)** the spectrum of energies is showed. The three rows of frames below give the corresponding valley populations for the 2$^{\rm nd}$ excited, 1$^{\rm st}$ excited, and ground (GS) states, respectively. From Fig. 8.7 one can clearly observe that the anti-crossing at $F_{\rm ch}$ in fact involves two anti-crossings. Therefore, the crossing that appears for the particular case of a real $V^I_{\rm vo}$ is just a limiting case in which the interface eigenstates do not involve complex phases.

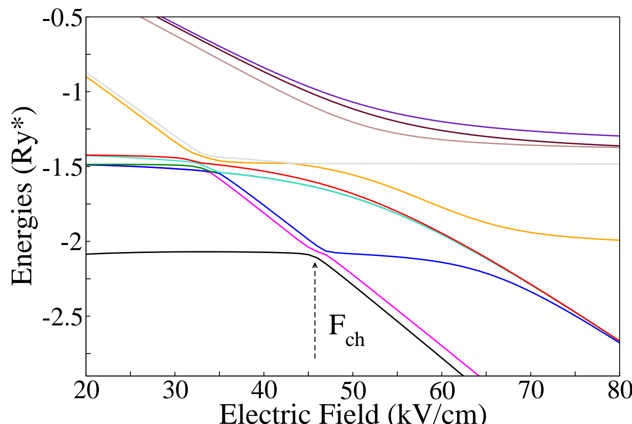

Figure 8.6: Full spectrum of eigenvalues for $d = 4a^*$ in a wide range of electric fields with a complex $V^I_{\rm vo}$. For small values of the electric field, the lowest six eigenvalues correspond to the donor states and the highest six to interface states. We use here $V^I_{\rm vo} = -|V^I_{\rm vo}|e^{i\pi/3}$ with $|V^I_{\rm vo}| = \lambda F$ and $\lambda = 1.36$ Å .

The valley contribution displayed in Fig. 8.7 **(upper panels)** was broadly maintained with respect to the straightforward cases ($\theta = \pi$ and $\theta = 0$) **(lower panels)** . Well below $F_{\rm ch}$, the GS is donor-like, while above the two anti-crossings the GS and 1$^{\rm st}$ excited are interface-like state. The 2$^{\rm nd}$ excited state is interface-like up to the second anti-crossing, becoming donor-like right above it. However, the symmetries are not easy to describe as it was represented in Table 8.1 for the extreme real cases.

We note that all the gaps obtained for $d = 5a^*$ and $d = 8a^*$ are extremely small compared to the relevant energy for scales here, so for most practical purposes the behavior would be equivalent to level crossing. The anti-crossings gaps also depend of valley orbit phase at interface. The anti-crossings gap control with the $V^I_{\rm vo}$ phase will be analyzed with more detail later.

The general results presented in Figs. 8.6 and 8.7 correspond to a relatively large value of the valley-orbit coupling at the interface, ($\lambda = 1.36$ Å). For these cases, the gap at anti-crossing is smaller than the value of the valley-orbit splitting ($2|V^I_{\rm vo}|$). Fig. 8.8 shows the valley composition of the three lowest states using a smaller value of $V^I_{\rm vo}$ with $\lambda = 0.215$Å for $d = 4a^*$ and $d = 5a^*$. For $d = 4a^*$, the value of the valley splitting is smaller that the gap at anticrossing, leading to a qualitatively different behavior. For instance, when $d = 4a^*$ and with $\theta = \pi/3$ the gap at anti-crossing (at $F = F_{\rm ch}$) is about three times larger than the value of the valley-orbit splitting at the interface. Due to the relatively smaller value of the valley-orbit splitting, the interface states are much closer: The two anti-crossings at $F_{\rm ch}$ seem to merge into a single one and the 1$^{\rm st}$ excited state is always an interface state. This is in contrast with results for the larger value of $V^I_{\rm vo}$ where the 1$^{\rm st}$ excited state is predominantly donor-like between the

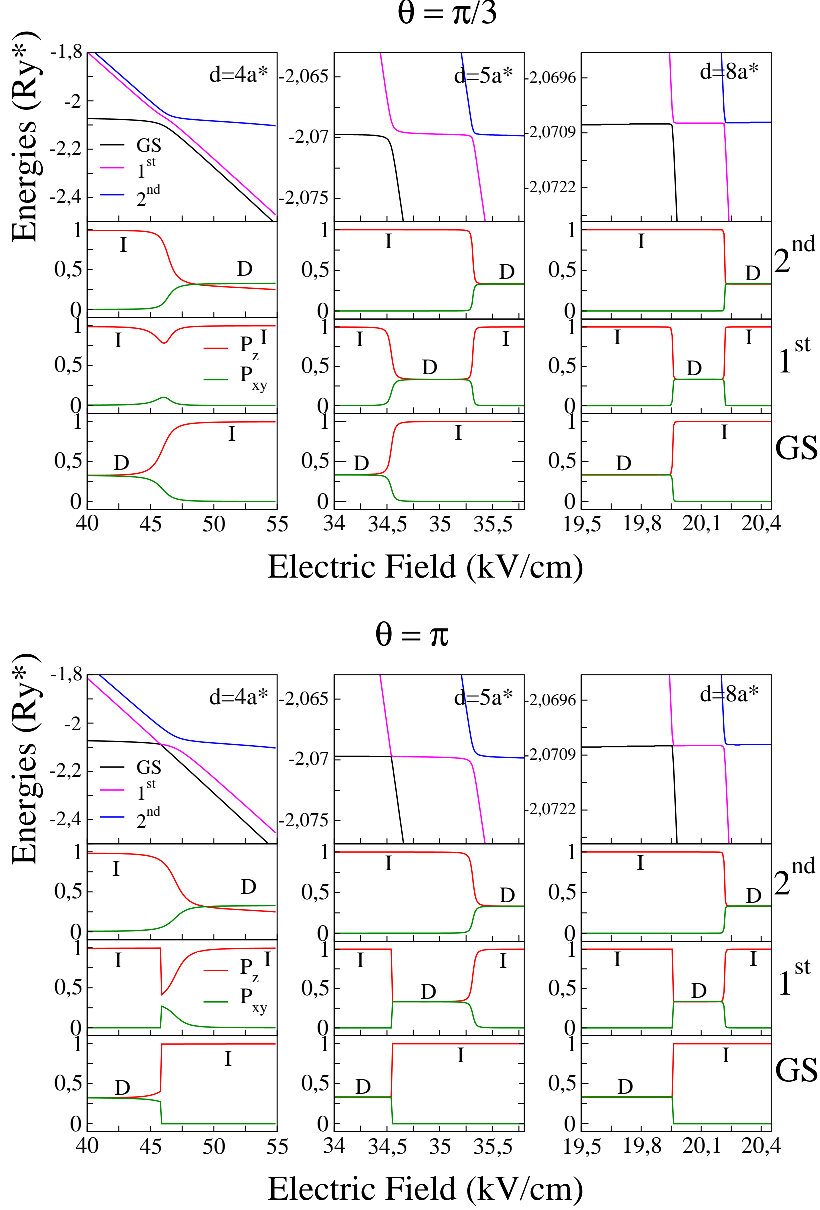

Figure 8.7: Evolution of the valley composition for the three lowest eigenvalues around the characteristic field (see Fig. 8.6) for three different distances $d = 4a^*$, $d = 5a^*$ and $d = 8a^*$. Upper panels show results for $V^I_{\text{vo}} = -|V^I_{\text{vo}}|e^{i\pi/3}$ with $|V^I_{\text{vo}}| = \lambda F$ and $\lambda = 1.36$ Å, while the lower panels were obtained with $|V^I_{\text{vo}}|$ real and positive ($\theta = \pi$). The top frames reproduce the eigenvalues involved in the lowest energy anti-crossing, which is in fact a sequence of two anti-crossings. All other frames show the valley composition in the second excited state, the first excited state, and the ground state (GS) in different lines. The red curves correspond to the weight of the $\pm z$ valleys or longitudinal weight (at donor and interface), and the green curves are the weight of the $\pm x$ and $\pm y$ valleys or transversal weight (at donor and interface). Labels D or I refer to donor-like or interface-like states in terms of real space location. Here D is a combination of the 6 valleys and I involves the z and -z valleys.

two anti-crossings. Another effect of the large gap/$2|V_{\rm vo}^I|$ ratio is an enhancement of the level splitting in a close proximity of F_{ch}.

Fig. 8.9 shows the anticrossing area at $F_{\rm ch}$ for different values of the $V_{\rm vo}^I$ phase for $d = 4a^*$. The complex phase of the valley-orbit coupling at the interface affects the symmetries of the eigenstates leading to different gaps at the two anti-crossings around $F_{\rm ch}$. Figs. 8.9(a) and (g) for $d = 4a^*$ show the limiting cases of $\theta = 0$ and $\theta = \pi$, which correspond to a real $V_{\rm vo}^I$. In these cases there is a zero-gap anticrossing (namely, a crossing) involving the symmetric donor-like eigenstate and the antisymmetric interface state, with all $C_L^\mu = 0$, except $C_I^z = -C_I^{-z} = 1/\sqrt{2}$. For a general θ, the two lowest interface states always have a symmetric component which "repel" the symmetric donor-like level. The size of the gap at the anti-crossing increases as the weight of the symmetric part of the interface-like state becomes larger. The two gaps become equal for $\theta = \pi/2$ which corresponds to a purely imaginary $V_{\rm vo}^I$. In summary, for a fixed $|V_{\rm vo}^I|$ and calling g_L and g_R the gaps to the left and to the right in energy, we get $g_L > g_R$ for $0 < \theta < \pi/2$ and $g_R > g_L$ for $\pi/2 < \theta < \pi$. In particular $g_R = 0$ ($g_L = 0$) for $\theta = 0$ (π), as presented in the initial results for real $V_{\rm vo}^I$ on Section 8.2.1. On the other hand, $g_L = g_R$ for $\theta = \pi/2$. The largest gap observed for $d = 4a^*$ is ~ 1 meV, of the same order than the interface valley-orbit splitting considered. In contrast, for example when $d = 5a^*$ (not shown here) the gap is ~ 0.035 meV, almost two orders of magnitude smaller.

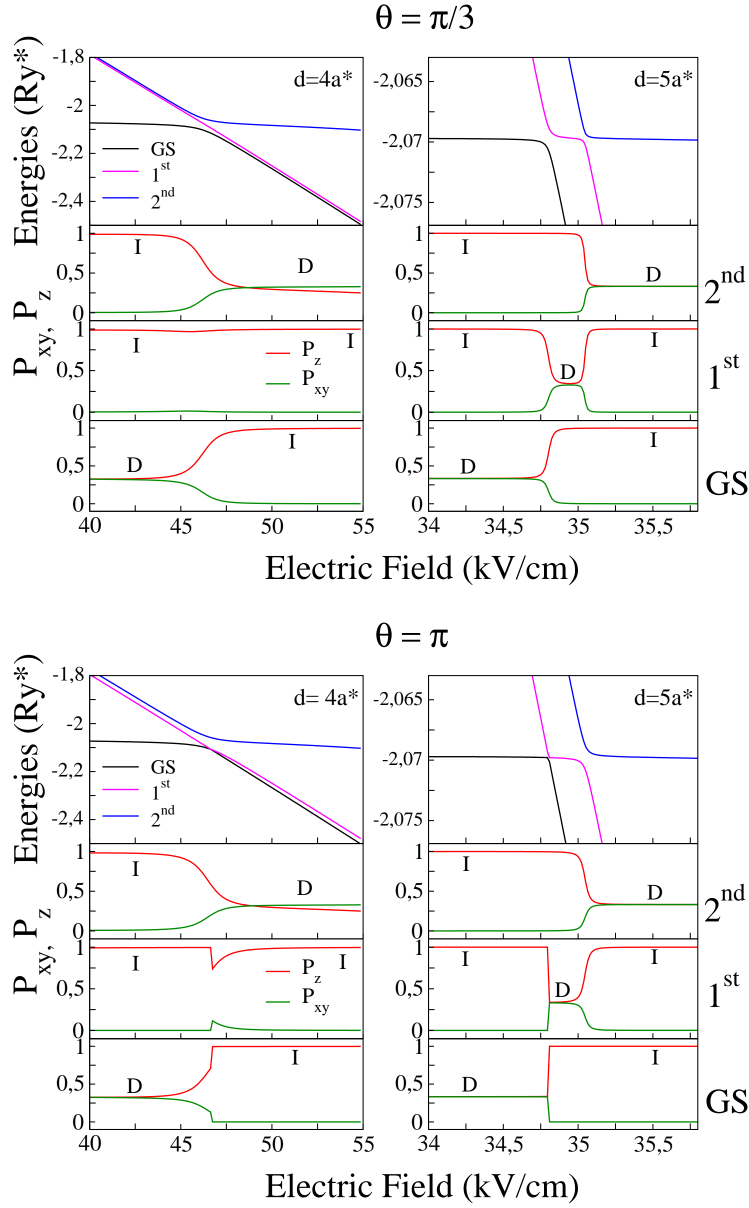

Figure 8.8: Valley composition of the three lowest eigenstates around the characteristic field, only for $d = 4a^*$ and $d = 5a^*$. Here the magnitude of the valley orbit coupling $|V_{\rm vo}^I| = \lambda F$ is defined by a smaller prefactor $\lambda = 0.215$ Åthan the for calculations shown in Fig 8.7. As well as Fig.8.7, the upper panels have been taken using a complex $V_{\rm vo}^I$ with $\theta = \pi/3$, whereas the lower panels were using $V_{\rm vo}^I$ real and positive ($\theta = \pi$). The gap at two anticrossings is changing due to the magnitude and phase of valley orbit coupling.

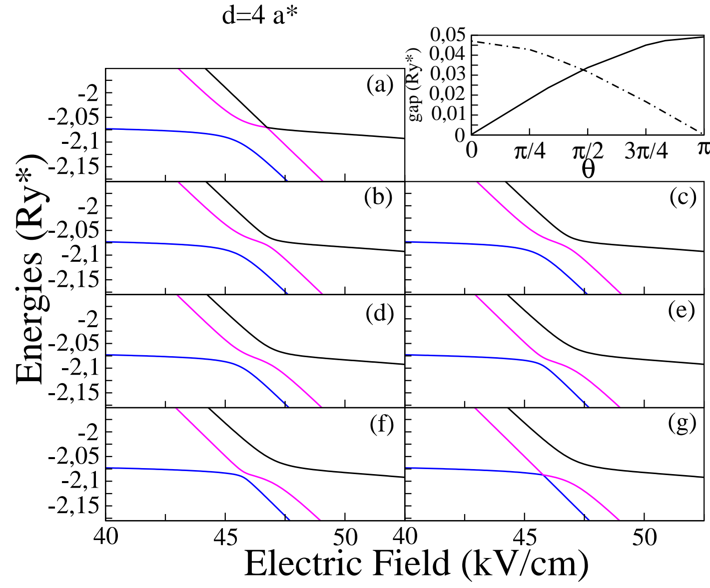

Figure 8.9: Three lowest eigenvalues around the anti-crossings region, corresponding to $d = 4a^*$ for different values of the phase θ of the valley-orbit coupling at the interface ($V^I_{\rm vo} = -|V^I_{\rm vo}|e^{i\theta}$) with $|V^I_{\rm vo}| = \lambda F$ and $\lambda = 1.36$ Å. The extra panel on the right top corner shows the values of the two anti-crossing gaps versus θ. The dashed line represents the gap for the first anti-crossing between the GS and the 1$^{\rm st}$ excited state while the solid line is the gap between the 1$^{\rm st}$ and 2$^{\rm nd}$ excited states. Note that for $\theta = 0$ and π, $V^I_{\rm vo}$ is a real quantity and one of the anti-crossings has zero gap (namely, it is actually a 2-level crossing). The two gaps are approximately equal for $\theta = \pi/2$ which corresponds to a pure imaginary $V^I_{\rm vo}$. Our results are obviously invariant for $\theta \leftrightarrow -\theta$.

Table 8.1: Evolution of the valley composition of the three lowest states for $V^I_{\rm vo}$ real and negative.
Ground state (GS), first excited state (1st) and second excited state (2nd) – in a close vicinity of the characteristic field. The symbols $F \rightarrow_> F_i$ and and $F \rightarrow_< F_i$ mean the limit as F approaches F_i from above and from below, respectively. The case (a) $d < d_0$ is obtained from data for $d = 4a^*$ and (b) $d > d_0$ from $d = 8a^*$. We use the following notation: For the donor state $|D\rangle_+ = \frac{1}{\sqrt{6}} \sum_\mu F^\mu_D(r)\phi_\mu(r)$, and for the interface states $|I\rangle_+ = [F^z_I(r)\phi_z(r) + F^{-z}_I(r)\phi_{-z}(r)]/\sqrt{2}$ and $|I\rangle_- = [F^z_I(r)\phi_z(r) - F^{-z}_I(r)\phi_{-z}(r)]/\sqrt{2}$. Note that the crossing levels are always the 1st and 2nd excited states – columns 3 and 4 in (a) and 4 and 5 in (b) – while the anticrossing takes place between the GS and the 2nd excited state in (a) – columns 4 and 5 – and between the GS and the 1st excited state in (b) – columns 3 and 4. The ordering of the levels for the largest F is the same in (a) and (b) – column 6 in both: GS is $|I\rangle_+$. 1st excited is $|I\rangle_-$ and 2nd excited is $|D\rangle_+$.

(a) $d < d_0 \Rightarrow F_a > F_c$

STATE	$F < F_c$	$F \rightarrow_< F_c$	$F_c < F < F_a$	$F \rightarrow_> F_a$	$F > F_a$
2nd	$\|I\rangle_-$	$\|I\rangle_-$	$A\|D\rangle_+ + B\|I\rangle_+$ $\|B\| > \|A\|$	$A\|D\rangle_+ + B\|I\rangle_+$ $\|A > \|B\|$	$\|D\rangle_+$
1st	$\|I\rangle_+$	$A\|D\rangle_+ + B\|I\rangle_+$ $\|B\| > \|A\|$	$\|I\rangle_-$	$\|I\rangle_-$	$\|I\rangle_-$
GS	$\|D\rangle_+$	$A\|D\rangle_+ + B\|I\rangle_+$ $\|A\| > \|B\|$	$A\|D\rangle_+ + B\|I\rangle_+$ $\|A\| > \|B\|$	$A\|D\rangle_+ + B\|I\rangle_+$ $\|B\| > \|A\|$	$\|I\rangle_+$

(b) $d > d_0 \Rightarrow F_a < F_c$

STATE	$F < F_a$	$F \rightarrow_< F_a$	$F_a < F < F_c$	$F \rightarrow_> F_c$	$F > F_c$
2nd	$\|I\rangle_-$	$\|I\rangle_-$	$\|I\rangle_-$	$\|D\rangle_+$	$\|D\rangle_+$
1st	$\|I\rangle_+$	$A\|D\rangle_+ + B\|I\rangle_+$ $\|B\| >> \|A\|$	$\|D\rangle_+$	$\|I\rangle_-$	$\|I\rangle_-$
GS	$\|D\rangle_+$	$A\|D\rangle_+ + B\|I\rangle_+$ $\|A\| >> \|B\|$	$\|I\rangle_+$	$\|I\rangle_+$	$\|I\rangle_+$

9

Discussion and Conclusions

In this part, we have analyzed in full depth the valley composition of the three lowest energy levels of a single electron in the donor-in-Si-near-a-barrier system under an applied external field. We have used a full six-valley effective mass model. This work has focused in the field range around the crossover between donor-like and interface-like character of the electron ground state.

As discussed in previous works (71, 182, 208), the characteristic field above which the electronic ground state is at the interface as well as the time required to shuttle the electron from the donor to the interface are determined by a level anticrossing process involving the electronic ground state. This time may be estimated from the size of the gap at the anti-crossing (namely, the degree of the level repulsion), which decreases as the distance between the donor and interface increases. These results are consistent with the ones obtained using our full multivalley problem. The shuttling time is a key parameter determining the feasibility of quantum computation in the doped-Si architecture. This should be orders of magnitude smaller than the coherence time to allow for many operations and error correction while coherent evolution of the qubit takes place. The tunneling process conserves the spin, but coherence would be lost for valley and/or charge degrees of freedom. Therefore, if quantum information is stored in a charge qubit, the electron should evolve adiabatically from the donor to the interface, while tunneling would be acceptable for spin qubits. In an adiabatic process, the modification of the Hamiltonian, for instance, when an external field is applied, is slow enough that the system is always in a known energy eigenstate, going continuously from the initial to the final eigenstate (213).

Strong hybridization occurs in the vicinity of the crossover between donor-like and interface-like character of the ground state (namely, around F_{ch}), leading to a mixed valley composition. An in depth study in this region shows that the anti-crossing at the characteristic field, in fact involves two anti-crossings: one between the ground and first excited states, and another one between the first and second excited states (see, Fig. 8.7).

A relevant result generated by this work is related to the strong dependence of the level crossing and anti-crossing on the phase θ of the valley-orbit coupling at the interface. This valley orbit coupling is related to the electric field, to the height, and to the quality of the interface barrier and is defined as $V_{VO}^I = -|V_{VO}^I|e^{i\theta}$ (described in section 6.3.1). The phases affect directly the symmetry of the states, thus the gaps of the two anticrossings. Even though this was expected, it is not easy to quantify to what extend the phase affects the symmetries of the levels. However, the effect can be well understood analyzing the extreme cases ($\theta = 0$ *or* π) when the V_{VO}^I is real. In these cases, when the electron is at the interface, namely for $F > F_{ch}$, its wave-function is a symmetric (for $\theta = 0$) or antisymmetric (for $\theta = \pi$) combination of the z and $-z$ valleys (see, Fig. 8.2). On the experimental side, it is important to highlight that it is not a straightforward task to predict, control or measure the valley orbit coupling phase, which should vary with the barrier material (203), interface roughness due to steps, interdiffusion, etc, and other sample properties related to design and nanofrabrication.

On the search of feasible manipulation of qubits in a doped-Si/barrier system, the results on the double anti-crossing shown in Fig 8.9 may play an important role. For instance, in the limit of $\theta \rightarrow 0$ the ground state is well separated from the excited states. This suggests the possibility to achieve an adiabatic shuttling of the electron from the donor site to the barrier interface. Further, this could be a suitable scenario for a spin qubit for which one needs the valley splitting to be larger than the Zeeman splitting (71). Then, an intrinsically large $|V_{VO}^I|$, like the one considered in Figs. 8.2 (first row), 8.6, 8.7 and 8.9 is needed, as well as a small d ($\lesssim 4a^*$) to guarantee a sufficiently large gap at anticrossing.

On the other hand, following the adiabatic theorem mentioned above, the donor-interface shuttling would be prohibitively slow for $\theta \rightarrow \pi$ due to the crossing between the ground state and the first excited level. Another effect related to the phase occurs due to the variable pinning point in the Bloch functions $\Phi_u(r)$ (namely, pinning site of the Bloch waves in a superposition state) (71, 196). This pinning point could be incorporated as a phase in the V_{VO}^I, which would produce a periodic dependence of the valley-orbit splitting on d leading to the closing of the gap at anticrossing at some particular values of d (71).

In section 6.4, we mentioned a proposal to use the valley degree of freedom to define qubits. A controllable valley orbit coupling (related to the energy splitting between the qubits states) is required for this scheme to work (152). This may be possible if the energy separation of two states with the same envelope function but different valley compositions (therefore, different oscillations in the atomic scale) varies significantly with the external applied fields. This situation can be attained above F_{ch} when the two lowest eigenstates are mainly interface states involving different combinations of the z and $-z$ valleys. A strong dependence of the splitting with electric field needed for valley qubits can be found close to F_{ch} in some cases presented in our results. For instance, in Fig 8.9(g) (corresponding to $\theta = \pi$ and $d = 4a^*$) the closing of the gap between the two lowest eigenvalues produces a fast decrease of the splitting as the electric

field is lowered from ~ 48 to ~ 46 kV/cm. Likewise, a variation of the splitting with electric field is presented in the case with smaller values of V_{VO}^{I}, as exemplified in Fig. 8.8. Here the hybridization leads to a relatively large gap compared to the value of V_{VO}^{I} and consequently the splitting increases fast from ~ 48 to ~ 46 kV/cm. However, the variation of the level splitting on the electric field is stronger when the donor-interface hybridization is large. This hybridization is mixing valleys in the different directions, potentially producing decoherence in the valley sector. Therefore, this is not a suitable regime for the valley qubit.

In summary, we concluded

- The main electronic states involved in the donor-interface shuttling of a single electron in the donor-in-Si-near-a-barrier system under an applied external field present a strong hybridization in the vicinity of the field range around the crossover the between donor-like and interface-like character of the ground state. The level of hybridization depends on the distance between donor and interface (inversely related to the gap at anticrossing), as well as on the modulus of the valley orbit coupling (namely, size of the valley splitting) related to the electric field, to the height, and to the quality of the interface barrier.

- In the hybridization region, we have identified two anticrossings, whose gap widths are also determined by the phase of the valley orbit coupling. The phases affect directly the valley symmetries. Therefore, the phases determine the level crossings and anti-crossings.

- The results described before, related to the double anticrossing and their dependence with the phase of the valley orbit coupling, may play an important role in applications for Si-based devices, providing the possibility of tuning suitable scenarios for quantum computation.

- A suitable scenario for spin qubits and charge qubits might be: For $\theta \to 0$, $d \lesssim 4a^*$ and with a relatively large value of $|V_{VO}^{I}|$ (as the one used here, with $\lambda = 1.36$Å). In this case, we may guarantee that the ground state is well separated from the first excited state, producing a large gap at anticrossing (inversely proportional to the tunneling time). This allows for the adiabatic shuttling of the electron from the donor site to the barrier interface. For spin qubits, we also need the valley splitting to be larger than the Zeeman splitting, condition that could be fulfilled in this case.

- A suitable scenario for valley qubits would be: For $\theta \to \pi$, $d \lesssim 4a^*$, with a relatively large value of $|V_{VO}^{I}|$ ($\lambda = 1.36$Å) and $F \gtrsim F_{ch}$. In this case, we can obtain two states with the same envelope functions but different valley compositions, with an energy splitting strongly dependent on F.

- Our results provide new guidelines for controlling the valley degree of freedom, therefore for the practical manipulation of donor electrons in Si nanostructures for quantum computation.

We have shown that both the modulus and the phase of V_{VO}^{I} affect clearly the quantum behavior of donor electrons in Si near an interface. The value of θ is hard to predict, and its calculation probably requires knowledge of the atomistic distribution at the interface and a complete electronic structure description of the combined Si/structured interface/barrier system. It is not clear whether a direct experimental measure is possible. We propose that the measurement of the separate gaps may provide an estimate of θ, as shown in the inset of Fig. 8.9.

In recent years, there has been a noticeable experiments progress on the characterization of donor states in Si nanostructures. In Ref (173) transport through a channel with a single donor allowed the identification of the ground state of neutral (D^0) and negatively charged donors (D^-) hybridized with the interface state. Only very recently (214) the electric field manipulation of donor electrons between a single donor and an interface has been achieved. In this case, only the ground state was identified.

Other transport experiments involving two donors in a Si nanostructure (184) have measured the level splitting between the ground state and the first excited state at a donor (valley-orbit-splitting).

On the other hand, the study of valley physics in Si has accelerated recently, as well as in other multivalley systems such as Graphene, Germanium and Bismuth intended for the design of the new generation of electronic devices. Valleytronics, for instance in Si, is essential because the valley degree of freedom imposes limitations to the spin manipulation and coherence. The valley degeneracy is often a problem for any system. However, if the degeneracy is lifted and there is an appropriate control over the valley splitting, it is possible to achieve certain valley manipulation and even think this as a possibility to encode quantum information (152). The valleys seem to be long lived. Therefore, our in depth analysis of the evolution of valley composition of the main energy levels of a donor electron near to Si/Si barrier, when an electric field is applied, as in Fig. 8.7, should bring new and valuable insight towards controlled valley manipulations, involving donors in Si-based devices.

El papel de las intercaras en heteroestructuras: El efecto del estrés en las Manganitas y el Silicio para Computación Cúantica.

Introducción General

Los fenómenos físicos presentes en superficies e intercaras de sólidos han motivado una intensa actividad investigadora a partir de trabajos como el de Grove en 1882 (1), el cual posiblemente marcó el inicio experimental de las "Películas Delgadas", evidenciando la formación de películas metálicas a partir de la pulverización (*sputtering*) de cátodos con iones positivos de alta energía. Así mismo trabajos como el de Tamm en 1932, con las primeras predicciones de estados electrónicos de superficie. Este campo ha dado como resultados aplicaciones que han cambiado nuestro estilo de vida. Uno de los ejemplos más destacados es el (MOSFET) *metal-oxide-semiconductor field-effect-transistor*, el cual es el corazón de muchos de los dispositivos electrónicos. Estos éxitos tecnológicos en heteroestructuras de semiconductores han venido junto a descubrimientos de nuevos fenómenos tales como el efecto Hall cuántico.

Otro tipo de materiales que son particularmente fascinantes son los óxidos de metal de transición, los cuales son sistemas electrónicos fuertemente correlacionados, además muchos de estos óxidos cristalizan en arreglos de red simples, entre ellos la estructura de tipo perosvskita cúbica con formula química ABO_3, donde A es típicamente un elemento alcalino o de tierras raras (Ca, Sr, Ba), B es un métal de transición y O es el oxígeno (ver Fig. 1.1). Estos materiales tienen una increible variedad de propiedades funcionales que en ocasiones son inaccesibles para los semiconductores. Las propiedades de los óxidos de metal de transición resultan de fuertes interacciones

entre el espín, la carga y la red, donde la competencia de varios estados da lugar a fenómenos complejos y a ricos diagramas de fase. Ejemplos representativos de estos fenómenos físicos son la superconductividad de alta temperatura (T_c) en Cupratos (3) y la magneto-rresistencia colosal (CMR) en Manganitas, compuestos objeto de estudio en este trabajo (3). En estos sistemas pequeñas perturbaciones llevan a importantes cambios en sus propiedades producto de las fuertes correlaciones. Por tal motivo, en estos sistemas la extrema sensibilidad a las distorsiones estructurales y a la química del cristal proporcionan muchas formas de controlar sus propiedades, así como de diseñar nuevas funcionalidades y por tanto podemos con seguridad esperar que en las intercaras entre óxidos complejos se de lugar a nuevos comportamientos de interés.

Las películas delgadas y las multicapas pueden proporcionar nuevos grados de libertad al diseñar nuevas propiedades y al controlar las ya existentes a través del estrés (*strain*), el tamaño y otros efectos presentes en las intercaras. La superconductividad, la ferroelectricidad y las uniones túnel mágneticas, son algunos ejemplos de los campos de investigación activos en heteroestructuras de perovskita donde los efectos de la intercara cumplen un rol crucial. Trabajos teóricos y experimentales han llevado al descubrimiento por ejemplo de estados metálicos y ferromágneticos en superredes compuestas por aislantes antiferromagnéticos (e.g. $LaMnO_3/SrMnO_3$) (5), un gas bidimensional de electrones superconductor entre dos dieléctricos (6), un aumento en la temperatura crítica en una heteroestructura superconductora de alta-T_c (7), y un tipo de ferroelectricidad de convencional en superedes que alternan capas paraeléctricas y ferroeléctricas ($PbTiO_3/SrTiO_3$), en donde fue posible modificar las propiedades ferroeléctricas manteniendo una constante dieléctrica muy grande e independiente de la temperatura. Esté comportamiento es diferente de la ferroelectricidad usual en donde la constante dieléctrica aunque es típicamente grande es fuertemente dependiente de la temperatura de transición de la fase (8).

Con el fin de aprovechar plenamente el estrés y otros efectos en la intercara, el crecimiento de la heterostructura debe ser controlado en el nivel del plano atómico y enormes progresos se han logrado en este campo, utilizando técnicas tales como deposición por laser pulsado, pulverización catódica *sputtering*, epitaxia de haz molecular (MBE), deposición química a vapor (CVD) y deposición de capas atómicas, entre otras, para el crecimiento de óxidos funcionales. Con respecto a la integración de estos óxidos en dispositivos (transistores, memorias, sensores, actuadores, etc), son pocos los que ahora han entrado en la corriente principal de producción. Debido a que existe mucha evidencia que presenta que el estrés podría ser relevante en las propiedades de películas delgadas y en las intercaras de heteroestructuras, nos hemos motivado en mejorar la comprensión del papel que cumple el estrés en las intercaras y como éste afecta las propiedades de las manganitas. En la primera parte de este trabajo, hemos analizado el efecto del estrés en manganitas crecidas epitaxialmente y estresadas homogéneamente en la dirección (001). Nos hemos enfocado en el efecto en el estado fundamental de una manganita de volumen con dopaje 0.5 (es decir, 0.5 electrones por manganeso), y en la influencia que ejerce el estrés

en la reconstrucción electrónica en la intercara entre una manganita ferromagnética-metálica y un aislante.

Algunos compuestos de óxidos complejos han sido propuestos actualmente para reemplazar a los basados en Silicio (Si) en algunos dispositivos electrónicos. Por ejemplo, recientemente Intel e IBM han sustituido en su último procesador, la puerta dieléctrica de SiO_2 por HfO_2, debido a la alta constante dieléctrica de este óxido de metal de transición; $SrTiO_3$ también ha sido considerado como una puerta de potencial oxidada para reemplazar la de SiO_2 en transistores. A pesar de esto, la plataforma tecnológica central para computación permanece basada en Si debido a la madurez de la tecnología con este material, la cual ha llevado a un progreso exponencial de la microeléctronica. Este progreso abarca desde los computadores cúanticos hasta un amplio espectro de aplicaciones para espintrónica.

El Si es un excelente material anfitrión para una completa nueva generación de dispositivos basados en las propiedades cúanticas de espines y cargas, puesto que este proporciona un ambiente ideal para espines en el estado sólido debido a su débil acoplamiento espín-órbita, así como la existencia de isótopos de Si con espín nuclear cero. Por lo tanto, el prospecto de combinar el control cúantico del espín con la tecnología sofisticada de fabricación ha motivado un esfuerzo extenso en dispositivos cúanticos basados en Si, muchos de ellos tratando de diseñar y construir un computador cúantico.

El progreso en técnicas de deposición como implantación iónica (aproximación de arriba hacia abajo) para realizar la nueva generación de dispositivos *Complementary metal-oxide-semiconductor* (CMOS) y Microscopía de barrido por sonda (aproximación de abajo hacia arriba) para localizar dopantes en Si ha permitido la creación de dispositivos electrónicos a escala atómica in Si. La habilidad para controlar la materia a escala átomica y construir dispositivos con una precisión atómica ha llevado a la fabricación de un transistor de un único electrón (11) y por lo tanto a ambicionar la construcción de un computador cuántico funcional basado en Si. En el diseño de estos nuevos dispositivos, tanto la elección de una intercara adecuada (las dos más comunes son Si/SiGe y Si/SiO_2), así como la calidad del crecimiento, juegan un papel muy importante para lograr el confinamiento cuántico de electrones en Si. Por ejemplo, la intercara es relevante para la operación de dispositivos de tunelamiento de un electrón, los cuales consisten de un pozo de potencial de Si acoplado a una fuente, a un drenador y a unos electrodos puerta. Sin embargo, los efectos de intercara son complicados por el hecho de que en dispositivos reales el pozo cuántico en la intercara no es perfectamente suave y orientado.

Efectos de intercara también son cruciales en las propuestas para la implementación física de un computador cuántico basado en Si. Entre estos, la propuestas original de Kane en (1998), que consiste de una red de donores de Fósforo (P) en Si. El diseño corresponde a electrones de donor en Si separado por una barrera (SiO_2) de unas puertas metálicas que están ubicadas en la superficie. Las puertas A controlan la frecuencia de resonancia de los espines que actúan

como qubits; Las puertas J controlan el acoplamiento mediado por electrones entre los espínes nucleares adjacentes. En esta propuesta, los parámetros del dispositivo, como el voltaje *bias* aplicado y las profundidad del donor con respecto a la superficie, afecta la función de onda del electrón en la posición del donor, por lo tanto el acoplamiento hiperfino. Además, la presencia de la intercara afecta los estados orbitales en el donor: algunas medidas en dispositivos de Si con dopantes mostraron una significante desviación de los estados orbitales de donor con respecto al espectro esperado en el volumen (13, 14).

Es importante resaltar que el Si tiene valles con degeneración múltiple en su banda de conducción. Estos valles cumplen un papel relevante tanto para dispositivos con dopantes como para dispositivos de puntos cuánticos y ellos determinan las propiedades de baja energía de los mismos. En la segunda parte de este trabajo, nos hemos enfocado en el papel de los valles sobre el control de electrones ligados a un donor substitucional de P, próximo a una intercara de Si(001)/SiO_2, insipirados en la propuesta del computador cuántico basado en Si. Usando un modelo completo de seis valles, hemos analizado la composición de valle de los estados involucrados en el proceso de ir y venir del electrón entre el donor y la intercara (*shuttling*), abriendo así las posibilidades para la manipulación del grado de libertad del valle en el sistema Si:P/barrera.

Este proyecto de tesis es una extensión de los trabajos publicados en (215) y (216).

Resumen Parte I: El efecto del estrés en el ordenamiento orbital y magnético de una película delgada de manganita y su intercara con un aislante

En esta parte del trabajo hemos estudiado el efecto del estrés uniaxial sobre la configuración electrónica del estado fundamental en películas delgadas de Manganitas. Nuestro Hamiltoniano modelo para las manganitas incluye la energía cinética, el acoplamiento electrón-red y el superintercambio antiferromágnetico entre vecinos cercanos. Hemos estudiado el estrés uniaxial que resulta del desajuste de la red entre una manganita y un sustrato cúbico y aislante, asumiento la dirección del crecimiento como (001). En nuestro modelo el efecto del estrés sobre el sistema es doble: El estrés modifica las amplitudes del *hopping* y también introduce una separación de la energía entre los niveles e_g del Mn. Nos hemos enfocado en dos casos: El efecto del estrés (i) en el estado fundamental de manganitas en volumen con dopaje $x = 0.5$ y (ii) en la reconstrucción electrónica que se presenta en la intercara de una manganita ferromagntica y metálica con un aislante. Los resultados presentan que el estrés juega un papel importante en las propiedades de una película delgada de manganita, particularmente este conlleva a una selección orbital que modifica la propiedades electrónicas y el orden magnético en las intercaras.

Los óxidos de metal de transición son una familia interesante de compuestos, los cuales pertenecen a los sistemas de electrones fuertemente correlacionados en donde el electrón interactúa fuertemente determinando las propiedades. En estos sistemas, la naturaleza dúal del electrón y como estos interaccionan con sus vecinos establece cual es el aspecto predominante en un sólido (onda o partícula). Por ejemplo, según el teorema de Bloch un electrón localizado en una red periódica se comporta como una onda plana extendida. Sin embargo, cuando el número de electrones libres en un sólido es comparable al número de los átomos que lo constituyen y la interacción

electrón-electrón se vuelve fuerte, los electrones pueden perder su movilidad y localizarse en sitios. Cuando un electrón se localiza, tiene tres atributos que determinan su comportamiento: carga (e), espín ($\pm\frac{1}{2}$) y una simetría orbital. Por lo tanto, la carga, el espín y el grado de libertad orbital, así como el acoplamiento entre ellos puede producir fases complejas y fenómenos tales como separación de fases electrónicas, entre otros.

Muchos óxidos cristalizan en arreglos de red simple tal como la estructura de perovskita cúbica, Fig. 1.1. La formula es ABO_3, siendo A típicamente un elemento alcalino o de tierras raras (Ca, Sr, Ba), B un metal de transición y O correspondiendo al oxígeno. Lo electrones activos están usualmente en los orbitales externos d de los metales de transición. A pesar de la simplicidad química y estructural, los óxidos de metal de transición muestran fenómenos físicos muy diferentes. Si se considera un átomo de metal de transición en un cristal con estructura perovskita, éste estará rodeado por seis iones de oxígeno O^{2-} que producirán un potencial del campo cristalino en donde las funciones de onda apuntando hacia los iones O^{2-} (orbitales e_g $d_{x^2-y^2}$, $d_{3z^2-r^2}$) tendrán una energía más alta que las que están entre ellos (orbitales t_{2g} d_{xy}, d_{yz}, d_{zx}). Como consecuencia, los orbitales d ilustrados en la Fig. 1.2 están separados. Por lo tanto, hay un gap entre los orbitales e_g y t_{2g} el cual actúa como un grado de libertad del espín o de la carga.

Entre los óxidos de metal de transición están las manganitas, las cuales han sido el foco de estudio en esta parte del trabajo de tesis. Un rango amplio de fenómenos y una gran variedad de trabajo experimental han hecho que estos sistemas sean especialmente atractivos para la comunidad científica. En las manganitas el acoplamiento fuerte entre el grado de libertad de la carga, el espín y la red produce una variedad de fases en un material químicamente homogéneo. Propiedades como la Magnetorresistencia Colosal reportada inicialmente en los años 90 por Jin y sus colaboradores, motivó el interés general y estimuló la investigación en manganitas debido a su potencial para aplicaciones en dispositivos electrónicos comerciales.

Las manganitas también son *half-metals* (ferromagnetos con un solo tipo de electrones de conducción, ya sea espín para arriba $\uparrow$ o espín para abajo $\downarrow$), lo que hace de estos sistemas unos buenos inyectores y detectores de espín para espintrónica, un campo muy atractivo y prometedor que se está desarrollando rápidamente.

Muchos trabajos en manganitas sugieren que las propiedades de conducción de estos sistemas, así como el orden orbital y la estructura magnética, entre otras, pueden ser modificadas bajo la influencia del estrés. La influencia del estrés del sustrato es el principal factor que distingue una película delgada de manganita de una manganita en volumen. Esto es debido al hecho de que los electrones e_g de los Mn, los cuales son los más determinantes de las propiedades físicas están acoplados al grado de libertad de la red. En particular, el estrés puede afectar las propiedades electrónicas a través del ordenamiento orbital, por ende altera las propiedades de magnetotransporte de las películas delgadas o de las heteroestructuras de manganitas. El efecto del estrés en películas delgadas de manganita ha sido el foco de este proyecto.

Una importante cantidad de trabajos teóricos y experimentales de gran relevancia presentan diferencias en las propiedades eléctricas y magnéticas que exhiben las películas delgadas de manganita con respecto a su homólogo en volumen. En particular, ha sido observado que la conductividad y la T_c magnética se reducen con respecto al volumen (81, 114). Estas diferencias pueden ser producto del desajuste de la red en toda la película que se presenta entre la manganita y el sustrato, así como debido a las modificaciones en la intercara sustrato/manganita, efecto conocido como reconstrucción electrónica. Este efecto puede ser más contundente en películas ultra delgadas que son usadas en multicapas y además puede verse modificado fuertemente por el estrés. Aunque las propiedades en la intercara de películas delgadas y en heteroestructuras pueden verse también afectadas por efectos como desorden, vacantes de oxígeno, variaciones en la composición química y otros efectos que dependen principalmente de las condiciones del crecimiento, muchos trabajos sugieren que el estrés estructural juega un papel clave en la determinación de las propiedades eléctricas y magnéticas de las manganitas.

Teniendo en cuenta esta perspectiva, este trabajo se ha enfocado en el efecto del estrés sobre las propiedades electrónicas y magnéticas de películas delgadas de manganita y en intercaras manganita/aislante.

En manganitas los orbitales activos son los e_g del Mn $3z^2 - r^2$ y $x^2 - y^2$ (como se representan en la Fig 1.2). Una distorsión tetragonal de la celda unidad (pseudo) cúbica produce una ocupación preferencial de uno de los niveles e_g anisotrópicos y una equivalente separación de la energía, lo que conlleva a un ordenamiento orbital (19, 64, 90, 105). A su vez, un ordenamiento orbital particular se asocia a un ordenamiento magnético particular (ver Fig 3.1). Consecuentemente, cuando una extensión de la red en el plano (xy) tiene lugar, lo que corresponde a un estrés de tracción (definido por $c/a < 0$; $e_{xy} > 0$), el orbital $x^2 - y^2$ es el preferido. Por lo tanto, los órdenes AFM de tipo CE y A son favorecidos ya que el $x^2 - y^2$ es dominante en estas configuraciones. Por otro lado, el estrés de contracción (definido por $c/a > 0$; $e_{xy} < 0$) implica que los orbitales $3z^2 - r^2$ sean los preferidos y por tanto el orden AFM de tipo C es favorecido, debido a que el $3z^2 - r^2$ es dominante en esta configuración. Esta situación es exactamente la que hemos encontrado para manganitas en volumen con dopaje $x = 0.5$, si incluimos la separación entre los orbitales e_g (denotada por δ y definida en la Eq. 2.17) causada por estrés suficientemente grande ($\delta \gtrsim 50 e_{xy} t$) (ver Figs. 3.3 (b) and 3.4). Este valor de δ es relativamente grande ($\sim t$ para un estrés del 2%) pero es un valor comparable a la típica separación Jahn-Teller. La modificación del ordenamiento orbital con el estrés se ha observado en varios experimentos (19, 80, 84, 95), en cálculos modelo para $LaMnO_3$ (82), y en cálculos ab-initio para $La_{0.66}Sr_{0.33}MnO_3$ (116), y para superredes $LaMnO_3/SrMnO_3$ (105).

El otro sistema objeto de estudio ha sido el efecto del estrs en los estados en la intercara entre un aislante y una manganita con dopaje $x = 0.3$ (es decir, ferromagntica y metálica). Los resultados son relevantes para dispositivos de multicapas tales como válvulas de espín. Las

tendencias generales de cómo el estrés afecta a este sistema son las mismas que en el volumen. Para este caso, el comportamiento del volumen (FM y metálico) es recuperado en pocas celdas unidad, mientras que en la capa de la intercara se espera una densidad de estados cercana a 0.5, debido a la redistribución de la carga. Cerca a $x = 0.5$ un orden AFM de tipo CE puede tener lugar. Este tipo de orden se vería favorecido por el estrés de tracción y desfavorecido por el de contracción, al igual que en volumen.

En manganitas el FM viene normalmente de la mano de la metalicidad debido al Doble-Intercambio. Debido a que el Doble-Intercambio es suprimido cuando la degeneración de los niveles e_g se rompe, se espera que al aplicar un estrés uniforme se disminuya la T_c. Este hecho ha sido corroborado por algunas investigaciones teóricas y experimentales (85, 89, 93). Por tal motivo, aunque el estrés de contracción no afecta mucho el estado fundamental de la intercara, aumenta la separación de los niveles e_g ($\delta > 0$) lo que puede llevar a una reducción de la conductancia en las intercaras con respecto al volumen.

Los resultados también evidencian una reconstrucción orbital en la intercara, incluso sin estrés: en la configuración FM de la intercara, el orbital $x^2 - y^2$ se ocupa preferentemente. Este orden ferro-orbital es reforzado por el estrés de tracción y afecta tanto a la configuración de tipo FM como la CE. No obstante, el comportamiento en superficies puede ser cualitativamente diferente cuando los octaedros de oxígeno que rodean los iones Mn están incompletos. En el caso de una superficie (001), el orbital $3z^2 - r^2$, el cual apunta hacia la superficie, baja en energía con respecto al orbital $x^2 - y^2$, el cual está más localizado alrededor del ion (54). Por otra parte, hibridación a través de una intercara podría llevar a una ocupación preferencial del orbital $3z^2 - r^2$ (111).

Cuando el orden CE es favorecido en una intercara manganita-aislante, hemos encontrado que en la mayoría de los casos la intercara presenta conducción metálica (no hay un gap a la energía de Fermi). Pudimos observar que tan solo aplicando estrés de tracción junto a un valor relativamente pequeño del parámetro α ($\alpha \lesssim 0.7$), se puede conducir a una propiedad aislante en la intercara.

En resumen:

- El efecto del estrés sobre los sistemas de maganitas es doble: Por un lado, éste afecta el solapamiento de los orbitales y por lo tanto a las amplitudes *hopping*. Por otro lado, el estrés puede inducir una separación δ de los orbitales e_g. La comparación con los resultados experimentales indica que la separación de los orbitales e_g inducido por el estrés domina sobre la modificación de las amplitudes de los *hoppings*. Esto implica que el δ tiene que ser suficientemente grande $\delta \gtrsim 50 e_{xy} t$.

- En el sistema de manganita en volumen con dopaje $x = 0.5$, el estrés de tracción (extensión en el plano xy) promueve una selección orbital: El orbital preferido es el $x^2 - y^2$. Por lo tanto, los órdenes AFM de tipo CE y A se ven favorecidos debido a que el orbital $x^2 - y^2$ es dominante en estas configuraciones. Por el contrario, el estrés de contracción produce una selección orbital donde los orbitales $3z^2 - r^2$ son los preferidos, y por ende el orden AFM de tipo C es favorecido, ya que el $3z^2 - r^2$ es dominante en esta configuración.

- En una heteroestructura aislante/manganita ($x = 0.3$)/aislante, el efecto del estrés sobre la reconstrucción electrónica en la intercara es consistente con el comportamiento observado para las manganitas en el volumen. En este caso, la configuración CE en la intercara es favorecida por el estrés de tracción debido a la ocupación preferencial del orbital $x^2 - y^2$. Por otro lado, la configuración FM se convierte en más estable con respecto a la CE, cuando se aplica un estrés de contracción. Sin embargo, la conductancia en la intercara con respecto al volumen puede ser reducida debido a la rotura de la degeneranción de los niveles e_g. Además, grandes valores de estrés pueden inducir un comportamiento aislante en la capa interfacial (se abre un gap a la energía de Fermi).

- La principal consecuencia del estrés es la selección orbital, la cual está intimamente relacionada con el grado de libertad del espín y con las propiedades de transporte. De esta manera, el estrés proporciona una forma de modificar la configuración del estado fundamental en manganitas y por tanto, controlar el funcionamiento de dispositivos electrónicos basados en estos compuestos. Cálculos recientes (94) presentan un aumento en la magnetoresistencia de una película delgada con dopaje 0.5 bajo el efecto de un estrés de tracción.

En este trabajo hemos considerado un estrés uniforme y un ratio de Poisson uniforme ν. Sin embargo, teniendo incluso un estrés uniforme en el plano, este puede ir acompañado de un estrés no uniforme en la dirección z (90). Por lo tanto, en ese caso δ podría tener signos diferentes en diferentes planos atómicos y dar como resultado ordenamientos orbitales más complejos que los presentados en este trabajo. Este caso corresponde con el reportado en la Ref (90) para una multicapa $(La_{0.7}Sr_{0.3}MnO_3)_3/(BaTiO_3)_3$ depositada sobre un sustrato STO(001) con parámetros de red muy similares.

Nuestros hallazgos presentan que el estrés produce un tipo de ordenamiento orbital que es coherente con el resultado de muchos trabajos experimentales y teóricos (19, 80, 84, 94, 95). Por ejemplo, el estrés de contracción aplicado en películas delgadas de LSMO produce un cambio en la fase, pasando de FM y metálico a un AFM de tipo C (93). Así mismo, para LCMO que en volumen es FM y metálico, un estrés de tracción aplicado favorece la ocupación electrónica de los orbitales $x^2 - y^2$, lo que lleva a que se produzca un ordenamiento orbital de tipo A.

Añadido a esto, nuestros resultados se acercan mucho más a los experimentales, cuando se toma la separación de los niveles e_g como el efecto más dominante del estrés en comparación con el cambio en la amplitud de los *hoppings*. Estas predicciones también están en muy buena concordancia con algunos trabajos teóricos y experimentales (19, 64, 82, 89, 90, 91).

Los efectos del estrés continuan siendo un foco de estudio para los sistemas de manganitas, con el objetivo de mejorar el conocimiento acerca de la modificación de las propiedades eléctricas y magnéticas en estos sistemas (117, 118). Las implicaciones del estrés que nosotros hemos propuesto en este trabajo, así como nuestros resultados, pueden ser de gran utilidad para las nuevas investigaciones enfocadas en la búsqueda de la posibilidad de manipulación y control de las propiedades deseadas en las novedosas películas delgadas y heteroestructuras que han sido concebidas para los nuevos dispositivos espintrónicos.

Resumen Parte II: Impacto del grado de libertad de valle en el control de electrones de donantes cerca a una intercara Si/SiO_2

En esta parte hemos analizado la composición de valle de un electrón ligado a un donor, específicamente un donor sustitucional de Fósforo (P) en Si, cercano a una Si/barrera (001) bajo el efecto de un campo eléctrico aplicado perpendicular a la intercara. Hemos adoptado un modelo completo de masa efectiva que incluye 6 valles, donde los valles corresponden a los mínimos de la banda de conducción a lo largo de las direcciones cristalográficas x, y y z. Para bajos campos eléctricos, el estado fundamental del electrón está confinado esencialmente en el donor, en donde la energía más baja se divide en estados con distintas contribuciones de los seis valles, debido al entorno de campo cristalino tetragonal. A campos suficientemente altos, el donor se ioniza y su electrón se mueve hacia la intercara, donde los niveles de valle se dividen en un estado excitado con degeneración cuádruple, que consiste en los valles $\pm x$ y $\pm y$ y un estado más bajo en energía con una degeneración doble que corresponde a los valles $\pm z$. La separación de valle en la intercara divide ligeramente el estado fundamental debido al acoplamiento órbita-valle, V^I_{VO}. En campos eléctricos intermedios cercanos al campo característico (el estado fundamental del electrón pasa de estar principalmente ligado al donor a estar más ligado a la intercara), los estados del electrón pueden estar constituidos por estados hibridizados con composición de valles diferentes a las del estado fundamental en el donor o en la intercara. El grado de repulsión entre los niveles, por ende el gap en el anticruce, dependen de la composición de valles relativa la cual varía con el módulo y la fase del acoplamiento órbita-valle, así como de la distancia entre el donor y la intercara. Nos hemos enfocado en la composición de valle de los estados involucrados en el proceso de ir y venir ''shuttling' del electrón que está determinado por el anticruce de los tres autoestados más bajos en energía. Una secuencia de dos anticruces tiene lugar y la fase compleja afecta la simetría de los autovalores y los gaps de los anticruces entre los niveles. Nuestros resultados contribuyen a un mejor entendimiento de la manipulación controlada de valles, la cual es muy relevante para la manipulación práctica de los electrones

de donores en nanoestructuras de Si y por lo tanto para algunas propuestas de computadores cuánticos basados en Si.

En los últimos años, la densidad de transistores en un chip ha sido incrementada significativamente cada 18 meses, como lo predice la ley de Moore (como puede verse en la Fig 5.3). El progreso exponencial de la microelectrónica ha estado basado en la tecnología del Silicio. El Silicio es un entorno ideal para los espines en el estado sólido debido a su acoplamiento débil espín-órbita y a la existencia de isótopos con espín nuclear 0. La perspectiva de combinar el control cuántico del espín con la sofisticada tecnología de fabricación existente en computadores clásicos ha estimulado en la última década grandes esfuerzos enfocados en dispositivos basados en Silicio.

Existen muchas propuestas para el diseño de procesadores de información cuántica, algunas de ellas basadas en semiconductores debido a sus semenjanzas con la electrónica clásica (Kane, 1998 (12)), Loss & Di Vicenzo, 1998 (128)). Inicialmente, la propuesta original de Loss & Di Vicenzo generó especial interés en los espines electrónicos en puntos cuánticos. A pesar de la gran madurez de la tecnología del Silicio en los transistores de campo tradicionales, los puntos cuánticos de GaAs estuvieron históricamente más consolidados, debido a trabajos previos en el crecimiento expitaxial de materiales III-V con similares parámetros de red. Así mismo experimentos en puntos cuánticos definidos litograficamente en heteroestructuras de GaAs/AlGaAs demostraron la inicialización de qubit, lectura de espín de único disparo y único electrón (140), y el control coherente de un solo espín y estados de dos espines (141, 142). De este modo los sistemas de GaAs que cumplen con los criterios de Di Vicenzo para computación cuántica descritos anteriormente en la sección 5.5.1(143).

No obstante, el GaAs tiene aspectos relevantes relacionados con la presencia inevitable de espines nucleares en el material húesped. Por ejemplo, en heteroestructures de AlGaAs/GaAs, tanto el Al como el Ga no presentan espín nuclear cero, lo que causa que el espín del electrón en un QD (*quantum dot* o punto cuántico) interactúe con muchos espines nucleares en el material húesped por acoplamiento hiperfino. Este acoplamiento tiene varios efectos adversos entre ellos la decoherencia del spín del electrón como resultado del campo magnético efectivo aleatorio generado por fluctuaciones del espín nuclear y la mezcla entre estados de espín electrónico y órbital electrónico por la dependencia orbital con el campo magnético. La aleatoriedad en el campo nuclear conduce a una decoherencia con un T_2 medido por espín echo $\sim 1\mu s$ e 0.1T (142).

Por otro lado, el Si natural consiste en un 95% en ^{28}Si sin espín nuclear y además puede ser purificado cerca del 100% de isótopos con espín nuclear cero. Adicionalmente el Si es un elemento más ligero que el Ga y el As lo que reduce el acoplamiento espín-órbita. Los experimentos ESR (*Electron Spin Resonance*) demostraron tiempos de coherencia mucho más largos en Si que en GaAs, con un orden de magnitud de segundos (149). Por estos motivos varias propuestas han sido hechas para qubits de espín electrónicos basados en Si en puntos cuánticos

(146) y en donantes (147, 148). Una de ellas es la propuesta hecha por Bruce Kane en 1998 (12) que consiste de un red lineal de átomos de Fósforo (P) incrustados por debajo de la superficie de un entramado de Si puro. En la propuesta original el qubit es el espín nuclear del donante P que puede ser manipulado a través del acoplamiento hiperfino con el espín del electrón ligado. El acoplamiento hiperfino es variado aplicando campos eléctricos en las puertas locales lo que permite llevar a cabo rotaciones de un qubit. Las operaciones de dos qubits se pueden lograr usando el acoplamiento de intercambio entre electrones ligados y donantes vecinos y cualquier compuerta lógica puede ser obtenida con la combinación apropiada de operaciones de uno y dos qubits.

Sin embargo, existen algunos retos presentes al desarrollar nanodispositivos basados en Si. Uno de ellos está relacionado con el efecto de múltiples valles presentes en la banda de conducción del Si en volumen, ya que este puede imponer limitaciones a la manipulación del espín y la coherencia, así como afectar las propiedades de transporte. También se ha propuesto codificar información directamente en el grado de libertad de valle. Por tal motivo la física de valles juega un papel crítico en la manipulación del grado de libertad del espín de electrones en dispositivos basados en Si.

En esta parte, hemos analizado a profundidad la composición de valle de los tres niveles más bajos en energía de un electrón ligado a un donor en Si que está cerca de una barrera, y que se encuentra bajo el efecto de un campo eléctrico externo aplicado. Hemos usado un modelo completo de masa efectiva que incluye los 6 valles de la banda de conducción del Si. Al aplicar un campo eléctrico, un electrón ligado a un donor puede ser transportado entre el donor y un estado en la intercara. Nos enfocamos en el rango de campos eléctricos en el que se puede producir esta manipulación, es decir, cerca del (anti)cruce entre el estado ligado al donor y el estado de intercara.

Como se ha discutido en trabajos previos (71, 182, 208), el campo característico por encima del cual el estado fundamental electrónico está en la intercara, así como el tiempo requerido para que el electrón vaya del donor a la intercara, están determinados por el proceso de anticruce entre los niveles que involucran al estado fundamental electrónico. Este tiempo se puede estimar a partir del tamaño del gap en el anticruce (determinado por el grado de repulsión entre los niveles), el cual decrece al incrementar la distancia entre el donor y la intercara. Estos resultados son consistentes con los que hemos obtenido resolviendo el problema completo de multivalles. Este tiempo de ir y venir es un parámetro clave para determinar la factibilidad de la computación cuántica en la arquitectura con Si-dopado y debe ser órdenes de magnitud menor que el tiempo de coherencia para que permita la realizacin de un gran nmero de operaciones as como la correccin de errores mientras tiene lugar la evolución coherente de los qubits. Aunque el proceso túnel conserva el espín, la coherencia se perdería en el grado de libertad del valle y/o carga. Por lo tanto, si la información cuántica es almacenada en un qubit de carga, el electrón debería evolucionar adiabáticamente del donor a la intercara para garantizar

la coherencia, mientras que el tunelamiento podría ser aceptable para qubits de espín. En un proceso adiabático, la modificación del Hamiltoniano, por ejemplo cuando un campo eléctrico externo es aplicado, es lo suficientemente lento para que el sistema esté siempre en un autoestado de energía conocido, y va continuamente del estado inicial al estado final (213).

Una fuerte hibridación ocurre en la proximidad del anticruce entre el estado fundamental con carácter de donor y este mismo con carácter de intercara (es decir alrededor de F_{ch}). Esta hibridación da lugar a una mezcla de valles en los estados involucrados. Sin embargo, un estudio a profundidad de está región presenta que el anticruce en el campo característico en realidad involucra dos anticruces: uno entre el estado fundamental y el primer estado excitado y el otro entre el primer estado excitado y el segundo (ver, Fig. 8.7).

Un resultado relevante generado por este trabajo es la fuerte dependencia del cruce y anticruce de los niveles con la fase compleja θ del acoplamiento órbita-valle en la intercara. Este acoplamiento órbita-valle está vinculado al campo eléctrico, así como a la altura y a la calidad de la barrera en la intercara, y se define como $V_{VO}^{I} = -|V_{VO}^{I}|e^{i\theta}$ (descrito en la sección 6.3.1). La fase afecta directamente a la simetría de los estados y por lo tanto a los gaps de los anticruces. Aunque está dependencia se esperaba, no es fácil cuantificar hasta qué punto la fase afecta a la simetría de los niveles. Sin embargo, el efecto puede entenderse analizando los casos extremos ($\theta = 0$ o π), es decir cuando el V_{VO}^{I} es real. En estos casos, cuando el electrón está en la intercara, es decir para $F > F_{ch}$, su función de onda es una combinación simétrica (para $\theta = 0$) o antisimétrica (para $\theta = \pi$) de los valles z y $-z$ (ver la Fig. 8.2). Desde el punto de vista experimental, es muy importante resaltar que no es una tarea fácil el predecir, controlar y manipular la fase compleja del acoplamiento órbita-valle, el cual puede variar con la barrera del material (203), con la rugosidad en la intercara debida a escalones, interdifusión, etc, y con otras propiedades de la muestra relativas al diseño y la nanofabricación.

En la búsqueda de una manipulación factible de qubits en un sistema de Si-dopado/barrera, los resultados del doble-anticruce presentados en la Fig. 8.9 pueden jugar un papel muy importante. Por ejemplo, en el limite $\theta \to 0$ el estado fundamental está bien separado de los estados excitados. Esto sugiere la posibilidad de lograr un transporte adiabático del electrón desde el sitio del donor hasta la barrera en la intercara. Añadido a esto, este podría ser un escenario adecuado para el qubit de espín, en el cual es necesario que la separación de los estados de valle sea más grande que la separación Zeeman (71). Por tal motivo sería necesario un valor intrínseco grande del $|V_{VO}^{I}|$, tal como el que consideramos en las Figs. 8.2 (primera fila), 8.6, 8.7 y 8.9, así como un valor pequeño de d ($\lesssim 4a^*$), para garantizar un gap lo suficientemente grande en el anticruce.

Por otro lado, continuando con el teorema adiabático mencionado anteriormente, el ir y venir del electrón entre el donor y la intercara podría ser prohibitivamente lento para $\theta \to \pi$, debido al cruce entre el estado fundamental y el primer estado excitado. Otro efecto relacionado con la fase ocurre debido al punto variable de fijación en las funciones de Bloch $\Phi_u(r)$ (que consiste en

el sitio de fijación de las ondas de Bloch en un estado de superposición) (71, 196). Este punto de fijación podría ser incorporado como una fase en el V_{VO}^{I}, que produciría una dependencia periódica de la separación órbita-valle con d, lo que produce que se cierre el gap del anticruce en algunos valores particulares de d (71).

En la sección 6.4, hemos mencionado una propuesta que usa el grado de libertad de valle para definir qubits. Para este esquema de trabajo es requerido un acoplamiento órbita-valle controlable (relacionado con la separación de la energía entre los estados de los qubits). Esto es posible si la separación de energía entre dos estados que tienen la misma función envolvente pero diferente composición de valle (por lo tanto, diferentes oscilaciones en la escala atómica) varían significativamente con el campo eléctrico externo. Esta situación puede ser alcanzada por encima de F_{ch}, cuando los dos estados más bajos en energía son principalmente estados de intercara que involucran diferentes combinaciones de los valles z y $-z$. La fuerte dependencia con el campo eléctrico necesaria para los qubits de valle puede ser encontrada cerca de F_{ch} y se presenta en algunos casos de nuestros resultados. Por ejemplo, en la Fig. 8.9(g) (que corresponde a $\theta = \pi$ y $d = 4a^*$) el cierre del gap entre los dos autovalores produce un rápido decrecimiento de la separación a medida que el campo eléctrico disminuye de $\sim$ 48 a $\sim$ 46 kV/cm. Así mismo, encontramos una variación de la separación entre niveles con el campo eléctrico en el caso correspondiente a un valor pequeño del V_{VO}^{I}, como se ejemplifica en la Fig. 8.8. En este caso, la hibridación lleva a un gap relativamente grande comparado con el valor de V_{VO}^{I} y consecuentemente la separación se incrementa rápido de $\sim$ 48 a $\sim$ 46 kV/cm. Sin embargo, la variación de la separación de los niveles con el campo eléctrico es más fuerte cuando la hibridación donor-intercara es grande. Esta hibridación implica una mezcla de valles en las diferentes direcciones, el cual produce potencialmente decoherencia en el sector de valle. Por lo tanto, este no es un régimen adecuado para el qubit de valle.

En resumen, nosotros concluimos:

- Los principales estados electrónicos involucrados en el ir y venir del electrón entre el donor y la intercara en un sistema constituido por un donor en Si cercano a una barrera que se encuentra bajo un campo externo aplicado, presentan una fuerte hibridación en la proximidad del rango de campo alrededor del cruce entre el estado fundamental en el donor y el mismo en la intercara. El nivel de hibridación depende de la distancia entre el donor y la intercara (inversamente relacionado con el gap en el anticruce), así como del módulo del acoplamiento valle-órbita (es decir la separación de los niveles en el anticruce) que está relacionado con el campo eléctrico, así como con la altura y con la calidad de la barrera en la intercara.

- En la región de la hibridación, hemos identificado dos anticruces, cuyas anchuras de gaps vienen también determinadas por la fase compleja del acoplamiento órbita-valle. Las fases afectan directamente a las simetrías de los valles. Por lo tanto, las fases determinan

el cruce y el anticruce de los niveles.

- Los resultados descritos antes, relacionados con el doble anticruce y su dependencia con la fase del acoplamiento órbita-valle, pueden jugar un papel importante para los dispositivos basados en Si, proporcionando la posibilidad de encontrar escenarios adecuados para la computación cuántica.

- Un escenario adecuado para qubits de espín y qubits de carga puede ser: Para $\theta \to 0$, $d \lesssim 4a^*$ y con un valor relativamente grande de $|V_{VO}^I|$ (como el que usamos aquí con $\lambda = 1.36\text{Å}$). En este caso, nosotros podemos garantizar que el estado fundamental está bien separado del primer estado excitado, produciendo un gap considerable en el anticruce (inversamente proporcional al tiempo de tunelamiento). Esto permite un ir y venir del electrón adiabático desde el sitio del donor hasta la barrera en la intercara. Para qubits de espín, nosotros también necesitamos que la separación de valle sea más grande que la separación Zeeman, condición que puede ser cumplida en este caso.

- Un escenario adecuado para qubits de valle podría ser: Para $\theta \to \pi$, $d \lesssim 4a^*$, con un valor relativamente grande de $|V_{VO}^I|$ ($\lambda = 1.36\text{Å}$) y $F \gtrsim F_{ch}$. En este caso, podemos obtener dos estados con la mismas funciones envolventes pero diferente composición de valle y con una separación de la energía dependiente de F.

- Nuestros resultados proporcionan nuevas directrices para el control del grado de libertad de valle, por lo tanto para la manipulación práctica de electrones del donor en nanoestructuras de Si consideradas para computación cuántica.

En está parte hemos presentado que tanto el módulo como la fase del V_{VO}^I afectan claramente el comportamiento de electrones del donor en Si cerca de una intercara. El valor de θ es muy díficil de predecir y su cálculo probablemente requiere conocimiento de la distribución atomística en la intercara y una descripción completa de la estructura electrónica del sistema combinado Si/estructurado intercara/barrera. No está claro si una medida experimental directa es posible. Nosotros proponemos que la medición de los gaps separados puede proporcionar una estimación de θ, tal y como se presenta en el recuadro de la Fig. 8.9.

En años recientes, ha habido un progreso notable de experimentos en la caracterización de estados de donor en nanoestructuras de Si. En la Ref. (173) el transporte a través de un canal con un único donor permitió la identificación del estado fundamental de donores neutrales (D^0) y cargados negativamente (D^-) que están hibridizados con el estado de intercara. Solo muy recientemente se ha logrado (214) la manipulación de electrones del donor entre el donor y una intercara con campo eléctrico. En este caso solo el estado fundamental fue identificado.

Otros experimentos de transporte involucrando dos donores en una nanoestructura de Si (184) han medido la separación entre el estado fundamental y el primer estado excitado en un donor (separación órbita-valle)

Por otra parte, el estudio de la física de valletrónica en Si se ha acelerado recientemente, así como en otros sistema multivalle tales como Grafeno, Germanio y Bismuto destinados para el diseño de la nueva generación de dispositivos electrónicos. Por ejemplo, el grado de libertad de valle en Si es esencial debido a que impone limitaciones a la manipulación del espín y a la coherencia. La degeneración de valle es frecuentemente un problema para cualquier sistema. Sin embargo, si la degeneración se rompe y hay un control apropiado sobre la separación entre los niveles de valle, es posible lograr cierta manipulación de éste e incluso pensar en la posibilidad de codificar información cuántica (152). Además los valles pueden tener una coherencia larga. Por estos motivos, nuestro análisis en profundidad de la evolución de la composición de valle de los principales niveles de energía del electrón de un donor cerca de un sistema Si/Si barrera, cuando un campo eléctrico es aplicado como en la Fig. 8.7 aporta nuevos y valiosos conocimientos relativos a las manipulaciones controladas de valle en dispositivos basados en Si que involucran donores.

Agradecimientos

Este proyecto de tesis ha sido el resultado de varios años de mi vida y se ha hecho una realidad no por mi esfuerzo personal si no gracias al aporte determinante de muchas personas a las cuales quisiera agradecer sinceramente y dedicar este gran logro.

Para empezar quisiera dar las gracias de una manera muy especial a mi directora de tesis María José Calderón. No tengo las palabras suficientes para mencionar lo agradecida y lo afortunada que me siento de haberla tenido como guía en este proceso de crecimiento personal y profesional. Gracias por tu confianza, paciencia y apoyo incondicional, he aprendido inmensamente trabajando a su lado y ha sido para mí un honor haber desarrollado mi proyecto de tesis bajo su dirección.

Durante este proyecto tuve la gran oportunidad de realizar una estancia en Brasil en la Universidad do Rio de Janeiro donde tuve la fortuna de trabajar en colaboración con la Dra Belita Koiller y el Dr André Saraiva. Quiero agradecerles por su hospitalidad y por la gran disposición de instruirme constantemente en el desarrollo del proyecto. Fue definitivamente una experiencia muy positiva en todos los aspecto que fue posible gracias a ellos y varias personas del departamento de fsica dos slidos que me acogieron de la mejor manera y me integraron a su equipo de trabajo.

Así mismo quiero darle las gracias al Dr Luis Brey por sus aportes en la primera parte de este proyecto y a varias personas integrantes del ICMM tanto del personal científico como del administrativo por su apoyo en momentos complicados de mi estadía en Espaa a lo largo de la tesis.

Este proyecto no hubiera sido posible sin el apoyo incondicional de mi familia mis padres Diosdado Baena y Luz Marina Vásquez, mi hermano Juan Sebastian Baena y los dems integrantes de mi familia en Colombia que desde la distancia me acompaaron durante todos los momentos álgidos y me dieron constantemente las palabras de ánimo pertinentes en los momentos que ms las necesitaba. A mi familia en España también les agradezco su disposición de ayudarme y brindarme la mano en todos los momentos para que yo tuviera una estancia agradable y con las mejores condiciones posibles.

A mis amigos mil gracias, no se que haría sin sus aportes, apoyo, confianza, han sido un pilar y un ejemplo para continuar en el camino de la construcción de mi vida en todos los aspectos. Gracias Juan David Oliveros Tamayo por acompañarme en todos y cada uno de los momentos de este proceso, he sido muy afortunada de contar con su compañia lo que hizo muy llevadero los momentos díficiles y muy gratificante el poder compartir los pequeos logros. Jorge Mario Gil quiero agradecerle porque siempre has confiando y creído en mí y desde la distancia estuviste presente y siempre dispuesto a brindarme ayuda para tener una tranquilidad en lo posible durante está étapa de mi vida. Harold Yepes Ramirez colega gracias por todo has sido para mi un ejemplo y por ende un motor para conseguir lo propuesto, compartiendo los logros desde hace muchos años y apoyándonos en todo momento de los proyectos profesionales. Por supuesto quiero agradecer a mis primas Yuliana María Lopez y Paola Andrea Tabares las que son mis mejores amigas, por siempre estar allí y brindarme constantemente el apoyo incondicional. A Fabian Andrés Cuellar muchas gracias por colaborarme en varios momentos de la culminación de este proyecto y durante el desarrollo del mismo.

Aunque no estaban cerca quiero agradecer a Alexander Ruden Muños y a Liliam Cristina Agudelo por las energías positivas que desde Colombia siempre me han aportado en todas las etapas de mi construcción profesional. A los colegas del ICMM que hicieron durante mi estadía un momento muy agradable, compartiendo las experiencias y aprendiendo en conjunto como llevar a cabo las gestiones que garantizaban nuestra calidad de vida aquí en España. Gracias a muchas más personas que aunque no he nombrado me aportaron y me acompañaron de alguna manera, lo que con toda seguridad ha sido determinante para alcanzar este gran logro en mi vida.

References

[1] JOHN S. COLLIGON. **Chapter 9 Physical vapor deposition**. In C. SURYANARAYANA, editor, *Non-equilibrium Processing of Materials*, **2** of *Pergamon Materials Series*, page 225. Pergamon, 1999. 1, 157

[2] S G DAVISON AND M STESLICKA. **Relativistic theory of Tamm surface states**. 1

[3] M. K. WU, J. R. ASHBURN, C. J. TORNG, P. H. HOR, R. L. MENG, L. GAO, Z. J. HUANG, Y. Q. WANG, AND C. W. CHU. **Superconductivity at 93 K in a new mixed-phase Y-Ba-Cu-O compound system at ambient pressure**. *Phys. Rev. Lett.*, **58**:908, 1987. 1, 158

[4] Y. TOKURA. *Colossal magnetoresistance oxides.* Gordon & Breach Monographs in Condensed Matter Science, London, 1999. 1, 19, 185

[5] T. KOIDA, M. LIPPMAA, T. FUKUMURA, K. ITAKA, Y. MATSUMOTO, M. KAWASAKI, AND H. KOINUMA. **Effect of A-site cation ordering on the magnetoelectric properties in** $[(LaMnO3)m/(SrMnO3)m]n$ **artificial superlattices**. *Phys. Rev. B*, **66**:144418, 2002. 2, 43, 158

[6] N. REYREN, S. THIEL, A. D. CAVIGLIA, L. FITTING KOURKOUTIS, G. HAMMERL, C. RICHTER, C. W. SCHNEIDER, T. KOPP, A.-S. RETSCHI, D. JACCARD, M. GABAY, D. A. MULLER, J.-M. TRISCONE, AND J. MANNHART. **Superconducting Interfaces Between Insulating Oxides**. *Science*, **317**:1196, 2007. 2, 14, 158

[7] L FITTING KOURKOUTIS AT BOLLINGER LA GIANNUZZI DA MULLER I BOZOVIC A GOZAR, G LOGVENOV. **High-temperature interface superconductivity between metallic and insulating copper oxides**. *Nature*, **455**:782, 2008. 2, 158

[8] STUCKI N LICHTENSTEIGER C HERMET P BOUSQUET E, DAWBER M. **Improper ferroelectricity in perovskite oxide artificial superlattices**. *Nature*, **452**:732, 2008. 2, 158

[9] **Technology and Research** [online]. 2011. 3, 86

[10] Billman C.A. McKee R.A. Hyunsang Hwang Walker, F.J. **Electrical Characteristics of Epitaxially Grown $SrTiO_3$ on Silicon for Metal-Insulator-Semiconductor Gate Dielectric Applications**. *Electron Device Letters, IEEE*, **24**:218, 2003. 3

[11] S. Mahapatra H. Ryu S. Lee O. Warschkow L. C. L. Hollenberg G. Klimeck M. Fuechsle, J. A. Miwa and M. Y. Simmons. **A single-atom transistor**. *Nature Nanotechnology*, **7**:242, 2012. 3, 97, 110, 111, 159

[12] B. E. Kane. **A Silicon Based nuclear spin quantum computer**. *Nature*, **393**:133, 1998. 4, 85, 87, 95, 118, 168, 169

[13] M. J. Calderón, Belita Koiller, and S. Das Sarma. **Model of valley interference effects on a donor electron close to a Si/SiO_2 interface**. *Phys. Rev. B*, **77**:155302, 2008. 4, 160

[14] Rajib Rahman, G. P Lansbergen, Seung H Park, J Verduijn, Gerhard Klimeck, S Rogge, and Lloyd C. L Hollenberg. **Orbital Stark effect and quantum confinement transition of donors in silicon**. *Phys. Rev. B*, **80**:165314, 2009. 4, 160

[15] Joerg Heber. **Materials science: Enter the oxides**. **459**, 2009. 7, 15

[16] N. Mott. *Metal-insulator transitions.* Taylor & Francis, London, New York, Philadelphia, 1990. 7

[17] R. von Helmot, J. Wecker, B. Holzapfel, L. Schultz, and K. Samwer. **Giant negative magnetoresistance in perovskite like $La_{2/3}Ba_{1/3}MnO_x$ ferromagnetic films**. **71**:2331, 1993. 7

[18] Y. Tokura. **Correlated-Electron Physics in Transition-Metal Oxides**. *Phys. Today*, page 50, 2003. 8, 9, 10, 12

[19] Y. Tokura and N. Nagaosa. **Strain vs OO**. *Science*, **288**:462, 2000. 9, 10, 16, 27, 41, 48, 63, 64, 66, 163, 165, 166

[20] E. Dagotto. **Complexity in Strongly Correlated Electronic Systems**. *Science*, page 8, 2005. 9, 13

[21] M. N. Iliev, A. P. Litvinchuk, M. V. Abrashev, V. N. Popov, J. Cmaidalka, B. Lorenz, and R. L. Meng. **Phonons and magnetic excitations in the Mott insulator $LaTiO_3$**. *Phys. Rev. B*, **69**:172301, 2004. 11

[22] Masahito Mochizuki and Masatoshi Imada. **Orbital physics in the perovskite Ti oxides**. *New Journal of Physics*, **6**:154, 2004. 11

[23] S. Nakatsuji and Y. Maeno. **Quasi-Two-Dimensional Mott Transition System $\mathbf{Ca_{2-x}Sr_xRuO_4}$**. *Phys. Rev. Lett.*, **84**:2666, 2000. 11, 13

[24] A. Ohtomo, D.A. Muller, J.L Grazul, and H.Y. Hwang. **Artificial charge modulation in atomic scale perovskite titanate superlattices**. *Nature*, **419**(378), 2002. 14, 15, 24

[25] Mark Huijben, Guus Rijnders, Dave H. A. Blank, Sara Bals, Sandra Van Aert, Jo Verbeeck, Gustaaf Van Tendeloo, Alexander Brinkman, and Hans Hilgenkamp. **Electronically coupled complementary interfaces between perovskite band insulators**. *Nature Materials*, **5**:556, 2006. 14

[26] A. Schmehl C. W. Schneider S. Thiel, G. Hammerl and J. Mannhart. **Tunable Quasi-Two-Dimensional Electron Gases in Oxide Heterostructures**. **29**:5353, 2006. 14

[27] Harold Y. Hwang Naoyuki Nakagawa and David A. Muller. **Why some interfaces cannot be sharp**. 14

[28] R. Pentcheva and W. E. Pickett. **Charge localization or itineracy at $\mathbf{LaAlO_3/SrTiO_3}$: Hole polarons, oxygen vacancies, and mobile electrons**. *Phys. Rev. B*, **74**:035112, 2006. 14

[29] Wolter Siemons, Gertjan Koster, Hideki Yamamoto, Walter A. Harrison, Gerald Lucovsky, Theodore H. Geballe, Dave H. A. Blank, and Malcolm R. Beasley. **Origin of Charge Density at $\mathbf{LaAlO_3}$ on $\mathbf{SrTiO_3}$ Heterointerfaces: Possibility of Intrinsic Doping**. *Phys. Rev. Lett.*, **98**:196802, 2007. 14

[30] G. Herranz, M. Basletić, M. Bibes, C. Carrétéro, E. Tafra, E. Jacquet, K. Bouzehouane, C. Deranlot, A. Hamzić, J.-M. Broto, A. Barthélémy, and A. Fert. **High Mobility in $\mathbf{LaAlO_3/SrTiO_3}$ Heterostructures: Origin, Dimensionality, and Perspectives**. *Phys. Rev. Lett.*, **98**:216803, 2007. 14

[31] S. Okamoto, A.J. Millis, and N.A. Spaldin. **Lattice relaxation in oxide heterostructures:$\mathbf{LaTiO_3/SrTiO_3}$ superlattices**. 14

[32] S. Okamoto and A.J. Millis. **Electronic reconstruction at an interface between a Mott insulator and a band insulator**. *Nature*, **428**:630, 2004. 14, 23

[33] A. Ohtomo. and H. Y. Hwang. **A high-mobility electron gas at the $\mathbf{LaAlO_3/SrTiO_3}$ heterointerface**. *Nature*, **427**(423), 2004. 14, 24

[34] A. Brinkman, M. Huijben, M. van Zalk, J. Huijben, U. Zeitler, J. C. Maan, W. G. van der Wiel, G. Rijnders, D. H. A. Blank, and H. Hilgenkamp. **Magnetic effects at the interface between non-magnetic oxides**. *Nature Materiales*, **6**:493, 2007. 14

[35] A. Hoffmann, S. G. E. te Velthuis, Z. Sefrioui, J. Santamar´, M. R. Fitzsimmons, S. Park, and M. Varela. **Suppressed magnetization in $La_{0.7}Ca_{0.3}MnO_3/YBa_2Cu_3O_{7-\delta}$ superlattices**. *Phys. Rev. B*, **72**:140407, 2005. 14

[36] J. Chakhalian, J. W. Freeland, H.-U. Habermeier, G. Cristiani, G. Khaliullin, M. van Veenendaal, and B. Keimer. **Orbital Reconstruction and Covalent Bonding at an Oxide Interface**. *Science*, **318**, 2007. 14, 55

[37] S. Jin, T.H. Tiefel, M. McCormack, R.A. Fastnacht, R. Ramesh, and J.H. Chen. **Thousandfold change in resistivity in magnetoresistive La-Ca-Mn-O films**. *Science*, **264**:413, 1994. 15, 21

[38] M. Bibes and A. Barthélémy. **Oxide Spintronics**. *IEEE Trans. Electron. Devices*, **54**:1003, 2007. 16

[39] C. Hilla Bog-Gi Kimb S.W. Cheongb R.L. Greene V.N. Smolyaninova, Amlan Biswasa. **Charge order to two-dimensional metal crossover in $Pr_{0.5}(Sr_{1-y}Ca y)_{0.5}MnO_3$**. *JMMM*, **267**(300), 2003. 16

[40] C.H. Chen and S.-W. Cheong. **Commensurate to incommensurate Charge ordering and its real-space images in $La_{1/2}$ $Ca_{1/2}$ $Mn0_3$**. 16

[41] Y. Tomioka, A. Asamitsu, Y. Moritomo, H. Kuwahara, and Y. Tokura. **Collapse of a Charge-Ordered State under a Magnetic Field in $Pr_{1/2}Sr_{1/2}MnO_3$**. *Phys. Rev. Lett.*, **74**:5108, 1995. 16

[42] H. Kawano, R. Kajimoto, H. Yoshizawa, Y. Tomioka, H. Kuwahara, and Y. Tokura. **Magnetic Ordering and Relation to the Metal-Insulator Transition in $Pr_{1-x}Sr_xMnO_3$ and $Nd_{1-x}Sr_xMnO_3$ with $x \sim 1/2$**. *Phys. Rev. Lett.*, **78**:4253, 1997. 16

[43] R. Kajimoto, H. Yoshizawa, Y. Tomioka, and Y. Tokura. **Stripe-type charge ordering in the metallic A-type antiferromagnet $Pr_{0.5}Sr_{0.5}MnO_3$**. *Phys. Rev. B*, **66**:180402, 2002. 16, 17, 28, 33

[44] G.H. Jonker and J.H. van Santem. **Ferromagnetic compounds of manganese with perovskite structure**. *Physica*, **16**:337, 1950. 16, 17

[45] J.H. van Santen G.H. Jonker. **Electrical conductivity of ferromagnetic compounds of manganese with perovskite structure**. **577**:3580, 1950. 16, 21

[46] E. Dagotto. *Nanoscale Phase Separation and Colossal Magnetoresistance*. Springer-Verlag, Berlin, 2003. 18, 19, 21, 37

[47] E. D. Wollan and W. C. Koehler. **Neutron diffraction study of the magnetic properties of the series of perovskite type compounds $[_{(}1-x)$La, $_x$Ca] MnO_3**. 18

[48] C. Zener. **Interaction between d shells in the transition metals**. 18

[49] C. Zener. **Interaction between d shells in the transition metals. II. Ferromagnetic compounds of manganese with perovskite structure**. 18, 19, 33

[50] Y. Okimoto, T. Katsufuji, T. Ishikawa, A. Urushibara, T. Arima, and Y. Tokura. **Anomalous Variation of Optical Spectra with Spin Polarization in Double-Exchange Ferromagnet: $\mathbf{La_{1-x}Sr_xMnO_3}$**. *Phys. Rev. Lett.*, **75**:109, 1995. 19

[51] P.-G. de Gennes. **Effects of double exchange in magnetic crystals**. 19

[52] P.W. Anderson and H. Hasewaga. **Considerations on Double Exchange**. 19, 34

[53] V. Martin-Mayor J.A. Verges and L. Brey. **Lattice-Spin mechanism in colossal magnetoresistive mangaites**. 19, 20, 38

[54] M. J. Calderón, L. Brey, and F. Guinea. **Surface electronic structure and magnetic properties of doped manganites**. 19, 24, 26, 40, 58, 65, 164

[55] J. L. Alonso, J. A. Capitán, L. A. Fernández, F. Guinea, and V. Martín-Mayor. **Monte Carlo determination of the phase diagram of the double-exchange model**. 19, 40

[56] J. van den Brink, G. Khaliullin, and D. Khomskii. **Charge and orbital order in half-doped manganites**. 20

[57] Luis Brey. **Phase diagram of half doped manganites**. *Phys. Rev. B*, **71**:174426, 2005. 20, 45

[58] H. Aliaga, D. Magnoux, A. Moreo, D. Poilblanc, S. Yunoki, and E. Dagotto. **Theoretical study of half-doped models for manganites: Fragility of CE phase with disorder, two types of colossal magnetoresistance, and charge-ordered states for electron-doped materials**. *Phys. Rev. B*, **68**:104405. 20, 38

[59] J. Fontcuberta, B. Martínez, A. Seffar, S. Pi nol, J.L. García-Mu noz, and X. Obradors. **Colossal Magnetoresistance of Ferromagnetic Manganites: Structural Tuning and Mechanisms**. 20

[60] Peter Senn. **A simple quantum mechanical model that illustrates the Jahn-Teller effect**. 20

[61] J. Kanamori. **Crystal distortion in magnetic compounds**. 21, 37

[62] Elbio Dagotto, Takashi Hotta, and Adriana Moreo. **Colossal Magnetoresistant Materials: The Key Role of Phase Separation**. *cond-mat/0012117. To appear in Physics Reports*, 2001. 22, 39

[63] M. Bibes, S. Valencia, Ll. Balcells, B. Mart´, J. Fontcuberta, M. Wojcik, S. Nadolski, and E. Jedryka. **Charge trapping in optimally doped epitaxial manganite thin films**. *Phys. Rev. B*, **66**:134416, 2002. 22

[64] Llibertat Abad, Vladimir Laukhin, Sergio Valencia, Andreas Gaup, Wolfgan Gudat, Lluis Balcells, and Benjamin Martnez. **Interfacial Strain: The Driving Force for Selective Orbital Occupancy in Manganite Thin Films**. *Advanced Functional Materials*, **17**, 2007. 22, 27, 48, 58, 63, 66, 163, 166

[65] W.; Ulrich B.D.; Lee-J.J.; Stecker L.; Burmaster A.; Evans D.R.; Hsu S.T.; Tajiri M.; Shimaoka A.; Inoue K.; Naka T.; Awaya N.; Sakiyama A.; Wang Y.; Liu S.Q.; Wu N.J.; Ignatiev A. Zhuang, W.W.; Pan. **Novel colossal magnetoresistive thin film nonvolatile resistance random access memory (RRAM)**. 22

[66] Shinji Kobayashi Yukio Tamai Nobuyoshi Awaya et al. Masayuki Fujimoto, Hiroshi Koyama. **Resistivity and resistive switching properties of $\mathbf{Pr_{0.7}Ca_{0.3}MnO_3}$ thin films**. 23

[67] Patrick R. Mickel Kristen Voigt Chelsey Morien et al. Hyoungjeen Jeen, Guneeta Singh-Bhalla. **Growth and characterization of multiferroic $\mathbf{BiMnO_3}$ thin films**. 23

[68] Stphane Fusil Karim Bouzehouane Josep Fontcuberta Agnes Barthemy Albert Fert Martin Gajek, Manuel Bibes. **Tunnel junctions with multiferroic barriers**. *Nature Materials*, **6**:296, 2007. 23

[69] Eric Langenberg Norbert M. Nemes Carmen Munuera Manuel Varela Mar Garcia-Hernandez Carlos Leon Rainer Schmidt, Jofre Ventura and Jacobo Santamaria. **Magnetoimpedance spectroscopy of epitaxial multiferroic thin films**. 23

[70] L. Brey. **Electronic phase separation in manganite-insulator interfaces**. **75**:104423, 2007. 23, 24, 43, 50, 53, 54, 60

[71] M. J. Calderón, J. Salafranca, and L. Brey. **Electron gas at the interface between two antiferromagnetic insulating manganites**. *Phys. Rev. B*, **78**:024415, 2008. 23, 43, 60, 126, 151, 152, 169, 170, 171

[72] M. Julliere. **Tunneling between ferromagnetic films**. *Physics Letters A*, **54**(3):225, 1975. 24

[73] M.-H. Jo, N. D. Mathur, N.K. Todd, and M. G. Blamire. **Very large magnetoresistance and coherent switching in half-metallic manganite tunnel junctions**. 25

[74] J.-H. Park, E. Vescovo, H.-J. Kim, C. Kwon, R. Ramesh, and T.Venkatesan. **Magnetic properties at surface boundary of a half-metallic ferromagnet $La_{0.7}Sr_{0.3}MnO_3$**. 24

[75] P. LeClair, H. J. M. Swagten, J. T. Kohlhepp, R. J. M. van de Veerdonk, and W. J. M. de Jonge. **Apparent Spin Polarization Decay in Cu-Dusted Co/Al_2O_3/Co Tunnel Junctions**. *Phys. Rev. Lett.*, **84**:2933, 2000. 24

[76] M. B. Salamon D. Niebieskikwiat, L. E. Hueso and N. D. Mathur. **Effect of ferromagnetic/antiferromagnetic interfaces on the magnetic properties of La2/3Sr1/3MnO3/Pr2/3Ca1/3MnO3 superlattices**. 26

[77] M.J. Calderon K. March C. Carretero M. Walls A. Rivera-Calzada-C. Leon R. Lopez Anton T. R. Charlton D. Imhoff L. Brey M. Bibes J.Santamaria Z. Sefrioui, C. Visani and A. Barthelemy. **All-Manganite Tunnel Junctions with Interface-Induced Barrier Magnetism**. 26

[78] S. Sanna P. G. Medaglia A. Tebano, C. Aruta and G. Balestrino. **Evidence of Orbital Reconstruction at Interfaces in Ultrathin $La_{0.67}Sr_{0.33}MnO_3$ Films**. *Phys. Rev. Lett*, **100**(137401), 2008. 26, 29

[79] F.Y. Bruno P. Thakur N.B. Brookes C. Utfeld A. Rivera-Calzada S.R. Giblin J.W. Taylor J.A. Duffy S.B. Dugdale T. Nakamura K. Kodama C. Leon S. Okamoto J. Garcia-Barriocanal, J.C. Cezar and J. Santamaria. **Spin and orbital Ti magnetism at $LaMnO_3$/$SrTiO_3$ interfaces**. 26

[80] H. Yamada, M. Kawasaki, T. Lottermoser, T. Arima, and Y. Tokura. **$LaMnO_3$/$SrMnO_3$ interfaces with coupled charge-spin-orbital modulation**. 27, 41, 64, 66, 163, 165

[81] C. Adamo, X. Ke, H. Q. Wang, H. L. Xin, T. Heeg, M. E. Hawley, W. Zander, J. Schubert, P. Schiffer, D. A. Muller, L. Maritato, and D. G. Schlom. **Effect of biaxial strain on the electrical and magnetic properties of (001) $La_{0.7}Sr_{0.3}MnO_3$ thin films**. 27, 41, 63, 163

[82] B. R. K. Nanda and S. Satpathy. **Magnetic and orbital order in $LaMnO_3$ under uniaxial strain: A model study**. *Phys. Rev. B*, **81**:174423, 2010. 27, 64, 66, 163, 166

[83] M. McCormack H. M. OBryan L. H. Chen et al. S. Jin, T. H. Tiefel. **Thickness dependence of magnetoresistance in La-Ca-Mn-O epitaxial films**. *Appl. Phys. Lett.*, **67**:557, 1995. 27

[84] P. G. Medaglia A. Tebano, A. Orsini and G. Balestrino. **Disentangling strain effects in manganite heterostructures**. *Appl. Phys. Lett.*, **94**(242503), 2009. 27, 64, 66, 163, 165

[85] J. Z. Sun, D. W. Abraham, R. A. Rao, and C. B. Eom. **Thickness dependent magnetotransport in ultra-thin manganite films**. 27, 28, 64, 164

[86] J. Zhang et al. **Strain effect and the phase diagram of $La_{1-x}Ba_xMnO_3$ thin films**. *Phys. Rev. B*, **64**(184404), 2001. 27

[87] J. H. Song, J.H. Park, K.B. Lee, J.M. Lee, and Y.H. Jeong. **Cooperative Jahn-Teller transition and resonant x-ray scattering in thin film $LaMnO_3$**. *Phys. Rev. B*, **66**(020407), 2002. 27

[88] V. G. Sathe Aditi Dubey and R. Rawat. **Signature of Jahn-Teller distortion and oxygen stoichiometry in Raman spectra of epitaxial $LaMnO_{3+}\ \delta$ thin films**. *J. Appl. Phys.*, **104**(113530), 2008. 27

[89] A. J. Millis, T. Darling, and A. Migliori. **Quantifying strain dependence in colossal magnetoresistance manganites**. 27, 41, 64, 66, 164, 166

[90] Aymeric Sadoc, Bernard Mercey, Charles Simon, Dominique Grebille, Wilfrid Prellier, and Marie-Bernadette Lepetit. **Large Increase of the Curie Temperature by Orbital Ordering Control**. *Phys. Rev. Lett.*, **104**:046804, 2010. 27, 41, 48, 63, 66, 163, 165, 166

[91] Yunoki Seiji Zhang Xiaotian Sen Cengiz Liu J.-M. Dong, Shuai and Elbio Dagotto. **Highly anisotropic resistivities in the double-exchange model for strained manganites**. *Phys. Rev. B*, **82**:035118, 2010. 27, 66, 166

[92] Yubin Ma Guijun Lian Yan Zhang Guangcheng Xiong Liping Chen, YuanshaChen. **Strain-stabilized charge ordering and magnetorelaxor behaviors in Cr-doped $Pr_{0.5}Ca_{0.5}MnO_3$ epitaxial thin films**. **324**:1189, 2012. 28

[93] N. G. Boggio P. G. Medaglia P. Orgiani et al. M. Angeloni, G. Balestrino. **Suppression of the metal-insulator transition temperature in thin $La_{0.7}Sr_{0.3}MnO_3$ films**. 28, 29, 64, 66, 164, 165

[94] Nandini Trivedi Mohit Randeria Patrick Woodward Anamitra Mukherjee, William S. Cole. **Strain controlled colossal magnetoresistance in manganite thin films**. 2012. arXiv:1209.6174. 29, 66, 165

[95] I.C. Infante, S. Estradé, F. Sánchez, J. Arbiol, F. Peiró, V. Laukhin, J. P. Espinós, M. Wojcik, E. Jedryka, and J. Fontcuberta. **Strain-driven competition between elastic and orbital ordering effects on thickness-dependent properties of manganites thin films**. 30, 64, 66, 163, 165

[96] E. Müller-Hartmann and E. Dagotto. **Electronic Hamiltonian for transition-metal oxide compound**. 34

[97] J.B.Goodenough. **Theory of the Role of covalency in the perovskite-tyoe manganites [La, M(II)]MnO$_3$**. 34

[98] A. Urushibara, Y. Moritomo, T. Arima, A. Asamitsu, G. Kido, and Y. Tokura. **Insulator-metal transition and giant magnetoresistance in La$_{1-x}$Sr$_x$MnO$_3$**. 34, 39

[99] J. C. Slater and G. F. Koster. **Simplified LCAO Method for the Periodic Potential Problem**. *Phys. Rev.*, **94**:1498, 1954. 36

[100] Y. Tokura. **Fundamental features of colossal magnetoresistance manganese oxides**. 1999. in (4). 39

[101] A.P. Ramirez. **Colossal magnetoresistance. 9**:8171, 1997. 39, 40

[102] T.G. Perring, G. Aeppli, Y. Moritomo, and Y. Tokura. **Antiferromagnetic Short Range Order in a Two-Dimensional Manganite Exhibiting Giant Magnetoresistance**. 39

[103] K. Ahn and A.J. Millis. **Interplay of charge and orbital ordering in manganese perovskites**. 40

[104] Luis Brey. **Continuous Charge Modulated Diagonal Phase in Manganites**. 2004. 40

[105] B. R. K. Nanda and Sashi Satpathy. **Effects of strain on orbital ordering and magnetism at perovskite oxide interfaces: LaMnO$_3$ / SrMnO$_3$**. *Phys. Rev. B*, **78**:054427, 2008. 41, 42, 63, 64, 163

[106] K. H. Ahn and A. J. Millis. **Effects of uniaxial strain in** $LaMnO_3$. *Phys. Rev. B*, **64**:115103, 2001. 41

[107] W.A. Harrison. *Electronic Structure and the Properties of Solids: The Physics of the Chemical Bond*. Dover Publications Inc, New York, 1989. 41

[108] J. Salafranca, M. J. Calderón, and L. Brey. **Magnetoresistance of an all-manganite spin-valve: A thin antiferromagnetic insulator sandwiched between two ferromagnetic metallic electrodes**. 2008. 43

[109] Chungwei Lin, Satoshi Okamoto, and Andrew J. Millis. **Dynamical mean-field study of model double-exchange superlattices**. page 041104, 2006. 43

[110] B. R. K. Nanda and Sashi Satpathy. **Polar catastrophe, electron leakage, and magnetic ordering at the LaMnO$_3$/SrMnO$_3$ interface**. *Phys. Rev. B*, **81**:224408, 2010. 48

[111] Satoshi Okamoto. **Magnetic interaction at an interface between manganite and other transition metal oxides**. *Phys. Rev. B*, **82**:024427, 2010. 58, 65, 164

[112] P. Yu, J.-S. Lee, S. Okamoto, M. D. Rossell, M. Huijben, C.-H. Yang, Q. He, J. X. Zhang, S. Y. Yang, M. J. Lee, Q. M. Ramasse, R. Erni, Y.-H. Chu, D. A. Arena, C.-C. Kao, L. W. Martin, and R. Ramesh. **Interface Ferromagnetism and Orbital Reconstruction in** $BiFeO_3-La_{0.7}Sr_{0.3}MnO_3$ **Heterostructures**. *Phys. Rev. Lett.*, **105**:027201, 2010. 58

[113] G. Milward, M. J. Calderón, and P. B. Littlewood. **Electronically soft phases in manganites**. *Nature (London)*, **433**:607, 2005. 60

[114] I. C. Infante, F. Sánchez, J. Fontcuberta, M. Wojcik, E. Jedryka, S. Estradé, F. Peiró, J. Arbiol, V. Laukhin, and J. P. Espinós. **Elastic and orbital effects on thickness-dependent properties of manganite thin films**. *Phys. Rev. B*, **76**:224415, 2007. 63, 163

[115] A.J. Millis. **Cooperative Jahn-Teller effect and electron-phonon coupling in** $La_{1-x}A_xMn\ O_3$. 64

[116] Chunlan Ma, Zhongqin Yang, and Silvia Picozzi. **Ab initio electronic and magnetic structure in** $La_{0.66}Sr_{0.33}MnO_3$**: strain and correlation effects**. **18**, 2006. 64, 163

[117] H. J. Xiang X. Z. Lu, X. G. Gong. **High Temperature Ferromagnetic-Ferroelectric Multiferroicity in Strained** $BiMnO_3$. *cond-mat/1301.3660*, 2013. 66, 166

[118] I. C. Tung M. Kareev Jian Liu D. J. Meyers M. J. Bedzyk J. W. Freeland J. Chakhalian B. A. Gray, E. J. Moon. **Enhanced Spin and Electronic Reconstructions at the Cuprate-Manganite Interface**. *cond-mat/1301.3736*, 2013. 66, 166

[119] R.P Feynman. **Simulating physics with computers**. *International Journal of Theoretical Physics*, **21**:467, 1982. 73, 80

[120] Charles H. Bennett, Gilles Brassard, Claude Crépeau, Richard Jozsa, Asher Peres, and William K. Wootters. **Teleporting an unknown quantum state via dual classical and Einstein-Podolsky-Rosen channels**. *Phys. Rev. Lett.*, **70**:1895, 1993. 77

[121] Aram Harrow, Patrick Hayden, and Debbie Leung. **Superdense Coding of Quantum States**. *Phys. Rev. Lett.*, **92**:187901, 2004. 77

[122] M. A. Nielsen and I. L. Chuang. *Quantum Computation and Quantum Information.* Cambridge University Press, Cambridge, 2000. 77, 78, 81, 82

[123] J. L. Brylinski and R. Brylinski. **Universal Quantum Gates**. *Mathematics of Quantum Computation*, 2002. 79

[124] Leonard M. Adleman Ronald L. Rivest, Adi Shamir. **A Method for Obtaining Digital Signatures and Public-Key Cryptosystem**. *Communications of the ACM*, **21**:120, 1978. 79

[125] P.W Shor. *SIAM J.Sci.Statist.Comput*, **26**:1484, 1997. 80

[126] David Biron, Ofer Biham, Eli Biham, Markus Grassl, and Daniel A. Lidar. **Generalized Grover Search Algorithm for Arbitrary Initial Amplitude Distribution**. *Selected papers from the First NASA International Conference on Quantum Computing and Quantum Communications*, **QCQC** '98:140, 1998. 80

[127] A.M Turing. *Proc. Lond. Math. Soc. Ser.* 2, **42**:230, 1936. 80

[128] Loss and DiVicenzo. **Quantum Computation with Quantum Dots**. *Phys.Rev.A*, **57**:120, 1998. 82, 84, 85, 168

[129] Thomas Monz, Philipp Schindler, Julio T. Barreiro, Michael Chwalla, and Nigg. 14**-Qubit Entanglement: Creation and Coherence**. 83

[130] Gregory Breyta Costantino S. Yannoni Mark H. Sherwood Lieven M. K. Vandersypen, Matthias Steffen and Isaac L. Chuang. *Nature*, **414**:883, 2001. 83

[131] R. Laflamme E. Knill and G. J. Milburn. **A scheme for efficient quantum computation with linear optics**. *Nature*, **409**:46, 2001. 83

[132] J. Clarke and F.K Wilhelm. **Superconducting quantum bits**. *Nature*, **453**:1031, 2008. 84

[133] F. Jelezko T. Gaebal I. Popa A. Gruber J. Wrachtrup A. P. Nizovtsev, S. Ya. Kilin. **A quantum computer based on NV centers in diamond: Optically detected nutations of single electron and nuclear spins**. *Optics and Spectroscopy*, **99**:233, 2005. 84

[134] Mark A. Eriksson, Mark Friesen, Susan N. Coppersmith, Robert Joynt, Levente J. Klein, Keith Slinker, Charles Tahan, P. M. Mooney, J. O. Chu, and S. J. Koester. **Spin-Based Quantum Dot Quantum Computing in Silicon**. *Quantum Information Processing*, **3**:133, 2004. 84

[135] M. Yanchenko L. Fedichkin and K.A. Valiev. **Novel coherent quantum bit using spatial quantization levels in semiconductor quantum dot**. *Quantum Computers and Computing*, **1**:58, 2000. 85

[136] L. C. L. Hollenberg, A. S. Dzurak, C. Wellard, A. R. Hamilton, D. J. Reilly, G. J. Milburn, and R. G. Clark. **Charge-based quantum computing using single donors in semiconductors**. *Phys. Rev. B*, **69**:113301, 2004. 85

[137] G. Raymond P. Grangier and N. Schlosser. **Implementations of Quantum Computing Using Cavitity Quantum Electrodynamics Schemes**. *Fortschr.Phys.*, **48**:859, 2000. 85

[138] N. Ohlsson, R. Krishna Mohan, and S. Kroll. **Quantum computer hardware based on rare-earth-ion-doped inorganic crystals**. *Optics Communication*, **201**:71, 2002. 85

[139] W. Harneit. **Fullerene-based-electron-spin quantum computer**. *Phys.Rev.A*, **65**:03322, 2002. 85

[140] J. Elzerman, R. Hanson, L. H. Willems van Beveren, B. Witkamp, L. M. K. Vandersypen, and L. P. Kouwenhoven. **Single-shot read-out of an individual electron spin in a quantum dot**. *Nature*, **430**:431, 2004. 85, 168

[141] F. H. L. Koppens, J. A. Folk, J. M. Elzerman, R. Hanson, L. H. Willems van Beveren, I. T. Vink, H. P. Tranitz, W. Wegscheider, L. P. Kouwenhoven, and L. M. K. Vandersypen. **Control and Detection of Singlet-Triplet Mixing in a Random Nuclear Field**. *Science*, **309**:1346, 2005. 85, 115, 168

[142] J. R. Petta, A. C. Johnson, J. M. Taylor, E. A. Laird, A. Yacoby, M. D. Lukin, C. M. Marcus, M. P. Hanson, and A. C. Gossard. **Coherent Manipulation of Coupled Electron Spins in Semiconductor Quantum Dots**. *Science*, **309**:2180, 2005. 85, 86, 168

[143] D. Loss and D. P. DiVincenzo. **Quantum computation with quantum dots**. *Phys. Rev. A*, **57**:120, 1998. 86, 168

[144] A. C. Johnson, J. R. Petta, J. M. Taylor, A. Yacoby, M. D. Lukin, C. M. Marcus, M. P. Hanson, and A. C. Gossard. **Triplet-singlet spin relaxation via nuclei in a double quantum dot**. *Nature*, **435**:925, 2005. 86

[145] R. Hanson, L. P. Kouwenhoven, J. R. Petta, S. Tarucha, and L. M. K. Vandersypen. **Spins in few-electron quantum dots**. *Rev. Mod. Phys.*, **79**:1217, 2007. 86

[146] M. Friesen, P. Rugheimer, D. E. Savage, M. G. Legally, D. W. van der Weide, and R. Joynt. **Practical design and simulation of silicon-based quantum-dot qubits**. *Phys. Rev. B*, **67**:121301, 2003. 86, 118, 169

[147] S. Das Sarma, R. de Sousa, X. Hu, and B. Koiller. **Spin quantum computation in silicon nanostructures**. *Solid State Communications*, **133**:737, 2004. 86, 169

[148] R. Vrijen, E. Yablonovitch, K. Wang, H-W Jiang, A. Balandin, V. Roychowdhury, Tal Mor, and D. DiVincenzo. **Electron-spin-resonance transistors for quantum computing in silicon-germanium heterostructures**. *Phys. Rev. A*, **62**:012306, 2000. 86, 169

[149] John J. L. Morton Helge Riemann Nikolai V. Abrosimov Peter Becker Hans-Joachim Pohl Thomas Schenkel Michael L.W. Thewalt Kohei M. Itoh Alexei M. Tyryshkin, Shinichi Tojo and S. A. Lyon. **Electron spin coherence exceeding seconds in high-purity silicon**. *Nature Materials*, **11**:143, 2012. 87, 100, 168

[150] A. ; Tonello S. ; McNamara P. ; Lucherini S. ; Minehane-S. ; Dolainsky C. ; Quarantelli M. Hess C.Karbasi, H. ; Rossoni. **Variation in Transistor Performance and Leakage in Nanometer-Scale Technologies**. *Electron Devices, IEEE Transactions on*, **55**:131, 2008. 87

[151] T. Shinada, S. Okamoto, T. Kobayashi, and I. Ohdomari. **Enhancing semiconductor device performance using ordered dopant arrays**. *Nature*, **437**:1128, 2005. 87, 88

[152] Dimitrie Culcer, A. L. Saraiva, Belita Koiller, Xuedong Hu, and S. Das Sarma. **Valley-Based Noise-Resistant Quantum Computation Using Si Quantum Dots**. *Phys. Rev. Lett.*, **108**:126804, 2012. 87, 102, 124, 152, 154, 173

[153] W. Kohn. *Solid State Physics Series*, **5**. Academic Press, 1957. edited by F. Seitz and D. Turnbull. 88

[154] J. Herbsommer S.J Burden P.L Gammel I.C Kizilyalli, H. Safar. **Power transistors fabricated using isotopically purified silicon (^{2}8Si)**. *Electron Device Letters IEEE*, **26**:404, 2005. 89

[155] Andrew Dzurak Alexander Hamilton Lloyd Hollenberg David Jamieson Robert G. Clark, P. Chris Hammel and Christopher Pakes. **Toward a Silicon-Based Nuclear-Spin Quantum Computer: Developing the Technology for a Scalable, Solid-State**. *Los Alamos, Science*, **27**:284, 2002. 93

[156] Andrea Morello Michelle Y. Simmons Lloyd C. L. Hollenberg Gerhard Klimeck-Sven Rogge Susan N. Coppersmith Mark A. Eriksson Floris A. Zwanenburg, Andrew S. Dzurak. **Silicon Quantum Electronics**. 2012. arXiv:1206.5202. 98, 114

[157] M. Pierre, R. Wacquez, X. Jehl, M. Sanquer, M. Vinet, and O. Cueto. **Single-donor ionization energies in a nanoscale CMOS channel**. *Nature Nanotechnology*, **5**:133, 2010. 97, 103, 105

[158] H. Sellier, G. P. Lansbergen, J. Caro, S. Rogge, N. Collaert, I. Ferain, M. Jurczak, and S. Biesemans. **Transport Spectroscopy of a Single Dopant in a Gated Silicon Nanowire**. *Phys. Rev. Lett.*, **97**:206805, 2006. 97

[159] Andrea Morello, Jarryd J. Pla, Floris A. Zwanenburg, Kok W. Chan, Hans Huebland Mikko Mottonen, Christopher D. Nugroho, Changyi Yang, Jessica A. van Donkelaar, Andrew Alves, David N. Jamieson, Christopher C. Escott, Lloyd C. L. Hollenberg, Robert G. Clark, and Andrew S. Dzurak. **Single-shot readout of an electron spin in silicon**. *Nature*, **467**:687, 2010. 97, 100

[160] Yoshihisa Yamamoto. **Present Status and Future Prospects of Quantum Information Processing: With Special Focus on Optically Controlled Semiconductor Spins and Single-Photon Technologies**. 98

[161] L. M. K. Vandersypen and I. L. Chuang. **NMR techniques for quantum control and computation**. *Rev. Mod. Phys.*, **76**:1037, 2005. 99

[162] R. de Sousa and S. Das Sarma. **Theory of nuclear-induced spectral diffusion: Spin decoherence of phosphorus donors in Si and GaAs quantum dots**. *Phys. Rev. B*, **68**:115322, 2003. 99

[163] W. M. Witzel, Xuedong Hu, and S. Das Sarma. **Decoherence induced by anisotropic hyperfine interaction in Si spin qubits**. *Phys. Rev. B*, **76**:035212, 2007. 99, 100

[164] A. M. Tyryshkin, S. A. Lyon, A. V. Astashkin, and A. M. Raitsimring. **Electron spin relaxation times of phosphorus donors in silicon**. *Phys. Rev. B*, **68**:193207, 2003. 99

[165] Andrea Morello Lukasz Cywinski S. Das Sarma Wayne M. Witzel, Malcolm S. Carroll. **Electron Spin Decoherence in Isotope-Enriched Silicon**. *Phys. Rev. Lett.*, **105**:187602, 2010. 100, 101

[166] Juan P. Dehollain Wee H. Lim John J. L. Morton David N. Jamieson Andrew S. Dzurak Jarryd J. Pla, Kuan Y. Tan and Andrea Morello. **A single-atom electron spin qubit in silicon**. *Nature*, **489**:541, 2012. 100, 101

[167] T. Schenkel, A. M. Tyryshkin, R. de Sousa, K. B. Whaley, J. Bokor, J. A. Liddle, A. Persaud, J. gkuan, I. Chakarov, and S. A. Lyon. **Electrical activation and electron spin coherence of ultra-dose antimony implants in Silicon**. *Appl. Phys. Lett.*, **88**:112101, 2006. 101

[168] S. Shankar, A. M. Tyryshkin, Jianhua He, and S. A. Lyon. **Spin relaxation and coherence times for electrons at the Si/SiO_2 interface**. *Phys. Rev. B*, **82**:195323, 2010. 101, 102

[169] A J Fisher A M Stoneham and P T Greenland. **Optically driven silicon-based quantum gates with potential for high-temperature operation**. *J. Phys.: Condens. Matter*, **15**:L447, 2003. 102

[170] S. A. Lynch A. F. G. Van der Meer B. N. Murdin C. R. Pidgeon B. Redlich N. Q. Vinh Greenland, P. T. and G. Aeppli. **Coherent control of Rydberg states in silicon**. *Nature*, **465**:7301, 2010. 102

[171] K. Litvinenko B. Redlich A. F. G. van der Meer S. A. Lynch M. Warner A. M. Stoneham G. Aeppli D. J. Paul C. R. Pidgeon N. Q. Vinh, P. T. Greenland and B. N. Murdin. **Silicon as a model ion trap: Time domain measurements of donor Rydberg states**. *Proceedings of the National Academy of Sciences*, **31**:10649, 2008. 102

[172] G. P. Lansbergen, R. Rahman, J. Verduijn, G. C. Tettamanzi, N. Collaert, S. Biesemans, G. Klimeck, L. C. L. Hollenberg, and S. Rogge. **Lifetime-Enhanced Transport in Silicon due to Spin and Valley Blockade**. *Phys. Rev. Lett.*, **107**:136602, 2011. 102, 104

[173] G. P. Lansbergen, R. Rahman, C. J. Wellard, I. Woo, J. Caro, N. Collaert, S. Biesemans, G. Klimeck, L. C. L. Hollenberg, and S. Rogge. **Gate-induced quantum-confinement transition of a single dopant atom in a silicon FinFET**. *Nature Physics*, **4**:656, 2008. 103, 104, 105, 107, 137, 154, 172

[174] D.N. Jamieson, C Yang, T Hopf, S.M. Hearne, C.I. Pakes, S. Prawer, M. Mitic, E. Gauja, S.E. Andresen, F.E. Hudson, A.S. Dzurak, and R.G. Clark. **Controlled shallow single-ion implantation in silicon using an active substrate for sub-**20**-keV ions**. 104

[175] T. Schenkel, A. Persaud, S. J. Park, J. Nilsson, J. Bokor, J. A. Liddle, R. Keller, D. H. Schneider, and D. W. Cheng andD. E. Humphries. **Solid state quantum computer development in silicon with single ion implantation**. 104

[176] J. L. O'Brien, S. R. Schofield, M. Y. Simmons, R. G. Clark, A. S. Dzurak, N. J. Curson, B. E. Kane, N. S. McAlpine, M. E. Hawley, and G. W. Brown. 104

[177] Mttnen M Morello A Yang C van Donkelaar J Alves A Pirkkalainen JM Jamieson DN Clark RG Dzurak AS. Tan KY, Chan KW. **Transport spectroscopy of single phosphorus donors in a silicon nanoscale transistor.** *Nano Lett.*, **1**:11, 2010. 104

[178] M. ; Guagliardo F. ; Ferrari G. ; Komatubara A. ; Kumagai K. ; Tanii T. ; Endo T. ; Ono Y. ; Prati E. Shinada, T. ; Hori. **Quantum transport in**

deterministically implanted single-donors in Si FETs. *Electron Devices Meeting (IEDM), 2011 IEEE International*, page 30.4.1, 2011. 105

[179] A. Fujiwara H. Yamaguchi H. Inokawa Y. Ono, K. Nishiguchi and Y. Takahashi. **Conductance modulation by individual acceptors in Si nanoscale field effect transistors**. *Appl. Phys. Lett*, **90**:102106, 2007. 105, 106

[180] X. Jehl M. Sanquer b G. Molas M. Vinet M. Hofheinz, a and S. Deleonibus. **Individual charge traps in silicon nanowires**. *Eur. Phys. J. B*, **54**:299, 2006. 105, 106

[181] H. Sellier, G. P. Lansbergen, J. Caro, S. Rogge, N. Collaert, I. Ferain, M. Jurczak, and S. Biesemans. **Subthreshold channels at the edges of nanoscale triple-gate silicon transistors**. *Appl. Phys. Lett.*, **90**:073502, 2007. 106

[182] M. J. Calderon, Belita Koiller, and S. Das Sarma. **External Field Control of Donor Electron Exchange at the Si/SiO$_2$ Interface**. *Phys. Rev. B*, **75**:125311, 2007. 105, 118, 128, 129, 130, 151, 169

[183] Giuseppe Carlo Tettamanzi Jan Verduijn and Sven Rogge. **Wave Function Control over a Single Donor Atom**. *Nano Lett*, **13**:1476, 2013. 108, 109

[184] B. Roche, E. Dupont-Ferrier, B. Voisin, M. Cobian, X. Jehl, R. Wacquez, M. Vinet, Y.-M. Niquet, and M. Sanquer. **Detection of a Large Valley-Orbit Splitting in Silicon with Two-Donor Spectroscopy**. *Phys. Rev. Lett.*, **108**:206812, 2012. 108, 109, 154, 173

[185] KEJ Goh T Hallam SR Schofield L Oberbeck NJ Curson AR Hamilton MJ Butcher RG Clark TCG Reusch MY Simmons, FJ Ruess. **Scanning probe microscopy for silicon device fabrication**. *Molecular Simulation*, **31**:505, 2005. 110

[186] H. Ryu S. Lee A. Fuhrer T. C. G. Reusch D. L. Thompson W. C. T. Lee G. Klimeck L. C. L. Hollenberg M. Y. Simmons B. Weber, S. Mahapatra. **Ohm's Law Survives to the Atomic Scale**. *Science*, **335**:64, 2012. 110

[187] S. R. Schofield, N. J. Curson, M. Y. Simmons, F. J. Ruess, T. Hallam, L. Oberbeck, and R. G. Clark. **Atomically Precise Placement of Single Dopants in Si**. 110

[188] Jasprit Singh. *Semiconductor devices*. Macgraw Hill, 2002. 114

[189] A. C. Johnson, J. R. Petta, C. M. Marcus, M. P. Hanson, and A. C. Gossard. **Singlet-triplet spin blockade and charge sensing in a few-electron double quantum dot**. *Phys. Rev. B*, **72**:165308, 2005. 115

[190] T.H. Ning and C.T. Sah. **Multivalley effective mass approximation for donor states in Si: shallow levels group V impurities**. *Phys. Rev. B*, **4**:3468, 1971. 115, 116, 117, 133

[191] T.H. Ning and C.T. Sah. **Multivalley effective mass approx for donor states in Si II. Deep level group-VI double donor impurities**. *Phys. Rev. B*, **4**:3482, 1971. 116

[192] A. Baldereschi. **Valley-Orbit Interaction in Semiconductors**. *Phys. Rev. B*, **1**:4673, 1970. 116, 132

[193] S. T. Pantelides. **The electronic structure of impurities and other point defects in semiconductors**. *Rev. Mod. Phys.*, **50**:797, 1978. 116, 132

[194] B. Koiller, X. Hu, and S. Das Sarma. **Strain effects on silicon donor exchange: Quantum computer architecture considerations**. *Phys. Rev. B*, **66**:115201, 2002. 116, 132

[195] H. G. Grimmeiss, E. Janzen, and K. Larsson. **Multivalley spin splitting of 1*s* states for sulfur, selenium, and tellurium donors in silicon**. *Phys. Rev. B*, **25**:2627, 1982. 116

[196] B. Koiller, R. B. Capaz, X. Hu, and S. Das Sarma. **Shallow-donor wave functions and donor-pair exchange in silicon: An initiop theory and floating-phase Heitler-London approach**. *Phys. Rev. B*, **70**:115207, 2004. 116, 117, 118, 152, 171

[197] T. Ando, A. B. Fowler, and F. Stern. **Electronic properties of two-dimensional systems**. *Rev. Mod. Phys.*, **54**:437, 1982. 118, 121, 134

[198] E. Vogt C. Herring. **Transport and deformation-potential theory for many-valley semiconductors with anistropic scattering**. *Phys. Rev.*, **101**:944, 1956. 119

[199] A. L. Saraiva, M. J. Calderon, Xuedong Hu, S. Das Sarma, and Belita Koiller. **Physical mechanisms of interface-mediated intervalley coupling in Si**. *Phys. Rev. B*, page 081305, 2009. 119, 120, 121, 123, 133, 144

[200] S. POLLITT1 C.J. ADKINS and M. PEPPER. **THE ANDERSON TRANSITION IN SILICON INVERSION LAYERS**. 120

[201] L. J. Sham and M. Nakayama. **Effective-mass approximation in the presence of an interface**. *Phys. Rev. B*, **20**:734, 1979. 120, 121, 122, 133, 134, 137, 139

[202] S. Chutia, S.N. Coppersmith, and M. Friesen. **Multiscale theory of valley splitting in the conduction band of a quantum well**. *Phys. Rev. B*, **77**:193311, 2008. 120, 121, 122, 134, 137, 139

[203] A. L. Saraiva, M. J. Calderón, Rodrigo B. Capaz, Xuedong Hu, S. Das Sarma, and Belita Koiller. **Intervalley coupling for interface-bound electrons in silicon: An effective mass study**. *Phys. Rev. B*, **84**:155320, 2011. 120, 121, 122, 123, 133, 152, 170

[204] K. Takashina, Y. Ono, A. Fujiwara, Y. Takahashi, and Y. Hirayama. **Valley Polarization in Si(100) at Zero Magnetic Field**. *Phys. Rev. Lett.*, **96**:236801, 2006. 121, 122

[205] Srijit Goswami, K. A. Slinker, Mark Friesen, L. M. McGuire, J. L. Truitt, Charles Tahan, L. J. Klein, J. O. Chu, P. M. Mooney, D. W. van der Weide, Robert Joynt, S. N. Coppersmith, and Mark A. Eriksson. **Controllable valley splitting in silicon quantum devices**. *Nat. Phys.*, **3**:41, 2007. 121

[206] A. S. Martins, R. B. Capaz, and B. Koiller. **Electric-field control and adiabatic evolution of shallow donor impurities in silicon**. *Phys. Rev. B*, **69**:085320, 2004. 125, 135, 137, 141

[207] D.B. MacMillen and U. Landman. **Variational solutions of simple quantum systems subject to variable boundary conditions. II**. *Phys. Rev. B*, **29**:4524, 1984. 126

[208] M. J. Calderon, Belita Koiller, Xuedong Hu, and S. Das Sarma. **Quantum control of donor electrons at the Si-SiO$_2$ interface**. *Phys. Rev. Lett.*, **96**:096802, 2006. 126, 130, 135, 137, 138, 141, 151, 169

[209] W. Kohn and J. M. Luttinger. **Theory of donor states in Si**. *Phys. Rev.*, **98**(4):915, 1955. 126, 128, 133

[210] B. Koiller, X. Hu, and S. Das Sarma. *Phys. Rev. Lett*, **88**:027903, 2001. 133

[211] B. E. Kane. **Silicon-based Quantum Computation**. *Fortschr. Phys.*, **48**:1023, 2000. 134

[212] A. Debernardi, A. Baldereschi, and M. Fanciulli. **Computation of the Stark effect in P impurity states in silicon**. *Physical Review B*, **74**:035202, 2006. 137

[213] C. Cohen-Tannoudji, B. Diu, and F. Laloë. *Quantum Mechanics.* John Wiley, 1977. 151, 170

[214] Wacquez Romain Roche Benoit Voisin Benoit Jehl Xavier Sanquer Marc Rogge Sven Verduijn Jan, Tettamanzi Giuseppe Carlo. **Mapping of single donors in nano-scale MOSFETs at low temperature**. *Silicon Nanoelectronics Workshop (SNW),* 2012 *IEEE*, Unpublished. 154, 172

[215] A. Baena, L. Brey, and M. J. Calderón. **Effect of strain on the orbital and magnetic ordering of manganite thin films and their interface with an insulator**. *Phys. Rev. B*, **83**:064424, 2011. 160

[216] A. Baena, A. L. Saraiva, Belita Koiller, and M. J. Calderón. **Impact of the valley degree of freedom on the control of donor electrons near a Si/SiO_2 interface**. *Phys. Rev. B*, **86**:035317, 2012. 160